

UNIVERSITY OF CALIFORNIA,
IRVINE

Condensed-Phase Photochemical Aging in Secondary Organic Aerosols

DISSERTATION

submitted in partial satisfaction of the requirements
for the degree of

DOCTOR OF PHILOSOPHY

in Chemistry

by

Vahe Joseph Baboosian

Dissertation Committee:
Professor Sergey A. Nizkorodov, Chair
Professor Ann Marie Carlton
Professor Craig Murray

2022

Chapter 2 © 2021 Royal Society of Chemistry

Chapter 3 © 2021 American Geophysical Union

Chapter 4 © 2020 American Chemical Society

Chapter 5 © 2022 Proceedings of the National Academy of Sciences

All other materials © 2022 Vahe Joseph Baboosian

Dedication

Իմ ընտանիքին և ընկերներին: To my family and friends.

Table of Contents

<i>List of Figures</i>	v
<i>List of Tables</i>	ix
<i>Acknowledgements</i>	xi
<i>Vita</i>	xiii
<i>Abstract of the Dissertation</i>	xvi
<i>Chapter 1: Introduction</i>	1
1.1 <i>Brief Context of Atmospheric Chemistry</i>	2
1.2 <i>Aerosol Chemistry</i>	3
1.3 <i>Secondary Organic Aerosol Complexity</i>	5
1.4 <i>Aerosol Aging</i>	7
1.4.1 <i>Particle Growth and Phase State at Varying Relative Humidity</i>	8
1.4.2 <i>SOA Viscosity</i>	10
1.4.3 <i>Photodegradation of SOA Leading to Particle Mass Loss</i>	11
1.4.4 <i>Photosensitized Particle Growth</i>	12
1.5 <i>Condensed-Phase Aging Techniques</i>	13
1.6 <i>General Methods of the Dissertation</i>	14
1.6.1 <i>SOA Generation in a Smog Chamber</i>	14
1.6.2 <i>SOA Generation in a Flow Tube Reactor</i>	16
1.6.3 <i>Collection Substrates</i>	17
1.6.4 <i>Ultra-performance liquid chromatography high resolution mass spectrometry</i>	18
1.7 <i>Structure of the Dissertation</i>	19
<i>Chapter 2: Quenching of ketones triplet excited states by atmospheric halides</i>	21
2.1 <i>Abstract</i>	22
2.2 <i>Introduction</i>	23
2.3 <i>Experimental</i>	24
2.4 <i>Results</i>	29
2.5 <i>Conclusion</i>	46
<i>Chapter 3: Naphthalene-derived secondary organic aerosols interfacial photosensitizing properties</i>	47
3.1 <i>Abstract</i>	48
3.2 <i>Introduction</i>	49
3.3 <i>Materials and Methods</i>	50
3.4 <i>Results and Discussion</i>	53
3.5 <i>Conclusions</i>	66
<i>Chapter 4: Photodegradation of Secondary Organic Aerosols by Long-term Exposure to Solar Actinic Radiation</i>	67
4.1 <i>Abstract</i>	68
4.2 <i>Introduction</i>	69
4.2 <i>Materials and Methods</i>	71
4.3 <i>Results and Discussion</i>	77

<i>4.4 Application to Ambient Conditions</i>	95
<i>4.5 Summary and Implications</i>	99
<i>Chapter 5: Sunlight can convert atmospheric aerosols into a glassy solid state and modify their environmental impacts</i>	102
<i>5.1 Abstract</i>	103
<i>5.2 Introduction</i>	104
<i>5.3 Materials and Methods</i>	106
<i>5.4 Results</i>	117
<i>5.5 Atmospheric Implications</i>	129
<i>Chapter 6: Summary and Future Work</i>	136
<i>6.1 Research Goals</i>	137
<i>6.2 Studying the Photosensitized Reactions Occurring in Anthropogenic SOA</i>	137
<i>6.3 Studying the Photodegradation of SOA</i>	138
<i>6.4 Preliminary Results on the UV degradation of Ambient BBOA</i>	140
<i>References</i>	152

List of Figures

Figure 1. 1: Radiative forcing for atmospheric species, relative to the year 1750	5
Figure 1. 2: A schematic of the steps involved in how a gaseous species interacts with a particle or droplet in the absence of a chemical reaction.....	9
Figure 1. 3: Commonly used methods of investigating photochemical aging of SOA resulting in the production of VOCs	13
Figure 1. 4: A diagram of the smog chamber used for this work.	16
Figure 1. 5: A diagram of the flow tube used for this work.....	17
Figure 1. 6: SOA substrates used for this work.	18
Figure 2. 1: Experimental setup for the laser flash photolysis.....	26
Figure 2. 2: Absorption and transient absorption spectra of solutions of xanthone, acetophenone and flavone.....	27
Figure 2. 3: Transient absorption decays of flavone triplet state in a deoxygenated aqueous solutions	30
Figure 2. 4: Transient absorption spectra of deoxygenated acetophenone solutions.....	34
Figure 2. 5: Transient absorption spectra of deoxygenated xanthone solutions.....	37
Figure 2. 6: A PDA chromatogram of naphthalene SOA integrated between 300 – 500 nm.....	41
Figure 2. 7: Steady state and transient absorption spectra of deoxygenated naphthalene SOA solutions	45
Figure 3. 1: Schematic of the experimental setup with the Go:PAM flow and aerosol flow reactors.....	51
Figure 3. 2: Median and mean diameter growths of Naphthalene-SOA exposed to UV light and SO ₂ in the aerosol flow tube	55
Figure 3. 3: Histograms of atom number in C and O containing compounds of the determined constituents in Naphthalene-derived SOA samples.....	63
Figure 3. 4: Van Krevelen diagrams for identified formulas in Naphthalene-SOA	63
Figure 3. 5: Median diameter growths of Naphthalene-derived SOA exposed to UV-A light and d-limonene and β -pinene	64
Figure 4. 1: SOA photodegradation setup using QCM.....	75
Figure 4. 2: A typical QCM experiment demonstrating how photodegradation rates are calculated from frequency data	78

Figure 4. 3: Control experiments showing mass loss under both dark and under 405 nm LED irradiation conditions	79
Figure 4. 4: Control experiments showing maximum mass loss rate from the QCM measurement scales linearly with the mass of SOA deposited on the QCM crystal during 305 nm irradiation experiments.....	80
Figure 4. 5: FMLR observed during 254 nm irradiation of TOL/OH and APIN/O ₃ SOA.....	81
Figure 4. 6: Mass loss rate, FMLR, and percent mass loss observed during 305 nm irradiation of various SOA types	82
Figure 4. 7: Repeated experiments with LIM/O ₃ SOA samples photodegraded under 305 nm LED radiation.....	83
Figure 4. 8: High-resolution ESI (+) mass spectra of irradiated and fresh LIM/O ₃ SOA	89
Figure 4. 9: Chemical composition characteristics of aged and unaged LIM/O ₃ SOA molecular species observed by ESI-MS	90
Figure 4. 10: Photodegradation of LIM/O ₃ SOA results in the formation/survival of compounds with a larger degree of aromaticity	93
Figure 4. 11: Photodegradation of APIN/O ₃ SOA and LIM/O ₃ SOA under different relative humidity conditions	94
Figure 4. 12: Spectral flux density of the 305 nm LED, 254 nm Pen Ray Lamp, Los Angeles summer solstice maximum, and the 24-hour average Los Angeles solar flux	96
Figure 4. 13: Scaling the FMLR and percent mass loss results to atmospheric conditions.....	96
Figure 4. 14: Predicted changes to the percent of mass remaining due to heterogenous OH aging alone, UV degradation alone, or the combined effect of UV and OH aging.....	98
Figure 4. 15: Comparison of percent mass loss with the extent of APIN/O ₃ photodegradation as found by O'Brien et al. (2019) and Zawadowicz et al. (2020).....	99
Figure 5. 1: The chamber used to irradiate SOA substrates	108
Figure 5. 2: Spectral flux density of the 305 nm LED and the 24-h averaged Los Angeles conditions (including day and night)	110
Figure 5. 3: Dependence of viscosity on the time particles spent in the poke-flow cell before the measurement	112
Figure 5. 4: Particle evaporation tests in the flow cell used for poke-flow experiments.....	113

Figure 5. 5: Summary of the experimental flow times as a function of relative humidity obtained from room temperature poke-flow experiments	114
Figure 5. 6: Viscosity of SOA derived from ozonolysis of d-limonene and α -pinene measured at room temperature	117
Figure 5. 7: Comparison of previously published viscosities of limonene SOA to the control d-limonene SOA produced in an environmental chamber and flow tube	118
Figure 5. 8: Control Experiments showing aging of hydrophobic coatings on glass slides by UV exposure	119
Figure 5. 9: Comparison of previously published viscosities of α -pinene SOA to the control α -pinene SOA.....	120
Figure 5. 10: Chemical composition of control and aged d-limonene ozonolysis SOA produced in the smog chamber	121
Figure 5. 11: HRMS analysis of d-limonene ozonolysis SOA produced in the flow tube and changes in chemical composition due to aging.....	123
Figure 5. 12: HRMS analysis of α -pinene ozonolysis SOA produced in the flow tube and changes in chemical composition due to aging.....	124
Figure 5. 13: Chemical composition-based viscosity predictions	128
Figure 5. 14: Parametrization of the dependence of viscosity on water activity for control and aged SOA derived from d-limonene ozonolysis.....	131
Figure 5. 15: Viscosity of control and aged d-limonene SOA as a function of RH and temperature	132
Figure 5. 16: A comparison of the effect of aging by UV-radiation on the zonally-averaged SOA viscosity as a function of altitude and latitude in the troposphere	133
Figure 5. 17: A comparison of the effect of aging by UV-radiation on the zonally-averaged mixing times of organic molecules within 200 nm SOA.....	134
Figure 6. 1: Ambient BBOA sampling on December 3, 2020.....	140
Figure 6. 2: Ambient BBOA photodegradation setup with a 305 nm LED as the irradiation source	141
Figure 6. 3: QCM and PTR-MS data showing the FMLR of Bond Fire Organic Aerosol compared to d-limonene ozonolysis SOA FMLR using the same 305 nm LED.....	143
Figure 6. 4: a) Cyclical photodegradation of Bond Fire organic aerosol.....	144

Figure 6. 5: Calibration experiments used to correct the VOC concentration measurements
detected by the PTR-MS 147

Figure 6. 6: Mass spectrum of ambient BBOA collected during the bond fire 150

List of Tables

Table 2. 1: First-order rate constants and triplet lifetimes of atmospheric ketones in the absence of quenchers	31
Table 2. 2: Rate constants for quenching of ketones triplet states by different halide ions following excitation at 266 nm and 355 nm, redox potentials ($E(X^-)/X$) for the anions and the free energy of the electron transfer ΔG_{ET}	32
Table 2. 3: Compounds identified in the presence of xanthone and halide ions upon irradiation or in darkness by UHPLC-MS	38
Table 2. 4: Ten most prominent NAPH/OH/NO _x compounds from UPLC-PDA-MS analysis of the SOA solution.....	42
Table 3. 1: Photosensitized uptake based Median Diameter Growth Factor of Naphthalene-SOA with different gaseous compounds and RH	54
Table 3. 2: Chemical composition of compounds tentatively determined in Naphthalene-derived SOA.....	58
Table 4. 1: QCM parameters determined from long-term photodegradation experiments	73
Table 4. 2: Peak abundance weighted average composition characteristics of aged and control LIM/O ₃ SOA.....	91
Table 4. 3: List of 10 molecular formulas with the largest peak abundances in ESI-MS(+) spectra in the fresh SOA, photorecalcitrant, and photolabile groups.....	92
Table 4. 4: Bi-exponential fit parameters used to fit percent mass loss profiles of different SOA types after correcting for evaporation and scaled to the 24-hour average Los Angeles flux.....	97
Table 5. 1: Summary of SOA production conditions in both the environmental chamber and aerosol flow tube for both viscosity measurements and HRMS analysis.....	107
Table 5. 2: COMSOL parameters used to simulate the experimentally observed flow times and determine the upper and lower bounds of viscosities of the SOA particles.	115
Table 5. 3: Summary of chemical composition characteristics of d-limonene ozonolysis SOA produced in an environmental chamber and a flow tube, and of flow tube produced α -pinene ozonolysis SOA	122

Table 6. 1: Calculated FMLR values for specific photoproduct VOCs, a VOC with an average mass of 50 g mol^{-1} , and the summed FMLR from formic acid, acetic acid, and acetaldehyde being produced.....	148
Table 6. 2: Top 20 most abundant compounds present in ambient BBOA collected during the Bond fire	150

Acknowledgements

There are many people that made this dissertation possible. First, I would like to thank my advisor, Professor Sergey Nizkorodov. I have loved every moment of being in his lab. He gave me the independence I needed to work at my own pace, but he was always there to offer advice or mentoring when I needed it. He was always available to chat about anything, whether it be about experiments or life in general, which I truly appreciated. When experiments weren't going well, he always had some idea to help me get on the right track again. Sergey really does care about his students and makes you feel as you're part of a family, this became increasingly evident as I progressed in this program. Thank you, Sergey, for providing me with so many amazing experiences and a fantastic mentorship. I'm honored to be graduating from your group and will miss you dearly.

Moreover, I would like to thank the past and present Nizkorodov group members for creating the best, most enjoyable work experience I could ask for. I wouldn't have enjoyed these last 5 years the way I have if it wasn't for the triplets (Alex, Natalie, and I) always making jokes no one can understand and making what seemed like endless amounts of "tar" coffee.

I would also like to thank my committee members, Professor Craig Murray and Professor Ann Marie Carlton. Both of you have guided me to where I am today and I am very thankful to you. I began my research career in Prof. Craig Murray's laboratory as an undergraduate student and have learned a lot from him. I am thankful for all the time Prof. Murray invested in my growth as a researcher and for constantly pushing me to do the best work I can possibly do. I really appreciate your straightforward attitude towards the importance of details and presentation of research. Your strive towards high quality work really stuck with me and is something I hope to carry on towards future careers.

Professor Carlton is a big reason why I returned to UCI for my graduate research work. After graduating UCI as an undergraduate, I was a bit apprehensive to return after hearing things like "You shouldn't go back to the same school." "You should expand and go somewhere else." "Returning to the same school is looked down upon by employers." I remember speaking to Prof. Carlton about this and she told me that if a company doesn't want to hire you because of returning to the same school, then that's a company you don't want to work for. This encouraged me to

continue my goal of conducting atmospheric chemistry research and return to UCI, one of the top places to accomplish this. A decision I never regret. Thank you Prof. Carlton for teaching me to be persistent with my goals and not letting others' opinions sway you away from them.

I am extremely thankful to our collaborators including Dr. Antoinette Boreave, Dr. Clement Dubois, Dr. Stephane Dumas, Dr. Corinne Emmelin, Dr. Dmitry Fishman, Dr. Rachel Gemayel, Dr. Christian George, Dr. Kangwei Li, Dr. Sébastien Perrier, Dr. Sophie Tomaz, and Dr. Xinke Wang, who worked on the photosensitized reactivity experiments discussed in Ch. 2 and 3. I would also like to thank Yiran Gu for her work on the humidity-dependent photodegradation experiments conducted in Ch. 4. Last but not least, I would like to thank Prof. Allan Bertram, Jesse Crescenzo, Dr. Yuanzhou Huang, Dr. Fabian Mahrt, and Prof. Manabu Shiraiwa for their work in Ch. 5 on the viscosity changes of SOA due to photodegradation. Working with you all has been an absolute joy and I have learned so much from you all. I will particularly cherish travelling to Lyon, France to work with Dr. Wang and Dr. George. I have so many fond memories with you during that time that I will hold onto forever.

I would also like to thank the National Science Foundation Graduate Research Fellowship Program for supporting a large amount of my PhD work. Also thank you to *ACS Earth & Space Chemistry*, *Environmental Science: Atmospheres*, *Geophysical Research Letters*, and *Proceedings of the National Academy of Sciences* for allowing me to reuse my published work as part of this dissertation.

Last, but not least, I would like to thank my family, especially my wife, and friends for their love and support over the past 5 years. Thank you for always being there for me and for all the endless fun we have together.

Vita

Vahe Baboosian

Education

Doctorate of Philosophy in Chemistry
GPA: 3.994

University of California, Irvine
September 2017 - Present

Masters of Science in Chemistry
GPA: 3.975

University of California, Irvine
September 2017 - September 2018

Bachelors of Science in Chemistry
GPA: 3.718

University of California, Irvine
October 2014 - June 2016

Skills

Instrumentation: HPLC-HRMS, GC-MS, PTR-ToF-MS, FTIR, UV-Vis Spectrometer, Quartz Crystal Microbalance, Laser Transient Absorption Spectroscopy, Direct Analysis in Real Time Mass Spectrometer, Aerosol Mass Spectrometer, Scanning Mobility Particle Sizer

Software: Python, R, Mathematica, Igor Pro, Origin, Tableau, Autodesk Inventor, MS Office, MzMine, Thermo Compound Discoverer, Xcalibur/Freestyle, PTR-Viewer, Photoshop, LaTeX

Certifications: R Studio Data Analysis, Bilingual in Armenian, Public Speaking, Mentoring Excellence Program

Work Experience

Graduate Student Researcher
Nizkorodov Laboratory

Irvine, California
February 2018 – Current

- Designed experiments to research the photo-chemical transformations of aerosols and their effects on the atmosphere.
- Prepared reports and presented findings at national conferences.
- Operated/calibrated instrumentation used to identify molecular species in atmospheric pollution samples: HPLC-MS(MS2), PTR-ToF-MS, GC-MS, FTIR, UV-Vis spectroscopy, Nanosecond transient absorption spectroscopy
- Performed data analysis on all data using Excel, Python, R, Mathematica.
- Maintained field and lab instrumentation including calibration, part repair/replacement, and troubleshooting.
- Mentored undergraduate students and two high school students on experimental design and chemical understanding of research projects. Their work resulted in peer-reviewed journal publications.
- Updated lab safety certifications, chemical inventory, and ensuring lab members are compliant with environmental health and safety (EH&S) standards.
- Acted as liaison between EH&S and all chemistry department labs to ensure the safety concerns of researchers are met. Organized safety training sessions and created transitional protocols during COVID-19.

Graduate Teaching Assistant
University of California, Irvine

Irvine, California
September 2017 – June 2019

- Worked as a teaching assistant for Quantum Principles and Nuclear Chemistry lecture courses as well as General Chemistry and Honors Analytical Chemistry labs.

- Lectured courses and prepared class materials including homework assignments, quizzes, midterms, and finals.

Undergraduate Researcher
University of California, Irvine

Irvine, California
 September 2015 – June 2016

- Investigated the gas phase kinetics of free radical reactivity produced from the oxidation of atmospheric volatile organic compounds using cavity ring down spectroscopy.
- Designed/performed experiments, aligned optics, calibrated instrumentation, conducted data analysis, and maintained/repared instrumentation.
- Prepared reports and presentations findings at conferences.

Stock Room Chemist
Glendale Community College

Glendale, California
 July 2013 - June 2014

- Prepared chemical solutions, calibrated instruments, and organized inventory in chemistry stock room.

LA Fashion Market Registration Manager
California Market Center

Los Angeles, California
 June 2012 - June 2016

- Managed a group of twenty employees who registered and verified credentials of retail store buyers to purchase wholesale goods.
- Led outreach to retail store owners to increase tradeshow attendance. This included calling retail stores to tailor their experience at the trade show.

Projects/Publications

Long Term SOA Photodegradation – *Quartz Crystal Microbalance, HRMS*

Quantifying the long term photodegradation of biogenic and anthropogenic secondary organic aerosols under dry and humid conditions. The degraded aerosol is characterized using high resolution mass spectrometry techniques. DOI:10.1021/acsearthspacechem.0c00088

Photosensitized Uptake of SO₂ – *Aerosol Mass Spectrometer, Scanning Mobility Particle Sizer*

Discovering a new chemical mechanism: the photosensitized reactive uptake of SO₂ into particle phase sulfate. The particle growth was quantified using a scanning mobility particle sizer while the production of sulfate in the particles was monitored with an aerosol mass spectrometer. DOI:10.1029/2021GL093465

Triplet Reactivity within SOA – *Nanosecond Transient Absorption Spectroscopy, HPLC-HRMS*

Studying triplet state reactivity within naphthalene derived secondary organic aerosol. The kinetics of the reactions were calculated using transient absorption spectroscopy. DOI:10.1039/d0ea00011f

Glassy aerosol formation in the atmosphere due to UV-aging - *HPLC-HRMS*

Discovering glassy/highly viscous aerosol formation in the atmosphere due to long-term UV aging. The global distribution of glassy aerosol were modelled and its effects on climate and cloud formation are discussed.

Manuscript Submitted

Light absorption properties of indole SOA under various oxidant and humidity conditions - *HPLC-PDA-HRMS, UV-Vis*

Quantifying the light absorption and scattering properties of indole SOA prepared under various oxidant (OH, O₃, NO₃) and humidity conditions. Extinction coefficients of the aerosol were calculated and chromophores responsible for the light absorption were identified.

Manuscript in Preparation

High Altitude Weather Balloon - *Python, Autodesk Inventor*

Custom made a high altitude weather balloon which reached a maximum altitude of 103,000 feet.

Programmed an Arduino Uno to collect/broadcast a live feed of pictures, video, as well as temperature, speed, and altitude measurements.

Team 696 FRC Robotics Competition - Python, Autodesk Inventor

Led mechanical team in engineering a custom made 6' robot designed to play basketball. Designed the mechanical system for collecting and shooting basketballs.

Presentations

Pacifichem 2021 Poster Presentation

Humidity dependent viscosity of the photo-recalcitrant fraction of biogenically derived SOA

Online
December 2021

AAAR 2021 Platform Presentation

Condensed phase photochemical aging of Secondary Organic Aerosol and its Effects on Viscosity

Online
October 2021

ISKPPA 2021 Kinetics Conference Oral Presentation

Viscosity of the photo-recalcitrant fraction of biogenically derived SOA

Online
February 2021

AAAR 2020 Platform Presentation

Photodegradation of secondary organic aerosols by long-term exposure to solar actinic radiation

Online
October 2020

AAAR 2019 Platform Presentation

Condensed Phase Photochemical Reactions of Secondary Organic Aerosols: Photodegradation and Photosensitized Reactions

Portland, Oregon
October 2019

ACS 2019 Oral Presentation

Long Term Photodegradation of Secondary Organic Aerosols

San Diego, California
August 2019

Air UCI Retreat Oral Presentation

Direct and Indirect Forms of Secondary Organic Aerosol Aging

Lake Arrowhead, California
September 2018

Southern California Undergraduate Research Conference Oral Presentation

Non-thermal Reactivity of Gas Phase Intermediates

Long Beach, California
April 2016

Awards and Fellowships

Pacifichem 2021 Travel Grant

Awarded to attend Pacifichem conference as a presenting author

ACS Pacifichem
December 2021

AAAR Travel Grant

Awarded to attend AAAR conference as a presenting author

American Association for Aerosol Research
October 2021

Safety Award

Recognized as a safety representative for implementing and following safe laboratory procedures

University of California, Irvine
May 2019

NSF Graduate Research Fellowship

Recognizes and supports outstanding graduate students who are pursuing research-based Master's and doctoral degrees

National Science Foundation
April 2019

Hypercube Scholar Award

Given to an outstanding undergraduate researcher

University of California, Irvine
May 2016

SCURC Outstanding Oral Presentation Award

Award given to the best oral presentation in the physical chemistry division of the SCURC conference

California State University, Long Beach
April 2016

Abstract of the Dissertation

Condensed-Phase Photochemical Aging in Secondary Organic Aerosols

By

Vahe Joseph Baboosian

Doctor of Philosophy in Chemistry

University of California, Irvine, 2022

Professor Sergey A. Nizkorodov, Chair

The net effect of aerosols on the Earth's climate is highly uncertain. Secondary organic aerosols (SOA) contribute heavily to this uncertainty due to their complex chemical composition. This uncertainty is enhanced by the fact that SOA can be physically and chemically transformed as it slowly disperses through the atmosphere, a process known as aging. These aging processes further complicate the interpretation of the climate effects of aerosols. The condensed-phase aging occurring inside aerosol particles is an active area of research, with condensed-phase photochemistry driven by ultraviolet (UV) solar radiation being an area of particular interest. Recently, a number of studies have found that condensed-phase photochemistry of SOA can have a profound effect on its chemical composition and subsequent effects on climate. However, the role of these aging processes in controlling the climate and air pollution is still highly uncertain.

In this dissertation, model SOA was generated in either an aerosol flow tube reactor or smog chamber from a variety of aerosol precursors and oxidants. Chapter 2 discusses the triplet reactivity of select carbonyl compounds that are known photosensitizers that can be found in SOA using nanosecond transient absorption spectroscopy. The photosensitized reactivity of SOA arising from the photooxidation of naphthalene was also investigated. Combining the study of these individual and known photosensitizers with those formed in the atmosphere demonstrates that tropospheric photosensitization may involve a large variety of compounds and will introduce previously unconsidered chemical pathways that impact atmospheric multiphase chemistry. Chapter 3 extends these ideas and discusses the photosensitized uptake of SO₂ into naphthalene photooxidation SOA. The aerosol particles were observed to grow in size and sustain photosensitized processes resulting in the production of particle phase sulfate ($0.2 - 0.3 \mu\text{g m}^{-3} \text{h}^{-1}$). As naphthalene and other polycyclic aromatics are important SOA precursors in the urban

and suburban areas, these photosensitized reactions are likely to play an important role in sulfate and SOA formation.

Chapter 4 discusses the long-term photodegradation of SOA produced from biogenic and anthropogenic precursors. The experiments relied on a quartz crystal microbalance (QCM) to quantify the mass loss rate from SOA materials while being irradiated by a 305 nm UV LED. Long-term changes in the chemical composition of SOA were examined using high-resolution electrospray ionization mass spectrometry. These experiments confirm that condensed-phase photochemistry is an important aging mechanism for SOA during long-range transport. Chapter 5 builds on the result of Chapter 4, and investigates the viscosity and phase state of UV-irradiated SOA. The viscosity of UV-irradiated SOA was measured after an equivalent UV exposure of 6–14 days at midlatitudes in summer. Results indicate that the viscosity and characteristic mixing times of organic molecules within an SOA particle can be as much as five orders of magnitudes larger for aged SOA. The increase in viscosity likely leads to an increased abundance of glassy SOA particles that can act as ice nuclei in the atmosphere. Furthermore, the increase in viscosity and mixing times can impede gas-particle partitioning and heterogeneous chemistry. Overall, results clearly demonstrate that aging driven by condensed-phase photochemistry needs to be considered when predicting the environmental impacts of SOA.

Chapter 6 discusses preliminary work on quantifying the mass loss and volatile organic compound (VOC) production from ambient biomass burning organic aerosol (BBOA). BBOA was collected using an impactor onto QCM crystals during the December 2020 Santiago Canyon Bond Fire. Experiments involved irradiating the BBOA substrates using a 305 nm LED while simultaneously measuring the mass loss rates using a QCM and photoproduced VOCs using a proton transfer reaction mass spectrometer. These preliminary experiments indicate that photodegradation of ambient BBOA can be a large source of VOCs, particularly formic acid, in the atmosphere.

On the whole, this dissertation makes a strong case for the critical importance of condensed-phase photochemistry in determining climate-relevant properties of organic aerosols.

Chapter 1: Introduction

1. Background

1.1 Brief Context of Atmospheric Chemistry

The Earth's atmosphere is comprised of several different layers, each with their own unique characteristics. The troposphere begins at sea level and continues for about 15 km. The troposphere is characterized by decreasing temperature with altitude and the air within the layer is vertically well-mixed due to the heating of the Earth's surface by solar radiation.¹ The stratosphere lies above the troposphere and continues until about 50 km. It is characterized by increasing temperature with altitude resulting in much slower vertical mixing compared to the troposphere. This is due to the ozone (O₃) layer absorbing incoming radiation in the stratosphere.¹

Although most of life on the planet would not exist without the stratosphere blocking incoming ultraviolet radiation, much of the atmospheric chemistry affecting living organisms occurs in the troposphere due to a combination of warm temperatures, convective transport, water prevalence, and their proximity to the biosphere and hydrosphere.²

Atmospheric chemistry has had its beginnings rooted in studying the fundamental chemical processes occurring in the troposphere and stratosphere. Considerable efforts have been placed in studying the photochemistry of small molecules (e.g., NO, O₃, H₂O).³⁻⁷ Different parts of the atmosphere have varying wavelengths of radiation accessible to them. For example, the troposphere only has access to wavelengths longer than 290 nm because the ozone layer in the stratosphere absorbs radiation between 200 and 290 nm.⁸ The stratosphere contains solar radiation that extends much further into the ultraviolet regime of the electromagnetic spectrum. This creates interesting differences in photochemistry for a given atmospheric species depending on if it is in the troposphere or stratosphere. For example, photochemistry of carbonyls in the troposphere are driven by weak $n \rightarrow \pi^*$ transitions but are driven by much stronger (shorter wavelength) $\pi \rightarrow \pi^*$ transitions in the stratosphere.⁹ These different transitions can affect the photochemical reactivity of the excited molecule. For example, the quantum yield of O(¹D) from the photolysis of ozone is constant at unity below 300 nm but sharply decreases at 308 nm down to a quantum yield below 0.1 above 313.5 nm.¹⁰ A similar effect is observed during the photolysis of nitrite ion in water where the quantum yield of hydroxyl radical formation decreases as the photolysis wavelength increases.¹¹

In more recent years, studies have shifted away from exclusively gas-phase reactions and towards multi-phase processes including gases, particles, aqueous droplets, and surfaces (both indoor and outdoor).^{12,13} This shift in research efforts are due to the inability to explain the mixing ratios of atmospheric constituents using only gas phase processes. Multi-phase processes needed to be considered in order to narrow the gap in uncertainty. Some of the most notable examples involving multi-phase reactions include the reactions of HCl and ClONO₂ on stratospheric ice clouds,¹⁴ the loss of glyoxal on aerosols,¹⁵ the loss of N₂O₅ on aerosols,^{16,17} and the oxidation of SO₂ in fog droplets.¹

1.2 Aerosol Chemistry

Aerosols are defined as liquid or solid particles that are suspended in a gas and typically consist of sizes ranging from 10⁻⁹ – 10⁻⁴ m.^{1,18,19} There are a variety of aerosol types in the Earth's atmosphere and are typically separated into inorganic aerosols and organic aerosols (OA). OA's predominantly contain organic compounds (i.e., compounds made from carbon, hydrogen, oxygen, nitrogen) while inorganic aerosols contain inorganic compounds such as sulfuric acid and its salts, nitric acid and its salts, black carbon, and metal oxides.²⁰ Both types of aerosols can contain varying amounts of liquid water in the particle phase known as aerosol liquid water (ALW).²¹ Compounds within aerosols internally mix though, which results in a continuum of compositions ranging from being completely inorganic to completely organic. Aerosols can also be externally mixed, where different types of particles are in the same air mass but are individually different.

OAs are further separated into two groups depending on how they are formed: primary organic aerosols (POA) and secondary organic aerosols (SOA). POA is produced directly by individual sources like biomass burning, automobile exhaust, and factory plumes.²² Global estimates of POA can be upward of 30 Tg y⁻¹.²² SOA are produced indirectly through the oxidation of anthropogenic and biogenic volatile organic compounds (VOCs).^{19,20,22} Atmospheric oxidants include ozone (O₃), hydroxyl radical (•OH), chlorine, and during the nighttime, nitrate radical (•NO₃).^{18,23} In more urban areas, oxides of nitrogen (NO_x) are present²⁴ and can react along with other oxidants to oxidize VOCs and produce OA.²⁵⁻²⁷ The oxidation of VOCs leads to lower volatility compounds, these lower volatility compounds can further react with oxidants. After multiple cycles of oxidation, the oxidized VOCs (OVOC) have a vapor pressure low enough that they can partition

into pre-existing particles or participate in new particle nucleation.^{28,29} Global estimates of SOA production are contested with values between a few to hundreds of Tg y^{-1} .^{18,30}

In practice, the differentiation between POA and SOA is difficult as OA is known to be quite complex. For example, semi volatile gasses from POA can evaporate in the atmosphere and partition into a pre-existing SOA particle. Another possibility is a gas evaporating from POA, reacting with an oxidant, and forming SOA.^{31,32} Thus, the line between POA and SOA is blurred in the atmosphere and is difficult to separate.

Aerosols have several important negative health implications. Exposure to aerosols smaller than $2.5 \mu\text{m}$ ($\text{PM}_{2.5}$) has been shown to have strong statistical correlations with cardiovascular disease,³³ respiratory cancers,³⁴ overall reduction in life expectancy,³⁵ and several other illnesses.³³⁻³⁷

Aerosols also have important climate effects as they can directly affect the Earth's climate by absorbing or scattering sunlight, which also reduces visibility.^{1,18,38,39} Depending on their chemical composition and thus their hygroscopicity, these particles can also indirectly affect climate by acting as nuclei onto which water can condense to form cloud droplets.⁴⁰ Since the chemical transformations of aerosol particles are still not fully understood, their net effect on climate remains uncertain.^{18,41-43} For example, the latest Intergovernmental panel on climate change (IPCC) report has shown radiative forcing by aerosols to span between positive and negative values, indicating a large uncertainty between the net cooling or warming of the atmosphere due to aerosols (Fig. 1.1).⁴⁴ Furthermore, the report suggests that the composition of the aerosols largely dictates if the aerosols have a warming or cooling effect.^{44,45} This uncertainty can be minimized if the chemistry of aerosols becomes more understood.

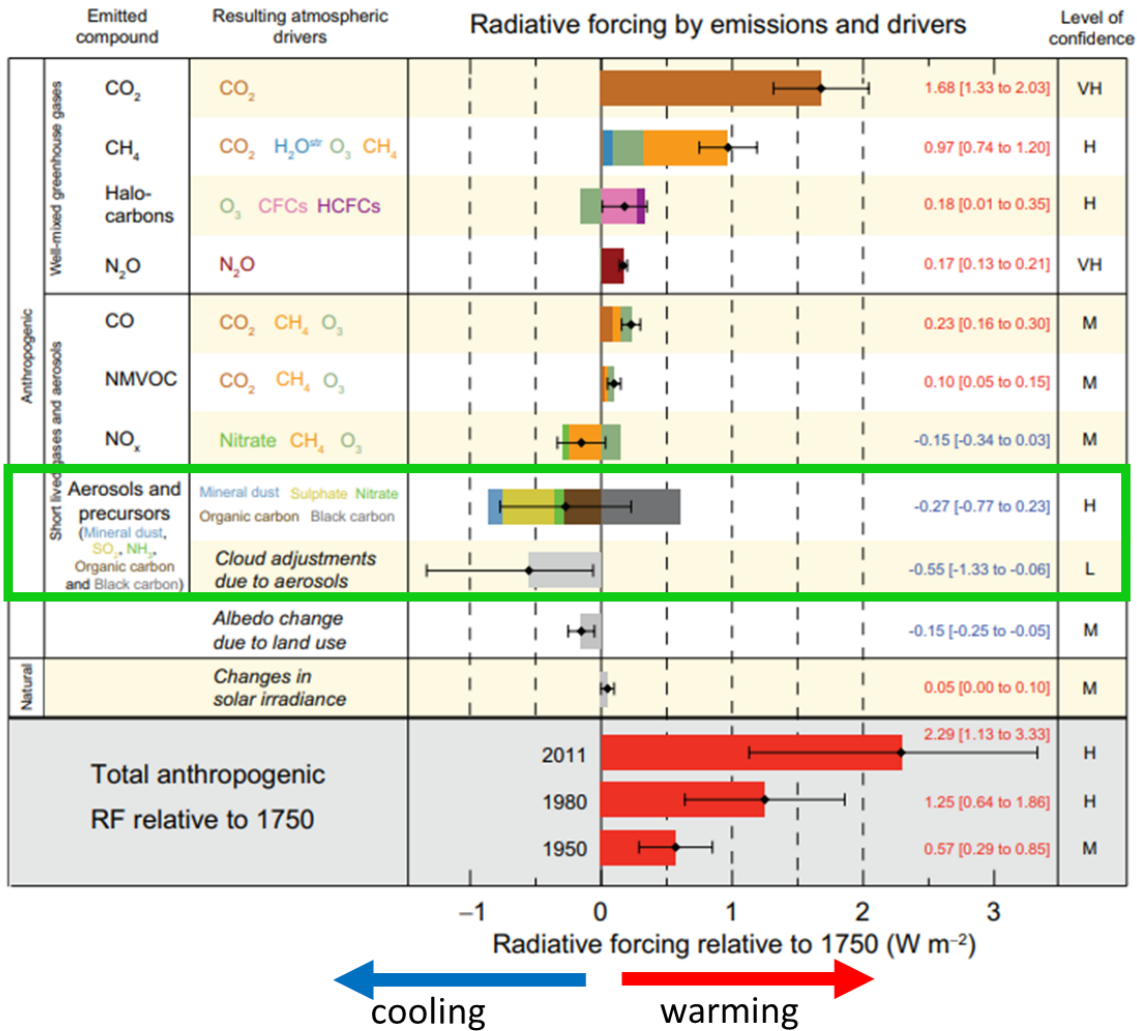


Figure 1. 1: Radiative forcing (W•m⁻²) for atmospheric species, relative to the year 1750. The green box highlights the contribution from aerosols. Figure adapted from Figure SPM.5 in IPCC, 2013: Summary for Policymakers.⁴⁴

1.3 Secondary Organic Aerosol Complexity

The composition of SOA is very complex and depends on multiple environmental factors. Even if SOA is produced from a single VOC, there can be thousands of oxidations products present.⁴⁶⁻⁵⁰ This can become even more complex if the SOA is formed by the oxidation products of multiple VOCs (e.g. α -pinene and isoprene).^{48,51-53} Furthermore, the composition strongly depends on the VOC type, oxidant type, VOC : oxidant ratio, presence of NO_x, temperature, humidity, ALW content, and actinic flux.

For example, under dry conditions, SOA produced from aromatic hydrocarbons and hydroxyl radical oxidation have a lower yield if NO_x is present compared to low NO_x conditions.⁵⁴ On the other hand, SOA formed through aqueous processing follows the opposite trend.⁵⁵ For example, SOA formed from the aqueous processing of methylglyoxal, a gas-phase oxidation product of many aromatic compounds, has higher SOA yields if NO_x is present.⁵⁵ The presence of NO_x does not only affect SOA derived from anthropogenic VOCs. Biogenic SOA (e.g., isoprene SOA) produced under high NO_x conditions contains less isoprene epoxydiols (IEPOX) relative to methyl vinyl ketone or methacrolein.⁵⁶ Furthermore, isoprene SOA formed in areas with NO_x contain more organic nitrate compounds, whereas isoprene SOA produced in areas free of NO_x contain more highly oxygenated C₅ compounds.⁵⁷ As mentioned, SOA composition also depends on the oxidant concentrations. For example, biogenic precursors produce a much higher yield of low volatility compounds when formed under elevated ozone conditions compared to high NO_x conditions.⁵⁸ SOA production yields and composition are also dependent on the amount of ALW present, as it affects the particle phase partitioning of semi-volatile compounds and the subsequent particle phase reactions of those compounds.²¹ For example, the SOA yield of acetylene SOA doubles in high ALW conditions relative to low ALW conditions and is attributed to increased aqueous phase partitioning and particle phase reactions of the glyoxal oxidation product.⁵⁹ Thus, the composition of SOA is highly variable and depends on the environmental conditions it is formed under. In order to obtain a broader understanding of SOA in the atmosphere, a variety of SOA types and oxidant conditions should be studied. Many SOA types in varying conditions were produced and studied for this dissertation.

The presence of seeds can also strongly influence the composition and yield of SOA. For example, isoprene derived SOA yield has been found to increase when formed in the presence of sulfate seeds⁶⁰ due to increased particle phase acidity and subsequent increased oligomer formation.⁶¹ This may result in an overestimate of the realistic aerosol yield found in the environment. Similar effects have been observed from the α -pinene SOA system by varying the seed type and acidity under which it is formed. α -pinene SOA yield increased by 40% under acidic seed conditions and the molecular species larger than 300 Da were also enhanced when formed with sulfuric acid seeds compared to ammonium sulfate seeds.⁶²

1.4 Aerosol Aging

Once formed in the atmosphere, SOA are transported throughout the troposphere.^{63–65} SOA have average lifetimes on the order of one to two weeks,⁶⁶ but can be considerably longer with increasing altitude. During this atmospheric transport, SOA particles can undergo “aging” (i.e., a gradual change in chemical composition and properties) by multiple processes, including heterogeneous oxidation,^{67–69} aqueous phase photooxidation,^{70–73} photosensitized uptake of gases,^{74–77} and ultraviolet (UV) photolysis of particle constituents.^{78–83} These processes transform aerosol composition and size, thus affecting their ability to absorb/scatter sunlight.^{20,45,84–87} One example of chemical aging processes is the gas phase oxidation of a semi-volatile compound that evaporated from a particle,³¹ followed by the oxidation products re-partitioning into the particle. However, there are other, potentially more important, forms of chemical aging such as heterogeneous reactions on the particle surface or condensed-phase reactions within the particle.^{68,88,89} For example, gaseous sulfur dioxide can be oxidized in fog droplets and form particle phase sulfate and sulfuric acid.⁹⁰ Furthermore, N_2O_5 (a reservoir species for NO_x) can be removed from the gas phase by aerosols, drastically reducing its ozone forming potential.^{16,17,91} Condensed phase UV photolysis has been reported to decrease mass, increase the oxidation state, decrease the volatility, and decrease the light absorption and scattering ability of SOA particles^{74,78,81,92–94}.

Experiments that simulate aging often involve exposing a chemical compound representative of the SOA to an oxidant in a reactor.^{95,96} More recent studies have studied the aging of the entire SOA sample, which consists of thousands of compounds and is more environmentally relevant. For example, after being formed in a chamber, SOA from α -pinene,⁸⁵ toluene,⁸⁶ and polycyclic aromatic hydrocarbons (PAHs)⁸⁷ were aged by exposing them to hydroxyl radical and UV irradiation. Depending on the aging process, organic aerosol concentrations have been found to increase or decrease. For example, the photochemical aging of toluene high NO_x SOA resulted in increased aerosol concentrations and increased oxidation and lower volatility compounds within the SOA.⁸⁶ Another interesting example is the aging of α -pinene SOA under either high OH concentrations or under low OH concentrations and UV irradiation. Aging under high OH concentrations led to increased organic aerosol by a factor of 2-3 due to gas phase vapors being functionalized, lowering their volatility, and subsequently partitioning into the particle phase. Under low OH concentrations and UV irradiation however, fragmentation of highly functionalized

secondary oxidation products leads to substantial organic aerosol loss.⁸⁵ These examples help demonstrate how complicated the chemistry occurring within SOA can become. More studies are needed to better understand the extent of aging and chemical mechanisms responsible for SOA aging in the atmosphere.

A large uncertainty in these chamber aging experiments is whether the effect of aging comes from gas phase or particle phase processes. One way to better understand this is to separate the two and study the particle phase processes individually. Multiple studies have done this and have found condensed phase aging to be very important.^{74,80-82,92,97} For example, in an experimental study by Epstein et al.,⁹² SOA was generated from a chamber and flowed through a series of denuders to remove any oxidants and some VOCs, allowing the particles to pass through. The particles were then aged with UV radiation in a flow tube and found that the mass loss from condensed phase photochemical reactions were fast enough to compete with other forms of aging and should be considered.

1.4.1 Particle Growth and Phase State at Varying Relative Humidity

Uptake of a gas into a particle causes the particle to grow, thus affecting its climate forcing properties as larger particles scatter sunlight more efficiently.^{98,99} The general mechanism for particle growth in the atmosphere is through uptake of gases. This mechanism involves several steps including diffusion through the gas phase to the surface, adsorption at the surface and mass accommodation, and diffusion through and incorporation into the bulk.¹⁰⁰⁻¹⁰² After the gaseous molecule is incorporated into the particle, it can either react with another molecule in the particle phase (reactive uptake) or can desorb back out into the gas phase (Figure 1.2).

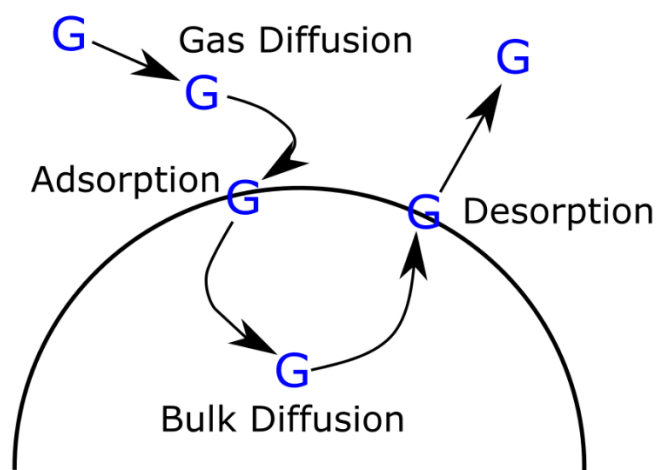


Figure 1. 2: A schematic of the steps involved in how a gaseous species (G) interacts with a particle or droplet in the absence of a chemical reaction.

The phase of the particle has important implications for mechanisms by which gases will interact with the particle and how it will grow. A liquid droplet will reach a thermodynamic quasi-equilibrium between the particle and gas phases very quickly with intraparticle diffusion timescales on the order of seconds.^{18,29,31,103–105} These particles will be well-mixed or homogenous in composition. However, under certain conditions (i.e., low RH and/or low temperature), SOA do not exist as a liquid droplet, but rather as a semi-solid or glassy phase state.^{106–114} In fact, a study by Shiraiwa et al.¹¹⁵ showed that a majority of the tropospheric SOA particles exist as a solid or semi-solid phase. In this case, the interactions between gasses and the particle phase will occur on a slower time scale and will be controlled by a kinetically limited, diffusion mechanism. Diffusion limitations from these viscous particles lead to hindered evaporation of bulk phase compounds. For example, a study using a particle core of limonene SOA coated with β -pinene observed that the outer surface layer of the particle evaporated preferentially over the inner core limonene compounds, due to the kinetic diffusion limitation of the inner core.¹¹⁶ Another study investigated the incorporation of organic nitrate compounds into the particle phase of glassy α -pinene derived SOA and found that the amount of organic nitrates incorporated into the particle phase was much larger if the incorporation occurred during particle growth rather than after particle growth. This suggested that enhanced uptake of organic nitrates during SOA formation and growth is due to a kinetically controlled “burying” mechanism, rather than equilibrium partitioning.¹¹⁷

Interestingly, whether or not an aerosol exists in a glassy phase state depends on the conditions in which it was formed. For example, one study found α -pinene derived SOA formed under humid conditions was less viscous than when formed under dry conditions, with an increased contribution from carboxylic acids under humid conditions and a decreased contribution from higher molecular mass products under dry conditions. Furthermore, α -pinene derived SOA that was formed dry and subsequently humidified remained solid even under high RH conditions.¹¹⁸ This makes a strong case for the importance of understanding the phase state dependence on RH for a variety of SOA types, formed under various conditions.

The humidity of the air surrounding the particle drastically affects its phase state.¹¹⁹ Increased humidity leads to water uptake into the particle and subsequently causes the particle phase state to more become more similar to a liquid droplet (with faster diffusion times).^{106,111,119,120} This has important implications for particle growth and reactivity mechanisms. For example, Renbaum-Wolff et al.¹¹¹ found that α -pinene SOA ranged from solid to liquid phases across the range of atmospheric relative humidity (RH) and found that gas-particle partitioning was limited to the surface of the particle at $\text{RH} \leq 30\%$. Assuming instantaneous equilibrium partitioning would result in an overprediction of particle phase semi-volatile and low-volatility organic compounds by an order of magnitude. Thus, SOA studies should be conducted at various RHs in order to accurately describe the various phases of SOA in all parts of the world.

1.4.2 SOA Viscosity

To predict the importance of SOA for air pollution and climate, information on viscosity and diffusion rates within SOA particles is needed.¹⁰⁶ Viscosity and diffusivity are inversely related as described with the Stokes-Einstein equation. Slower diffusion rates have been found to affect gas-particle partitioning and hence the evolution of mass and size distributions of SOA.^{113,121} Molecular diffusion also affects rates and mechanisms of multiphase reactions within SOA, which in turn dictate SOA composition^{122,123} and long-range transport of pollutants such as polycyclic aromatic hydrocarbon.¹²⁴⁻¹²⁸ The viscosities of SOA can also be used to infer the phase state of the SOA particles. SOA will be liquid when the viscosity is below 10^2 Pa s, semi-solid when the viscosity is between 10^2 to 10^{12} Pa s, and glassy when the viscosity is greater than 10^{12} Pa s.¹²⁹ Viscous aerosols

have been shown to create anoxic conditions as well as limit molecular motion, resulting in the stabilization of photochemically produced radicals, trapping them in the organic matrix.^{130,131} Furthermore, the viscosity of SOA can impact their ability to act as cloud condensation nuclei¹³² and ice nuclei.¹³³ For example, if SOA particles are in a glassy phase state, defined as a material with a viscosity greater than 10^{12} Pa s, they may act as heterogeneous ice nuclei in clouds.⁶⁴

1.4.3 Photodegradation of SOA Leading to Particle Mass Loss

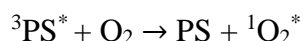
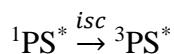
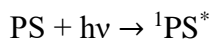
Previously, there had not been many studies investigating the condensed phase photolytic processes of SOA particles. These studies investigated the VOCs produced from irradiating SOA material using cavity ring down spectrometry (CRDS),¹³⁴⁻¹³⁶ Fourier transform infrared spectrometry (FTIR),¹³⁷ and gas chromatography (GC).¹³⁵ More recently, there has been an increased interest in studying the extent of SOA photodegradation and its effect on particle composition and size, particularly over longer timescales. Photodegradation reactions tend to fragment the SOA organics into smaller, more volatile compounds which can evaporate into the gas phase leading to SOA mass loss.^{80,81,85,92,138} These higher volatility species have been shown to include CO, CO₂, methane, acetic acid, formic acid, acetone, acetaldehyde, and other small organic molecules.^{81,135,139} These photodegradation processes affect the Earth's climate because they reduce the mass concentration and particle diameter, making SOA scatter sunlight less efficiently.⁴⁵ Indeed, a recent study found that the average SOA concentration in the Amazon rain forest would decrease by ~50% if photolysis reactions were considered.¹⁴⁰

Compounds containing carbonyl and peroxide functional groups are examples of photochemically active species responsible for the SOA mass loss under tropospheric sunlight ($\lambda > 295$ nm).^{95,134,135} The C-C(O) bond in carbonyls can be broken by Norrish I and Norrish II type photocleavage processes to form smaller products.^{79,92,135} Peroxides break at the weak O-O bond, forming two O-centered radicals, which undergo secondary processes on a picosecond time scale.¹⁴¹ However, not all photochemical processes result in fragmentation. Secondary reactions of free radicals in the SOA particles can also lead to oligomerization products that increase the carbon number of SOA species and lead to a lower volatility SOA mixture.⁷⁹

As previously mentioned, RH can dramatically affect the phase state and viscosity of SOA, which in turn affect the diffusion time for molecules within the particle. These changes in diffusivity can also affect the aging mechanisms of SOA. For example, Wong et al.¹³⁸ re-aerosolized chamber produced SOA into another chamber (in order specifically study the condensed phase) and aged them with UV light. The resulting aged SOA was more oxidized and they found photodegradation rates to increase by a factor of 2 under humid conditions due to decreased particle viscosity. Therefore, a more accurate view of organic aerosol aging should include condensed-phase photochemical reactions occurring over long time scales and various RH as they can drastically effect the OA chemical composition and physical properties, which in turn affect OA's influence on climate and health.^{80,81,92,142,143}

1.4.4 Photosensitized Particle Growth

Another important form of photochemical aging is photosensitized reactions.^{74–76,144,145} Rather than photolysis, which is considered a direct form of photodegradation, photosensitized reactions occur more indirectly with multiple steps required to lead to photodegradation.^{74,75,144,146,147} These steps involve a molecule (photosensitizer) being promoted to an excited singlet state through the absorption of a photon, followed by intersystem crossing into a triplet state and the subsequent reaction between the excited triplet molecule and an adjacent molecule. The reaction between the photosensitizer and the adjacent molecule are most commonly energy transfer, proton transfer, or electron transfer reactions and lead to the formation of organic radicals and reactive oxygen species (ROS).^{146,148,149} An example of this is shown below where the photosensitizer (PS) absorbs a photon and is promoted to an excited singlet state ($^1\text{PS}^*$), followed by intersystem crossing into a triplet state ($^3\text{PS}^*$). The triplet state PS then reacts with ground state oxygen and transfers its energy to form singlet oxygen, a well-known and very reactive oxidant in the atmosphere.



These types of processes do not only occur with gaseous oxygen, but rather, can also occur between organic molecules within an aerosol particle or even between the particle and gas phase.^{74–76,144,149}

Not all molecules can act as efficient photosensitizers. An efficient photosensitizer generally requires efficient intersystem crossing from to form a long-lived triplet state and usually have delocalized π electrons (e.g., aromatic species).¹⁴⁷ Many molecules identified in POA and SOA have aromatic characteristics and have potential for photosensitization — with porphyrins, quinones, imidazoles, and PAHs being good examples.^{146,147,149–151} The presence of these molecules in SOA have important implications for climate as these photosensitized reactions lead to particle growth. For example, Monge et al.⁷⁵ found that particles containing a photosensitizer were able to grow in diameter and mass in presence of UV irradiation and limonene vapor. Their proposed mechanism involved the excited photosensitizer ($^3\text{PS}^*$) oxidizing the limonene vapor either directly or through ROS (i.e., $^1\text{O}_2$, O_2^- , $\bullet\text{OH}$) and the subsequent uptake of the oxidized limonene product into the particle phase. They also found a strong correlation between the presence of molecular oxygen and the amount of photosensitized particle growth — indicating that limonene oxidation primarily occurs through the formation of ROS. This form of photochemical aging can occur with various other gaseous vapors such as SO_2 ⁷⁶ and other VOCs^{74,75} and can account for almost 70% of the particle growth observed in some field studies.⁷⁵

1.5 Condensed-Phase Aging Techniques

Various methods of studying condensed-phase photochemical aging of SOA are discussed below. Some of the most commonly used techniques include batch chamber, flow tube, and substrate aging. An illustration of the three techniques are shown in Figure 1.3.

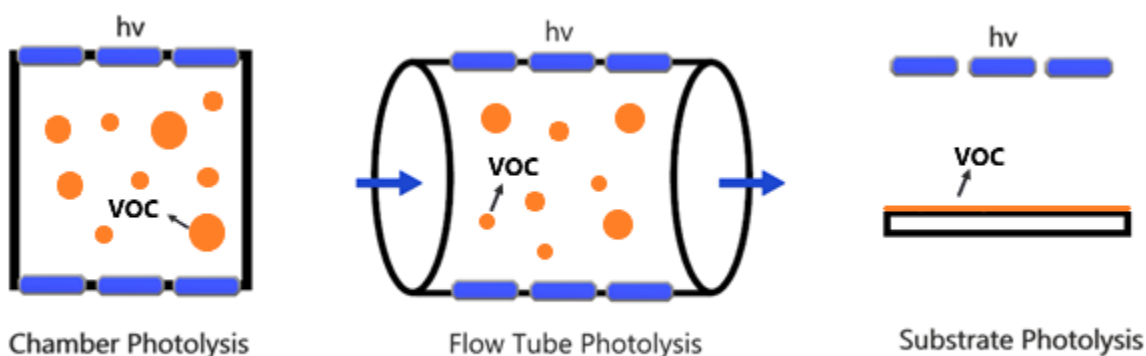


Figure 1. 3: Commonly used methods of investigating photochemical aging of SOA resulting in the production of VOCs. The orange spheres correspond to SOA dispersed in a gaseous phase or collected on a substrate. The blue bars represent a UV light source while $h\nu$ corresponds to the photons of lights inducing the photochemical aging of SOA.

Chamber photochemical aging studies involve aging SOA in the same chamber it is generated in,^{87,97,140,152,153} or is collected, extracted, and re-aerosolized (in order to remove gaseous species formed during SOA generation) before being aged.¹³⁸ This method provides useful insight into the condensed phase photochemical processes of SOA but suffers from the added interference from gas phase photochemistry. This method may also introduce artifacts from the collection, extraction, and re-aerosolization process, where the SOA phase and composition may be altered.

Flow tube aging is another useful method which involves generating OA in a chamber/flow reactor/atomizer, flowing them through a denuder (to strip away any aerosol related gasses), and then sending them through a quartz flow tube surrounded by UV lights.^{75,76,92,154} This method has some advantages over the static chamber aging method. By flowing the aerosols through a denuder and using a dynamic flow, secondary oxidation by photoproduct oxidants and gasses is minimized. However, this method still suffers from interference from the re-evaporated gas phase aerosol components.⁹² For example, even after flowing through the denuder, aerosols can evaporate in the flow tube, thus re-populating the gas phase with photolyzable molecules.

Aging on substrates is also a commonly used method,^{74,79,81,134,135} where SOA are collected on an inert substrate such as a Teflon filter or CaF₂ window, before being irradiated directly on the substrate. The main disadvantage of this method is that it can suffer from mass-transfer limitations during the photochemical aging process.^{109,113,155–157} More specifically, the thickness of the SOA material film can be thicker than the diameter of an aerosol particle, which would hinder the diffusion of photoproduct VOCs out of the film and/or hinder the diffusion of water or oxygen (which participates in photochemical reactions) into the film. This method does, however, have the advantage of removing some of the interference from gas-phase photochemistry and allows us to specifically study the condensed-phase photochemical reactions of SOA. This dissertation utilized both the flow tube and substrate aging method.

1.6 General Methods of the Dissertation

1.6.1 SOA Generation in a Smog Chamber

SOA was generated in a smog chamber for the work presented in Chapters 2, 4, and 5. The general specifications of the chamber are discussed in this section, while the experiment specific details are discussed in each corresponding chapter. The chamber is approximately 5 m³ in volume and

uses FEP Teflon as the chamber walls. The chamber is enclosed by an opaque, rigid, acrylic structure to support the chamber and prevents UV radiation from escaping the chamber. Forty-two UV-B lamps (SolarcSystems, Inc. Model FS40T12/UBV) centered at 310 nm surround the walls of the chamber and are used to initiate the photooxidation process. Incoming purified purge air (Parker FT-IR purge gas generator model 75-62NA) can be optionally humidified by a Nafion exchanger (Perma Pure model FC125-240) coupled to a heated water circulator (Julabo model HE-BASIS). This allows for studies investigating the aging of SOA formed under various RHs in different parts of the world.

Various oxidation conditions were used in this work in order to investigate the aging of SOA formed in more urban (high-NO_x) or more rural (low-NO_x) conditions. For OH/Low NO_x conditions, a measured volume of a 30% wt. hydrogen peroxide aqueous solution (typically tens of μL) was injected into a glass trap with 10 SLM of zero air flowing through it. The zero air carried the peroxide through a partially heated stainless-steel tube (40 °C) before flowing into the chamber. For OH/high NO_x conditions, after adding the peroxide solution, NO gas was added from a premixed gas cylinder with a calibrated mass flow controller opened for a set time duration. For ozonolysis oxidation conditions, ozone was generated by flowing UHP oxygen (AirGas) at 6 SLM through an ozone generator and into the chamber. The SOA precursor (pure VOC liquid) was then added into the chamber the same way as the peroxide solution — with naphthalene SOA as an exception and is discussed in further chapters. The oxidant(s) and SOA precursor were then allowed to mix in the chamber for several minutes before the chamber lights were turned on (except for ozonolysis conditions) to initiate the photooxidation process.

The SOA generation can be monitored through multiple instruments and sensors. The chamber temperature and RH were monitored using a Vaisala HMT333 probe. The ozone and NO_y (nitrogen oxides & compounds from the oxidation of these oxides) mixing ratios were monitored using Thermo Scientific 49i and 42i-Y monitors, respectively. The particle number concentration and size distribution were monitored using a scanning mobility particle sizer (SMPS, TSI model 3936). The gas phase VOC concentrations were monitored using a Proton Transfer Mass Spectrometer (PTR-MS). After the maximum particle mass concentration was reached in the SMPS readings (typically 2-4 hours), the chamber lights were turned off (except for ozonolysis conditions) and SOA collection began.

As previously mentioned, this work relied on the substrate collection method. SOA were collected using a Micro-Orifice Uniform-Deposit Impactor (MOUDI, MSP Corporation model 110-R) operating in the rotating mode at a flow rate of 30 standard liters per minute (SLM). A charcoal denuder was placed before the MOUDI collection flow in order to strip away any excess oxidants or gasses which may age the particles while being collected. A diagram of the chamber and collection setup is shown below in Figure 1.4.

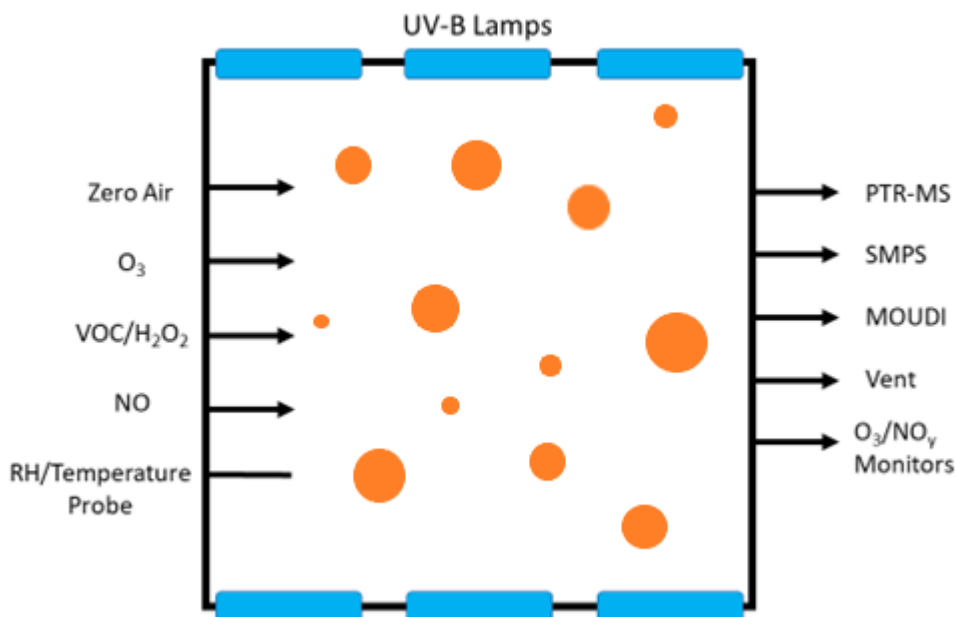


Figure 1. 4: A diagram of the smog chamber used for this work. The oxidants, VOC precursors, monitoring instruments, and collection devices are shown connected to the chamber.

1.6.2 SOA Generation in a Flow Tube Reactor

The aerosol flow tube consisted of a 20 L Plexiglas tube. A syringe pump (World Precision Instruments, Model: SP100I) was used to inject ($25 \mu\text{L h}^{-1}$) a liquid VOC into a Swagelok T-fitting that was flushed (5 L min^{-1}) with air from a zero-air generator (Parker, FTIR purge gas generator model 75-62NA). A 1 L min^{-1} flow of oxygen was passed through an ozone generator and homebuilt ozone photometric detector before mixing with the VOC air flow within the flow tube. The residence time within the flow tube was 3.5 min.

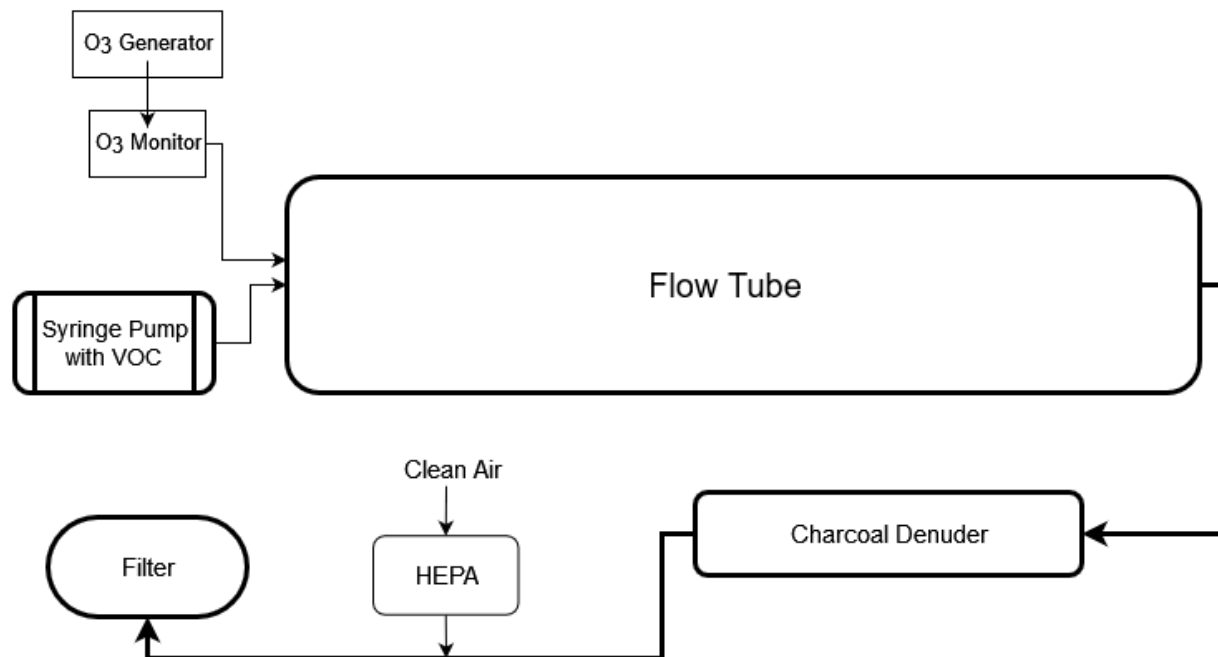


Figure 1. 5: A diagram of the flow tube used for this work. The O₃, VOC precursors, charcoal denuder, and filter collection are shown connected to the flow tube.

At the exit of the chamber and the flow tube, the SOA containing air flow was passed through a charcoal denuder to denude excess O₃. SOA particles were then collected either onto poly(tetrafluoroethylene; PTFE) filters (FGLP04700, Millipore, 47 mm diameter, 0.2 mm pore diameter), quartz crystal microbalance (QCM) crystals, or onto hydrophobic glass slides (12 mm diameter, Hampton Research, HR3-277).

1.6.3 Collection Substrates

The aerosols generated for experiments were collected on various substrates for aging and measurements.

In some experiments (Chapter 4) SOA was collected onto a QCM crystal. This was done by using a Micro-orifice Uniform Deposit Impactor (MOUDI; MSP Corp. model 110-R) at a flow rate of $\sim 25 \text{ L min}^{-1}$ for 1-4 h with custom adapters to accommodate a 2.54 cm diameter chrome/gold QCM crystal, as shown in Figure 1.6a below. The MOUDI was used in the rotating mode in order to ensure a more uniform deposition of particles on the substrate. In these experiments, Stage 7 was used since it provided the largest amount of SOA mass to be collected.

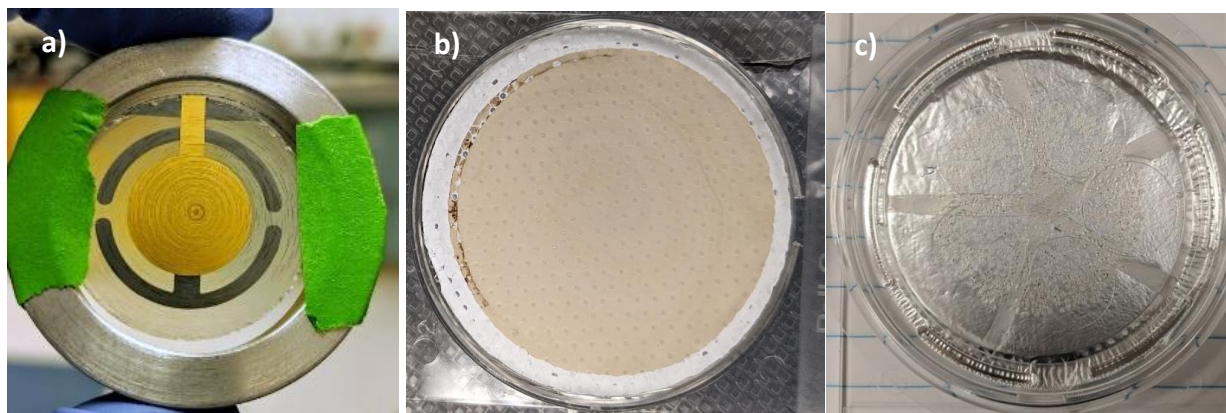


Figure 1. 6: a) SOA collected onto a quartz crystal microbalance crystal using a MOUDI in the rotating mode. b) SOA collected onto a Teflon filter using an external pump. c) SOA collected onto hydrophobic glass slides using a MOUDI in the non-rotating mode.

In some cases SOA was collected onto poly(tetrafluoroethylene; PTFE) filters (FGLP04700, Millipore, 47 mm diameter) by connecting the filter holder to an air pump, with typical flows of $\sim 20 \text{ L min}^{-1}$. An example is shown in Figure 1.6b. These substrates were used to dissolve SOA material into solution for either laser spectroscopy (Chapter 2) or mass spectrometry measurements (Chapters 2-5).

For the viscosity measurements discussed in Chapter 5, SOA was collected onto hydrophobic glass slides (12 mm diameter, Hampton Research, HR3-277). This was done using the MOUDI in a non-rotating mode using stage 8 operated at a flow rate of 20 L min^{-1} . Sampling with the non-rotating MOUDI created discrete spots of aggregated SOA particles of $\sim 35\text{--}60 \mu\text{m}$ in diameter after a typical collection time of 1 h (Fig 1.6c). Glass slides were made hydrophobic by coating with FluoroPel 800 (Cytonix).

1.6.4 Ultra-performance liquid chromatography high resolution mass spectrometry

In many experiments the chemical composition of SOA was analyzed using ultra-performance liquid chromatography coupled with a Thermo Q Exactive Plus orbitrap mass spectrometer equipped with an ESI source. A Luna $1.6 \mu\text{m}$ Omega Polar C_{18} (150 x 2.1 mm) column was used for separation. Solvents A and B used during liquid chromatography were HPLC grade acetonitrile (with 0.1% formic acid) and water (0.1% formic acid), respectively. The gradient elution protocol included a 3 min hold at 5% solvent A, an 11 min linear gradient to 95% solvent A, a 2 min hold at this level, and a linear gradient back to 5% solvent A in preparation for the next run. The column

was maintained at 30 °C. The UV–vis spectrum was measured with a photodiode array (PDA) detector from 250 to 700 nm. The ESI settings were +4.0 kV spray potential, 35 units of sheath gas flow, 10 units of auxiliary gas flow, and 8 units of sweep gas flow. The instrument was operated in either in a positive or negative ion mode with a mass resolving power of $\sim 10^5$ at m/z 200.

1.7 Structure of the Dissertation

Despite the growing literature on the photochemical aging processes of SOA, many unanswered questions remain. The studies in this dissertation were guided by the following questions.

- How can photosensitized reactions change the chemical composition of SOA?
- What types of compounds can be oxidized into the particle phase through photosensitized reactions?
- How fast do these photosensitized reactions occur?
- What are the photolytic lifetimes of SOA from various precursors?
- How does relative humidity affect the photodegradation rates of SOA?
- What are the chemical composition changes due to long term photodegradation?
- What effect does this composition change have on the physical and chemical properties of SOA?

Chapter 2 discusses the triplet reactivity of known photosensitizers that are likely found in organic aerosols. The photosensitized chemistry of three aromatic ketones (xanthone, flavone, and acetophenone) was investigated by means of transient absorption spectroscopy. Halide ions were selected to probe the reactivity of the generated triplet state. The photosensitized reactivity of SOA arising from the photo-oxidation of naphthalene was also investigated. Combining the study of these individual and known photosensitizers with those formed in the atmosphere demonstrates that tropospheric photosensitization may involve a large variety of compounds and will introduce new, unconsidered chemical pathways that impact atmospheric multiphase chemistry.

Chapter 3 extends the previous study of triplet reactivity occurring in organic aerosols. Naphthalene photooxidation SOA was generated, injected into an aerosol flow tube, and exposed to UV radiation and gaseous volatile organic compounds or sulfur dioxide (SO₂). The aerosol particles were observed to grow in size and the resulted in the production of particle phase sulfate.

As naphthalene and other polycyclic aromatics are important SOA precursors in the urban and suburban areas, these photosensitized reactions are likely to play an important role in sulfate and SOA formation.

Chapter 4 discusses the long-term photodegradation of secondary organic aerosols produced from biogenic and anthropogenic VOCs. The experiments relied on a quartz crystal microbalance (QCM) to quantify the mass loss rate from SOA materials while being irradiated by a 305 nm UV LED. The mass loss rates were observed to increase at a higher relative humidity because volatile photoproducts could diffuse out of SOA faster. Long-term changes in the chemical composition of SOA were examined using high-resolution electrospray ionization mass spectrometry. These experiments confirm that condensed-phase photochemistry is an important aging mechanism for SOA during long-range transport.

Chapter 5 is an extension of the previous SOA photodegradation study and investigates the viscosity and phase state of UV-aged SOA. The viscosity of UV-aged SOA was measured after an equivalent UV exposure of 6–14 days at midlatitudes in summer. Results indicate that the viscosity and characteristic mixing times of organic molecules within an SOA particle can be as much as five orders of magnitudes larger for aged SOA. The increase in viscosity likely leads to an increased abundance of glassy SOA particles that can act as ice nuclei in the atmosphere. Furthermore, the increase in viscosity and mixing times can impede gas-particle partitioning and heterogeneous chemistry. Overall, our results clearly demonstrate that UV-aging needs to be considered when predicting the environmental impacts of SOA.

Chapter 6 discusses preliminary work done on quantifying the mass loss and VOC production from ambient biomass burning organic aerosol (BBOA). BBOA was collected using a MOUDI onto QCM crystals during the December 2020 Santiago Canyon Bond Fire. Experiments involved irradiating the BBOA substrates using a 305 nm LED while simultaneously measuring the mass loss rates using a QCM and photoproducted VOCs using a Proton Transfer PTR-MS. These preliminary experiments indicate that photodegradation of ambient BBOA can be a large source of VOCs, particularly formic acid, in the atmosphere.

Chapter 2: Quenching of ketones triplet excited states by atmospheric halides

Portions of this chapter were reproduced with permission from Gemayel, R., Emmelin, C.; Perrier, S.; Tomaz, S.; Baboomian, V. J., Fishman, D. A.; Nizkorodov, S. A.; George, C. (2021). Quenching of ketone triplet excited states by atmospheric halides. *Environmental Science: Atmospheres*, 1, 31-44. <https://doi.org/10.1039/D0EA00011F>

2.1 Abstract

The photosensitized chemistry of three aromatic ketones (xanthone, flavone, and acetophenone) and also of secondary organic aerosol (SOA) arising from the photo-oxidation of naphthalene was investigated by means of transient absorption spectroscopy. Halide ions were selected to probe the reactivity of the generated triplet states. The quenching rate constants ranged from $10^9 \text{ M}^{-1}\text{s}^{-1}$ with iodide ion to less than $10^5 \text{ M}^{-1}\text{s}^{-1}$ with chloride ion. The halide-triplet state interactions produced the corresponding radical anion ($\text{X}_2^{\cdot-}$) along with halogenated and more oxidized organic compounds as identified by liquid chromatography and mass spectrometry. Deoxygenated naphthalene SOA solutions showed strong transient absorption at 420 nm when excited at 355 nm, which were also quenched by iodide ion similar to the single compound experiments indicating that compounds in naphthalene SOA can act as a photosensitizer. Combining the study of these individual and known photosensitizers with those formed in the atmosphere (in this case through the oxidation of naphthalene), demonstrates that tropospheric photosensitization may involve a large variety of compounds of primary or secondary nature and will introduce new, unconsidered chemical pathways that impact atmospheric multiphase chemistry.

2.2 Introduction

The hydroxyl radical ($\bullet\text{OH}$) is certainly one of the dominant tropospheric oxidants in both gas and aqueous phases.¹⁵⁸ However, besides the $\bullet\text{OH}$ radicals, a number of other oxidative pathways including nitrate radicals, ozone, halogenated radicals, singlet molecular oxygen, peroxy radicals, peroxides, and triplet excited states of organic compounds ($^3\text{C}^*$) have also been shown to play a significant role in the troposphere.^{159,160}

Very recently, the potential importance of triplet state chemistry has been unraveled for the atmospheric aqueous phase by novel ambient measurements of triplet state concentrations in fog and aerosol water, and by reactivity measurements under atmospheric conditions of various photosensitizers known to be present in the particulate matter.^{154,160–167} For instance, triplet excited states of aromatic ketones have been shown to oxidize phenols commonly found in biomass burning aerosol,^{168,169} and halide ions commonly found in sea spray aerosol.¹⁷⁰ In the latter case, the halide ion oxidation induces the formation of halogen atoms (X^*) or radical anions ($\text{X}_2^{\bullet-}$),¹⁶⁶ which are important reactive species for the oxidation of organic and inorganic compounds throughout the troposphere. The halide ions such as iodide, bromide, and chloride represent compounds of interest because of the high reactivity of their associated atomic radicals and because of their ubiquity.^{171–174}

This chapter reports the reactivity of common halide ions towards organic triplet states from three aromatic ketones: xanthone, acetophenone, and flavone. These compounds are present in different environmental compartments and were previously considered as aqueous phase photosensitizers.¹⁴⁶ They are also present in the gaseous and particulate atmospheric phases. Of these three compounds, xanthone is more abundant in the particulate phase having a concentration of hundreds of pg m^{-3} in urban areas.^{175,176} Different primary and secondary sources of xanthone have been identified such as wood and agricultural waste burning, and combustion of diesel, gasoline, and city gas.^{177–181} Acetophenone has been detected in aerosols but it mainly partitions into the gas phase.¹⁷⁷ Primary and secondary sources of acetophenone have also been identified, including wood combustion and diesel emissions.^{178,179} Flavone has been identified in biogenic emissions as flavonoids are known as a plant-protective antioxidant.¹⁸⁰ In a recent study, flavone has also been identified in biomass burning emissions.¹⁸¹

To answer the question whether direct emissions are the unique way to introduce primary photosensitizing compounds into the troposphere, the possibility of producing such compounds in-situ in the air was also investigated. Previous work showed that particulate phase chemistry induces the production of such secondary photosensitizers.¹⁴⁵ This study extended this approach to secondary organic aerosol (SOA). Specifically, the examination of the triplet-state reactivity towards I for a complex mixture of organic compounds in SOA produced by the photooxidation of naphthalene under high-NO_x conditions. This naphthalene SOA has been shown to strongly absorb near-UV and visible radiation.¹⁸² UV irradiation of naphthalene SOA has been shown to result in an efficient photosensitized production of singlet oxygen,¹⁴⁹ and reactivity towards limonene.⁷⁴ The working hypothesis was that a subset of compounds in naphthalene SOA has sufficiently high triplet state energies to oxidize halide ions.

This work aims to explore the effect of the triplet state chemistry of these compounds on the formation yield of reactive halogen species (X^{\bullet} , $X_2^{\bullet-}$) and their kinetics. The identification of products from these aqueous photosensitized reactions is also providing insights into the potential chemical mechanisms. It is noteworthy to point out that the chemistry investigated here is not only of importance for liquid particles, but also for the description of photochemical processes at the air/sea interface. As recently highlighted by our previous work, there is rich photochemistry taking place in the sea surface microlayer,¹⁸³ which has now been demonstrated to involve PAHs and organic compounds of marine interest.^{184,185} Therefore, PAHs can also be efficient photosensitizers at the sea surface and in aerosols as well.

2.3 Experimental

2.3.1 Materials and Solution Preparation for Single-Component Experiments:

Experiments with single ketones were conducted by the Christian George group in IRCELYON. The chemicals used in this study - xanthone (97% Sigma-Aldrich), acetophenone (96% Sigma-Aldrich), flavone (97% Sigma-Aldrich), sodium chloride (>99% Sigma-Aldrich), sodium iodide (>99% Sigma-Aldrich), sodium bromide (>99% Sigma-Aldrich) – were all used without further purification. All solutions were freshly prepared using 18 M Ω ultra-pure water. The photosensitizer was dissolved in water using magnetic agitation in the dark for two hours. Aqueous solutions containing $\approx 2 \mu\text{M}$ of photosensitizer were deoxygenated with a stream of argon for 20

min to avoid any interference or electron transfer with singlet oxygen. All the experiments are performed at a temperature maintained at 23°C.

2.3.2 SOA Preparation:

Naphthalene SOA was prepared under high NO_x conditions (NAPH/OH/NO_x) and 40% relative humidity (RH) in a 5 m³ Teflon batch chamber surrounded by 42 UV-B lamps. The chamber was equipped with a proton-transfer-reaction mass spectrometer to monitor naphthalene concentrations and a scanning mobility particle sizer to monitor particle concentrations and size distributions in the chamber. The NO_x concentration and RH of the chamber were monitored by a Thermo Scientific 42i-Y and Vaisala HMT333 probe, respectively. The starting naphthalene, H₂O₂, and NO_x mixing ratios were 0.4, 2, and 0.4 parts per million by volume (ppm), respectively. After the naphthalene was added to the chamber and the concentration stabilized, H₂O₂ and NO were added and the UV-B lamps were turned on to initiate the photo-oxidation process (with a steady state OH concentration of ~10⁶ molecules cm⁻³). The OH steady-state concentration was determined from the rate at which the starting organic compound is removed from the chamber as measured by PTR-MS. Once the particle mass concentration peaked (~3 h), the SOA was collected onto a poly(tetrafluoroethylene) (PTFE) filter (FGLP04700, Millipore, 47 mm diameter, 0.2 μm pore size). The filter was then extracted with HPLC-grade water to produce a 0.170 g/mL SOA solution. Aliquots of an aqueous KI solution were added to the SOA solution for quenching studies. All the samples were deoxygenated for 20 minutes before the transient absorption experiments, as mentioned for single compound photosensitizer experiments.

2.3.3 Laser transient absorption

The transient absorption spectrum of the excited photosensitizer (xanthone, flavone, and acetophenone) was followed with a classical laser transient absorption apparatus.¹⁸⁶ It corresponds to a standard laser transient absorption system except the reaction cell is replaced with a Teflon AF liquid waveguide (Fig. 2.1). The fourth harmonic (266 nm) of an Nd:YAG laser (Surelite II 10, Continuum) was used as the excitation source for most experiments. In the case of xanthone the third harmonic (355 nm) was also used. The laser output was shaped by a dispersing lens to irradiate homogeneously the outer surface of this 1 m long transparent waveguide wound in a reel. Using a peristaltic pump, the solutions containing all reactants were flowing through the waveguide to constantly replenish its content between each laser shot (the residence time of the

sample in the cell being less than one second). All connections were made from either glass or PTFE tubing. This is important to limit the exposure of the solution to repeated laser pulses to maintain a constant temperature in the flow cell and to reduce the degradation/photolysis of the solution. Transient species produced by the pulsed laser beam were monitored employing time-resolved absorption spectroscopy. A continuous wave 150 W high-pressure Xenon arc lamp was used as a broadband radiation source. The light from the lamp passed along the axis the waveguide and the optical fibers and was collected then by a ¼ m monochromator (Spectral Products DK240) equipped with a 2400 grooves/mm grating and coupled with a photomultiplier (PMT, Hamamatsu H7732-01). The output signal of the PMT passed through a high-speed current amplifier/discriminator (Femto) and the AC component recorded on a 300 MHz oscilloscope (Tektronix TDS3032c). Typically, signal from 512 laser pulses were averaged for each measurement. To construct the transient absorption spectrum, measurements were repeated every 10-15 nm between 300 and 650 nm. The full transient absorption spectrum was reconstructed from the steady and transient signals (330 ns after the laser pulse), and reported in a wavelength region free of spectral interferences from the ground state solution.

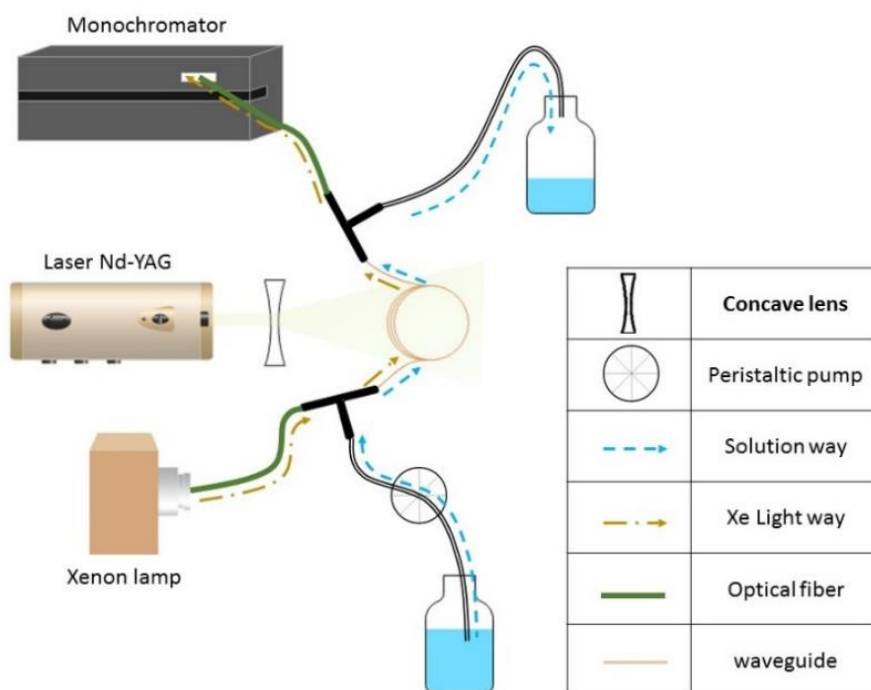


Figure 2. 1: Experimental setup for the laser flash photolysis.

Based on the photosensitizers' absorption spectra (Fig. 2.2), the laser wavelength was set at 266 nm where the three photosensitizers absorb. The laser was operated in a single-shot mode, and its energy was set to ~ 10 mJ per pulse for 266 nm photolysis experiments. Using moderate energy helps to limit as much as possible the direct photolysis of the photosensitizer and therefore avoid possible interferences from its products. To get closer to the atmosphere conditions, another set of experiments was carried out at a laser wavelength of 355 nm. At this wavelength, only xanthone absorbs efficiently, but 1.7 times less than at 266 nm. Therefore in this case a slightly higher laser energy was used.

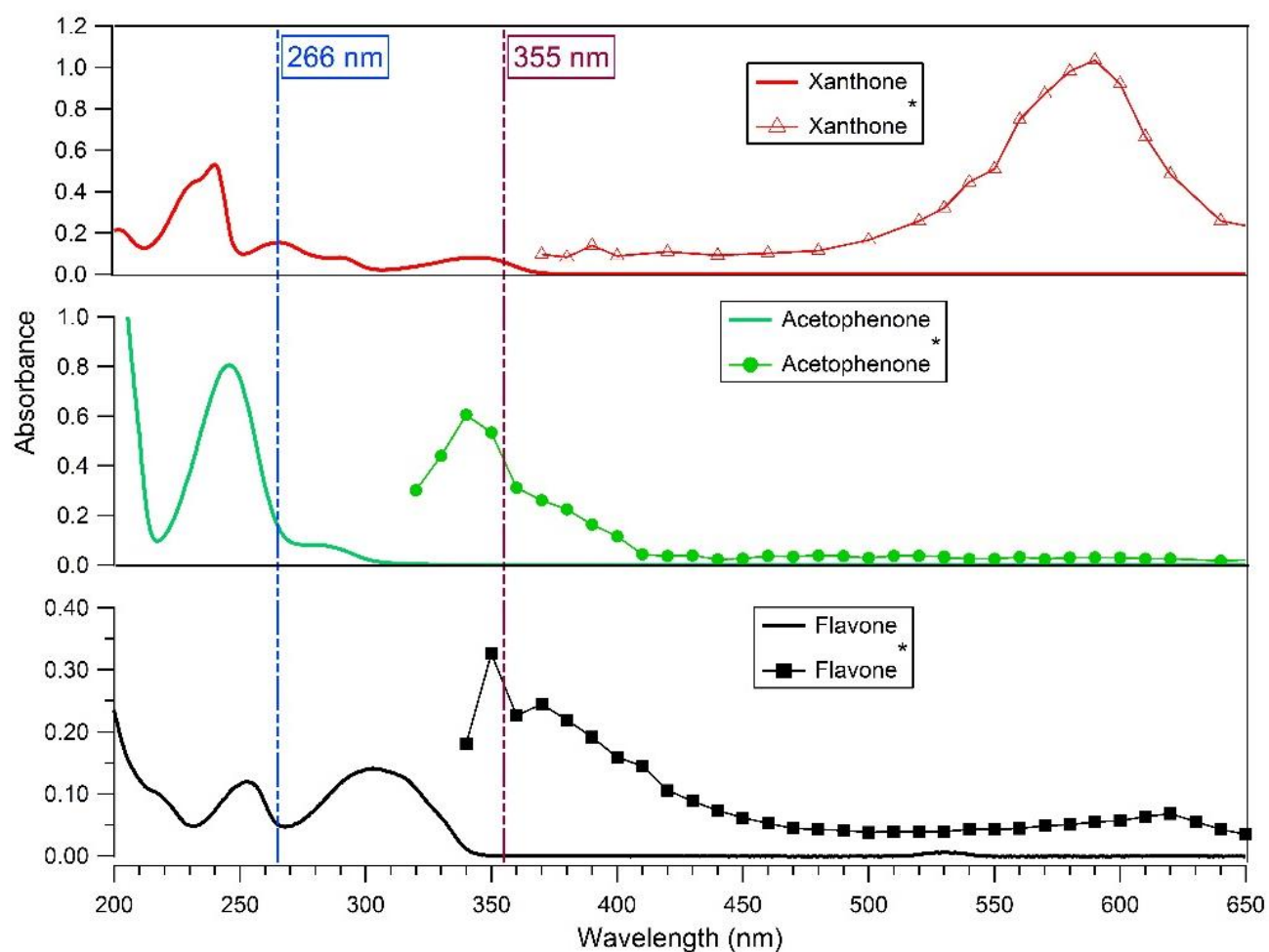


Figure 2. 2: Absorption and transient absorption spectra of solutions of xanthone, acetophenone and flavone. The solid line (–) shows the (UV-Vis) absorption spectra of solutions before the laser excitation (266 nm). Absorption spectra recorded 330 ns after the laser pulse of an aqueous solution of xanthone (– Δ –), acetophenone (– \bullet –) and flavone (– \blacksquare –) (10^{-2} mM). Spectra were recorded in the absence of salts.

The transient absorption experiments on NAPH/OH/NO_x SOA solutions were conducted using a different laser transient absorption apparatus at the University of California, Irvine. The sample was placed in a standard 10 mm fused silica cuvette. Circulation was not used due to the limited amount of available sample. The solution was excited at 355 nm (40 mJ per pulse) and the transients were probed using a similar Xenon arc lamp, monochromator, and oscilloscope setup (averaging 40 pulses). Exciting the molecules at 355 nm ensured that the transients formed would be tropospherically relevant and would lead to photochemical aging of organic aerosols in the lower atmosphere.

2.3.4 Chemical characterization

Chemical analysis of the reaction products was performed in the case of xanthone. For this purpose, solutions were prepared, containing the same concentration of xanthone, without halide ions, with sodium iodide (0.89 mM) and finally with sodium bromide (0.1 M). Half of each solution was kept in the dark for reference, and the remaining half was exposed to laser pulses at 355 nm in the waveguide. These six solutions were then desalinated and concentrated by solid phase extraction (SPE) (Waters, Oasis MAX 6 cc Vac Cartridge, copolymer, 30 μm). The extracts were dried under a nitrogen flow and reconstituted in 1 ml of acetonitrile. Samples were analyzed by ultra-high performance liquid chromatography (UPLC, Dionex 3000, Thermo Scientific) coupled with a Q-Exactive Hybrid Quadrupole-Orbitrap mass spectrometer (Thermo Scientific) with an electrospray ionization source. The separation relied on a Water Acquity HSS C₁₈ column (1.8 μL, 100 x 2.1 mm) at a flow rate of 0.3 ml/min with a mobile phase gradient using acidified water (eluent A: 0.1%, v/v, formic acid; Optima liquid chromatography (LC/MS), Fisher Scientific) and acidified acetonitrile (eluent B: 0.1%, v/v, formic acid; Optima LC/MS, Fisher Scientific).

In addition, the distribution of compounds found in NAPH/OH/NO_x SOA was examined using the same UPLC-Q-Exactive system equipped with UV photo-detector array (PDA). The instrument was operated in the negative polarity mode. The most relevant compounds in SOA are the ones that strongly absorb near-UV radiation, and were assigned by examining the correlation between chromatographic peaks detected by both PDA and mass spectroscopy detectors. In addition, the chromatograms were analyzed using Compound Discoverer to locate compounds with high abundance in the mass spectrum regardless of their light-absorption properties. All peaks were

assigned to formulas of $[C_cH_hO_oN_n - H]^-$, where c,h,o, and n represent the corresponding number of atoms in the ions. Identified peaks met a sample:blank ratio greater than 5 and the formula assignments were limited to 30 C, 50 H, 20 O, and 10 N atoms with a maximum error of 5 ppm. When multiple formula possibilities existed, compounds that could be conceivably derived from naphthalene were selected. Assignments were not verified with standards, so the formulas cited below should be regarded as tentative.

2.4 Results

2.4.1 Triplet state transient absorption spectra

The transient absorption spectrum recorded after the 266 nm laser pulse is characterized by a strong absorption peak with a maximum absorption wavelength of around 590 nm for xanthone, 340 nm for acetophenone, and 350 nm for flavone (Fig. 2.2). These wavelengths are in reasonably good agreement with previously published spectra as discussed below. The wavelength of maximum absorption for excited xanthone and acetophenone depends on the nature of the solvent. In non-polar solvents, the maximum absorption wavelength is at 600 nm for xanthone and 350 nm for acetophenone when excited at 355 nm.^{6,187-190} As shown in Figure 2.2, the triplet flavone transient absorption spectrum presents three peaks at 350, 370 (appearing as shoulder due to broad absorption and limited spectral resolution), and 620 nm. The strongest one is at 350 nm and the weakest one is at 620 nm. These results are in good agreement with the work published by Avila and Previatli,¹⁹¹ who observed two absorption maxima at 370 nm (the most intense) and 620 nm when excited at 337 nm. These maxima were practically independent of the solvent used (benzene, ethanol, acetonitrile). For the determination of lifetimes and quenching rate coefficients, the triplet state decay was monitored at the wavelengths reported above.

2.4.2 Characteristics of the photosensitizer triplet state

Laser flash photolysis of deoxygenated solutions containing the selected photosensitizers showed strong transient absorptions as shown in Figure 2.3A for flavone. Over the 0-7 μ s range, the absorption decay was fitted with a single exponential decay with an offset (Equation 2.1) (Fig. 2.3B). The triplet state lifetime without quenchers was thus calculated following equation 2.2 where k_{decay} is the observed rate constant.

$$y = A_m + be^{-k_{decay}t} \quad (2.1)$$

$$\tau = \frac{1}{k_{decay}} \quad (2.2)$$

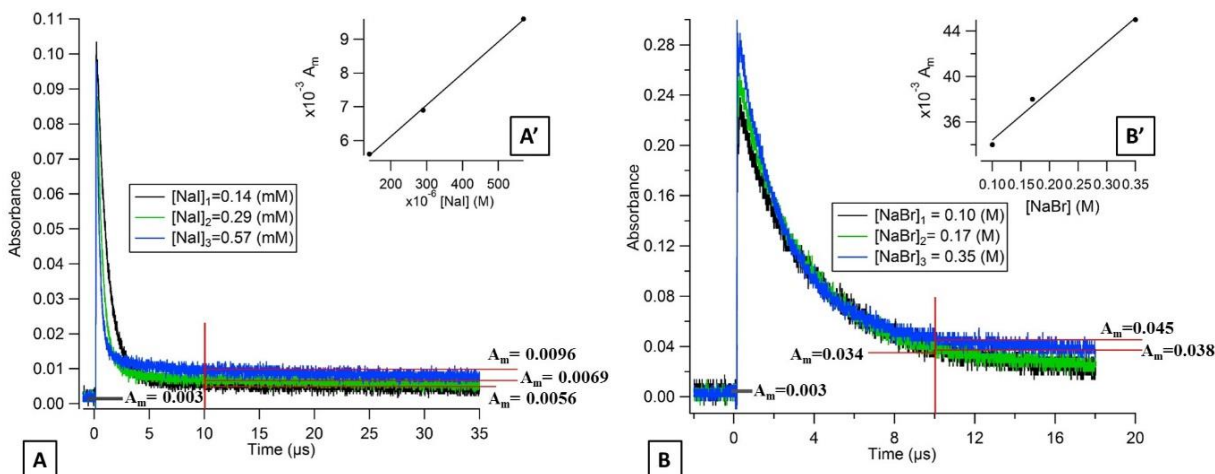


Figure 2. 3: (A) Transient absorption decays of flavone triplet state (excited at 266 nm) in a deoxygenated aqueous solutions containing different concentrations of NaI observed at 390 nm and (B) with different concentrations of NaBr observed at 350 nm.

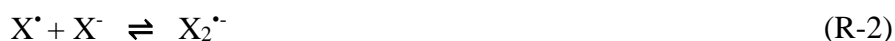
These constants in deoxygenated solutions are presented in Table 2.1. For the three compounds, the lifetime of the triplet state ranged from $1.85 \mu\text{s}$ for acetophenone to $5.5 \mu\text{s}$ for flavone. These values are in agreement, with triplet state lifetimes reported in the literature for a large variety of compounds, which are in the range of $10^{-7} - 1$ s.¹⁹² The triplet lifetimes of cyclic ketones vary with the ring size and with the degree of substitution; for cyclohexanone it varies between 0.6 to 40 ns.¹⁹³ In the presence of oxygen, the decay became faster indicating a quenching by oxygen, probably by energy transfer producing reactive oxygen species such as singlet oxygen.¹⁹⁴ Singlet oxygen can then undergo reactions with nearby molecules, as discussed in Section 2.4.5.

Table 2. 1: First-order rate constants and triplet lifetimes in the absence of quenchers such as oxygen or halides. The ground state reduction potential E° , the triplet state energy E_T , and the triplet state reduction potentials $E^{\circ*}$ of the three photosensitizers are also given.^{195–200}

	$k_{decay} (\mu s^{-1})$ 266 nm	$\tau (\mu s)$ 266 nm	$k_{decay} (\mu s^{-1})$ 355 nm	$\tau (\mu s)$ 355 nm	$E^* (V)$	$E_T (V)$	$E^{**} (V)$
Xanthone	0.44±0.02	2.27±0.10	0.43±0.03	2.33±0.16	-1.21 ¹⁹⁷	3.17 ¹⁹⁸	1.96
Acetophenone	0.54±0.04	1.85±0.14			-1.42 ¹⁹⁹	3.19 ²⁰⁰	1.77
Flavone	0.18±0.02	5.5±0.61			-1.18 ¹⁹⁵	2.69 ¹⁹⁶	1.51

2.4.3 Triplet state quenching rate constant

The quenching of the selected photosensitizers by halide ions was investigated. Different concentrations of NaI, NaBr, and NaCl were added in the deoxygenated aqueous solution of the different photosensitizers. Their decay became faster with increasing concentration. This chemistry is expected to produce atomic halogens according to R1 in the next mechanism:¹⁷⁰



Under pseudo-first-order conditions, where the quenchers being added are in excess compared to the triplet state, the quenching rate coefficients can be determined by the following Stern-Volmer equation (Equation 2.3):

$$-\frac{d[{}^3P^*]}{dt} = (k_0 + k_1[X^-])[{}^3P^*] = k_{decay}[{}^3P^*] \quad (2.3)$$

In equation 2.3, k_0 corresponds to the rate constant of the triplet state decay in the absence of oxygen and other quenchers in pure water, while k_1 corresponds to the quenching rate constant by the halide X^- in reaction 1.¹⁹² For a constant concentration of photosensitizer, k_1 corresponds to the slope of the line obtained from the plot of the observed rate coefficient as a function of quencher concentration. The different quenching rate coefficients are summarized in Table 2.2.

Table 2. 2: Reaction 1 rate constants k_1 for quenching of ketones triplet states by different halide ions following excitation at 266 nm and 355 nm, redox potentials ($E(X^-/X)$) for the anions and the free energy of the electron transfer ΔG_{ET} . Values were obtained with 3 experimental repetitions.^{195–200}

	I⁻		Br⁻		Cl⁻	
	0.535		1.087		1.36	
	ΔG_{ET}	$k_I (M^{-1} s^{-1})$	ΔG_{ET}	$k_{Br} (M^{-1} s^{-1})$	ΔG_{ET}	$k_{Cl} (M^{-1} s^{-1})$
Xanthone (266 nm)	-1.425	$(8.34 \pm 0.43) \times 10^9$	-0.873	$(6.46 \pm 0.01) \times 10^8$	-0.6	$\leq 10^5$
Xanthone (355 nm)		$(1.86 \pm 0.82) \times 10^9$		$(1.06 \pm 0.23) \times 10^7$		$\leq 10^5$
Acetophenone (266 nm)	-1.235	$(3.47 \pm 0.28) \times 10^9$	-0.683	$(9.89 \pm 0.6) \times 10^6$	-0.41	$\leq 10^5$
Flavone (266 nm)	-0.975	$(4.85 \pm 0.35) \times 10^9$	-0.423	$(1.28 \pm 0.28) \times 10^5$	-0.15	$\leq 10^5$

The ground state reduction potential E° and the triplet state energy E_T for the different photosensitizers studied are presented in Table 2.1. The triplet state reduction potentials $E^{*\circ}$ is the sum of E_T and E° . Using these values, one can calculate the free energy (ΔG) of one electron transfer between the excited photosensitizer and the quencher, (Equation 2.4) presented in Table 2.2. The deactivation of the excited photosensitizer by reaction (R1) will take place spontaneously only if ΔG_{ET} is negative. This quantity may be calculated using the Rehm-Weller equation:²⁰¹

$$\Delta G_{ET} = nF(E(X^-/X) - E^\circ - E_T) + C \quad (2.4)$$

where nF is the total charge transferred during the reaction. The entropic variation and the coulombic term (C) are considered here as negligible. Considering each photosensitizer individually and comparing ΔG_{ET} with different halides, shows that thermodynamically, the electron transfer reactions are the most favorable through reactions with iodine, with the ΔG_{ET} ranging from -0.975 to -1.425 (eV). In the presence of bromide and chloride, the electron transfer is thermodynamically less favorable than for iodide with ΔG_{ET} values ranging from -0.873 to -0.423 (eV) and -0.6 to -0.15 (eV), respectively. These results may explain the different measured values of k_1 for the same photosensitizer with the different halide ions. And indeed, efficient quenching assumed to correspond to a rapid electron transfer, has been measured for iodide, but with somewhat lower rates for the bromide, and a much slower rate for chloride.

Comparing the measured values of k_1 for the different photosensitizers with the same halide ion, shows that in all cases, xanthone presents the highest values for k_1 . This can be explained by considering the triplet state reduction potential, E^{o*} , which is a critical value for the kinetics of electron transfer reactions.²⁰² The E^{o*} for xanthone is the highest, compared to those of acetophenone or flavone, and corresponds to 1.96, 1.77, and 1.51 V, respectively.²⁰¹ This observation has been proven in the literature where two studies show that the E^{o*} influence and control the kinetics of the quenching oxidation reaction.^{148,203} Based on the same concept and comparing the measured values obtained for acetophenone to those obtained for flavone, shows that E^{o*} can explain the differences observed with bromide where acetophenone k_1 is almost a 100 times higher than k_1 of flavone. In the case of iodide, a different trend is observed with flavone k_1 being 1.4 times higher than acetophenone k_1 . This difference, a factor 10 to 100 with bromide while a factor 1.4 for iodide, can be due to the diffusion effect in the solution which plays a limiting role in this case.

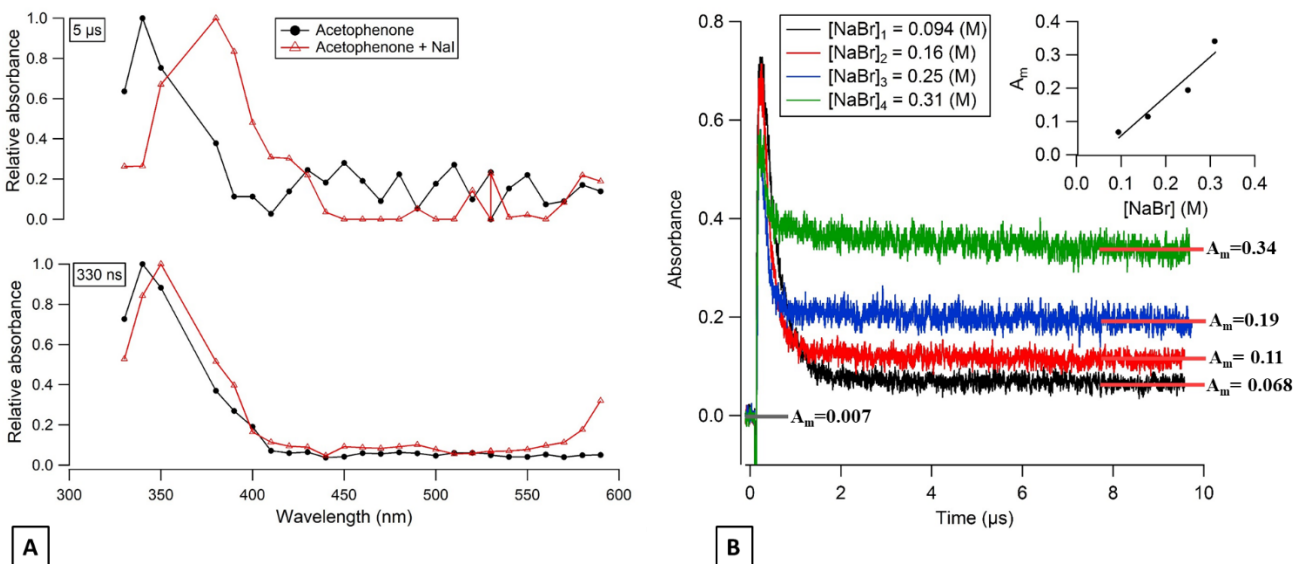


Figure 2. 4: (A)- Transient absorption spectra of deoxygenated acetophenone solution (red triangles) and deoxygenated acetophenone with NaI (black circles) at 330 ns (bottom) and at 5 μ s (top) after the 266 nm laser shot. (B)- Transient absorbance decays of acetophenone triplet state in aqueous solutions containing different concentrations of NaBr observed at 350 nm after 266 nm excitation.

Figure 2.4A shows the transient absorption spectrum of acetophenone in the presence of I^- at 330 ns after the laser shot. The maximum absorption corresponds to 350 nm, which is slightly higher than the value obtained for acetophenone in absence of any quencher (340 nm). This shift may correspond to the formation of an absorbing transient compound (see below) produced rapidly after the laser discharge. Consequently, the underlying decay kinetics are affected and more uncertain. These measurements have also been carried out for xanthone, at an excitation wavelength of 355 nm. At this wavelength, there is still a pronounced reactivity with the halide ions, which is in the same order of magnitude with iodide whereas with bromide the kinetics are more than 50 times slower than at 266 nm (Table 2.2).

2.4.4 Transient absorption spectra of transient species and products

Based on reactions (R1) and (R2), iodine and bromine atoms are expected to be produced after the triplet quenching. While no transient compounds were observed in the absence of photosensitizers, the situation appeared more complex with added iodide or bromide ions in the solution. Indeed, after the laser discharge, the transient absorption should return to its initial background absorption

(A_0) due to the relaxation of the triplet state. The time needed to return to the initial background absorption depends on the lifetime of the triplet and the presence of other quenchers. When the absorption does not return to the A_0 level, or does so over much longer timescales than expected for triplet state reactions, it indicates the formation of a transient or new product.

2.4.4.1 Flavone

In the presence of NaI and NaBr, the absorption decay of the flavone triplet does indeed not return to its background value, indicating the presence of transient species. Figure 2.3 shows the flavone absorption decays at different concentrations of NaI at 390 nm (Fig. 2.3A) and at different concentrations of NaBr at 350 nm (Fig. 2.3B). The long-lived absorption values at these wavelengths are a function of the halide concentrations. It is important to note that the maximum intensity of this long-lived absorption is observed at 390 nm for NaI and at 350 nm for NaBr and that lower values are observed at wavelengths of 20 nm around these wavelengths. Based on the literature, for NaI solutions, this maximum absorption wavelength could be assigned to the radical $I_2^{\bullet-}$ exhibiting absorption bands at 385 and 725 nm with an extinction coefficient of 9500 and 3000 $L mol^{-1} cm^{-3}$, respectively.²⁰⁴ This system did not allow for the detection of the second peak at 725 nm because of its lower intensity. For the NaBr solutions, the maximum absorption wavelength at 350 nm would correspond to $Br_2^{\bullet-}$ having an absorption band at 354 nm with an extinction coefficient of 9900 $L mol^{-1} cm^{-3}$.²⁰⁵

Considering the extinction coefficient of $I_2^{\bullet-}$ at 390 nm (9000 $L mol^{-1} cm^{-3}$) and for $Br_2^{\bullet-}$ at 350 nm (9900 $L mol^{-1} cm^{-3}$), calculations show that the yield of $I_2^{\bullet-}$ is 239 times higher than the one for $Br_2^{\bullet-}$ at 10 μs after the laser pulse, which is consistent with the results presented above.

Flavone presents the lowest values of triplet state energy and triplet state reduction potentials compared to acetophenone and xanthone. In consequence, it should lead to the lowest halide ion oxidation rates.

2.4.4.2 Acetophenone

For acetophenone solutions in the presence of halide ions (Br^- and I^-), transient products have also been detected. A comparison of the transient absorption spectra, between acetophenone in pure water or in the presence of NaI, at 330 ns and 5 μs after the laser discharge is shown in Figure 2.4A. A new absorption band at 390 nm appears a few μs after the laser discharge for the solution

containing NaI. The acetophenone triplet lifetime is 1.85 μs and therefore the observed absorption band at 5 μs is unlikely to be explained by the acetophenone triplet state but could be attributed to $\text{I}_2^{\cdot-}$.

The long-lived absorption at 350 nm for acetophenone solutions in the presence of a different concentration of NaBr is presented in Figure 2.4B. In this case, the long-lived absorption is more pronounced than for flavone for the same NaBr concentration range. To quantify the yield of $\text{Br}_2^{\cdot-}$ formed and to compare to the results obtained with flavone, the correlation between the absorption at 10 μs and the different concentrations of NaBr is presented in Figure 2.4B'. A simple first-order fit for this data gives a slope of about 1.2, i.e., corresponding to 6 times more $\text{Br}_2^{\cdot-}$ production with acetophenone than with flavone. This observation could be explained by the different values of triplet state energies. Acetophenone has an E_T higher than that for flavone and slightly higher than the E_T for xanthone, while a value of triplet state reduction potential is in between the two values of other photosensitizers.

2.4.4.3 Xanthone

Because of technical limitations, the transient absorption spectra of xanthone alone, xanthone with NaI and xanthone with NaBr, at 330 ns and at 5 μs after the laser pulse, start at 370 nm in Figure 2.5A and 2.5A' (no signal is detected for wavelength < 370nm). Approximately 5 μs after the laser pulse, half of the absorbance at 590 nm decreases in the absence of any quencher, while a new absorbance appears with a maximum at 390 nm for a solution containing NaI. Another weaker peak appears around 700 nm. The ratio of the absorbance (0.56/0.19) of these two peaks (390nm/700nm) equals the ratio of the extinction coefficients (6/1.8) of these two peaks from the $\text{I}_2^{\cdot-}$ spectrum²⁰⁴ confirming the formation of these transient radicals. For the solutions containing NaBr, the new absorbance band appears around 370 nm but we cannot confirm the wavelength of the maximum absorbance.

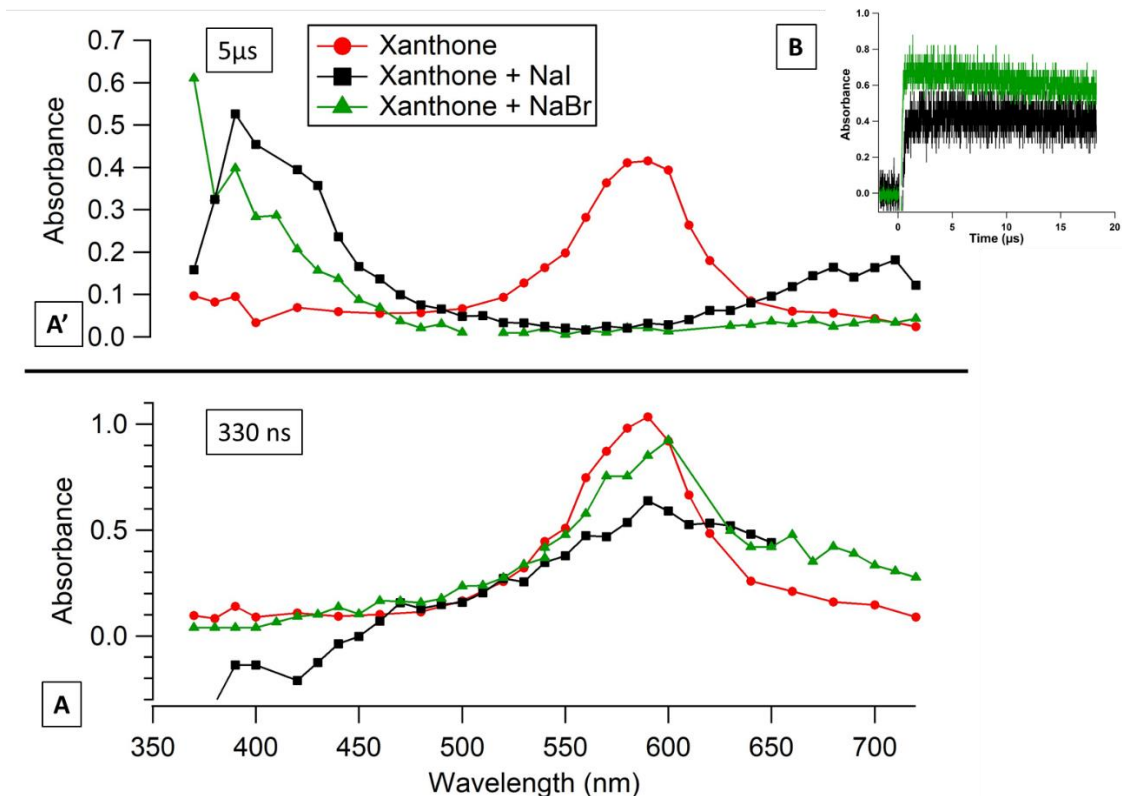


Figure 2. 5: Transient absorption spectra of deoxygenated xanthone solution (red circles), deoxygenated xanthone with NaI solution (black squares) and deoxygenated xanthone with NaBr solution (green triangles) A- at 330 ns (bottom) and A'- at 5 μ s (top) after the laser shot. B- transient absorption decays of xanthone triplet state in a deoxygenated aqueous solution, in black containing NaI observed at 390 nm, and in green containing NaBr observed at 370 nm. All spectra acquired after 266 nm excitation.

Figure 2.5B shows the absorbance as a function of time at 370 nm for xanthone in a 0.21 M NaBr solution and at 390 nm for Xanthone in a 0.56 M NaI solution. An absorbance at 370 nm and at 390 nm were seen in the literature, showing the formation of these anion radicals.^{205,206} Taking into account the extinction coefficient of $\text{Br}_2^{\cdot-}$ at 370 nm ($9200 \text{ L mol}^{-1} \text{ cm}^{-3}$), the concentration of NaBr in the solution and the values of long-lived absorbance, indicates that photoexcited xanthone can oxidize Br^- to Br^{\cdot} , followed by the formation of $\text{Br}_2^{\cdot-}$ 4 times more efficiently than acetophenone and 24 times more efficiently than flavone. Likewise, xanthone shows a high capacity to oxidize iodide, up to 42 times larger than for flavone. Compared to the other photosensitizers, xanthone has the highest E^{0*} , the highest ΔG_{ET} , and the fastest kinetics with halides, which can explain the behavior of this photosensitizer.

2.4.5 Chemical characterization

Based on (R-3) and (R-4), electron transfer and H abstraction reactions are expected due to the reaction between the radicals X^{\bullet} , X_2^{\bullet} and the surrounding organic compounds. As a result, halogenated products should be detected in the aqueous phase and some of them may escape to the gas phase.²⁰⁷ Previous studies have detected the formation of halogenated products and X_2 in the gas phase from photosensitized reactions.^{170,208} In this study only the products present in the aqueous phase were examined.

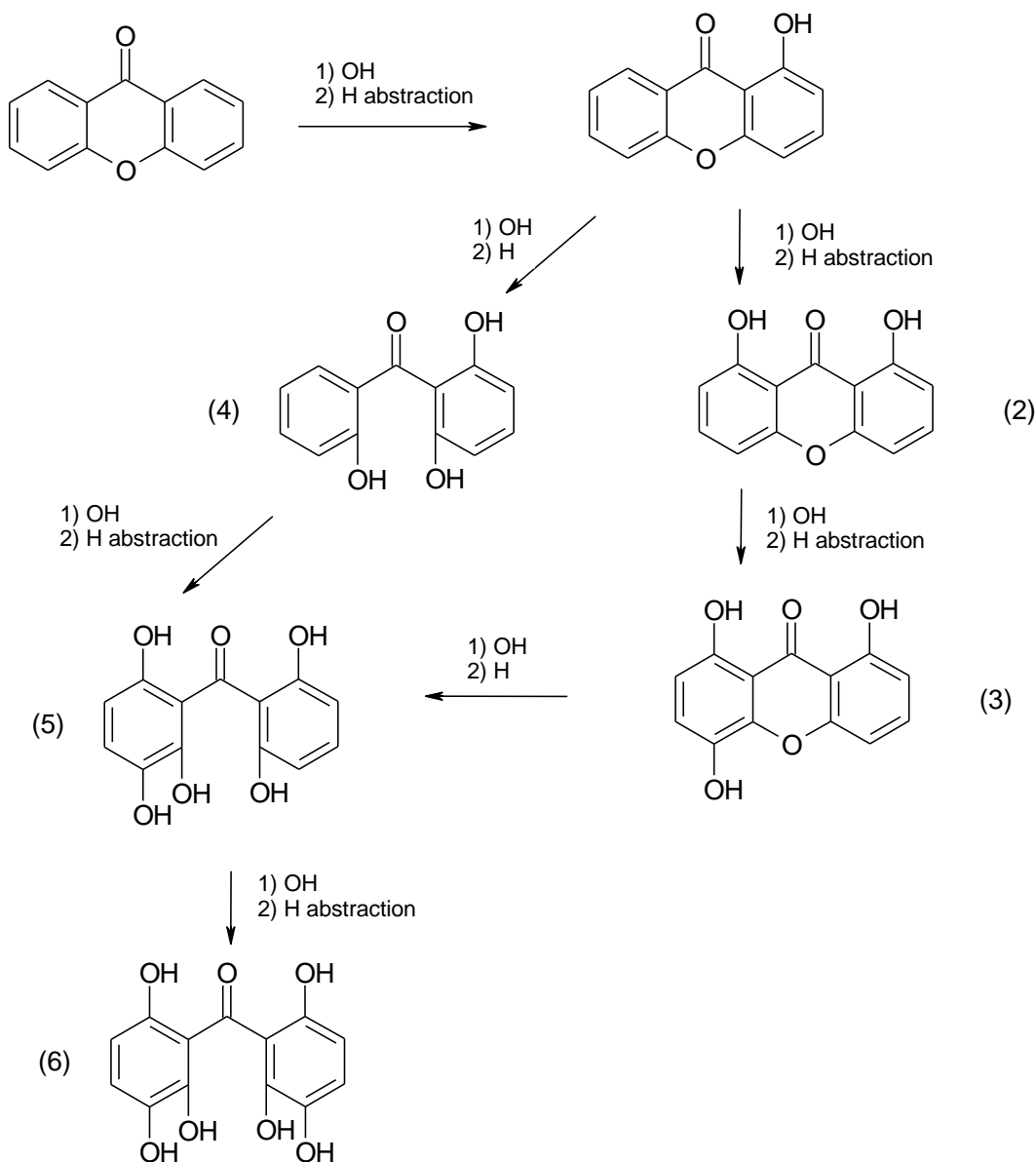
As the solutions were not degassed, in absence of halide ions, the products after the laser discharge correspond to chemistry involving oxygen (and peroxy radicals).^{209,210} Using the UPLC-MS analyses, the molecular formulae were identified based on their molecular masses and isotopic abundance. Without tandem analysis (MS-MS) only the empiric formula could be confirmed (Table 2.3).

Table 2. 3: Compounds identified (D, Detected; ND, Not Detected) in the presence of xanthone and halide ions upon irradiation (I) or in darkness (NI) by UHPLC-MS: theoretical m/z , measured m/z , empirical formula, and normalized peak abundances.

Theoretical mass-to-charge ratio (m/z)	Measured mass-to-charge ratio (m/z)	Empirical formula	Normalized peak abundances			
			Xanthone (NI)	Xanthone (I)	Xanthone + NaI (I)	Xanthone + NaBr (I)
197.0603	197.19	$C_{13}H_8O_2$	1	1	1	1
223.0759	223.08	$C_{15}H_{10}O_2$	ND	2.1×10^{-1}	1.8×10^{-1}	1.9×10^{-1}
229.0501	229.0511	$C_{13}H_8O_4$	ND	4.3×10^{-2}	7.2×10^{-3}	3.8×10^{-4}
245.0450	245.0462	$C_{13}H_8O_5$	ND	1.7×10^{-2}	1.4×10^{-3}	1.3×10^{-4}
247.0606	247.05	$C_{13}H_{10}O_4$	ND	7.1×10^{-3}	3.0×10^{-3}	5.0×10^{-5}
263.0556	263.0569	$C_{13}H_{10}O_6$	ND	1.5×10^{-2}	2.5×10^{-3}	1.4×10^{-4}

279.0504	301.03	C ₁₃ H ₁₀ O ₇	ND	1.4 x 10 ⁻²	4.3 x 10 ⁻³	1.5 x 10 ⁻⁴
341.9389	341.93	C ₁₂ H ₇ O ₄ I	ND	ND	7.9 x 10 ⁻⁴	ND
372.9573	372.95	C ₁₃ H ₉ O ₅ I	ND	ND	1.5 x 10 ⁻³	ND
421.2331	421.2353	C ₂₁ H ₄₁ I	ND	ND	5.6 x 10 ⁻⁴	ND

Only xanthone (m/z 197.19) was identified in the non-irradiated sample, however, six new products were identified in the irradiated samples in the presence or absence of halide ions. The most abundant product was C₁₅H₁₀O₂, and it represents the only product that has not gained additional oxygen atoms. This molecule could be simply the combination of an excited xanthone with C₂H₂ fragment produced from photolysis. Five molecules gaining two or more oxygens have been identified in the three irradiated samples. These molecules are the most abundant in the samples without halide ions. This could be due to the concentration of oxygen in the solution, by increasing the concentration of salt in a solution the solubility of oxygen decreases, which explains the decrease in the abundance of these products with increasing salt concentration ([NaBr] > [NaI]).²¹¹ This observation can also show that oxygen is the limiting reagent in this photosensitized reaction. Organo-iodide molecules were detected only in the irradiated sample containing NaI. While no molecule containing bromine could be identified, it can be due to an insufficient concentration of NaBr to produce a detectable concentration by the instrument. Some of the observations presented above can be explained by the mechanism depicted in scheme 2.1, which only shows the first oxidation steps. In fact, the production of halogenated and organic radicals is inducing a rich and complex chemistry where a multitude of radical recombination reactions may take place. These reactions would correspond to the halogen-halogen or organic radicals recombination reactions has shown by Roveretto et al.,²⁰⁸ explaining some of the products listed in Table 2.3.



Scheme 2. 1: Xanthone photosensitized oxidation mechanism.

2.4.6 Naphthalene SOA Composition

An aqueous solution of NAPH/OH/NO_x SOA was analyzed using a UPLC-PDA high resolution mass spectrometer to help identify potential photosensitizers. The PDA chromatogram (Fig. 2.6) showed several absorbing species in the 300 – 500 nm spectral region, and these peaks correlated well with peaks appearing in the total ion chromatogram (TIC), which allowed for the assignment of absorbing species to specific ions. The neutral formulas of the chromophores are listed beside each of their mass spectrometry chromatograms (Fig. 2.6) and include multiple nitrogen containing

species such as nitro-catechol ($C_6H_5O_4N$), nitro-naphthol ($C_{10}H_7O_3N$), and dinitro-naphthol, one isomer of which is known as Martius Yellow ($C_{10}H_6O_5N_2$). Most of these compounds were previously observed in naphthalene photooxidation by Kautzman et al.²¹² The ten most prominent compounds found by the Compound Discoverer (regardless of their absorbing characteristics) are shown in Table 2.4, and are also dominated by nitrogen containing compounds. Although much lower in intensity, smaller amounts of compounds with the same formula as acetophenone (0.3% of the sum of all assigned compound intensities) were found.

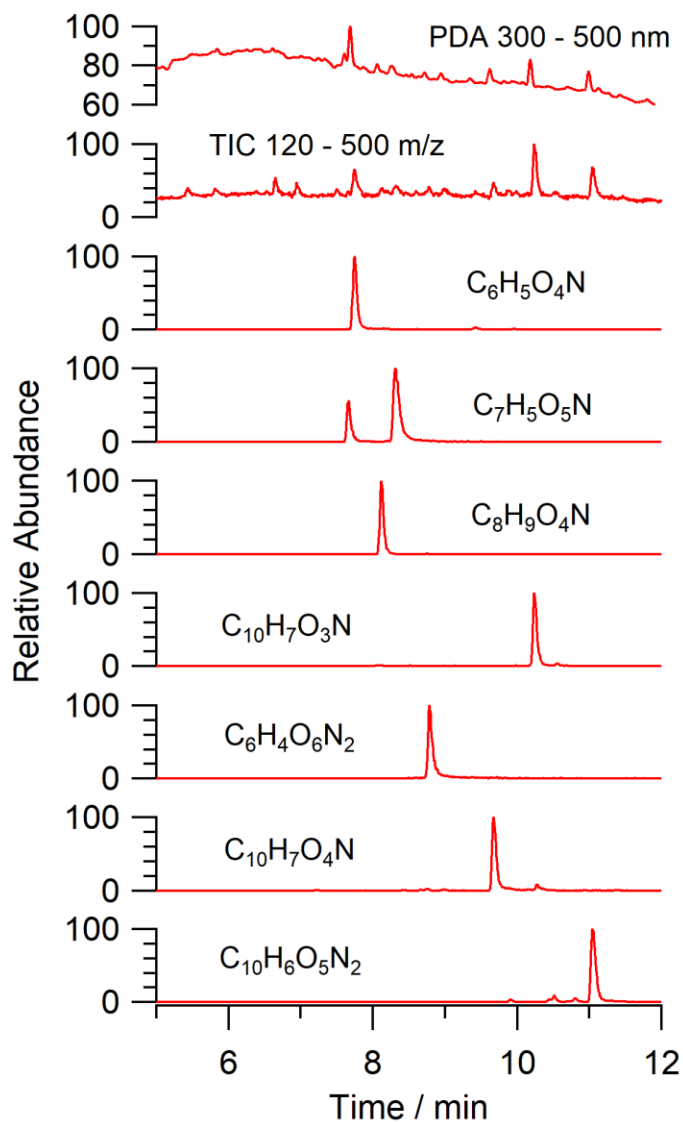
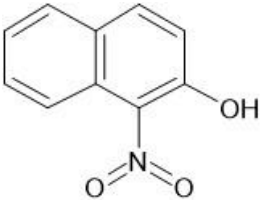
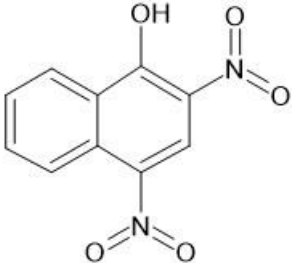
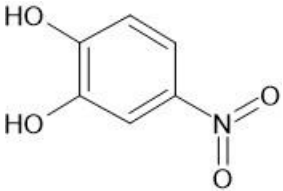
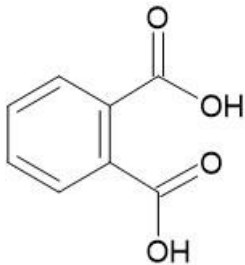
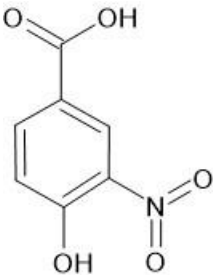
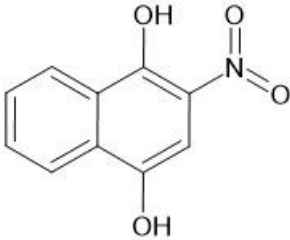
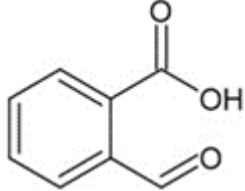


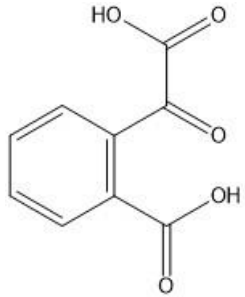
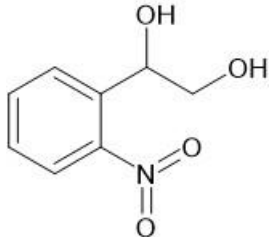

Figure 2. 6: A PDA chromatogram of naphthalene SOA integrated between 300 – 500 nm shows multiple absorbing species. TIC of molecular species between m/z 120 – 500 overlap with peaks in the PDA chromatogram affording

molecular formula assignment to major chromophores. The neutral formulas of the chromophores are listed beside each of their single ion chromatograms.

Table 2. 4: Ten most prominent NAPH/OH/NO_x compounds (in descending order of abundance) from UPLC-PDA-MS analysis of the SOA solution. Proposed structures are also given but are not confirmed as no standards or MS-MS were conducted on the sample.

MW	Compound Formula	Representative Structure with this formula	Retention Time / min	Measured <i>m/z</i>	Delta Mass / ppm
189	C ₁₀ H ₇ O ₃ N	<p>1-nitro-2-naphthol</p> 	10.24	188.03491	2.14
234	C ₁₀ H ₆ O ₅ N ₂	<p>Martius Yellow</p> 	11.05	233.01987	2.25
155	C ₆ H ₅ O ₄ N	<p>4-Nitrocatechol</p> 	7.74	154.01424	2.23

166	$C_8H_6O_4$	<p>Phthalic acid</p> 	6.64	165.01891	2.57
183	$C_7H_5O_5N$	<p>4-hydroxy-3-nitrobenzoic acid</p> 	8.31	182.00903	2.53
205	$C_{10}H_7O_4N$	<p>2-nitronaphthalene-1,4-diol</p> 	9.67	204.02977	2.25
150	$C_8H_6O_3$	<p>2-carboxybenzaldehyde</p> 	6.95	149.02402	2.67

194	C ₉ H ₆ O ₅	2-oxalobenzoic acid 	5.43	193.01375	2.57
183	C ₈ H ₉ O ₄ N	1-(2-nitrophenyl)ethane-1,2-diol 	8.11	182.04544	2.41
139	C ₆ H ₅ O ₃ N	4-Nitrophenol 	8.59	138.01936	2.29

2.4.7 Naphthalene SOA Transient Reactivity

Laser flash photolysis of deoxygenated naphthalene SOA solutions showed strong transient absorption at 420 nm (Figure 2.7a) when excited at 355 nm. A strong fluorescence was also observed immediately after the laser excitation. This was expected, as naphthalene SOA is known to fluoresce with an effective quantum yield of a few percent.^{182,213} After the fluorescence, there was a buildup of transient absorption, followed by a slow exponential decay ($\sim 20 \mu\text{s}$). The decay portion was fitted with a single exponential (Equation 2.1) as done for single photosensitizer molecule solutions (Figure 2.7b). As expected, the transient lifetimes from the exponential fits decreased with increasing KI concentrations and were then used to conduct a Stern-Volmer analysis to obtain the reaction rate constant (k_1) of $3.0 \times 10^8 \text{ M}^{-1} \text{ s}^{-1}$. This is similar to the single

compound experiments but is an order of magnitude lower, which is reasonable considering that not every absorber in naphthalene SOA can act as a photosensitizer.

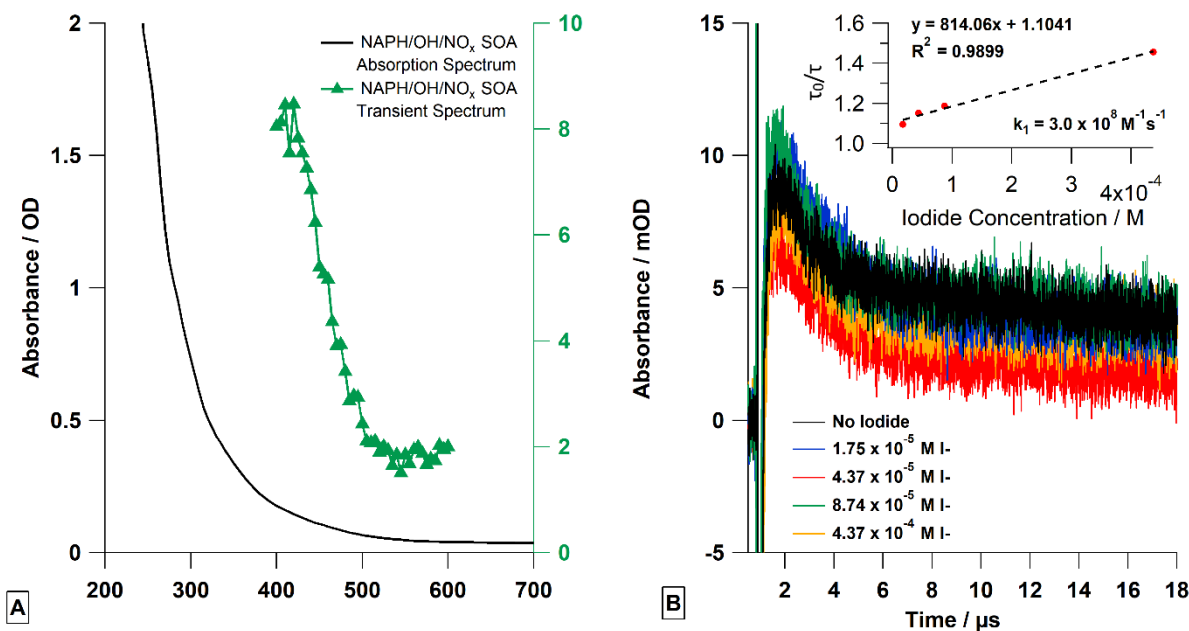


Figure 2. 7: (A)- Steady state (black line) and transient absorption spectra (green triangles) of deoxygenated naphthalene SOA solution. The transient spectrum was the average signal from 1.2 – 2 μs after 355 nm excitation. Please note the transient spectrum is measured in mOD. (B)- The transient absorption decays at 420 nm were measured and fitted to produce a Stern-Volmer analysis at varying concentrations of KI. All solutions were deoxygenated.

Comparing the SOA solution to the single photosensitizer experiments indicate some similarities as the absorption values at later times were not equal to the absorption values before the laser pulse, indicating the formation of a long-lived transient or a stable product (Figure 2.7b). Unlike the single compound experiments where the long-time absorption increased linearly with quencher concentration, the long-time absorption was independent of quencher concentration for SOA solution experiments. The reason for this is not entirely clear but is not entirely surprising either, as the SOA solution is a mixture of thousands of molecular species including quinones, and other aromatic ketones, many of which can exhibit transient absorption ~420 nm. Although speculative, it is expected that the transient absorption at 420 nm is most likely a composite absorption of multiple triplets and free radicals, some of which react with iodide and/or other SOA species. Similar behavior has been observed in the chromophoric dissolved organic matter (CDOM) community.^{214–216} Thus, the formation of new transients and products at long-times is expected to be complex and will include atomic iodine as well as multiple cross reaction products between

atomic iodine, radical iodide, and SOA radical species — the amounts of which depend on the initial amount of iodide present. Increasing the amount of iodide present may increase the yield of one photoproduct but may decrease it for another, resulting in a similar absorption signal. This is further demonstrated by the y-intercept of the Stern-Volmer plot. The y-intercept of the plot is larger than the theoretical value of 1, where the y-axis is the ratio of the lifetime without iodide (τ_0) and the lifetime with a certain concentration of iodide (τ). At the y-intercept, the ratio should equal one, but the larger value here indicates chemical reactivity even when the iodide concentration is zero, likely due to the aforementioned chemical complexity and cross reactions in the solution.

The SOA system is complex, with multiple reactive species undergoing multiple generations of cross reactions with each other, and cannot be well-explained by a classical triplet-quencher mechanism. As such, results should be considered as a study of the “effective” reactivity of the system based on the triplet/radical pool at 420 nm.

2.5 Conclusion

These experimental results indicate that aromatic ketones contribute towards photosensitized reactivity in atmospheric particles as a source of anion radical formation in the atmosphere. Compounds that come from primary emissions (xanthone, flavone, and acetophenone) as well as from secondary oxidation of aromatic compounds (such as naphthalene) can act as potential photosensitizers that are capable of abstracting electrons from halide ions. The rate of the resulting radical anion formation depends on the free energy of the electron transfer of the photosensitizer, and the oxidation potential of the halide ions. Furthermore, oxidized compounds and halogenated organic compounds are also formed by irradiation at 355 nm in the presence of oxygen, which is atmospherically relevant. These products are highly oxygenated, and their presence in the atmosphere can be a marker of the photosensitization process from xanthone in the atmosphere. This study demonstrates that tropospheric photosensitization may involve a large variety of compounds of primary or secondary nature and will introduce new, unconsidered chemical pathways that impact atmospheric multiphase chemistry.

Chapter 3: Naphthalene-derived secondary organic aerosols interfacial photosensitizing properties

Portions of this chapter were reproduced with permission from Wang, X., Gemayel, R., Baboomian, V. J., Li, K., Boreave, A., Dubois, C., et al. (2021). Naphthalene-derived secondary organic aerosols interfacial photosensitizing properties. *Geophysical Research Letters*, 48, e2021GL093465. <https://doi.org/10.1029/2021GL093465>

3.1 Abstract

We investigated the photosensitizing properties of secondary organic aerosol (SOA) formed during the hydroxyl radical (OH) initiated oxidation of naphthalene. This SOA was injected into an aerosol flow tube and exposed to UV radiation and gaseous volatile organic compounds or sulfur dioxide (SO₂). The aerosol particles were observed to grow in size by photosensitized uptake of d-limonene and β-pinene. In the presence of SO₂, a photosensitized production (0.2-0.3 μg m⁻³ h⁻¹) of sulfate was observed at all relative humidity (RH). Some sulfate also formed on particles in the dark, probably due to the presence of organic peroxides. The dark and photochemical pathways exhibited different trends with RH, unravelling different contributions from bulk and surface chemistry. As naphthalene and other polycyclic aromatics are important SOA precursors in the urban and suburban areas, these dark and photosensitized reactions are likely to play an important role in sulfate and SOA formation.

3.2 Introduction

Organic compounds and sulfate anions are ubiquitous in ambient aerosols, accounting for 20-90% and 10-60% of the fine particulate mass, respectively.^{22,217} A large fraction of these organic compounds and sulfate are secondary in nature, i.e., they are produced through atmospheric oxidation of volatile organic compounds (VOCs)¹⁸ and sulfur dioxide (SO₂).^{218,219} Both sulfate and secondary organic aerosol (SOA) significantly impact air quality, climate, as well as human and ecosystem health.^{220,221} Despite extensive research spanning nearly a century, we still do not fully understand all possible pathways for their formation and transformation in the atmosphere.^{222,223}

Many previous studies showed that photosensitized chemistry may be an important pathway for promoting the oxidation of VOCs^{163,224} in atmospheric particles, which can increase the mass of SOA. For example, irradiation of imidazole-2-carboxaldehyde (IC) and humic acid in the presence of various gaseous VOCs, such as d-limonene, has been shown to produce highly oxygenated compounds and thereby initiate aerosol growth by photosensitized mechanisms.^{75,144,145,154,225} Previous studies have suggested that the photosensitized chemistry of humic-like substances (HULIS) is not fast enough to compete with the conventional free-radical-driven growth under ambient concentrations of d-limonene.²²⁶ However, while not being a major growth pathway of aerosols, photosensitized processes have the potential to change the particle phase oxidation capacity. For instance, significant amounts of oxygenated molecules with low-volatility have been observed during photosensitized oxidation of some VOCs.^{154,165,167} The importance of such processes is obviously linked to the concentration of triplet state in the condensed phase as underlined by Kaur et al.,¹⁶³ who pooled all active triplet state into a one single T* family. In other words, in contrast to well identified radicals (such as OH), the key feature of tropospheric photosensitization is related to numerous compounds with diverse sources. Understanding those is therefore key. To further illustrate this potential importance, it has been shown that photosensitized chemistry involving the humic fraction of aerosols during Chinese haze events can explain a significant fraction of the observed sulfate formation.⁷⁶ The authors highlighted the specific role played by biomass burning (for cooking and heating during the cold season) as the main source of the aerosol's photosensitizing properties.

Naphthalene, emitted primarily from fossil fuel combustion and biomass burning, represents the smallest, most volatile, and most abundant polycyclic aromatic hydrocarbon (PAH) in the

atmosphere.²²⁷ Naphthalene is ubiquitous in suburban and urban areas, with a median concentration of $0.94 \mu\text{g m}^{-3}$ in 11 U.S. cities.²²⁸ The OH-initiated oxidation of naphthalene produces a number of different oxygenated compounds with high molecular weight and low-volatility, which can partition into particles and contribute to SOA mass.⁸⁷ Naphthoquinone, a naphthalene oxidation product,²²⁹ is commonly found in atmospheric aerosols (e.g., Shanghai, China;²³⁰ Tempe, USA;²³¹ Kurashiki City, Japan;²³² Yangtze River Channel²³³), and is known to be an efficient photosensitizer, inducing redox chemistry or producing reactive oxygen species.^{146,234} SOA derived from oxidation of naphthalene under high- NO_x conditions has been shown to be weakly fluorescent,²¹³ resilient to photobleaching,¹⁸² efficient in photosensitizing singlet oxygen in aqueous solutions,¹⁴⁹ capable of photosensitized oxidation of halide ions,²³⁵ and moderately effective in photosensitized oxidation of d-limonene.⁷⁴ It is therefore likely that aerosol particles containing naphthalene oxidation products (as well as oxidation products of PAHs in general) contribute to photosensitized chemistry in the atmosphere.

In this study, we investigated the photosensitizing activity of naphthalene-derived SOA using both gaseous VOCs and SO_2 as reaction partners. These experiments were collaborative and involved travelling to Christian George's Laboratory in Lyon, France (IRCELYON) to conduct the experiments. Naphthalene-SOA was generated in a laminar-flow Gothenburg (Go:PAM) oxidation flow reactor, then its photosensitizing properties were investigated by explicitly measuring particle growth in aerosol flow tube (AFT) experiments, in which particles were exposed to near-UV radiation in presence of VOCs or SO_2 . Our data suggests that these aerosols do indeed exhibit photosensitized chemistry, by converting SO_2 into sulfate and d-limonene and β -pinene into particle-phase organic products.

3.3 Materials and Methods

As shown in Figure 3.1, the experimental setup mainly consisted of a Go:PAM oxidation flow reactor and an aerosol flow reactor.

3.3.1 Go:PAM Description

The Go:PAM flow reactor (9.6 cm inner diameter, 100 cm length) is made of quartz glass and surrounded by two 30 W Philips ultraviolet lamps capable of producing 254 nm radiation.²³⁶ The gas flow injected into the Go:PAM chamber consisted of 250 mL min^{-1} of pure air bubbled through

hydrogen peroxide (H_2O_2 , Sigma Aldrich, 26.4 wt. % in H_2O) solution, 20 mL min^{-1} of pure air containing naphthalene (Sigma Aldrich, 99%) vapor, 1 L min^{-1} of humidified air, and 2.78 L min^{-1} of dry air, leading to a residence time of 1.8 min. The Go:PAM was operated at room temperature in the range of $297 \pm 2 \text{ K}$, whilst a fan was used to homogenize and maintain the temperature. As calculated under the above conditions, the relative humidity (RH) and the concentrations of H_2O_2 and naphthalene in the Go:PAM reactor were around 29%, $5.2 \times 10^3 \text{ ppb}$, and $5.5 \times 10^2 \text{ ppb}$, respectively.

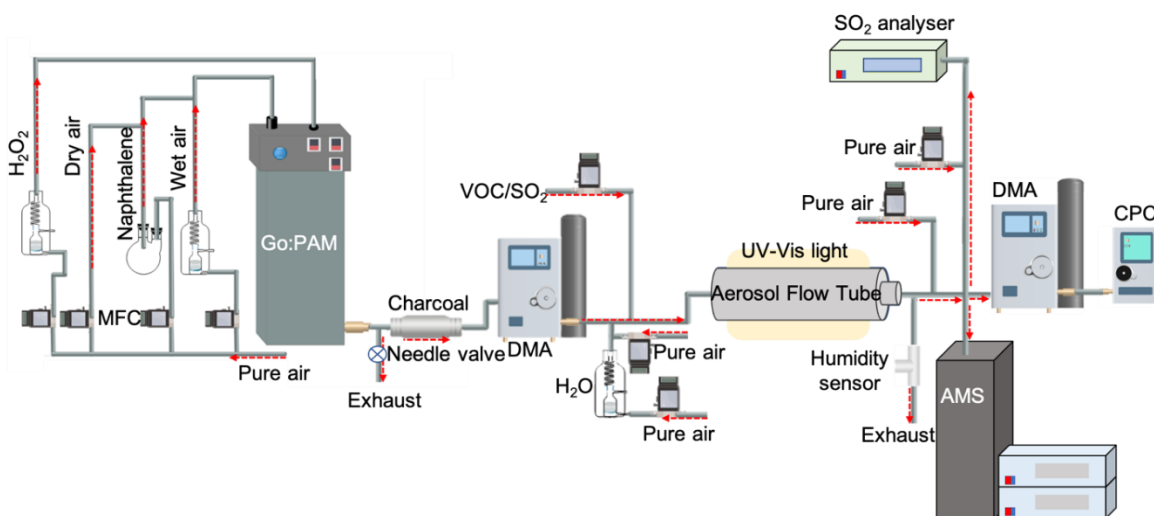


Figure 3. 1: Schematic of the experimental setup with the Go:PAM flow and aerosol flow reactors.

3.3.2 Aerosol Flow Tube Experiment

The Naphthalene-SOA air-flow was controlled by a needle valve and sent into a charcoal denuder ($100\text{-}160 \text{ mL min}^{-1}$) (Sigma Aldrich, Norit RBAA-3) to reduce concentrations of gaseous compounds and then into a differential mobility analyzer (DMA, TSI model 3081, impactor size 0.0508 cm) to produce monodispersed particles of desired size (mobility-equivalent diameter). The size selection by DMA further reduced the concentration of gaseous compounds in the flow. The size-selected SOA and VOC or SO_2 (Linde, France) were injected into a temperature-controlled horizontal jacketed aerosols flow tube (AFT) (6 cm internal diameter, 180 cm length) made of Pyrex.⁷⁶ In order to reduce the evaporative loss of the naphthalene-SOA particles that is known to happen after size selection,^{237,238} the temperature inside the AFT was kept at 285 K . The RH inside the AFT was calculated based on the measured temperature and RH of the aerosol flow upon exiting the AFT. The AFT was surrounded by eight UV-lamps (Cleo, Philips, Netherlands) with a

continuous emission spectrum over 300-420 nm and a total irradiance of 6×10^{15} photon $\text{cm}^{-2} \text{s}^{-1}$.²³⁹

As shown in Figure 3.1, the aerosol flow was diluted by a factor of ~ 2 with pure air before being sent to a scanning mobility particle sizer (SMPS, TSI 3936, impactor size 0.071 cm), an SO_2 analyzer (Thermo 43i) and an Aerodyne compact time-of-flight (cTOF) aerosol mass spectrometer (AMS), to characterize the particle size distributions in the range of 15-700 nm, gaseous SO_2 concentration, and particle-phase sulfate production, respectively. The diluted aerosol flow was further diluted with pure air before being analyzed by a stander SO_2 analyzer. In some experiments, a selected VOC was continuously injected in the AFT together with the particles. For this purpose, a permeation tube placed in a temperature-controlled oven (Dynacal, Valco Instruments Co. Inc., U.S., using VICI Metronics, U.S., Dynacalibrator, model 150) was used to generate a specific concentration of d-limonene or β -pinene.¹⁵⁴ A high-resolution proton-transfer-reaction time-of-flight mass spectrometer (PTR-TOF-MS 8000, Ionicon Analytik) was then used to measure their concentrations. The detailed setup and calibration of the PTR-MS were described in a previous study.²⁴⁰

3.3.3 SMPS and AMS

The SMPS instrument consists of a differential mobility analyzer (DMA, TSI 3081) and a condensation particle counter (CPC, TSI 3772, or TSI 3776). The gas flow was 0.3 L min^{-1} and the corresponding sheath flow was 3 L min^{-1} .

The ionization efficiency (IE) and relative ionization efficiency (RIE) of the AMS were calibrated using 300 nm ammonium nitrate particles. Ammonium nitrate (NH_4NO_3) particles were generated by a constant-output atomizer (TSI Model 3076), then dried by a silica dryer, size selected by a DMA, and then sent to the AMS and CPC simultaneously. Notably, the Naphthalene-SOA used for the sulfate production measurement experiments were size selected at 100 nm diameter before being injected into the AFT. Therefore, dried monodispersed ammonium sulfate ($(\text{NH}_4)_2\text{SO}_4$) particles with the same size (i.e., 100 nm) were flowed into the AMS and SMPS simultaneously, and the collection efficiency (CE) of the AMS was derived by comparing the sulfate concentrations measured by the AMS and calculated by the SMPS. The particle size distributions of $(\text{NH}_4)_2\text{SO}_4$ measured by the SMPS were converted to mass concentrations using a density of 1.77 g cm^{-3} .²⁴¹ The study of Allan et al.²⁴² showed that the CE value depends on the RH of the sample air. As

such, all experiments in our study had the aerosol flow RH prior to the analysis by AMS below 25%; therefore, the calculated CE is applicable for all experiments. The AMS analysis software Squirrel version 1.60P and Pika version 1.20P were used to analyze the obtained mass spectra.

3.3.4 HRMS analysis of Naphthalene-SOA

Naphthalene-SOA was collected onto 47 mm quartz fiber filters (Tissuquartz 2500QAT, PALL Life Sciences) with a sampling time of 15 min at the flow rate of 4.05 L min⁻¹. The blank samples were collected using the same procedure but without injecting naphthalene. All filter samples were extracted with two subsequent 6 mL extractions of acetonitrile (Optima® LC/MS, Fischer Scientific, USA) and agitated for 20 min on an orbital shaker set at 1000 rpm. The combined extracts were filtered through a 0.2 µm polytetrafluoroethylene membrane (13 mm, Pall Corporation, USA) using a glass syringe. Next, 0.5 mL of the extracts were diluted by adding 0.5 mL of water (Optima® LC/MS, Fischer Scientific, USA), before being analyzed by an Orbitrap high resolution mass spectrometer (HRMS, Q Exactive, Thermo Scientific, Bremen, Germany) with heated electrospray ionization (HESI). The diluted extracts were injected in a direct-infusion mode using a Hamilton syringe at a flow rate of 5 µL min⁻¹ and analyzed in negative (ESI) mode. The details of the HRMS analysis has been described in previous studies.^{233,243}

In this study, Xcalibur software (V2.2, Thermo Scientific) was used to analyze the obtained mass spectra and export mass lists.²⁴⁴ All ions with a signal-to-noise ratio (s/n) ≥ 3 , signal intensity : background ratio > 10 , and in the m/z range of 50-750 were exported. Chemical formula (i.e., [M-H]⁻) assignments for these ions were calculated using a mass tolerance of ± 3 ppm.²⁴⁴ Additionally, formulas were further constrained by setting H/C and O/C in the ranges of 0.3-3 and 0-3, respectively.

3.4 Results and Discussion

3.4.1 Photosensitized uptake of SO₂

In previously published control experiments, only one VOC or SO₂ was injected into the AFT (without Naphthalene-SOA) under similar conditions to other experiments (i.e., the same RH, UV exposure, temperature, and residence time). During these experiments, no loss of VOC or SO₂ and no particle formation were observed,¹⁴⁵ indicating that gas-phase oxidation of the VOC or SO₂ was not taking place in the AFT, due to an absence of gaseous oxidants.

In the first series of experiments, Naphthalene-SOA (~ 5700 particles cm^{-3} , median size ~ 46 nm) and SO_2 (1 ppm after dilution) were injected into the AFT with a residence time of 16 min at a high RH of 86-90%. Figure 3.2A shows a typical profile for the evolution of the median and mean diameters of the particles at the outlet of the AFT. Notably, both the median and mean diameters of particles (before UV irradiation) were smaller than selected inlet sizes, indicating some particle evaporation in the first DMA and AFT. A small particle growth was observed once the UV lights were switched on, growing 2 nm in terms of median and mean diameters.

Table 3. 1: Median Diameter Growth Factor (DGF, %) of Naphthalene-SOA with different gaseous compounds and RH. D_{p0} , initial particle median diameter; D_p , particle median diameter after irradiation.

Gaseous compounds	Concentration (ppm)	Residence time (min)	RH	D_{p0} (nm)	D_p (nm)	DGF (%)
None	0	16	47-49%	44.1 \pm 0.2	43.5 \pm 0.3	-1.4
	0	16	68-71%	43.8 \pm 0.3	42.2 \pm 0.4	-3.8
	0	16	85-89%	42.4 \pm 0.2	41.4 \pm 0.3	-2.4
	1	16	40-43%	44.8 \pm 0.2	43.0 \pm 0.3	-4.2
	1	16	61-65%	42.5 \pm 0.2	41.3 \pm 0.8	-2.9
SO_2	1	16	86-90%	42.8 \pm 0.4	44.7 \pm 0.7	4.3
	0.7	16	86-90%	42.9 \pm 0.2	43.9 \pm 0.2	2.3
	0.4	16	86-90%	42.9 \pm 0.2	43.1 \pm 0.2	0.5
d-Limonene	0.1	25	39-43%	36.4 \pm 0.7	71.4 \pm 1.3	50.8
	0.1	25	84-88%	34.0 \pm 0.2	85.4 \pm 1.6	58.7
β -pinene	0.8	25	45-47%	37.0 \pm 0.4	40.6 \pm 0.3	8.9
	0.8	25	85-89%	35.7 \pm 0.3	47.1 \pm 0.3	24.2

In addition, the Diameter Growth Factor (DGF (%)) = $((D_p - D_{p0}) / D_p) \times 100$ was calculated for different experimental conditions (see Table 3.1). As RH decreases to 61-65% and 40-43%, the particle size measurements indicate particle shrinking instead of growth when Naphthalene-SOA were exposed to 1 ppm SO₂ and UV irradiation. This is likely due to the particle phase undergoing photodegradation when exposed to UV irradiation, resulting in smaller particle sizes. Indeed, it has been shown that the photodegradation of SOA particles could produce small oxygenated VOCs evaporating to the gas phase.^{80,138} Notably, at RH 40-49%, the DGF was even lower when SOA particles were exposed to SO₂ compared to control experiments, possibly due to the more acidic aerosol phase enhancing the evaporation of small organic acids from particles. Slade et al.²⁴⁵ suggested that degradation of SOA under viscous conditions (i.e., low RH), where diffusion into the bulk is prevented, tends to promote the production of multiple generations of oxidation of the same molecule, resulting in fragmentation and evaporation. Such processes could also be occurring in our experiments at low RH when SO₂ is present.

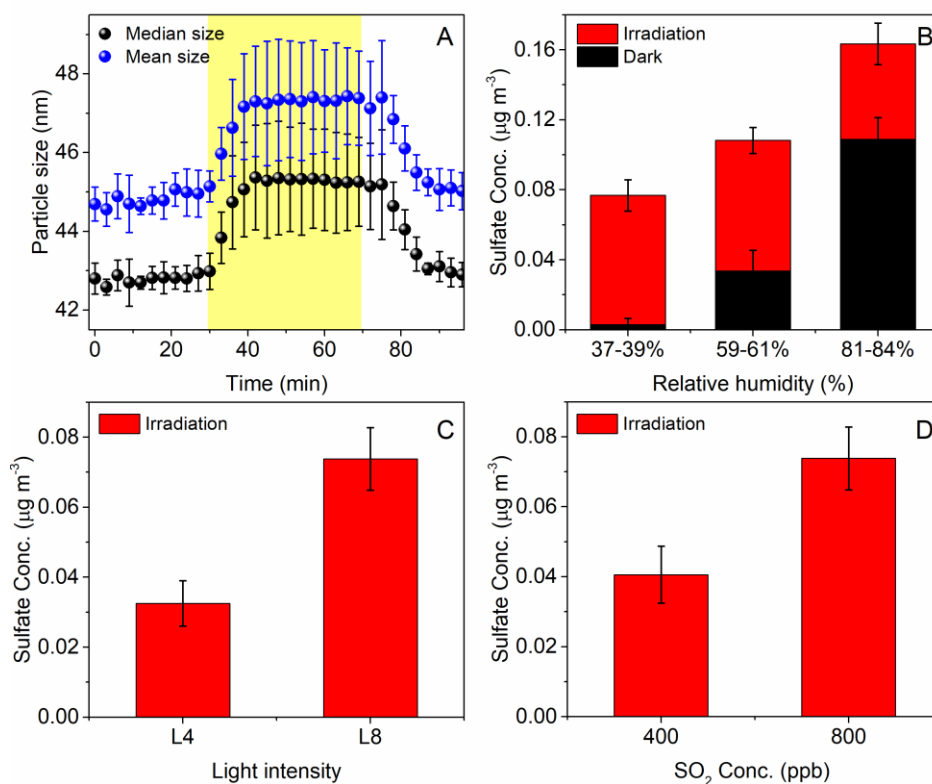


Figure 3. 2: Median and mean diameter ($\pm 2\sigma$) growths of Naphthalene-SOA exposed to UV light and SO₂ for 16 min in the AFT (A). The yellow region corresponds to the irradiation time. Sulfate production as measured by the cTOF-

AMS of Naphthalene-SOA exposed to SO₂ at different RH (B), under different light intensities (C), and with different SO₂ concentrations (D). L4 means four lamps were turned on; and L8 means eight lamps were turned on.

In the second series of experiments, 100 nm Naphthalene-SOA particles, up to 6000 particles cm⁻³, were size-selected and exposed to 0.8 ppm SO₂ for sulfate production measurement experiments. The particle size-selection was changed (from 46 to 100 nm) due to the low transmission efficiency of the cTOF-AMS for particles less than 60 nm. The total amount of all sulfate was then monitored (the cTOF instrument has limited capabilities to distinguish between the inorganic and organic sulfate). Figure 3.2B shows that at different RHs, particulate sulfate was produced from both dark and photosensitized chemistry. The dark production of particulate sulfate can be explained by a couple of factors. Firstly, organic peroxides were found to account for ~26.2% of the total naphthalene-SOA mass,²¹² which are believed to oxidize SO₂ to sulfate and organosulfates.²⁴⁶⁻²⁴⁸ In addition, dissolved S(IV) may react with aldehydes and quinones in Naphthalene-SOA²¹² to produce organosulfonates.^{249,250} All these pathways could contribute to the measured sulfate in the dark, which are in the range of 0.003-0.11 μg m⁻³. In addition, a previous study showed that the sulfate production from the reaction between SO₂ and α-pinene-derived SOA exhibits an exponential dependence on RH,²⁴⁸ which is similar to the result obtained in the present study (Figure 3.2B).

When the UV lights were switched on, 0.05-0.08 μg m⁻³ of sulfate (i.e., 0.2-0.3 μg m⁻³ h⁻¹) were produced at all RHs (Figure 3.2B). However, although the total sulfate production increases as the RH increases, the sulfate production attributable to the photosensitized oxidation at RH 81-84% is the lowest. This indicates a more complex RH dependence on the photochemical mechanism. Saukko et al.¹¹⁹ have investigated the physical phase state (solid, semi-solid, or liquid) of SOA derived from various precursors by measuring their bounce behavior after inertial impaction on a solid substrate. The measured bounce fraction was evaluated as a function of RH and SOA oxidation level (O / C). In the case of Naphthalene-SOA, the bounce factor was indicative of an amorphous solid or semi-solid state, up to RH close to 70%. At greater RH values, this factor decreased, indicating a phase change with particles having a less viscous, more "liquid-like" material. These trends are to be compared with the data shown in Figure 2B, where the dark chemistry was predominant only at high RH. Such chemistry could be driven, among other factors, by the peroxide, aldehyde, and quinone (i.e., naphthoquinone) compounds present in such particles²¹² forming organosulfates, organosulfonates and sulfate.²⁴⁶⁻²⁵⁰ But the fact that it occurs

more efficiently at high RH (i.e., on more liquid particles), points towards a bulk process where the chemistry occurs after solubilization of the incoming SO₂ molecules. In addition, the sulfate formed from dark chemistry can also impact physical properties such as hygroscopicity, acidity, and phase state,^{119,251} which may further influence the solubility of S(IV) in the aerosol phase.

In contrast, the photochemical fraction of sulfate production is reduced at higher RHs but gains in importance at low RH, where potentially the surface, or a small shell close to the surface, is available for reaction. Notably, previous studies showed that in-particle diffusion is not rate-limiting to SO₂ uptake by α -pinene-derived SOA at low RH (<10%), whilst toluene-derived SOA starts to lose the resistance above 20% RH.^{248,252,253} Therefore, a significant diffusion limitation is not expected in the present study. Besides, SO₂ could also be excited into the triplet state (by direct absorption of light into an excited singlet state followed by intersystem crossing) with wavelengths of 240-330 nm, which could react with H₂O to produce sulfate.^{254,255} However, this sulfate formation pathway was shown to be minor in our AFT system due to the weak overlap of SO₂ light absorption and spectral irradiance of our lamps.⁷⁶ Additionally, the bulk chemistry may also consume the existing photosensitizers and explain the reduced fraction of photochemically produced sulfate at high RHs. Thus, at higher RHs sulfate production is dominated by bulk phase solubilization and subsequent oxidation of SO₂, whereas photosensitized oxidation at the surface of the particles dominates at lower RHs.

It is notable that the mean particle size of SOA decreased from 93 nm to 85 nm as the RH increased from 37-39% to 81-84% in the dark, possibly due to the moisture-induced changes in SOA morphology or phase and high evaporation of SOA at high RH,^{120,121,138,256} reducing the surface area and volume by ~16% and ~24%, respectively. Figures 3.2C and 3.2D show that sulfate production decreases as the light intensity and SO₂ concentration decrease.

Traditionally, SO₂ oxidation is known to be mainly driven by gas-phase reactions with OH radicals, ozone, H₂O₂, nitrogen dioxide (NO₂), and transition-metal ions in the aqueous phase,²⁵⁷ whilst interfacial SO₂ oxidation on acidic microdroplets²⁵⁸ and SO₂ triplet state chemistry^{254,255} were also suggested to play a role in the sulfate formation. However, the photosensitized oxidation of SO₂ has recently been discussed as an important contributor to sulfate formation on biomass burning type particles.⁷⁶ Our findings here now extend such observations also to more

anthropogenic particles and are posing the question whether such photosensitized processes are widespread.

3.4.2 Chemical characteristics of Naphthalene-derived SOA

A total of 97 organic compounds were identified in ESI-. All formulas, together with their m/z , intensities, ring and double bond equivalence (RDBE), and elemental ratios are listed in Table 3.2. Notably, ESI-HRMS is highly sensitive to polar compounds, while being quite insensitive to non-polar ones, as those exhibit very poor ionization efficiency.²⁵⁹ Therefore, many non-polar compounds might not have been measured in this study. In addition, ESI techniques are prone to matrix effects and varying ionization efficiencies for different compounds, meaning the signal intensities reported here do not represent actual concentrations.

Table 3. 2: All formulas, together with their m/z , intensities, ring and double bond equivalence (RDBE), and elemental ratios tentatively determined in Naphthalene-derived SOAs.

m/z	assigned formula	Intensity	H/C	O/C	RDBE
105.0345	C ₇ H ₆ O	3.52×10 ⁴	0.86	0.14	5
107.0501	C ₇ H ₈ O	1.35×10 ³	1.14	0.14	4
119.0499	C ₈ H ₈ O	2.43×10 ⁵	1.00	0.13	5
123.0087	C ₆ H ₄ O ₃	1.13×10 ⁴	0.67	0.50	5
131.0501	C ₉ H ₈ O	2.27×10 ⁵	0.89	0.11	6
133.0294	C ₈ H ₆ O ₂	3.92×10 ⁵	0.75	0.25	6
135.0450	C ₈ H ₈ O ₂	1.52×10 ⁵	1.00	0.25	5
137.0242	C ₇ H ₆ O ₃	5.95×10 ⁵	0.86	0.43	5
142.9984	C ₅ H ₄ O ₅	1.56×10 ⁴	0.80	1.00	4
143.0500	C ₁₀ H ₈ O	1.15×10 ⁵	0.80	0.10	7
145.0293	C ₉ H ₆ O ₂	3.12×10 ⁵	0.67	0.22	7
147.0450	C ₉ H ₈ O ₂	7.93×10 ⁵	0.89	0.22	6
149.0241	C ₈ H ₆ O ₃	3.77×10 ⁶	0.75	0.38	6

151.0034	C ₇ H ₄ O ₄	8.24×10 ³	0.57	0.57	6
151.0399	C ₈ H ₈ O ₃	1.47×10 ⁵	1.00	0.38	5
153.0191	C ₇ H ₆ O ₄	1.59×10 ⁵	0.86	0.57	5
154.9985	C ₆ H ₄ O ₅	8.56×10 ³	0.67	0.83	5
159.0449	C ₁₀ H ₈ O ₂	1.60×10 ⁵	0.80	0.20	7
161.0242	C ₉ H ₆ O ₃	5.92×10 ⁵	0.67	0.33	7
161.0606	C ₁₀ H ₁₀ O ₂	2.17×10 ³	1.00	0.20	6
163.0035	C ₈ H ₄ O ₄	5.48×10 ⁵	0.50	0.50	7
163.0399	C ₉ H ₈ O ₃	2.05×10 ⁶	0.89	0.33	6
165.0191	C ₈ H ₆ O ₄	1.44×10 ⁷	0.75	0.50	6
166.9983	C ₇ H ₄ O ₅	9.55×10 ³	0.57	0.71	6
167.0347	C ₈ H ₈ O ₄	4.17×10 ⁴	1.00	0.50	5
169.0140	C ₇ H ₆ O ₅	3.55×10 ⁴	0.86	0.71	5
173.0090	C ₆ H ₆ O ₆	4.63×10 ³	1.00	1.00	4
173.0241	C ₁₀ H ₆ O ₃	9.04×10 ⁵	0.60	0.30	8
173.0450	C ₇ H ₁₀ O ₅	1.42×10 ⁴	1.43	0.71	3
175.0398	C ₁₀ H ₈ O ₃	5.12×10 ⁶	0.80	0.30	7
177.0191	C ₉ H ₆ O ₄	7.30×10 ⁵	0.67	0.44	7
177.0553	C ₁₀ H ₁₀ O ₃	2.10×10 ⁵	1.00	0.30	6
178.9984	C ₈ H ₄ O ₅	1.35×10 ⁴	0.50	0.63	7
179.0347	C ₉ H ₈ O ₄	2.00×10 ⁶	0.89	0.44	6
181.0136	C ₈ H ₆ O ₅	4.43×10 ⁵	0.75	0.63	6
181.0504	C ₉ H ₁₀ O ₄	3.33×10 ⁴	1.11	0.44	5
183.0295	C ₈ H ₈ O ₅	2.57×10 ⁴	1.00	0.63	5
185.0089	C ₇ H ₆ O ₆	1.08×10 ⁴	0.86	0.86	5

189.0191	C ₁₀ H ₆ O ₄	4.70×10 ⁵	0.60	0.40	8
191.0347	C ₁₀ H ₈ O ₄	2.48×10 ⁶	0.80	0.40	7
193.0139	C ₉ H ₆ O ₅	1.10×10 ⁶	0.67	0.56	7
193.0501	C ₁₀ H ₁₀ O ₄	7.06×10 ⁵	1.00	0.40	6
195.0296	C ₉ H ₈ O ₅	6.49×10 ⁵	0.89	0.56	6
197.0088	C ₈ H ₆ O ₆	2.84×10 ⁴	0.75	0.75	6
197.0452	C ₉ H ₁₀ O ₅	9.20×10 ³	1.11	0.56	5
199.0245	C ₈ H ₈ O ₆	2.03×10 ⁴	1.00	0.75	5
201.0401	C ₈ H ₁₀ O ₆	8.90×10 ³	1.25	0.75	4
203.0346	C ₁₁ H ₈ O ₄	2.89×10 ⁴	0.73	0.36	8
203.0571	C ₈ H ₁₂ O ₆	1.12×10 ⁵	1.50	0.75	3
205.0139	C ₁₀ H ₆ O ₅	9.57×10 ⁴	0.60	0.50	8
205.0513	C ₁₁ H ₁₀ O ₄	1.66×10 ⁴	0.91	0.36	7
207.0295	C ₁₀ H ₈ O ₅	1.41×10 ⁶	0.80	0.50	7
209.0088	C ₉ H ₆ O ₆	7.31×10 ⁴	0.67	0.67	7
209.0450	C ₁₀ H ₁₀ O ₅	6.48×10 ⁵	1.00	0.50	6
211.0245	C ₉ H ₈ O ₆	6.55×10 ⁴	0.89	0.67	6
213.0401	C ₉ H ₁₀ O ₆	5.14×10 ³	1.11	0.67	5
215.0204	C ₈ H ₈ O ₇	3.48×10 ⁴	1.00	0.88	5
219.0295	C ₁₁ H ₈ O ₅	1.35×10 ⁴	0.73	0.45	8
221.0092	C ₁₀ H ₆ O ₆	1.28×10 ⁴	0.60	0.60	8
221.0454	C ₁₁ H ₁₀ O ₅	4.10×10 ⁴	0.91	0.45	7
223.0245	C ₁₀ H ₈ O ₆	2.38×10 ⁵	0.80	0.60	7
223.0608	C ₁₁ H ₁₂ O ₅	4.49×10 ⁴	1.09	0.45	6
225.0401	C ₁₀ H ₁₀ O ₆	1.55×10 ⁵	1.00	0.60	6

227.0193	C ₉ H ₈ O ₇	6.79×10 ³	0.89	0.78	6
229.0351	C ₉ H ₁₀ O ₇	1.10×10 ³	1.11	0.78	5
233.0451	C ₁₂ H ₁₀ O ₅	9.71×10 ³	0.83	0.42	8
237.0401	C ₁₁ H ₁₀ O ₆	2.84×10 ⁴	0.91	0.55	7
237.0766	C ₁₂ H ₁₄ O ₅	2.23×10 ⁴	1.17	0.42	6
239.0194	C ₁₀ H ₈ O ₇	5.56×10 ⁴	0.80	0.70	7
239.0563	C ₁₁ H ₁₂ O ₆	3.23×10 ⁴	1.09	0.55	6
241.0351	C ₁₀ H ₁₀ O ₇	3.12×10 ⁴	1.00	0.70	6
249.0401	C ₁₂ H ₁₀ O ₆	7.66×10 ³	0.83	0.50	8
253.0714	C ₁₂ H ₁₄ O ₆	6.84×10 ³	1.17	0.50	6
295.0606	C ₁₇ H ₁₂ O ₅	6.92×10 ³	0.71	0.29	12
303.0658	C ₁₉ H ₁₂ O ₄	9.70×10 ³	0.63	0.21	14
307.0608	C ₁₈ H ₁₂ O ₅	8.97×10 ³	0.67	0.28	13
309.0764	C ₁₈ H ₁₄ O ₅	1.36×10 ⁴	0.78	0.28	12
311.0557	C ₁₇ H ₁₂ O ₆	5.84×10 ³	0.71	0.35	12
319.0604	C ₁₉ H ₁₂ O ₅	1.12×10 ⁴	0.63	0.26	14
321.0762	C ₁₉ H ₁₄ O ₅	7.23×10 ³	0.74	0.26	13
323.0553	C ₁₈ H ₁₂ O ₆	1.35×10 ⁴	0.67	0.33	13
325.0710	C ₁₈ H ₁₄ O ₆	2.41×10 ⁴	0.78	0.33	12
335.0553	C ₁₉ H ₁₂ O ₆	7.33×10 ³	0.63	0.32	14
335.0938	C ₂₀ H ₁₆ O ₅	2.09×10 ⁴	0.80	0.25	13
337.0711	C ₁₉ H ₁₄ O ₆	3.96×10 ⁴	0.74	0.32	13
339.0869	C ₁₉ H ₁₆ O ₆	1.63×10 ⁴	0.84	0.32	12
341.0662	C ₁₈ H ₁₄ O ₇	1.30×10 ⁴	0.78	0.39	12
349.0712	C ₂₀ H ₁₄ O ₆	7.60×10 ³	0.70	0.30	14

351.0870	C ₂₀ H ₁₆ O ₆	3.73×10 ⁴	0.80	0.30	13
353.0662	C ₁₉ H ₁₄ O ₇	2.63×10 ⁴	0.74	0.37	13
353.1025	C ₂₀ H ₁₈ O ₆	7.92×10 ³	0.90	0.30	12
355.0820	C ₁₉ H ₁₆ O ₇	1.04×10 ⁴	0.84	0.37	12
365.0661	C ₂₀ H ₁₄ O ₇	8.09×10 ³	0.70	0.35	14
367.0818	C ₂₀ H ₁₆ O ₇	4.32×10 ⁴	0.80	0.35	13
369.0609	C ₁₉ H ₁₄ O ₈	8.74×10 ³	0.74	0.42	13
369.0974	C ₂₀ H ₁₈ O ₇	1.53×10 ⁴	0.90	0.35	12
383.0767	C ₂₀ H ₁₆ O ₈	1.18×10 ⁴	0.80	0.40	13

As shown in Figure 3.3, C₁₀ compounds (i.e., compounds with ten carbon atoms) are the most dominant ones, accounting for 18.4% of total determined formulas and represent the ring-retaining products.²⁶⁰ Both the ring-opening products (i.e., C₇, C₈, and C₉ series) and the dimers (i.e., C₁₈, C₁₉ and C₂₀) are also important products from the OH-initiated oxidation of naphthalene. In addition, more than 78% of determined organic compounds contained more than 3 oxygen atoms (Fig. 3.3), suggesting that these compounds bear multiple oxidation functional groups. Moreover, Figure 3.4 shows that most of these compounds have high degrees of unsaturation and oxygenation, highlighting their aromatic and polycyclic aromatic structures. Notably, excitation in natural waters typically involves the promotion of an electron from an n or π orbital (the electronic orbitals common in carbonyl and aromatic compounds) to a higher energy anti-bonding orbital (π^*), suggesting that carbonyl-containing aromatic compounds are well-suited candidates to act as photosensitizers.^{148,261} Therefore, in addition to naphthoquinone, other carbonyl-containing aromatic products existing in Naphthalene-SOA²⁶² probably also play an important role in the photosensitized oxidation of SO₂ and VOCs.

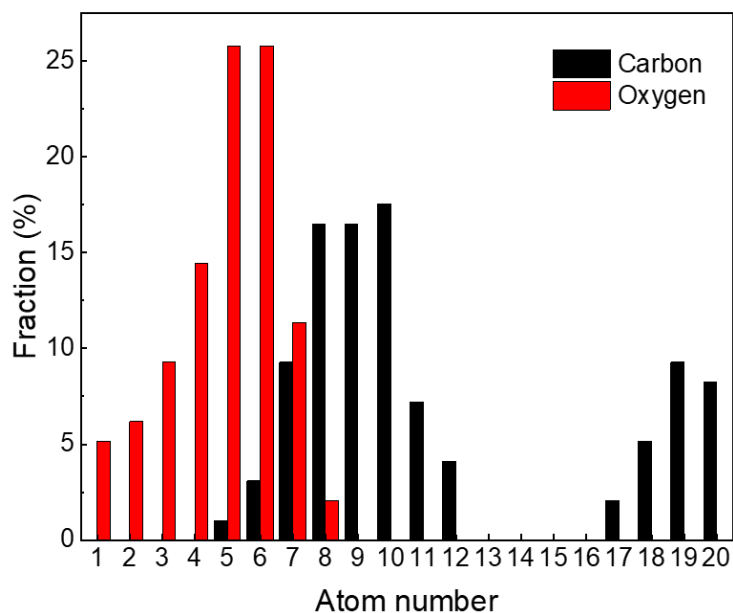


Figure 3. 3: Histograms of atom number in C- (black) and O- (red) containing compounds of the determined constituents in Naphthalene-derived SOA samples.

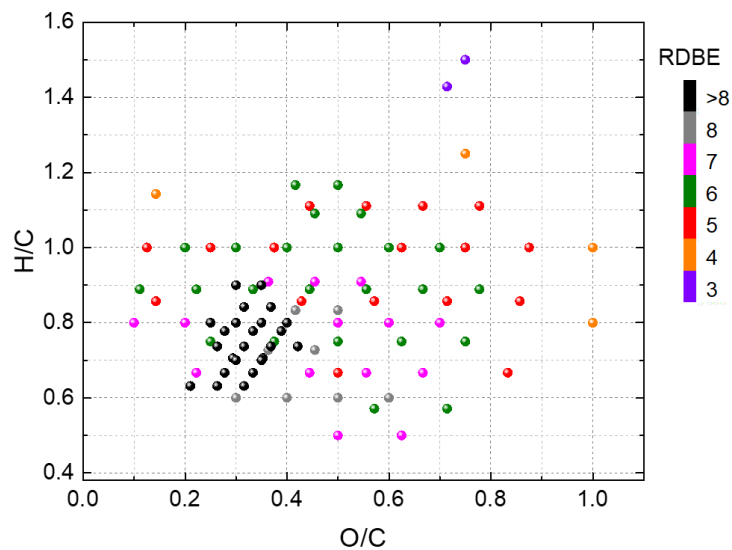


Figure 3. 4: Van Krevelen diagrams for identified formulas in Naphthalene-SOA. The color-coding indicates the RDBE values.

3.4.3 Photosensitized uptake of VOCs

To test whether these particles exhibit photosensitized reactivity toward different partner molecules, we also exposed them to gaseous d-limonene or β -pinene. Control experiments using

seed particles containing only ammonium sulfate or ammonium sulfate/succinic acid exposed to limonene and UV light did not lead to particle growth.^{75,145} In contrast, as shown in Figure 3.5 and Table 3.1, the particle size of Naphthalene-SOA particles (starting diameter of 37 nm) in the presence of 0.1 ppm limonene increased by 50.8% and 58.7% at RH 39-43% and 84-88%, respectively, corresponding to a residence time of 25 min. This is a remarkable amount of growth, implying that particle volume goes up by $(2.0-2.5)^3$ or by a factor of 8-16. In addition, the reaction with 0.8 ppm β -pinene at RH 45-47% and 85-89% resulted in similarly large DGFs of 8.9% and 24.2%. The RH dependence of particle growth is mainly driven by the enhanced solubility of Naphthalene-SOA.²⁴⁸ Such experiments are meant to show that these particles are reactive toward unsaturated VOCs,^{75,145} since d-limonene was found to be a more efficient SOA precursor compared to β -pinene, but are not meant to suggest a strong involvement in particle growth in the ambient atmosphere (due to the unrealistic experimental conditions). Similar to the study of Aregahegn et al.¹⁴⁵, such growth is probably caused by the formation of highly oxygenated products through limonene or β -pinene reacting with the triplet state of the photosensitizers.^{75,154}

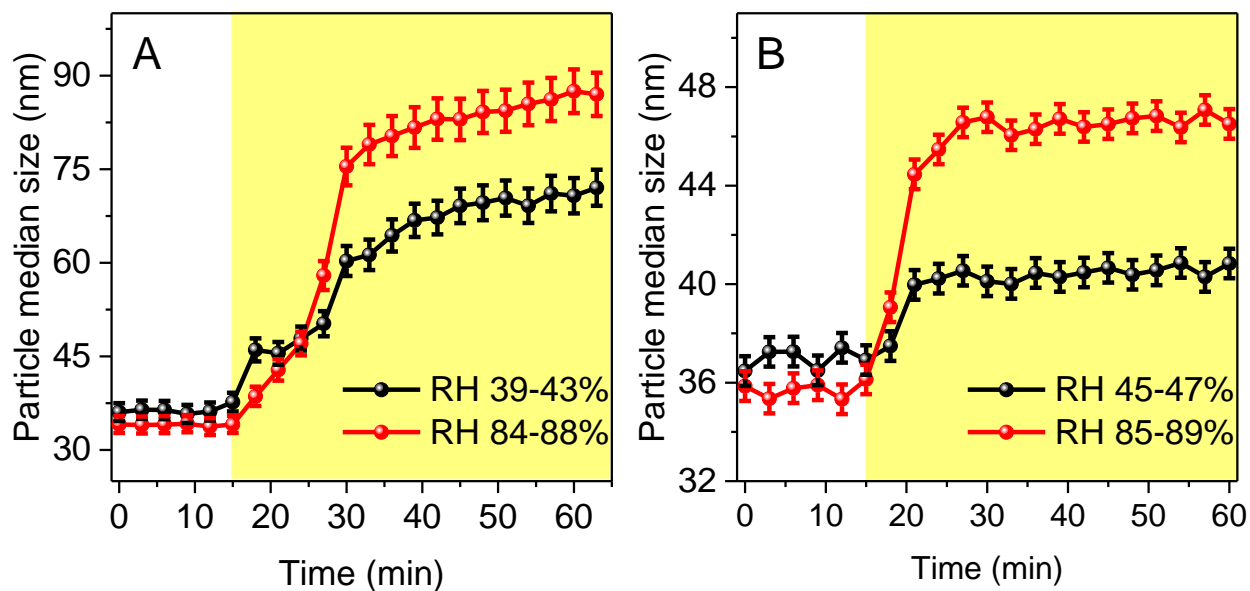


Figure 3. 5: Median diameter ($\pm 2\sigma$) growths of Naphthalene-derived SOA exposed to UV-A light and 0.1 ppm d-limonene (A) and 0.8 ppm β -pinene (B) for 30 min in the AFT. The yellow region corresponds to the irradiation time.

For example, the excited photosensitizer can abstract a hydrogen from an organic molecule (i.e., d-limonene or β -pinene), through either a direct transfer or proceed via an electron transfer

followed by a proton transfer.¹⁵⁴ Since the initial step triggering the photosensitized uptake is a H-abstraction reaction (and not an addition to a double bond), VOCs having weak C-H bonds will react faster, which is observed here for limonene. The reduced photosensitizer radical can be oxidized to the original ground state in the presence of O₂, at the same time, producing superoxide radicals (HO₂[·]/O₂^{·-}).¹⁴⁵ The photoproduct VOC and photosensitizer radicals can further react with other molecules or be oxidized by HO₂ or O₂, to produce new products. The study of Rossignol et al.¹⁵⁴ found that highly oxygenated organic compounds including compounds retaining the same number of carbons as d-limonene were produced from the reaction of the IC triplet state and d-limonene in the aerosol phase through ring-opening and intramolecular isomerization during the limonene oxidation process.

Interestingly, both Naphthalene-SOA and seed particles containing photosensitizers grow efficiently even at low RH when exposed to limonene and β-pinene VOCs (Table 3.1).^{75,145} This indicates that the photosensitized processes may occur at the surface and be sustained even on solid or semi-solid particles without passivation. This is in contrast to the expected behavior of a solid where it is expected that the high viscosities promote radical recombination and the surface is expected to be rapidly passivated. It is beyond the capabilities of these experiments to unravel the molecular reason for this observation, but one could speculate that the presence of a photochemically active surface may locally change the nature of the surface or induce chain reactions that may propagate some surface reactivity. Another possibility is the triplet state of these photoactive compounds convert molecular oxygen into reactive oxygen (e.g., O₂^{·-} or ¹O₂) sustaining surface reactivity, which would be in agreement with high ¹O₂ yield from naphthalene-SOA in aqueous solutions.¹⁴⁹ The produced oxygenated VOC may also form a new phase beneath the surface, thus keeping the surface open for more reactions. This type of liquid-liquid phase separation has been observed for various SOA types even under lower RH conditions observed here.²⁶³ Whatever the underlying reason, these observations tend to support that the surface of such solid or semi-solid particles will not passivate while being illuminated with actinic light.

Notably, the increased DGF under high RH conditions indicates that the underlying photochemical mechanisms are different for the VOCs and for SO₂. Wang et al.⁷⁶ suggested a direct reaction of SO₂ with the organic triplet states through different pathways, possibly influenced by pH. On the other hand, Rossignol et al.¹⁵⁴ suggested that the underlying mechanism for the VOC uptake is H

abstraction followed by the production of multiple generation multiple products (by condensed phase autooxidation). As previously mentioned, at low RH, these first-generation products are concentrated at the surface (because they cannot diffuse to the bulk under highly viscous conditions) where they remain fully exposed to oxidants and undergo rapid further oxidation and fragmentation, yielding highly-oxygenated products with lower molar mass. Those may therefore degas (or desorb) preferably at low RH compared to high RH where diffusion into the bulk is possible. Therefore, the different trends between the VOCs and SO₂ is possibly to a combination of mass transport limitations, and different chemistries being influenced by pH.

3.5 Conclusions

Naphthalene is ubiquitous in suburban and urban areas and its OH radical driven oxidation produces oxygenated aromatic compounds with low volatility forming secondary organic aerosols. Those particles are found to be reactive in the dark toward SO₂ where the reaction of dissolved S(IV) with naphthalene oxidation products such as quinones, aldehydes, and organic peroxides are expected to produce organosulfonates, organosulfates and sulfates. The dark production of sulfate was observed to increase at high humidity and hence on liquid like particles. In addition, these particles possess photosensitizing properties at lower humidity (< 70% RH), and can oxidize SO₂ even on solid or semi-solid particles. Moreover, the particle size of Naphthalene-SOA grows efficiently under irradiation in the presence of VOCs, especially d-limonene. As the RH increases, the photosensitized particle growth becomes more efficient. These results indicate that the formation of sulfate and oxygenated organic compounds through Naphthalene-SOA photoinduced reactions contribute to the sulfate concentration and size/mass of SOA particles.

Chapter 4: Photodegradation of Secondary Organic Aerosols by Long-term Exposure to Solar Actinic Radiation

Portions of this chapter were reproduced with permission from Baboomian, V. J., Gu Y., Nizkorodov, S. A., (2020). Photodegradation of Secondary Organic Aerosols by Long-Term Exposure to Solar Actinic Radiation. ACS Earth and Space Chemistry, 4(7), 1078 – 1089. DOI: 10.1021/acsearthspacechem.0c00088

4.1 Abstract

Sunlight-driven chemical transformations of secondary organic aerosol (SOA) are important for understanding the climate and health-relevant properties of atmospheric particulate matter, but these photochemical processes are not well understood. We measured photodegradation rates of SOA by condensed-phase photochemical processes observed over many days of UV exposure. The experiments relied on a quartz crystal microbalance to quantify the mass loss rate from SOA materials prepared by ozonolysis of d-limonene and α -pinene and photooxidation of toluene under either high or low NO_x conditions. We observed that 254 nm irradiation degraded SOA almost entirely after 24 h. The mass loss rates were higher for toluene-derived SOA, which absorbs strongly at 254 nm. Irradiation at 305 nm, which is more relevant for the troposphere, resulted in larger mass loss rates from SOA generated from α -pinene and d-limonene, even though toluene-derived SOA had a higher absorption coefficient. In all 305 nm irradiation experiments, the initial mass loss rate was high (corresponding to 1-5% fractional mass loss per hour) but it slowed down after 24 h of irradiation with a photorecalcitrant fraction of SOA degrading much slower (< 1% fractional mass loss per hour). The mass loss rates were observed to increase at higher relative humidity because volatile photoproducts could diffuse out of SOA faster. Long term changes in chemical composition of limonene ozonolysis SOA were examined using high-resolution electrospray ionization mass spectrometry and revealed a more complex mixture of species after photodegradation compared to the initial SOA. The compounds in the photodegraded sample had on average lower molecular weights, lower H/C ratios, and higher O/C ratios compared to the compounds in the unphotolyzed sample. These experiments confirm that condensed-phase photochemistry is an important aging mechanism for SOA during long-range transport.

4.2 Introduction

Secondary organic aerosol (SOA) represents the dominant fraction of atmospheric particulate matter and is formed in the atmosphere by the condensation of oxidation products of volatile organic compounds (VOCs). VOCs are emitted from both biogenic sources, such as vegetation, and anthropogenic sources, such as incomplete fossil fuel combustion and industrial processes.²⁶⁴ Common biogenic VOCs include isoprene, α -pinene, d-limonene, and other terpenes, while common anthropogenic VOCs include aromatic hydrocarbons and saturated aliphatic hydrocarbons found in fossil fuel. Once emitted, VOCs undergo oxidation to form lower volatility oxygenated VOCs which can contribute to new particle formation or partition into pre-existing particulate matter.^{18,265,266} Once formed, SOA travels through the atmosphere and undergoes various chemical aging reactions that change its physiochemical properties. The current understanding of SOA aging processes is limited, and this uncertainty contributes to the challenges of quantifying environmental impacts of SOA.^{267,268}

The production, aging, and loss of SOA sensitively depend on environmental conditions such as humidity, temperature, trace gas concentrations, and solar irradiance. Aging is especially challenging to integrate into models due to the multiple mechanisms by which it can occur. Aging processes include heterogeneous oxidation of particles by OH, reactive and non-reactive uptake of semi-volatile species, and various condensed phase reactions such as direct photolysis, photosensitized reactions, reactions involving free radicals produced inside particles, and non-radical processes, such as hydrolysis.^{20,84,269} Photodegradation reactions tend to fragment the SOA organics into smaller, more volatile compounds which can evaporate into the gas phase leading to SOA mass loss.^{80,81,85,92,138} These higher volatility species have been shown to include CO, CO₂, methane, acetic acid, formic acid, acetone, acetaldehyde, and other small organic molecules.^{81,135,139} These photodegradation processes affect the Earth's climate because they reduce the mass concentration and particle diameter, making SOA scatter sunlight less efficiently.⁴⁵

Compounds containing carbonyl and peroxide functional groups are examples of photochemically active species responsible for the SOA mass loss under tropospheric sunlight ($\lambda > 295$ nm).^{95,134,135} The C-C(O) bond in carbonyls can be broken by Norrish I and Norrish II type photocleavage processes to form smaller products.^{79,92,135} Peroxides break at the weak O-O bond, forming two O-centered radicals, which undergo secondary processes on a picosecond time scale.¹⁴¹ However, not

all photochemical processes result in fragmentation. Secondary reactions of free radicals in the SOA particles can also lead to oligomerization products that increase the carbon number of SOA species and lead to a lower volatility SOA mixture.⁷⁹

Previous experimental studies have shown that photodegradation of condensed phase material in SOA can occur on atmospherically relevant timescales.^{20,80,92,138} A modeling study has predicted that SOA mass would decrease by 40-60% after 10 days of atmospheric aging if condensed-phase photochemical processes are permitted and proceed at the same rate as in the gaseous phase.²⁷⁰ A recent combined experimental and modeling study also predicted about 50% reduction in biogenic SOA in the Amazon region due to SOA photodegradation.¹⁴⁰ Such photodegradation processes are particularly important for free tropospheric aerosols, which can have mean residence times four times as large compared to those trapped by the boundary layer,⁶³ and have more time to contribute to cloud formation and the Earth's energy budget.²⁷¹⁻²⁷³ Obtaining a better understanding of long-term photochemical aging processes is necessary to understand the fate of SOA and can potentially improve model-measurement discrepancies.^{30,271}

Insights into SOA aging by condensed-phase photochemistry have been gained via laboratory experiments where SOA was aged in batch chambers,^{85,97,138,140} flow tubes,⁹² immobilized on substrates,^{79,82,137} or extracted into solution.^{72,73,182,274-276} Aerosols have lifetimes of ~ 1 week in the atmosphere but typical chamber studies are conducted for several hours or 1-2 days at the longest.^{97,138,140} Long term aging is usually investigated by selecting experimental conditions to allow laboratory time scales to reach atmospheric values. In studies of aging driven by heterogeneous OH oxidation, unrealistically high OH radical concentrations to reach equivalent atmospheric exposure times of ~1-2 weeks in a matter of seconds in an oxidation flow reactor. For photochemistry, a related approach would be equivalent to increasing the intensity of UV radiation way above the level normally found in the atmosphere.⁹² In either case, the results are then extrapolated to atmospheric conditions assuming the processes scale linearly with OH concentration and/or UV radiation flux and wavelength dependence. This method may not be entirely accurate though, as the mechanism of aging processes in SOA can change under elevated oxidant concentrations and solar fluxes.⁷⁹ Indeed, recent studies have begun investigating condensed phase long term aging and have found appreciable differences in the aging mechanisms and changes in composition compared to short term aging studies.^{79,97} For example, Walhout et al.

irradiated α -pinene ozonolysis SOA collected on Teflon filters for 4 days and found photofragmentation reactions to be the dominant process in the first two days of aging, after which oligomerization reactions between photoproducts become more important.⁷⁹ Further experiments are needed over long laboratory time scales with more typical levels of oxidants and UV radiation in order to better understand the rates of aging processes occurring in the atmosphere.

Until recently, observations of aging driven by condensed-phase photochemistry in SOA have been largely fundamental and at best gave only a rough estimate on the mass loss rate. More recent studies have been able to directly measure the rate of photodegradation of SOA material but only for a limited number of SOA types and under short timescales.^{81,140} The humidity dependence of SOA photodegradation rates also remains an open question because most of the previous studies, with a few exceptions,^{82,138,140} relied on dry conditions. The goal of this work was to extend the study done by Malecha et al.⁸¹ by quantifying the long-term photodegradation of SOA derived from representative biogenic and anthropogenic VOCs and investigate the effects of humidity on the mass loss rate. This was accomplished by using a Quartz Crystal Microbalance (QCM) to directly track the changes in SOA mass due to photodegradation as a function of time. Our results support the conclusion that condensed-phase photochemistry can lead to large mass loss from SOA particles over long periods of solar radiation exposure thus counteracting aerosol particle growth due to gas-to-particle partitioning.

4.2 Materials and Methods

4.2.1 SOA Samples

Four different types of SOA were investigated for this study: α -pinene ozonolysis (APIN/O₃), d-limonene ozonolysis (LIM/O₃), toluene low-NO_x photooxidation (TOL/OH), and toluene high-NO_x photooxidation (TOL/OH/NO_x). The ozonolysis samples were collected using the flow tube in Chapter 1 (Section 1.6.2) with starting mixing ratios of 14 and 10 ppm for O₃ and VOC, respectively. The TOL/OH samples were prepared using a different flow tube discussed below. The TOL/OH/NO_x samples were prepared in a smog chamber (see Chapter 1, Section 1.6.1). A summary of all the samples made in this study can be found in Table 4.1.

For the TOL/OH sample, a different flow reactor was used as described in Veghte et al. (2018).²⁷⁷ Briefly, this oxidation flow reactor involved an 8 L quartz reaction vessel surrounded by two 254

nm UV lamps inside a Rayonet RPR100 photochemical reactor. The pure VOC was injected using a syringe pump into zero air flowing into the reaction vessel where it mixed with O₃. The UV lamps converted O₃ to OH by reacting with H₂O, OH reacted with toluene, and the SOA was collected from the exit tube.

The aerosol smog chamber was used for making TOL/OH/NO_x SOA (Chapter 1, Section 1.6.1). The SOA was prepared similar to previous experiments on TOL/OH/NO_x SOA.²⁷⁸ The starting VOC, H₂O₂ and NO_x mixing ratios were 1 ppm, 2 ppm, and 0.5 ppm, respectively. After the VOC was injected and its concentration stabilized, H₂O₂ and NO₂ were injected in the chamber, and finally, panels of UV-B lights were turned on, resulting in a steady-state OH concentration of ~10⁶ molecules cm⁻³. After 4 h of photooxidation of the VOC by OH, the SOA was collected. It is important to note that the VOC concentrations used in this study are much higher than those found in the atmosphere. These conditions can favor certain reaction pathways that can lead to differences in SOA composition (which in turn, may affect their photodegradation processes). For example, the higher mass loadings used in this study can increase the particle phase partitioning of volatile carbonyl containing compounds, which may lead to an overestimate of the photodegradation extent in the atmosphere.²⁶⁵

Table 4. 1: C_f is the QCM sensitivity factor determined for every sample by dividing the frequency reduction of the loaded crystal by the SOA mass on the crystal. In the experimental conditions column, “dry-long term” means hours or days of exposure of SOA to UV radiation under dry conditions, an RH value means shorter term exposure to quantify the initial photodegradation rate in humidified air, and control means irradiation under 405 nm LED.

SOA Type	Wavelength of the irradiation source (nm)	Mass on Crystal after Annealing (μg)	C_f (Hz/μg)	Experimental Conditions	Maximum FMLR (h^{-1})
LIM/O3	305	2337	21.60	Dry Long-term	0.031
LIM/O3	305	1729	12.33	Dry Long-term	0.034
LIM/O3	305	1319	12.12	Dry Long-term	0.036
LIM/O3	305	457	14.28	Dry Short-term	0.014
LIM/O3	305	452	14.34	42% RH	0.026
LIM/O3	305	858	10.41	60% RH	0.043
LIM/O3	305	556	13.74	78% RH	0.054
LIM/O3	305	1712	12.35	Long-term 63% RH	0.050
APIN/O3	305	856	10.18	Dry Long-term	0.055
APIN/O3	305	1373	10.85	Dry Short-term	0.027
APIN/O3	305	1466	13.57	42% RH	0.053
APIN/O3	305	1473	12.52	62% RH	0.062

APIN/O3	405	1365	13.28	Dry Control	n/a
APIN/O3	Dark	1934	10.61	Dark Control	n/a
APIN/O3	254	3429	13.56	Dry Long-term	0.933
TOL/OH	254	53	13.89	Dry Long-term	0.368
TOL/OH	305	185	10.83	Dry Long-term	0.008
TOL/OH/NO _x	305	194	24.21	Dry Long-term	0.020

In all cases, the SOA was collected onto Stage 7 (0.32 – 0.56 μm particle size) of a Micro-orifice Uniform Deposit Impactor (MOUDI; MSP Corp. model 110-R) for 1-4 h with custom adapters to accommodate a 2.54 cm diameter chrome/gold QCM crystal as the substrate. The MOUDI was used in order to ensure a more uniform deposition of particles on the substrate, and Stage 7 was used since it provided the largest amount of SOA mass to be collected. The resulting SOA material was preconditioned by keeping the QCM crystal under a flow of clean, dry air overnight at 40°C to remove the more volatile compounds and allow the particles to better adhere to the QCM substrate and merge into a more continuous film. During this preconditioning step, the more labile SOA compounds such as peroxide likely decomposed, so these measurements probe the behavior of more thermally stable SOA compounds, such as carbonyls.^{279,280} The masses collected ranged from 0.05 to 3.4 mg (Table 4.1) as determined by weighing the crystal before and after the collection (and after preconditioning) with a Sartorius ME5-F microbalance (1 μg precision). Assuming an SOA material density of 1.2 g cm^{-3} and 1 mg of SOA deposited, we estimate the effective SOA material thickness to be 1.6 μm on the 5 cm^2 QCM crystal.

4.2.2 SOA Photodegradation Setup

A commercial QCM was modified to include a sealed space above the QCM crystal with a CaF_2 window on top to allow the sample to be irradiated (Fig. 4.1).⁸¹ A flow of 70 SCCM of clean air passed over the sample to drive off the photoproducts. In order to investigate the effects of

humidity on photodegradation rates, the humidity of the air flow above the sample was controlled by mixing dry air with humid air that had passed through a Nafion single-channel humidifier (PermaPure). Two light sources were used in this study to drive photodegradation: a light-emitting diode (LED) centered at 305 nm (Thorlabs Inc., model M300L4) and a mercury pen-ray lamp centered at 254 nm (Spectronics Corp. model Spectroline 11SC-1). The 305 nm LED was used to represent tropospheric UV radiation (below ozone layer), while a 254 nm lamp was used in proof-of-concept experiments. In addition, an LED centered at 405 nm (Thorlabs Inc., M405L4) was used in control experiments where samples were irradiated but not expected to undergo photodegradation.⁸¹ Using selected wavelengths of radiation as opposed to a full solar spectrum made it possible to investigate the wavelength dependence of the photodegradation. It also avoided unnecessary heating of the sample with visible and near-infrared radiation coming from broadband radiation sources, such as arc lamps. The incident power of each lamp was measured using a Coherent PS19Q power meter in the same geometry that was experienced by the QCM crystal. The resulting powers were 2.6 mW for the 305 nm LED and 3.7 mW for the 254 nm lamp. Previous experiments have shown that these power meter measurements agree reasonably well with actinometry experiments.^{74,80}

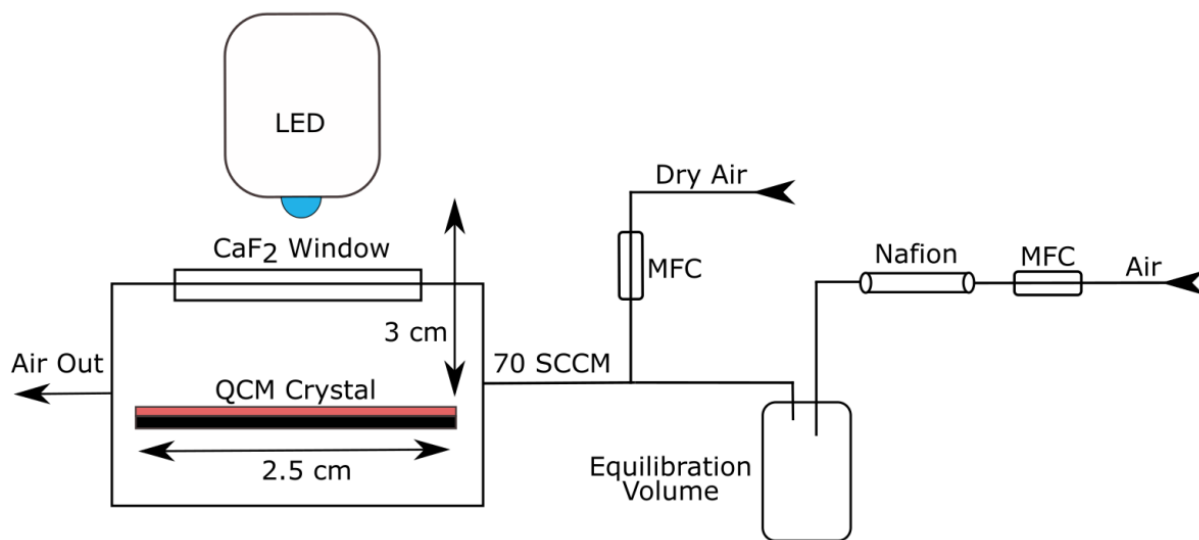


Figure 4. 1: SOA photodegradation setup. The QCM crystal with SOA is placed into the QCM oscillator. A 305 nm LED, 405 nm LED or a 254 nm pen-ray lamp is mounted above the sample and irradiates the SOA continuously. The photoproducts are purged out of the QCM setup through an exit port by a slow flow of VOC and particle free air. A humidifier is used to control the relative humidity of the air flow.

Exposure to UV radiation reduces the SOA mass on the crystal (due to the evaporation of volatile photoproducts) and increases the crystal oscillation frequency. To convert the observed change in frequency into change in SOA mass, a modified version of Sauerbrey's equation was used:²⁸¹

$$\frac{dm}{dt} = -\frac{1}{C_f} \frac{df}{dt} \quad (4.1)$$

where $\frac{df}{dt}$ is the rate of frequency change during irradiation (Hz/hr), C_f is the sensitivity factor (Hz/ μ g), and $\frac{dm}{dt}$ is the mass change rate (μ g/hr). The C_f was determined empirically through calibration experiments as performed in previous studies.^{81,282} C_f was calculated by measuring the frequency of the clean crystal, collecting SOA on the crystal, weighing the amount of mass impacted onto the crystal (Δm), and noting the frequency change (Δf) experienced by the QCM. The sensitivity factor was then calculated through the integrated form of Equation 4.1.

$$C_f = -\frac{\Delta f}{\Delta m} \quad (4.2)$$

The resulting sensitivity factors for different SOA samples are listed in Table 4.1. They ranged from about 10 to 24 Hz/ μ g. With the 0.1 Hz precision of the instrument, this translates into an effective sensitivity of 4-10 ng for the SOA mass change on the crystal.

4.2.3 Characterization of SOA

A direct infusion electrospray ionization mass spectrometer (ESI-MS) was used to assess the extent of composition changes of LIM/O₃ SOA due to long term photodegradation. The instrument and operation settings are discussed in Chapter 1, Section 1.6.4 with the caveat that the instrument was operated under direct injection for these experiments with no chromatographic separation. The lack of chromatographic separation and its effects on chemical ionization are further discussed in Chapter 5. The ESI-MS was operated in a positive ion mode and the analyte was extracted off the QCM crystal using a 1:1 solution of acetonitrile:water with an analyte mass concentration of 0.8 mg/mL. Peak positions and relative abundances were extracted from the raw data using Decon2LS (<https://omics.pnl.gov/software/decontools-decon2ls>). The peaks were assigned with 0.001 m/z accuracy with formulas of $[C_cH_hO_o+Na]^+$ (formation of sodium adducts was the dominant ionization mechanism, no protonated ions $[C_cH_hO_o+H]^+$ were detected). The mass spectra below are plotted as a function of the molecular weight of the unionized compounds $C_cH_hO_o$.

4.3 Results and Discussion

4.3.1 Analysis of sample measurements

Figure 4.2a shows the observed QCM frequency change in a typical experiment. The frequency of the clean crystal is shown as the green line, and it was of the order of 5.010 MHz in this particular case. With LIM/O₃ SOA on the crystal surface, the frequency decreased to ~ 4.994 MHz. Without irradiation under dry conditions, the frequency was changing very slowly due to slow evaporation of SOA compounds from the substrate; an example of dark control measurements can be found in Figure 4.3. The frequency began to increase once the 305 nm LED was turned on at the 0 h mark due to the loss of the volatile photoproducts. The frequency increase to the maximum value was not instantaneous as it takes time for the photoproducts to diffuse through and evaporate from the SOA matrix.⁸² After the frequency began to stabilize, i.e., photodegradation has slowed down, the LED was turned off (around 118 h in this example). We observed that turning off the LED slowed down the frequency change suggesting that photodegradation was still faster than spontaneous evaporation.

Taking the derivative of the frequency curve and using Equation 4.1 yielded the mass loss rate of the SOA (Figure 4.2b). A boxcar smoothing algorithm with a 10 min rolling averaging window was applied in order to remove the measurement noise caused by the clean air generator periodic purges. The smoothing did not distort the time dependence of the curves shown in Figure 4.2.

Plotting the mass loss as a percent mass loss (Figure 4.2c) shows the LIM/O₃ degrading until ~30% of the initial mass is lost and stagnates afterwards. This is particularly important, as it confirms that a photorecalcitrant (i.e., non-photodegradable) fraction of SOA remains after the more photolabile compounds are photodegraded.^{79,97} The photorecalcitrant fraction is thought to consist of photochemically inactive SOA compounds left behind after photolabile carbonyl and peroxide compounds have undergone photodegradation.⁹⁷ Due to the photorecalcitrant SOA remaining on the crystal the crystal frequency never recovered to its initial frequency (green line in Figure 4.2a). The overall accuracy of the mass loss rates were quantified by integrating the mass loss rates over the irradiation period to obtain the total mass lost. This value was compared to the mass lost by directly weighing the crystal before and after irradiation using the Sartorius ME5-F microbalance. The average percent deviation between QCM measurements and direct weighing was 8%, representing a reasonable accuracy.

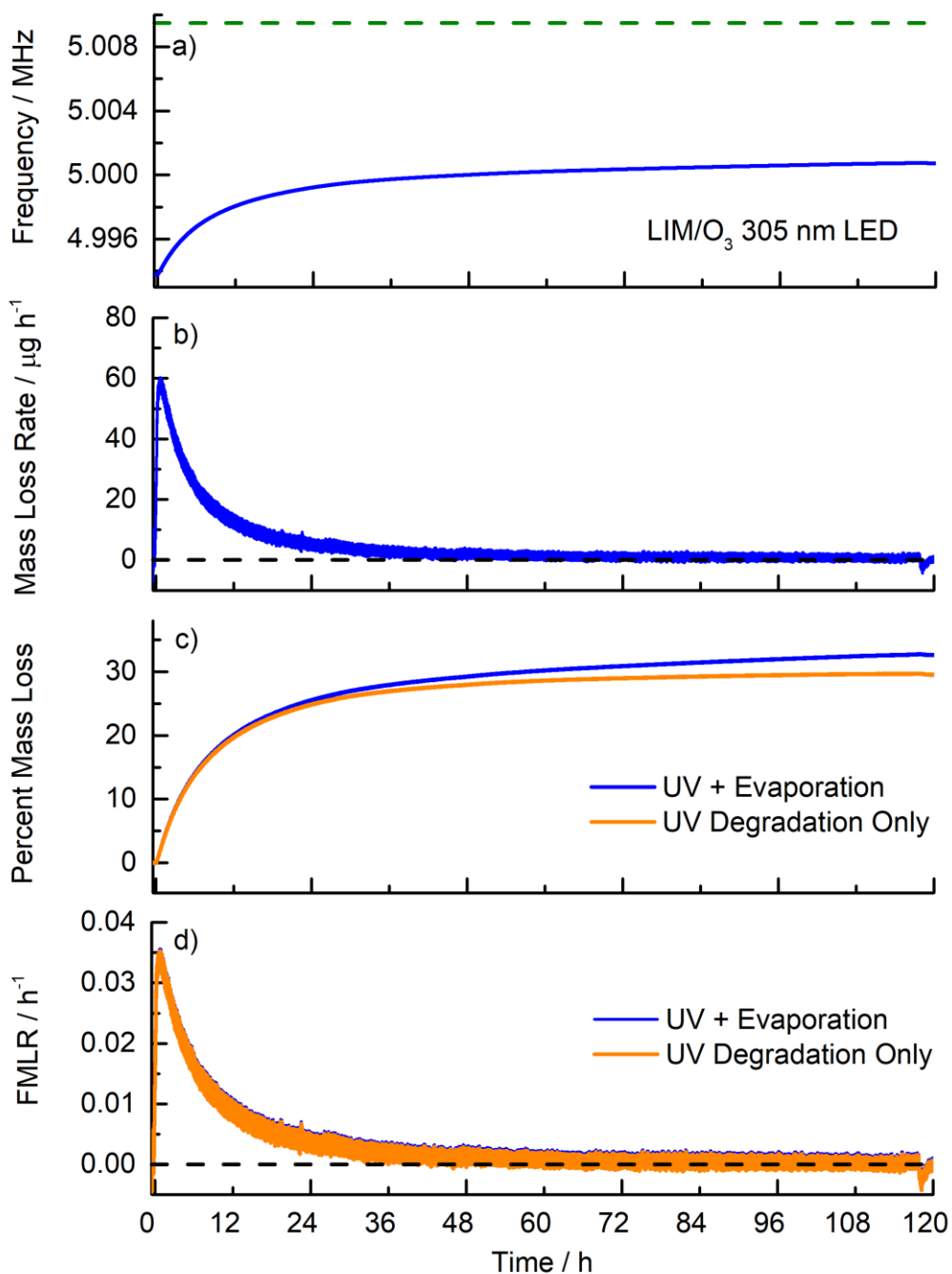


Figure 4. 2: a) A typical QCM experiment where the clean crystal frequency (green line) decreases once SOA has been impacted onto it. The LED was turned on at the 0 h mark, and the frequency began to increase due to the evaporation of photoproducts. After ~118 h, the LED was turned off. b) Mass loss rate profile of the LIM/O₃ sample. The black dashed line shows the zero point. c) Percent mass loss of the same sample. d) Fractional mass loss rate of the sample, where 0.035 h⁻¹ corresponds to 3.5% mass loss per hour. The blue curves correspond to mass loss due to evaporation and UV degradation while the orange curves correspond to mass loss from UV degradation alone.

Since the mass loss rate scaled linearly with the amount of SOA deposited on the crystal (Fig. 4.4), the mass loss rates were normalized to the SOA mass remaining on the crystal to calculate the fractional mass loss rate (FMLR) (i.e., 0.035 h^{-1} at the peak of Figure 4.2d corresponds to 3.5% mass lost per hour). The FMLR curve (Fig. 4.2d) has a similar shape to the mass loss rate (Fig. 4.2b), but it decays to zero slower because the SOA mass on the crystal was decreasing with irradiation time. FMLR is a more useful metric to incorporate into models since it can be treated as a rate constant (with the caveat that it is not actually constant).

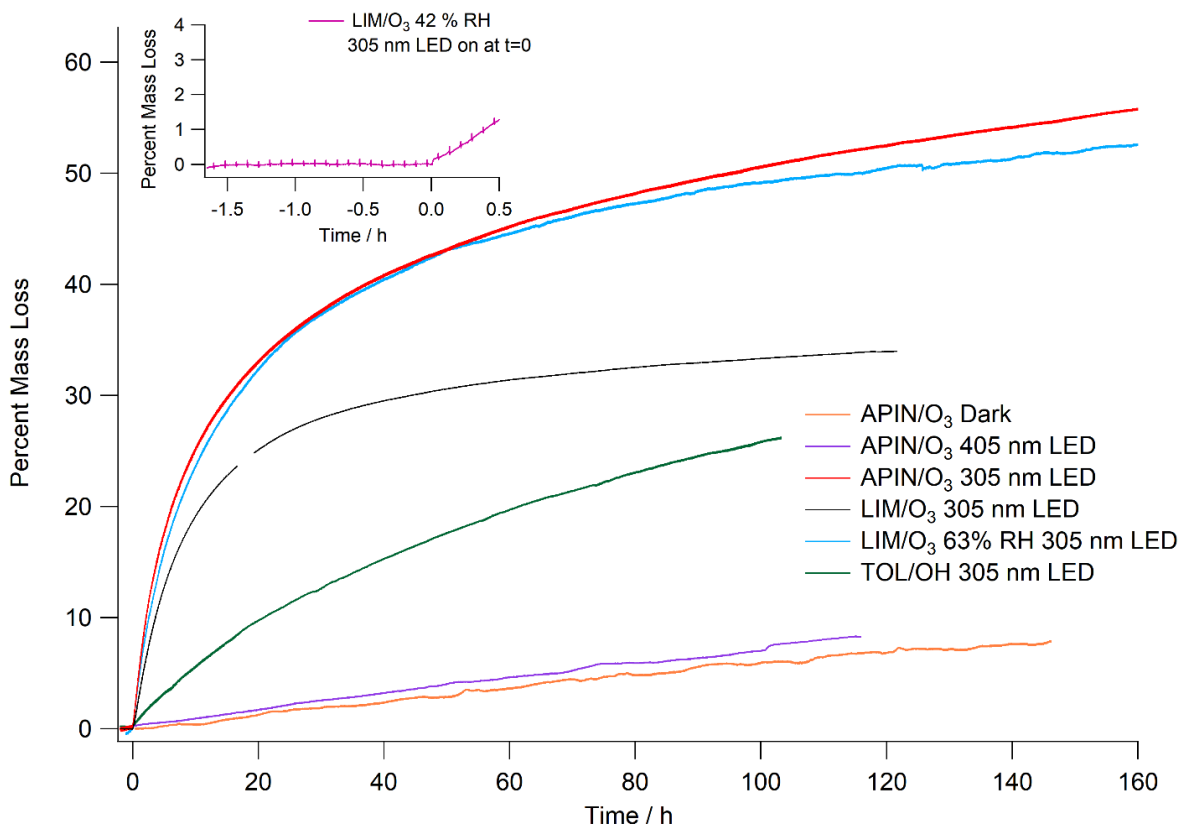


Figure 4. 3: Control experiments showed that mass loss under both dark and under 405 nm LED irradiation conditions were similar and smaller compared to the mass loss due to photodegradation. APIN/O₃ (highest mass loss), LIM/O₃, and TOL/OH (lowest mass loss) SOA trials are shown for comparison to the control experiments. The inset shows LIM/O₃ SOA photodegradation under 42 % RH has a minimal percent mass loss before the LED is turned on at the zero-hour mark. The data shown here are not yet corrected for evaporative loss and represent a combination of evaporation and degradation effects (PML_{total}).

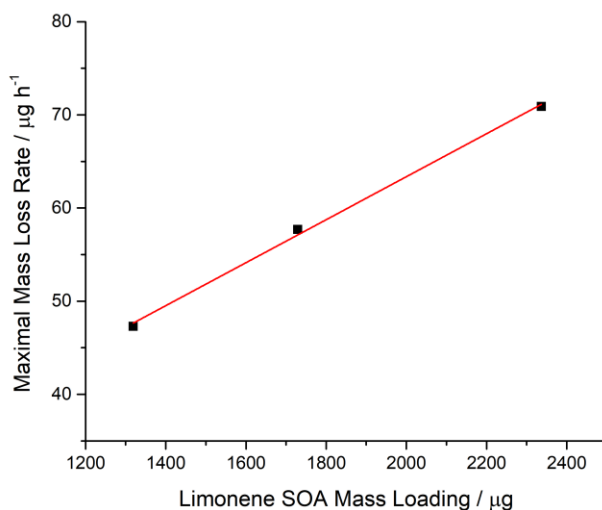


Figure 4. 4: The maximum mass loss rate from the QCM measurement scaled linearly with the mass of SOA deposited on the QCM crystal during 305 nm irradiation experiments with LIM/O₃ SOA. This made it possible to normalize the mass loss rate by the mass loading on the crystal to calculate the fractional mass loss rate (*FMLR*).

4.3.2 Photodegradation at 254 nm

As mentioned in the experimental section, two different light sources were used to examine SOA photodegradation. Figure 4.5 show the results of irradiating APIN/O₃ and TOL/OH SOA with 254 nm radiation, which represents an extreme case and serves as a proof of concept of the experimental technique before investigating more subtle processes under tropospheric wavelengths. The TOL/OH sample exhibited a higher maximum *FMLR* and reached a degradation plateau faster than the APIN/O₃ sample. This is likely due to TOL/OH SOA having a much higher absorption coefficient than APIN/O₃ SOA.¹⁴³ In both samples, under 254 nm irradiation, nearly 100% of the mass was degraded. The APIN/O₃ sample exhibited a complex time dependence of *FMLR*, with an initial maximum at early times and a secondary maximum at later times (~40 h). This could suggest two fractions of SOA mass, one that is initially present and highly photodegradable, and another that is slowly produced by secondary reactions of the initial photoproducts. Our results agree with the previous 254 nm photodegradation experiments on APIN/O₃ SOA,⁸¹ which also observed rapid mass loss of SOA during irradiation. These experiments prove that organic aerosols are capable of being fully degraded under harsh UV radiation and show that we are able to accurately measure the mass loss rates of the process.

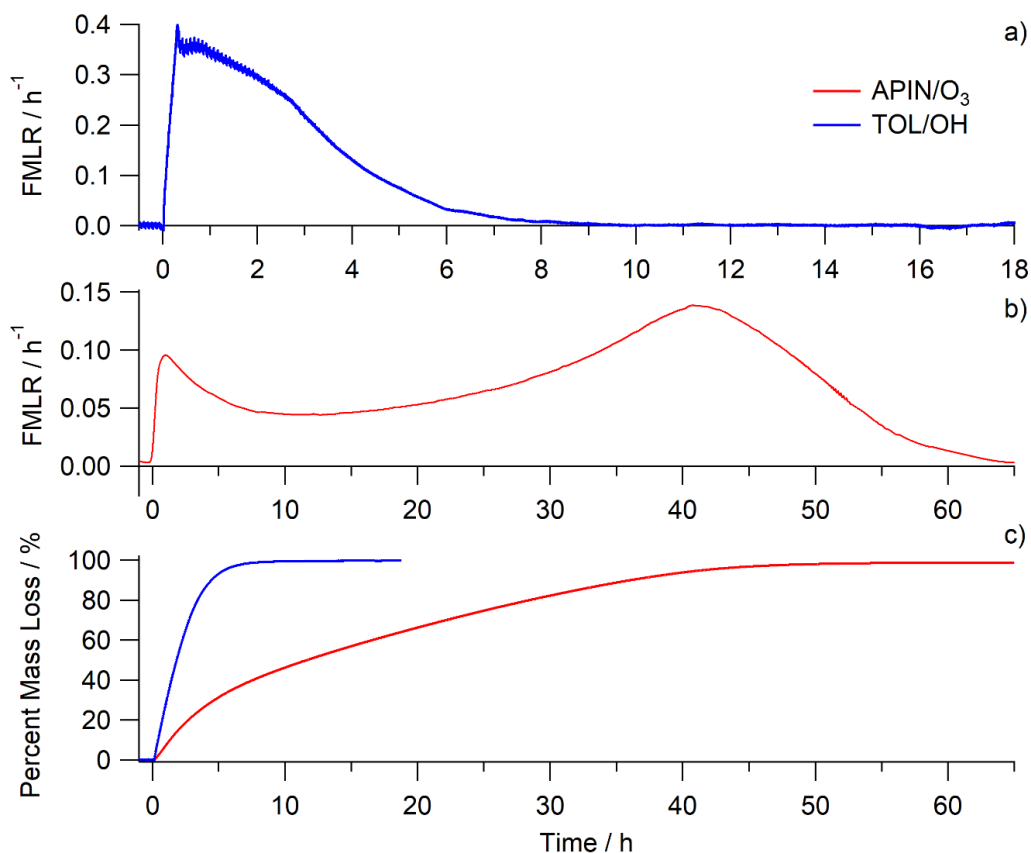


Figure 4. 5: FMLR observed during 254 nm irradiation of (a) TOL/OH and (b) APIN/O₃ SOA leads to nearly 100% of the SOA being degraded with no photorecalcitrant fraction remaining (panel c). The UV lamp was turned on at the 0 h mark.

4.3.3 Photodegradation at 305 nm

The majority of our experiments relied on the 305 nm irradiation, which is more relevant for the lower atmosphere. Figure 4.6 summarizes the results for four different types of SOA. The LIM/O₃ experiments were repeated in triplicate to check for reproducibility and showed good quantitative agreement in the measured FMLR values. The average of the three LIM/O₃ trials is shown in Figure 4, and the individual LIM/O₃ data are shown in Figure 4.7. There is a gap in the LIM/O₃ average trace due to QCM signal disconnection for a brief period in one of the runs.

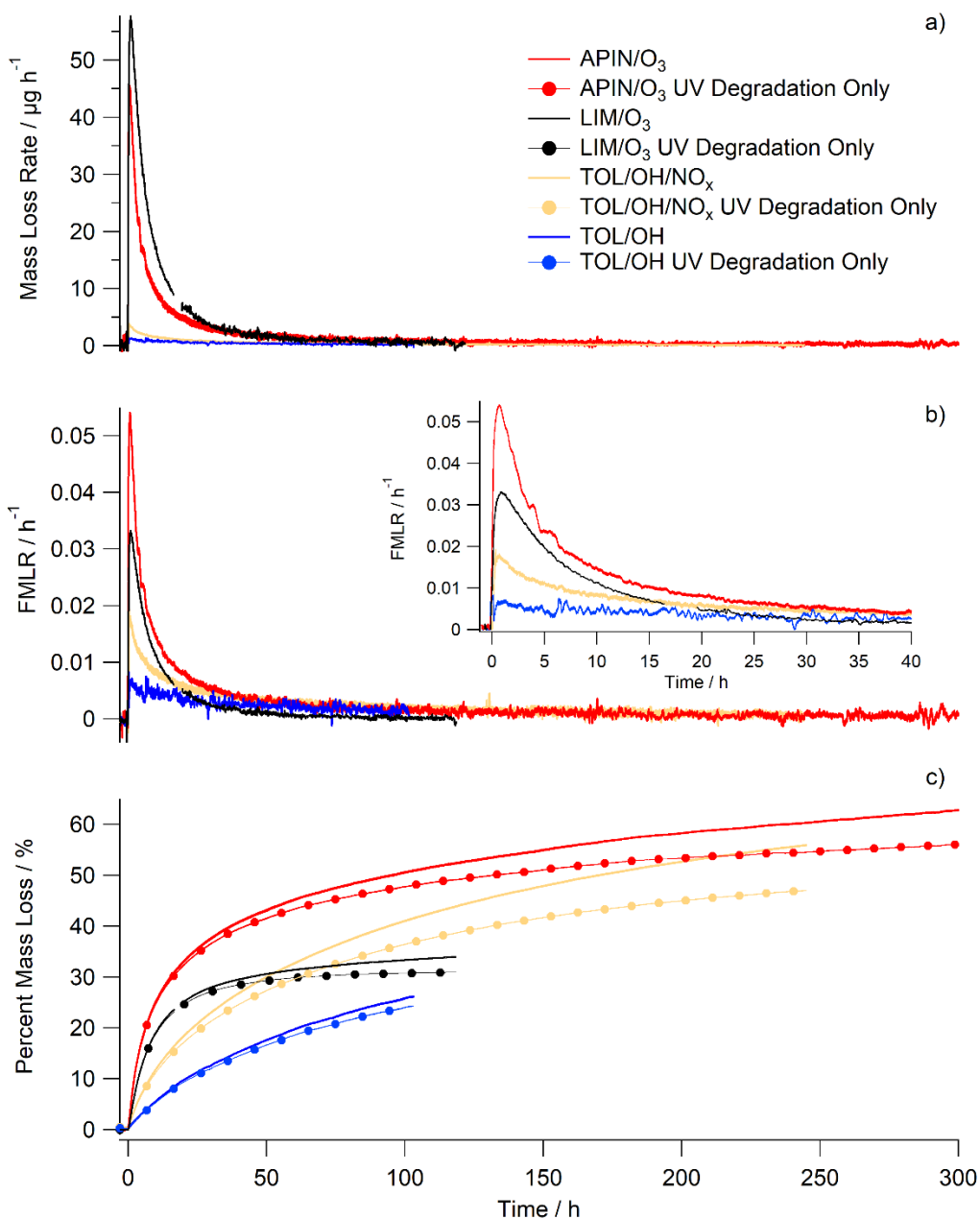


Figure 4. 6: Mass loss rate (a), FMLR (b), and percent mass loss (c) observed during 305 nm irradiation of various SOA types. A photorecalcitrant fraction is observed in all samples with APIN/O₃ SOA only degrading to ~60% after 300 h of irradiation. In panel (c), the dotted lines represent percent mass loss due to photodegradation only, after correcting for the dark evaporation (the equations used for the correction are discussed below).

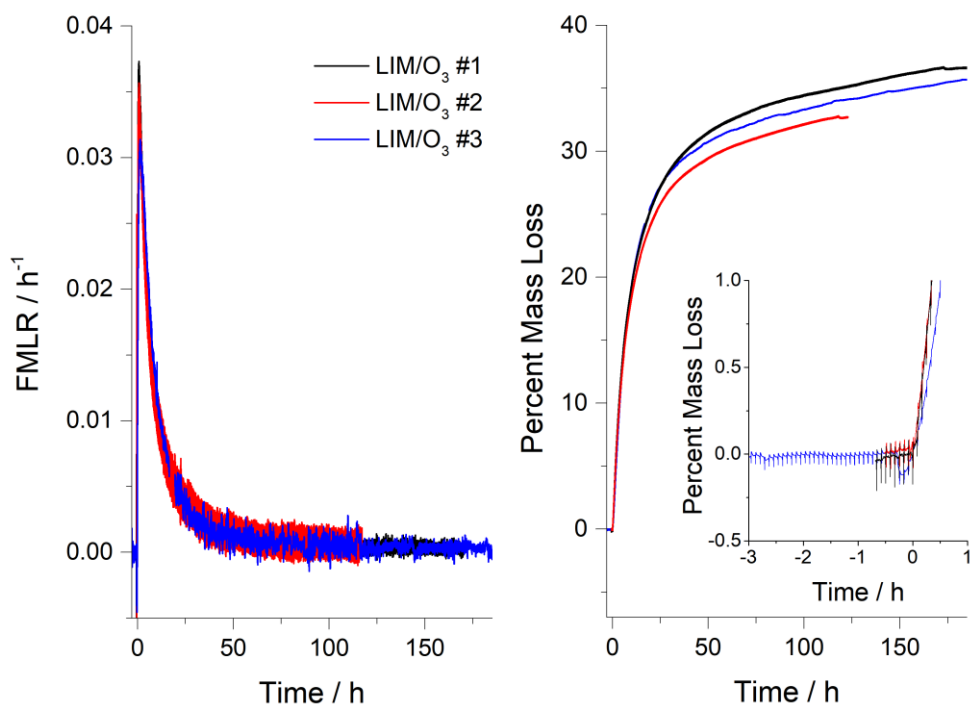


Figure 4. 7: Repeated experiments with LIM/O₃ SOA samples photodegraded under 305 nm LED radiation. The three samples had different mass loadings resulting in different absolute mass loss rates, but normalization to the mass loading resulted in similar FMLR values and time dependence. The inset zooms on the data at negative times (before the LED was turned on) and shows that the mass loss due to evaporation was minimal compared to the effects of irradiation. Periodic spikes in the data were due to the clean air generator periodic purges. The data shown here are not yet corrected for evaporative loss and represent a combination of evaporation and degradation effects ($FMRL_{total}$ and PML_{total}).

Control experiments were conducted (Fig. 4.3) and results showed mass loss due to spontaneous evaporation (no UV irradiation) played a relatively minor role in comparison to photochemically-driven mass loss. A control experiment was also conducted using a 405 nm LED in order to reproduce any thermal evaporation due to possible heating the QCM crystal by the LED operation. The 405 nm LED was configured to the same power output as the 305 nm LED but was not expected to produce significant photodegradation.⁸¹ In agreement with this expectation, the 405 nm LED produced the same mass loss rate as evaporation in darkness. Thus, we can conclude that although spontaneous evaporation did occur in this experiment, its rate was small compared to the effect due to photodegradation. Furthermore, effects of heating the QCM crystal by the LED were also unimportant. Although mass loss due to evaporation was found to be small compared to

photodegradation the percent mass loss was corrected to remove the effects of evaporation (Fig. 4.6c) and further reveals the stagnation in photodegradation and the presence of a photorecalcitrant fraction. Removing the influence of evaporation from the FMLR (Fig. 4.6b) resulted in a nearly identical mass loss profile. The evaporation correction method is discussed below (Section 4.3.4)

After normalizing by mass loading and correcting for the effects of dark evaporation (Fig. 4.6b), APIN/O₃ SOA showed the fastest photodegradation, followed by LIM/O₃, TOL/OH/NO_x, and finally TOL/OH had the slowest rate. Interestingly, at 305 nm, the FMLR of APIN/O₃ SOA is larger than that for TOL/OH SOA, but the opposite order applies at 254 nm (Fig. 4.5). This demonstrates the strong dependence of these processes on the types of electronic transitions accessible at the two wavelengths, specifically $n \rightarrow \pi^*$ transitions at 305 nm vs $\pi \rightarrow \pi^*$ transition at 254 nm. The TOL/OH/NO_x sample showed a maximum FMLR ~2.5 times larger than the TOL/OH sample. This can be explained by TOL/OH/NO_x SOA absorbing more strongly than TOL/OH SOA due to the incorporation of nitrogen containing organics.¹⁴² In fact, the mass normalized absorption coefficient at 305 nm of similarly prepared TOL/OH/NO_x SOA have been shown to be ~2.8 times higher than the MAC for TOL/OH SOA.¹⁴³

The percent mass loss (from UV degradation alone and from the combination of evaporation and UV degradation) shown in Figure 4.6c is significant, with APIN/O₃ showing the largest percent of mass loss (~50% after 100 h) and TOL/OH showing the smallest (~20% after 100 h). After the initial rapid photodegradation, it slows down considerably for APIN/O₃ and LIM/O₃ even though organic material still remains on the QCM crystal, signifying the formation of a more stable photorecalcitrant fraction. Previous studies have also noted a photorecalcitrant fraction after 40 hours of irradiation of APIN/O₃ in a smog chamber, and attributed this fraction to molecules that do not contain photochemically active groups, such as carbonyl and peroxide groups.⁹⁷ The formation of a photorecalcitrant fraction is less obvious in TOL/OH and TOL/OH/NO_x SOA but their photodegradation also slows down with irradiation time. These measurements clearly demonstrate that the kinetics of SOA photodegradation cannot be modeled as a simple first-order process; at least two rate constants are needed to parameterize the mass loss rate in models.

While the number of SOA types investigated in this study is limited due to the long time required for these experiments, the data suggest that the biogenic SOA degrades more readily than SOA from aromatic precursors. The differences in FMLR are due to a combination of possible effects.

One effect is that α -pinene and d-limonene ozonolysis products include more carbonyl and peroxide groups (which are expected to undergo efficient photofragmentation)^{79,92,97,135} than the oxidation products produced from toluene photooxidation.^{283–285} Experiments and theoretical calculations show that photolysis of carbonyls and peroxides remains efficient in the condensed phase, producing products with high quantum yields on picosecond time scales following the excitation.^{83,141,286,287} Another effect is that the TOL/OH/NO_x SOA compounds may be more efficiently disposing of the electronic excitation energy by internal energy relaxation without breaking up into smaller products. TOL/OH/NO_x SOA components include aromatic species such as nitrophenols, which have photolysis quantum yields approaching unity in the gaseous phase but only $\sim 10^{-4}$ - 10^{-5} in the condensed phase.^{288,289} The excitation of nitrophenol clusters has been shown to result in fast internal conversion mediated by intramolecular hydrogen bonding.²⁹⁰ These studies suggest that the SOA components may channel most of excitation energy into heat, thus slowing the photodegradation and resulting in a low FMLR despite a high absorption coefficient. Guaiacol high NO_x SOA was also found to photodegrade slowly in previous experiments, and was also attributed to rapid internal energy relaxation in aromatic compounds.⁸¹

These results also indicate that the photodegradation is a dynamic process, which starts at a high rate, slows down, and eventually stops (Fig. 4.6). Therefore, treating the initial photodegradation rates (e.g., rates determined by Malecha et al.)⁸¹ as constant will lead to an overestimation of the effect of condensed phase photochemistry on SOA mass concentration. A more reasonable representation is a biexponential decay of the SOA mass concentration as proposed by O'Brien et al. (2019).⁹⁷

4.3.4 Dark Evaporation Correction

The correction for the spontaneous dark evaporation competing with photodegradation is not trivial since the chemical composition of the SOA material is changing with time. However, it can be done with a simplifying assumption of a time-invariant evaporation rate constant (k_{evap}). This assumption is consistent with observations of slow first-order mass loss in control experiments shown in Figure 4.3.

The *FMLR* is assumed to obey the first-order kinetics with the time-invariant evaporation rate constant k_{evap} and time-dependent photodegradation rate constant $J(t)$:

$$FMLR_{total}(t) = -\frac{1}{m} \frac{dm}{dt} = k_{evap} + J(t) \quad (4.3)$$

The subscript “total” refers to the fact that both UV irradiation and evaporation contribute to the mass loss. Based on the above equation, $FMLR$ can be corrected for evaporation by directly subtracting results of a dark experiment from results of an irradiated experiment done on an identical sample:

$$FMLR_{UV}(t) = J(t) = FMLR_{total}(t) - FMLR_{dark}(t) = FMLR_{total}(t) - k_{evap} \quad (4.4)$$

The value of k_{evap} can be determined from a separate experiment (e.g., Fig. 4.3) or from the short segment of the data collected before the irradiation started.

Percent Mass Loss (PML) is related to $FMLR(t)$ as follows:

$$-\int \frac{dm}{m} = \int FMLR(t) dt \quad (4.5)$$

$$m(t) = m_0 \times \exp\left[-\int_0^t FMLR(t) dt\right] \quad (4.6)$$

$$PML(t) = 100 \times \frac{m_0 - m(t)}{m_0} = 100 \times \left[1 - \exp\left[-\int_0^t FMLR(t) dt\right]\right] \quad (4.7)$$

Since k_{evap} is assumed to be constant, the equation for time-dependent mass becomes:

$$m(t) = m_0 \times \exp[-k_{evap} \times t] \times \exp\left[-\int_0^t J(t) dt\right] \quad (4.8)$$

PML under the conditions of both UV irradiation and evaporation, UV irradiation only and evaporation only are, respectively:

$$PML_{total}(t) = 100 \times \left[1 - \exp[-k_{evap} \times t] \times \exp\left[-\int_0^t J(t) dt\right]\right] \quad (4.9)$$

$$PML_{UV}(t) = 100 \times \left[1 - \exp\left[-\int_0^t J(t) dt\right]\right] \quad (4.10)$$

$$PML_{dark}(t) = 100 \times \left[1 - \exp[-k_{evap} \times t]\right] \quad (4.11)$$

By combining the three equations for PML above, the following method was developed for getting corrected PML_{UV} from the uncorrected PML_{total} :

$$PML_{UV}(t) = \frac{PML_{total}(t) - 100 \times [1 - \exp[-k_{evap} \times t]]}{e^{-k_{evap} \times t}} \quad (4.12)$$

Based on the considerations and equations above, the effects of evaporation were corrected by following these steps:

1. Calculate mass as a function of time, $m(t)$, directly from the QCM frequency data, which gives $PML_{total}(t)$ directly.

$$PML_{total}(t) = 100 \times \frac{m_0 - m(t)}{m_0} \quad (4.13)$$

2. Calculate $FMLR_{total}(t)$ from the QCM data for the irradiated system with evaporation occurring in parallel.
3. Fit the dark segments of the data collected before the irradiation started to obtain the evaporation rate constant k_{evap} . Since the evaporation process is slow, a linear fit was used as follows:

$$PML_{dark}(t) = 100 \times [1 - \exp[-k_{evap} \times t]] \approx 100 \times k_{evap} \times t \quad (4.14)$$

The k_{evap} values determined for this study were:

SOA Type	k_{evap} (h^{-1})
APIN/O ₃	5.55×10^{-4}
LIM/O ₃	3.74×10^{-4}
TOL/OH/NO _x	7.52×10^{-4}
TOL/OH	2.41×10^{-4}

4. With the values of k_{evap} determined, $FMLR$ was corrected using the following equation.

$$FMLR_{UV}(t) = FMLR_{total}(t) - k_{evap} \quad (4.15)$$

5. Finally, *PML* was corrected using the following equation.

$$PML_{UV}(t) = \frac{PML_{total}(t) - 100 \times [1 - \exp[-k_{evap} \times t]]}{e^{-k_{evap} \times t}} \quad (4.16)$$

4.3.5 Effect on Chemical Composition

High-resolution ESI(+) mass spectrometry was used to study the difference between the chemical composition of fresh SOA and the photorecalcitrant fraction in 305 nm experiments with LIM/O₃ SOA. Figure 4.8 shows a mass spectrum of both the non-irradiated (using the same collection and annealing method) and photorecalcitrant fraction of LIM/O₃ SOA. The signals were normalized to the total peak abundance. It is important to note that this analysis only probed molecular formulas. Thus, some of the newly formed products may have the same formula as the fresh sample, but different chemical structure (for example *cis*-pinonic acid is known to photoisomerize into its structural isomer limononic acid).⁸³ Also, while the effect of evaporation on the differences in mass spectra is expected to be small compared to the effects of photodegradation, some of the minor differences in the mass spectra are due to evaporation. The photorecalcitrant fraction showed a more complex mixture of compounds with less well-defined transitions between the monomer, dimer and trimer regions. The fresh SOA sample contained 1010 compounds while the photorecalcitrant fraction contained 1434 compounds, of which 495 were unique to the recalcitrant fraction. Photolysis of the initial SOA molecules splits them in smaller fragments and increases the degree of oxidation. However, this process can be partly counteracted by free-radical (RO₂) cross-reactions within the SOA matrix producing new oligomers.

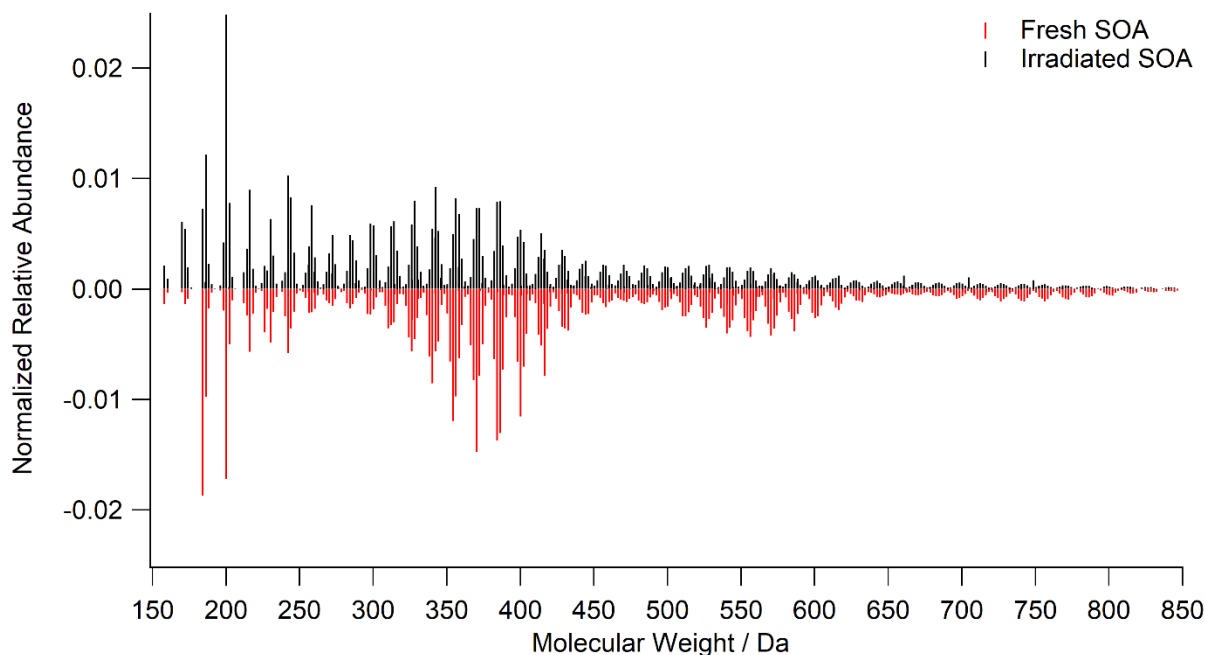


Figure 4. 8: High-resolution ESI (+) mass spectra of irradiated (black) and fresh (red) LIM/O₃ SOA. The peaks are normalized to the combined peak abundance. The irradiated data are inverted for the ease of comparison. While the fresh SOA has clearly separated monomer, dimer, and trimer regions, this distinction becomes less obvious in the irradiated SOA due to a combination of fragmentation, functionalization, and radical recombination reactions in SOA.

To help compare fresh and irradiated LIM/O₃ SOA, the observed compounds were separated into three groups: (1) compounds that increased in normalized peak abundance by at least an order of magnitude compared to the fresh sample; (2) compounds that experienced a change in the normalized peak abundance by less than an order of magnitude; and (3) compounds that disappeared after irradiation. Compounds in groups 1 and 2 represent the photorecalcitrant fraction remaining in the irradiated LIM/O₃ SOA, while compounds in group 3 are photolabile. The O:C and H:C ratios of the compounds in each of the groups are compared in Figure 4.9a, and double bond equivalent (DBE) values are compared in Figure 4.9b. The DBE values are a useful metric to track the number of double bonds/conjugations in the assigned molecule. The abundance weighted average O:C, H:C, DBE, and number of C atoms for each of the groups, as well as for all the observed peaks in the fresh SOA and irradiated samples are listed in Table 4.2. The overall trend shows larger O:C and smaller H:C ratios in molecules that are formed due to irradiation and contribute to the photorecalcitrant fraction (i.e., groups 1 and 2). Compounds in group 3 tend to have higher C-numbers consistent with the expectation that larger molecules have a higher

probability of photodegradation. This is also seen in Table 4.3, with the most prominent compounds in group 3 containing higher C-numbers. Furthermore, photolabile group 3 compounds tend to have smaller DBE/C ratios suggesting they have fewer double bonds per carbon atom. These results are consistent with previous short-term (2 h) photolysis of LIM/O₃ SOA in an aqueous solution and on a filter, in which O:C ratio increased, and C-number decreased during photolysis.²⁷⁴

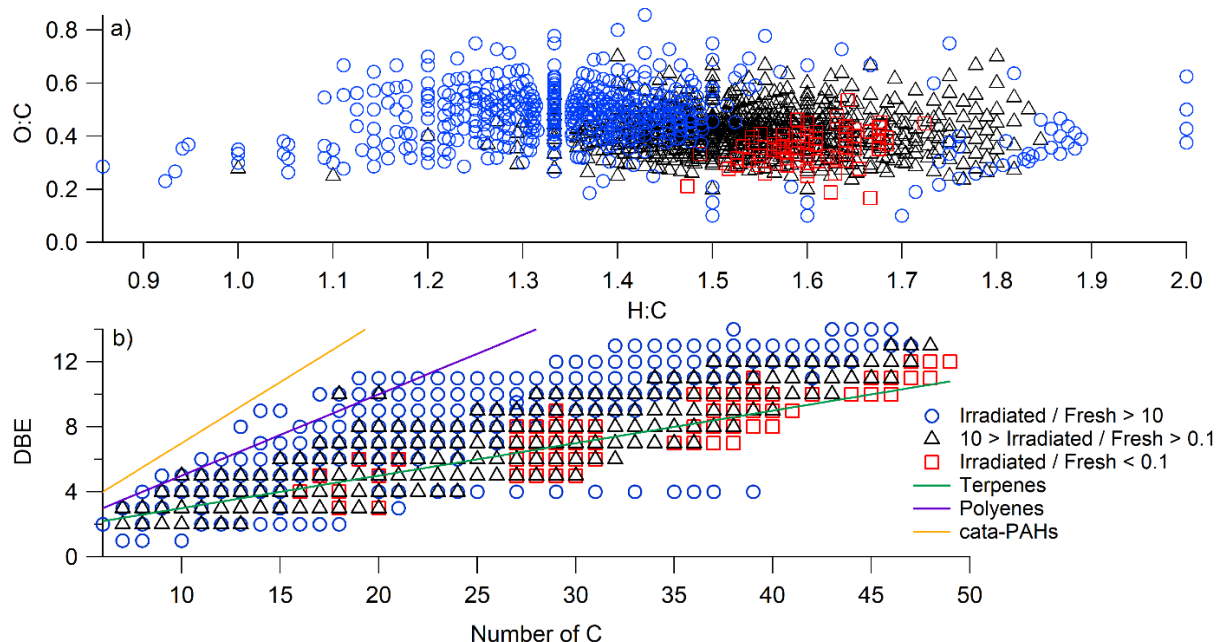


Figure 4. 9: a) O:C and H:C of LIM/O₃ SOA molecular species observed by ESI-MS. Please note the atypical Van Krevelen diagram, with the interchanged traditional axes. b) Double bond equivalent (DBE) of the same compounds plotted as a function of carbon number. In both panels, blue circles correspond to molecules with a normalized peak abundance that increased by over an order of magnitude after long term irradiation. Black triangles correspond to molecules whose normalized peak abundance changed by less than an order of magnitude, while red squares correspond to molecules that disappeared after irradiation. Green, purple, and orange lines correspond to the expected DBE vs C dependence for terpene, polyene, and cata-PAH compounds, respectively. Photorecalcitrant molecules (blue circles and black triangles) tend to have a lower H:C ratio, higher O:C ratio, and increased DBE compared to photolabile compounds (red squares).

Table 4. 2: Peak abundance weighted average composition characteristics of LIM/O₃ SOA. The spread in the observed values corresponds to 1 σ .

Compounds	Average O:C	Average H:C	Average DBE	Average C atoms
Group 1 Irradiated/Fresh > 10	0.48 \pm 0.27	1.39 \pm 0.86	7.63 \pm 2.69	21.76 \pm 8.85
Group 2 10 > Irradiated/Fresh > 0.1	0.42 \pm 0.22	1.54 \pm 0.81	5.55 \pm 2.01	19.61 \pm 7.32
Group 3 Irradiated/Fresh < 0.1	0.34 \pm 0.17	1.60 \pm 0.63	7.37 \pm 1.89	32.22 \pm 8.91
Fresh SOA	0.39 \pm 0.21	1.57 \pm 0.79	5.75 \pm 2.00	22.19 \pm 7.87
Irradiated SOA	0.43 \pm 0.31	1.51 \pm 0.82	5.82 \pm 2.24	19.50 \pm 7.48

Table 4. 3: List of 10 molecular formulas with the largest peak abundances in ESI-MS(+) spectra in the fresh SOA, photorecalcitrant (groups 1 & 2), and photolabile (group 3) groups. The formulas are listed in the order of decreasing normalized peak abundance. Some of the most prominent formulas present in both fresh and irradiated samples may correspond to limonic acid (C₉H₁₄O₄), limononic acid (C₁₀H₁₆O₃), or 7OH-limononic acid (C₁₀H₁₆O₄) as found in previous studies.^{46,291,292}

Fresh SOA Formulas	Group 1 & 2 Formulas	Group 3 Formulas
C ₁₀ H ₁₆ O ₃	C ₁₀ H ₁₆ O ₄	C ₂₀ H ₃₂ O ₅
C ₁₀ H ₁₆ O ₄	C ₁₀ H ₁₆ O ₃	C ₂₉ H ₄₄ O ₈
C ₁₉ H ₃₀ O ₇	C ₉ H ₁₄ O ₄	C ₃₉ H ₆₂ O ₁₃
C ₂₀ H ₃₂ O ₇	C ₁₉ H ₃₀ O ₇	C ₃₉ H ₆₄ O ₁₅
C ₁₉ H ₃₀ O ₈	C ₁₉ H ₃₀ O ₈	C ₂₉ H ₄₈ O ₈
C ₁₉ H ₃₀ O ₆	C ₂₀ H ₃₂ O ₇	C ₁₉ H ₂₈ O ₄
C ₂₀ H ₃₂ O ₈	C ₁₈ H ₂₈ O ₇	C ₃₈ H ₆₀ O ₁₂
C ₉ H ₁₄ O ₄	C ₂₀ H ₃₂ O ₈	C ₃₉ H ₆₄ O ₁₄
C ₁₈ H ₂₈ O ₇	C ₁₂ H ₁₈ O ₅	C ₃₀ H ₄₈ O ₈
C ₁₈ H ₂₈ O ₆	C ₁₉ H ₃₀ O ₆	C ₃₉ H ₆₄ O ₁₆

Calculating the aromaticity index^{293,294} for these molecules, $AI = (1 + C - O - 0.5H)/(C - O)$, shows that photodegradation results in the formation/survival of compounds with a larger aromaticity index (Fig. 4.10), although only a small fraction of compounds (<1%) reach the aromaticity index threshold of 0.5 for true aromatic compounds.^{293,294} This is also seen in Figure 4.9b, where photolabile group 3 compounds scatter around the expected DBE-vs-C asymptote for terpene compounds, while the photorecalcitrant compounds (groups 1 and 2) are closer to the polyenes suggesting an increase in the number of C=C bonds. All of the observed compounds are below the

DBE-vs-C dependence for the cata-PAHs, ruling out formation of condensed aromatic products. It is worthy to note that enhancement in aromaticity after irradiation has also been observed in dissolved organic matter irradiation studies.^{295,296}

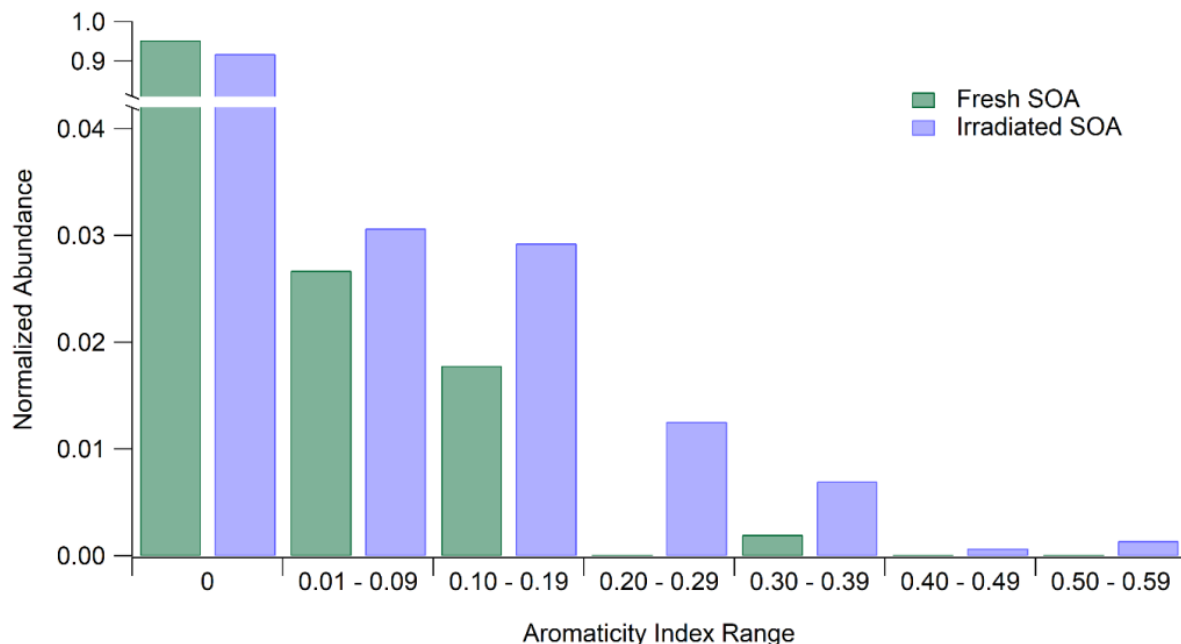


Figure 4. 10: Photodegradation of LIM/O₃ SOA results in the formation/survival of compounds with a larger degree of aromaticity. The histogram shows the normalized abundance of molecules binned into Aromaticity Index (AI) ranges, where AI > 0.5 corresponds to aromatic compounds.^{293,294}

4.3.6 Effect of Relative Humidity on Photodegradation

The effect of relative humidity (RH) on photodegradation rates was investigated by flowing air with variable RH over APIN/O₃ and LIM/O₃ SOA during the irradiation (Fig. 4.11). These experiments were limited to early photodegradation times (several hours) because of the difficulties of controlling RH over longer time periods. In both cases, the mass loss increased with increasing RH. Similar effects have been seen in previous photodegradation studies, with mass loss increasing at elevated RH.^{82,138,140,297} One of the effects of water vapor is making the SOA matrix less viscous, making it possible for the products of photodegradation to escape more easily from the SOA material. Indeed, the viscosities of α -pinene¹¹¹ and d-limonene²⁹⁷ ozonolysis SOA have been found to decrease with increasing RH. The observation that the mass of dry samples continued to decrease (0% RH traces in Fig. 4.11) even after the LED was switched off supports the idea of slow diffusion of photoproducts out of the SOA matrix. Our results indicate an increase

in maximum FMLR at ~60% RH by a factor of 2.3 and 3.1 for APIN/O₃ and LIM/O₃ SOA, respectively (Table 4.1). These findings agree well with the findings of Wong et al.,¹³⁸ who observed an increase of APIN/O₃ SOA mass loss rates by a factor of 2 at high RH conditions compared to dry conditions, and with result Arroyo et al.,⁸² who reported 2-4 times higher photodegradation rate for LIM/O₃ SOA at 30-70% RH compared to dry conditions. We should note that at elevated RH, turning the LED off actually resulted in an apparent mass gain. We believe that this is an artifact of the slightly elevated temperature of the QCM crystal under irradiated conditions becoming lower in darkness leading to an uptake of water vapor.

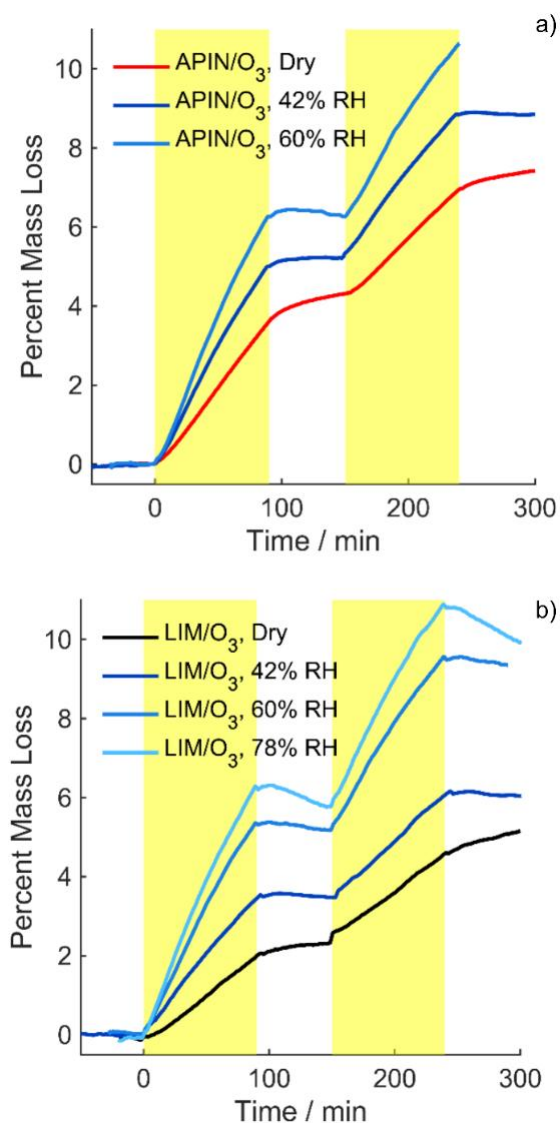


Figure 4. 11: Photodegradation of (a) APIN/O₃ SOA and (b) LIM/O₃ SOA under different relative humidity (RH) conditions. Yellow-shaded regions indicate when SOA was being irradiated.

Although we attribute the increase in the observed photodegradation rate at higher RH to diffusion transport limitations, we cannot completely rule out changes in the photochemical mechanism brought about by the presence of water in the SOA material.

4.4 Application to Ambient Conditions

To estimate the photodegradation rate of SOA under atmospheric conditions, we assumed that it scales in proportion to the convolution of spectral flux $F(\lambda)$, quantum yield $\phi(\lambda)$, and absorption cross section $\alpha(\lambda)$ (Equation 4.17).

$$FMLR = -\frac{1}{m} \frac{dm}{dt} = \int F(\lambda)\phi(\lambda)\alpha(\lambda)d\lambda \quad (4.17)$$

The absorption cross sections and quantum yields of many of these molecules rapidly decay at longer wavelengths,^{1,9,81} so the integration can be limited to a narrow range over which the 305 nm LED emits. For a narrow integration range, the ratio of FMLR values for two different radiation sources can be approximated as the ratio of integrated spectral flux densities (Equation 4.18).

$$Scaling = \frac{\int F(\lambda)_{LED}d\lambda}{\int F(\lambda)_{atm}d\lambda} \quad (4.18)$$

The photodegradation profiles were scaled (scaling factor = 1.4) to the 24-hour average flux in Los Angeles at sea level (Fig. 4.12) from the TUV model (with model inputs shown below).²⁹⁸ This flux corresponded to a 24-hour average J_{NO_2} value of $4.05 \times 10^{-3} \text{ s}^{-1}$. The scaled photodegradation rate (Fig. 4.13) shows that the largest mass loss takes place in the first 24 h of exposure, after which the degradation substantially decreases. The scaled percent mass loss profiles of the SOA were also fit to a bi-exponential decay function and are shown in Figure 4.14 and Table 4.4 with the intention that they can be utilized by modelers in future studies.

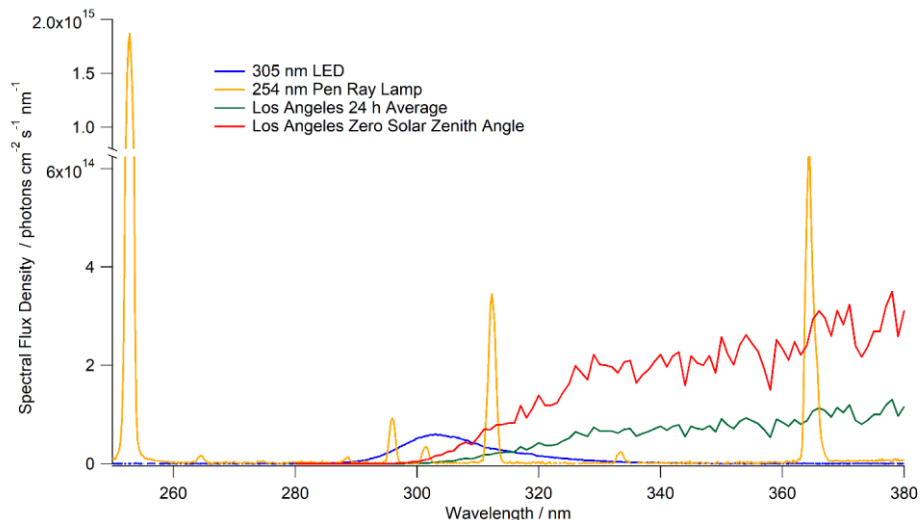


Figure 4. 12: Spectral flux density of the M300L4 305 nm LED, Spectroline 11SC-1 Pen Ray Lamp, Los Angeles summer solstice maximum, and the 24-hour average Los Angeles solar flux. Los Angeles spectral flux densities were obtained using the TUV model.²⁹⁹ The following parameters were input into the Quick TUV calculator: Latitude/Longitude: 34°/-118°; Date and Time: June 20, 2017 – data from each hour in the day were acquired and averaged to obtain a 24-hour average spectral flux density or 19:00:00 GMT, representative of the summer solstice maximum; Overhead Ozone: 300 du; Surface Albedo: 0.1; Ground Altitude: 0 km; Measured Altitude: 0 km; Clouds Optical Depth/Base/Top: 0.00/4.00/5.00; Aerosols Optical Depth/S-S Albedo/Alpha: 0.235/0.990/1.000; Sunlight Direct Beam/Diffuse Down/Diffuse Up: 1.0/1.0/1.0; 4 streams transfer model

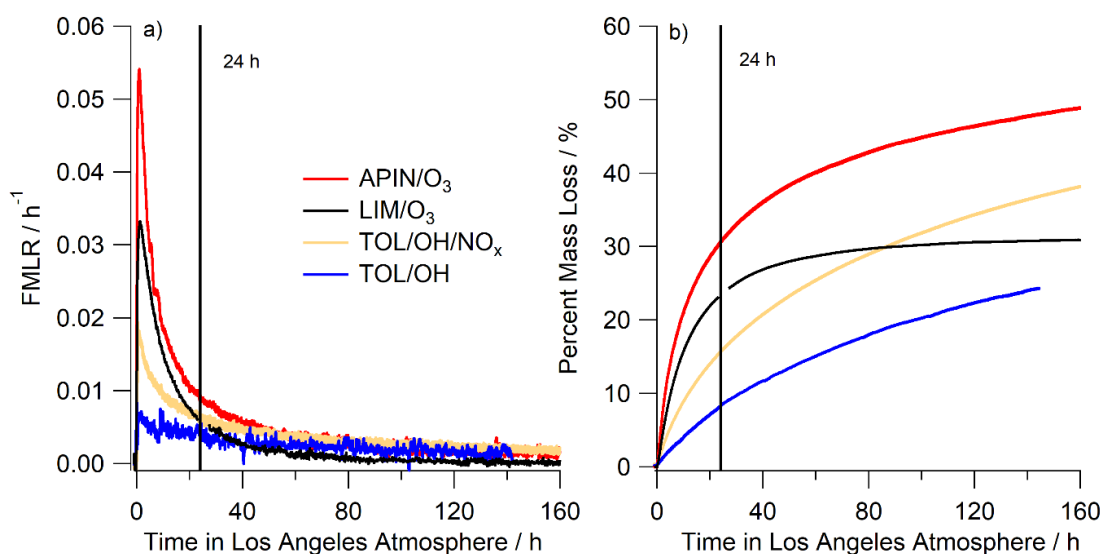


Figure 4. 13: Scaling the results to atmospheric conditions reveals that FMLR (a) and percent mass loss (b) are most important in the first 24 hours of photodegradation. After that, the photodegradation continues at a decreasingly slow rate and other mechanisms of aging become more important.

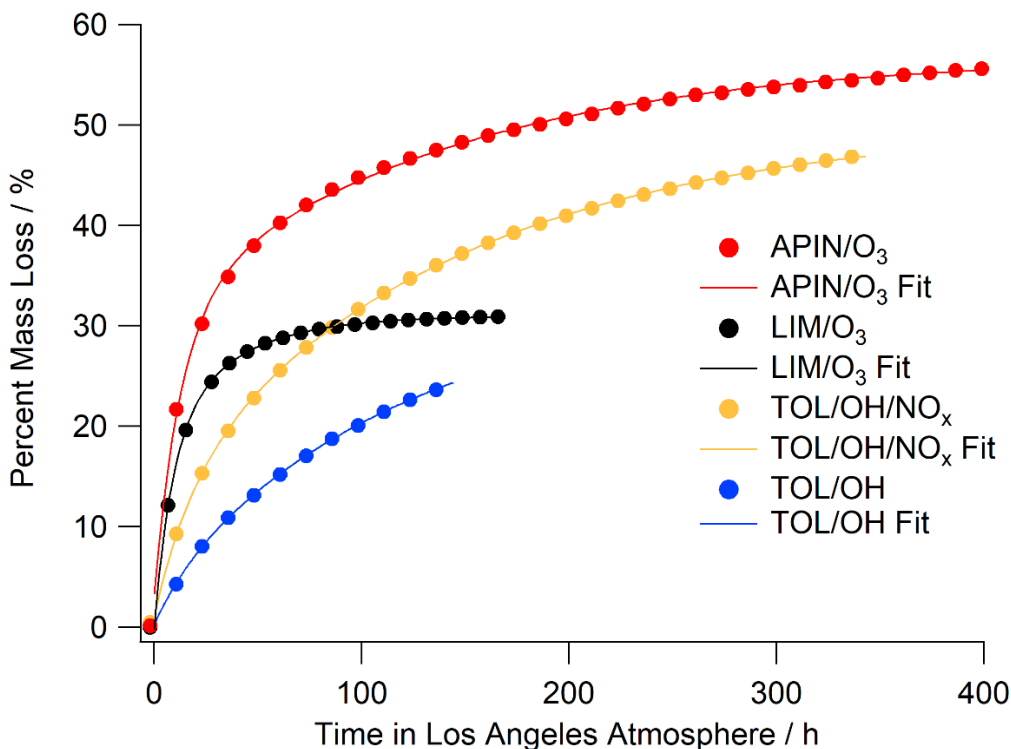


Figure 4.14: The UV degradation percent mass loss profiles (PML_{UV}) were scaled to the 24-hour average Los Angeles flux ($J_{NO_2} = 4.05 \times 10^{-3} \text{ s}^{-1}$) and fit to a bi-exponential function. Data points correspond to the degradation profile, while the curve is the fit to the data.

Table 4. 4: Bi-exponential fit parameters used to fit percent mass loss profiles of different SOA types after correcting for evaporation and scaled to the 24-hour average Los Angeles flux. Traces were fit to $y = y_0 + A_1 e^{\frac{-x}{\tau_1}} + A_2 e^{\frac{-x}{\tau_2}}$ with 95% confidence intervals.

SOA Type	$y_0 \pm 95\% \text{ CI}$	$A_1 \pm 95\% \text{ CI}$	$\tau_1 \pm 95\% \text{ CI}$	$A_2 \pm 95\% \text{ CI}$	$\tau_2 \pm 95\% \text{ CI}$
APIN/ O_3	56.884 ± 0.003	-28.292 ± 0.008	12.876 ± 0.008	-25.357 ± 0.005	138.59 ± 0.06
LIM/ O_3	30.976 ± 0.006	-18.556 ± 0.080	8.571 ± 0.041	-12.692 ± 0.082	34.728 ± 0.185
TOL/OH/ NO_x	50.176 ± 0.002	-11.967 ± 0.003	17.98 ± 0.01	-36.962 ± 0.002	141.77 ± 0.03
TOL/OH	33.661 ± 0.016	-3.498 ± 0.009	16.275 ± 0.044	-29.914 ± 0.007	123.53 ± 0.15

Although photodegradation continues after 24 h, it is substantially slower and other forms of chemical aging, such as heterogeneous oxidation of particles by hydroxyl radical, may become

more important.^{89,97} This is highlighted in Figure 4.15, where the UV degradation mass loss trends are combined with predicted changes as a result of heterogeneous oxidation via OH radicals. This prediction showed that UV degradation dominates in the first 24 h; but heterogeneous OH oxidation became increasingly more important after that. It is important to note that the OH aging trend used for this comparison has a few important assumptions:³⁰⁰ $[\text{OH}] = 1.5 \times 10^6$ molecules cm^{-3} , γ (uptake coefficient) = 1, average O:C = 0.8, average H:C = 1.5, and particle density = 1.5 g cm^{-3} .

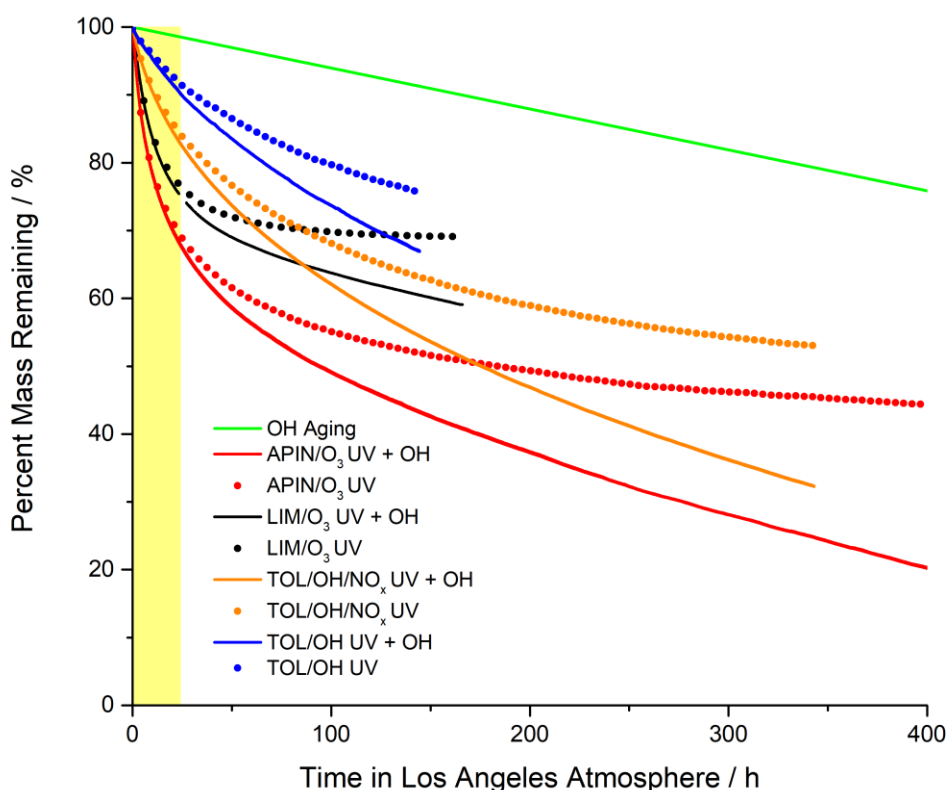


Figure 4. 14: Predicted changes to the percent of mass remaining due to heterogenous OH aging alone (green line), UV degradation alone (circles), or the combined effect of UV and OH aging (solid curves). The shaded region shows the initial time period where photodegradation is dominant; thereafter, other atmospheric aging mechanisms will drive the mass loss.

The percent of SOA degraded before reaching the photorecalcitrant fraction was also compared to recent studies by O’Brien et al.⁹⁷ and Zawadowicz et al.¹⁴⁰ (Fig. 4.16). Overall, our results are similar, especially when comparing the initial photodegradation rate, and all agree on the existence of a photorecalcitrant fraction. Despite the different methods of SOA preparation (flow tube in this study versus a chamber in the other two studies) as well as different irradiation sources used,

the measurements agree reasonably well, with a lifetime of 12 h (this study), 7 h (O'Brien et al., 2019), and 23 h (Zawadowicz et al., 2020) of APIN/O₃ SOA degradation (under dry conditions) after scaling to the 24-hour average Los Angeles flux. There are however, differences in the photorecalcitrant fraction. This difference may be due to differences in SOA preparation with a higher mass loading used in this study which would increase particle phase partitioning of photo-reactive carbonyl group containing species.

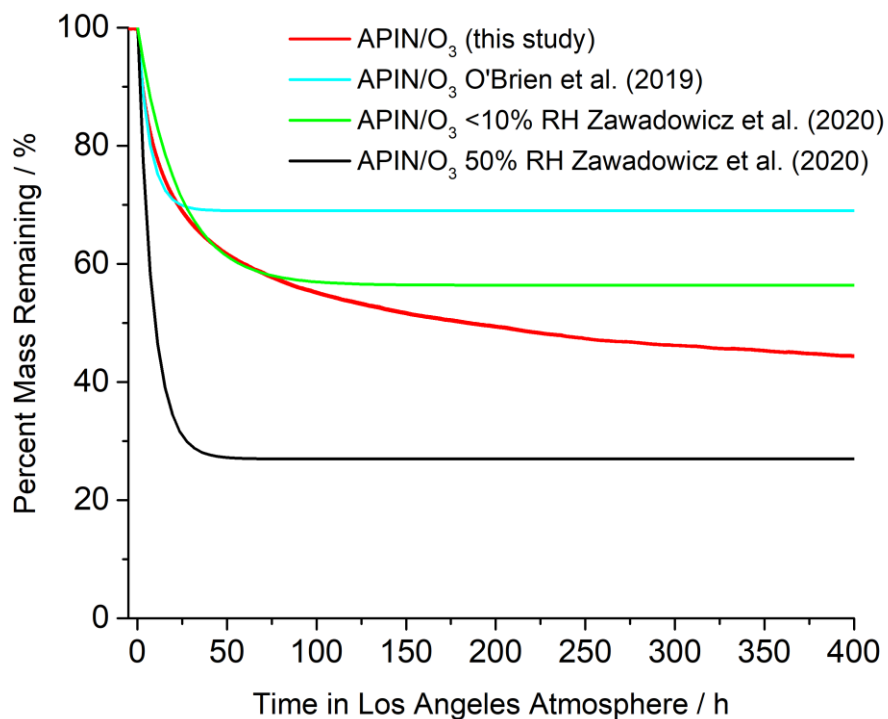


Figure 4. 15: Converting the APIN/O₃ percent mass loss to a percent mass remaining allows for comparison with the extent of APIN/O₃ photodegradation as found by O'Brien et al. (2019)⁹⁷ and Zawadowicz et al. (2020).¹⁴⁰ It is important to note that the Zawadowicz et al. (2020) study did not report a recalcitrant fraction under dry conditions due to the uncertainty in the fit. In order to compare our study with theirs under dry conditions we assumed the recalcitrant fraction to be the average between our study (43.8%) and the O'Brien et al. study (69 %). The Zawadowicz et al. (2020) study also found increased photodegradation rates under humid conditions, also included in Figure 4.16.

4.5 Summary and Implications

These results have several important implications. First, the mass loss rates observed here are atmospherically relevant. The photodegradation with 254 nm photons showed a maximum FMLR

as high as 35 % h⁻¹ and a complete destruction of the SOA material, proving that SOA can fully degrade under harsh UV radiation. The tropospheric UV irradiation also showed substantial photodegradation, with FMLR up to 5% h⁻¹, and almost half the SOA mass eventually being lost. Thus, SOA photodegradation is an important and substantial component of aging in the atmosphere, especially in the first 24 h after the initial SOA formation, and is crucial to incorporate into models in order to fully understand the effect SOA has on climate and visibility through light absorption/scattering and cloud formation.¹⁴⁰ Overall, while these mass loss rates cannot compete with particle growth for ultrafine particles, which can exceed 10 nm/h,³⁰¹ these photodegradation processes can limit growth for larger particles in the accumulation mode which dominate the overall SOA mass loading in the atmosphere.¹

Second, these photodegradation processes should be able to efficiently deplete organic aerosols from the upper troposphere/lower stratosphere after deep convective transport.³⁰² While we have not done explicit measurements at low temperatures, it can be argued that photodegradation should become relatively more important as the aerosol's viscosity increases in these cool temperatures,¹¹⁵ thus slowing diffusion in the particle and limiting aging by heterogeneous oxidants like OH radicals. Photodegradation can still occur in these situations because UV radiation can easily penetrate the entire volume of the particle, regardless of its viscosity. It is however, important to note that the increased viscosity is also expected to decrease the diffusion rates of volatile photoproducts, slowing the photodegradation rate.

Third, tropospheric photodegradation leads to a photorecalcitrant fraction of SOA remaining which should be considered when discussing the role of photodegradation on SOA sinks in the atmosphere. Extrapolating the initial mass loss rates and degradation processes to longer time scales would be incorrect and would lead to an overestimate of mass loss, as suggested by O'Brien et al and Zawadowicz et al.^{97,140} Furthermore, the compounds found in the photorecalcitrant fraction are chemically different from those in the initial SOA. More research is needed to better understand the chemical and physical properties of the photorecalcitrant fraction such as its viscosity and morphology (See Chapter 5).

And finally, this study shows that elevated relative humidity increases the mass loss of SOA during photodegradation by acting as a plasticizer to reduce the diffusion transport limitations of volatile photoproducts and allowing them to more easily escape from particles. Thus, the relative

importance of photodegradative aging versus heterogeneous oxidative aging may shift depending on the environmental conditions, with photodegradation becoming more important in areas with higher relative humidity.

Chapter 5: Sunlight can convert atmospheric aerosols into a glassy solid state and modify their environmental impacts

Portions of this chapter were reproduced with permission from Baboomian, V. J., Crescenzo G. V., Huang, Y., Mahrt, F., Shiraiwa, M., Bertram, A. K., Nizkorodov, S. A., (2022). Sunlight can convert atmospheric aerosols into a glassy solid state and modify their environmental impacts. Proceedings of the National Academy of Sciences, under revision

5.1 Abstract

Information on the viscosity of secondary organic aerosol (SOA) particles is needed to predict their role in air quality and climate. Solar ultraviolet (UV) radiation is known to change the chemical composition and mass concentration of SOA. Nevertheless, the effect of solar UV radiation on the viscosity of SOA particles is unknown, leading to uncertainties when predicting their impacts on air quality and climate. Here, the viscosity of SOA aged by exposure to 305 nm UV radiation for 12 days was measured, and compared to the viscosity of control SOA samples that remained in darkness for 12 days. This is equivalent to a UV exposure of 6–14 days at midlatitudes in summer, and captures typical tropospheric lifetimes of SOA particles. SOA particles were generated by the ozonolysis of d-limonene and α -pinene, two abundant biogenic volatile organic compounds in the atmosphere. Results indicate that the viscosity and characteristic mixing times of organic molecules within a 200 nm diameter SOA particle can be as much as five orders of magnitudes larger for aged SOA compared to the control throughout most of the troposphere. This increase in viscosity and mixing times is consistent with an increase in average molecular mass and oxygen-to-carbon ratio of the organic molecules constituting the SOA material, as determined by high-resolution mass spectrometry. The increase in viscosity likely leads to an increased abundance of glassy SOA particles that can act as ice nuclei in the atmosphere. Furthermore, the increase in viscosity and mixing times can impede gas-particle partitioning and heterogeneous chemistry. Overall, results clearly demonstrate that UV-aging needs to be considered when predicting the environmental impacts of SOA.

5.2 Introduction

Secondary organic aerosol (SOA) represents a considerable mass fraction of atmospheric aerosol particles. SOA can directly affect climate by scattering shortwave radiation, or indirectly by acting as nuclei for cloud droplets and ice crystals.^{1,22,44,303} SOA also contributes to poor air quality in urban areas.^{4,35,304–306}

SOA is often formed through the oxidation of anthropogenic and biogenic volatile organic compounds (VOCs), followed by gas–particle partitioning of the semivolatile and low-volatility oxidation products.^{18,307,308} Of the total mass of global VOCs, approximately 90% originates from biogenic sources, with monoterpenes (C₁₀) being one of the most important types of biogenic VOCs.^{18,22,307,308} Since α -pinene and d-limonene often dominate the atmospheric monoterpene emissions, they have been commonly used as representative monoterpenes in laboratory and modelling studies investigating SOA properties.^{22,309–311}

Once formed in the atmosphere, SOA are transported throughout the troposphere^{63–65}. SOA have average lifetimes on the order of one to two weeks,⁶⁶ but can be considerably longer with increasing altitude. During this atmospheric transport, SOA particles can undergo aging by multiple processes, including heterogeneous oxidation,^{67–69} aqueous phase photooxidation,^{70–73} photosensitized uptake of gases,^{74–77} and ultraviolet (UV) aging.^{78–83} Aging processes can change the physicochemical properties of aerosols. For example, UV aging was reported to decrease mass, increase the oxidation state, decrease the volatility, and decrease the light absorption and scattering ability of SOA particles.^{74,78,81,92–94}

To predict the importance of SOA for air pollution and climate, information on viscosity and diffusion rates within SOA particles is needed.¹⁰⁶ Viscosity and diffusivity are inversely related as described with the Stokes-Einstein equation. Slower diffusion rates have been found to affect gas-particle partitioning and hence the evolution of mass and size distributions of SOA.^{113,121} Molecular diffusion also affects rates and mechanisms of multiphase reactions within SOA, which in turn dictate SOA composition^{122,123} and long-range transport of pollutants such as polycyclic aromatic hydrocarbons.^{124–128} Viscous aerosols have been shown to create anoxic conditions as well as limit molecular motion, resulting in the stabilization of photochemically produced radicals, trapping them in the organic matrix.^{130,131} Furthermore, the viscosity of SOA can impact their ability to act as cloud condensation nuclei¹³² and ice nuclei.¹³³ For example, if SOA particles are

in a glassy phase state, defined as a material with a viscosity greater than 10^{12} Pa s, they may act as heterogeneous ice nuclei in clouds.⁶⁴

The viscosity of fresh, unaged SOA types has been reported in previous laboratory studies.^{110,111,312–315} In contrast, the viscosity of SOA material after aging has rarely been measured, and so far, no measurements of the SOA viscosity after UV exposure, hereafter referred to as UV-aging, have been reported. It is especially important to understand the effect of UV-aging on the viscosity of SOA in the upper troposphere, where particles can spend a long time interacting with solar radiation, and where the dry and cold conditions in this part of the troposphere favor higher SOA viscosity. In addition to laboratory studies, recent modelling studies have used parameterizations based on viscosity measurements and glass transition temperatures to predict global distributions of viscosities and diffusion rates within SOA particles.^{115,121,316–319} However, the effect of UV-aging on viscosity and diffusion rates within SOA was not explicitly considered in these studies. As a result, global distributions of viscosity and diffusion rates within SOA and associated atmospheric impacts remain highly uncertain.

To address these important gaps in knowledge, the viscosity of SOA after exposure to UV radiation with a wavelength (λ) of 305 nm for 12 days was measured, and compared to the viscosity of control SOA samples that remained in darkness for the same period of time. This exposure time corresponds to an equivalent exposure of 6–14 days at midlatitudes during the summer.^{299,320} Such UV-aging leads to considerable increases in viscosity and mixing times of organic molecules within a SOA particle by as much as five orders of magnitude compared to the unirradiated SOA particles. These increases are consistent with an increase in average molecular mass and oxygen-to-carbon ratio of the organic molecules constituting the SOA material, as determined by high-resolution mass spectrometry. The increased viscosity of aged SOA likely leads to increased abundance of highly viscous, glassy SOA particles that can act as ice nucleating particles with implications for climate predictions. The increased viscosity and mixing times of organic molecules within a SOA particle can potentially impact gas-particle partitioning and heterogeneous chemistry with implications for air quality and climate predictions.

5.3 Materials and Methods

5.3.1 SOA Preparation and Collection

SOA was prepared by dark ozonolysis in either an environmental chamber or a flow tube (see Chapter 1 Section 1.6). Table 5.1 summarizes the SOA production trials conducted for this experiment.

In the environmental chamber experiments, a solution of liquid d-limonene (Fischer Scientific, 97% purity) in methanol (Thermo Scientific, Optima LC/MS Grade) (1:10 v/v) was injected into a glass bulb, and a particle- and hydrocarbon free air flow (3 L min^{-1}) from a zero-air generator (Parker, FTIR purge gas generator model 75-62NA) was used to carry the organic vapors through a heated inlet ($T = 300 \text{ K}$) into the chamber. O_3 was injected into the chamber and the VOC and O_3 mixing ratios within the chamber were approximately 200 ppb and 7 ppm, respectively, at the start of an experiment and the RH was 40%. SOA particles were collected from the chamber once maximum mass concentrations in the range of approximately $290\text{--}600 \mu\text{g m}^{-3}$ were reached, corresponding to a residence time of 40 min. The mass concentration during the collection time was approximately $250 \mu\text{g m}^{-3}$.

In the aerosol flow tube experiments the starting mixing ratios of VOC and O_3 were approximately 11 ppm and 7 ppm, respectively. At the start of an experiment, the RH was 0% and the SOA mass concentration was approximately 1.7 mg m^{-3} .

Table 5. 1: Summary of SOA production conditions in both the environmental chamber and aerosol flow tube. In the case of SOA generated in the flow tube, SOA samples for viscosity measurements and high-resolution mass spectrometry (HRMS) analysis were collected consecutively on the same day.

VOC Precursor	Production Method	VOC concentration / ppm	Ozone concentration / ppm	SOA mass concentration / $\mu\text{g m}^{-3}$	Aged or Control	Use
d-limonene	Environmental chamber	0.20	7.4	396	Aged	Viscosity measurements
d-limonene	Environmental chamber	0.20	6.5	286	Control	Viscosity measurements
d-limonene	Environmental chamber	0.20	7.0	604	Aged	HRMS analysis
d-limonene	Environmental chamber	0.20	6.0	530	Control	HRMS analysis
d-limonene	Flow tube	11	7.5	1700	Aged/Control	Viscosity measurements & HRMS analysis
α -pinene	Flow tube	11	7.0	1700	Aged/Control	Viscosity measurements & HRMS analysis

At the exit of the chamber and the flow tube, the SOA containing air flow was passed through a charcoal denuder to denude excess O_3 . SOA particles were then collected either onto poly(tetrafluoroethylene; PTFE) filters (FGLP04700, Millipore, 47 mm diameter, 0.2 mm pore diameter) for high resolution mass spectrometry (HRMS) analysis, or onto hydrophobic glass slides (12 mm diameter, Hampton Research, HR3-277) for viscosity and phase behavior

experiments. SOA were collected on the hydrophobic slides using stage 8 of a non-rotating microorifice uniform deposit impactor (MOUDI; MSP Corp. model 110-R) operated at a flow rate of 20 L min^{-1} . With the remaining stages removed the resulting 50% cut-off diameter was below 180 nm. Sampling with the non-rotating MOUDI created discrete spots of aggregated SOA particles of $\sim 35\text{--}60 \mu\text{m}$ in diameter after a typical collection time of 1 h. Glass slides were made hydrophobic by coating with FluoroPel 800 (Cytonix).

5.3.2 SOA Aging

Aging was achieved by placing the SOA-containing substrates (filters or hydrophobic glass slides) into an irradiation chamber (Fig. 5.1). The irradiation chamber was continuously flushed ($860 \text{ cm}^3 \text{ min}^{-1}$) with air from a zero-air generator (Parker, FTIR purge gas generator model 75-62NA), to remove any volatile products formed during photoaging. The irradiation chamber was separated into two compartments using a high purity aluminum foil barrier (Sigma Aldrich, 99.999% purity, 1.0 mm thickness). One compartment was equipped with a UV-LED, and the other compartment was kept dark to simultaneously produce an aged and a control SOA sample, respectively. This separation ensured that the control (unaged) sample experienced the same amount of evaporative loss as the aged (irradiated) sample. This approach allowed us to cleanly separate the effects of UV exposure from evaporative aging.

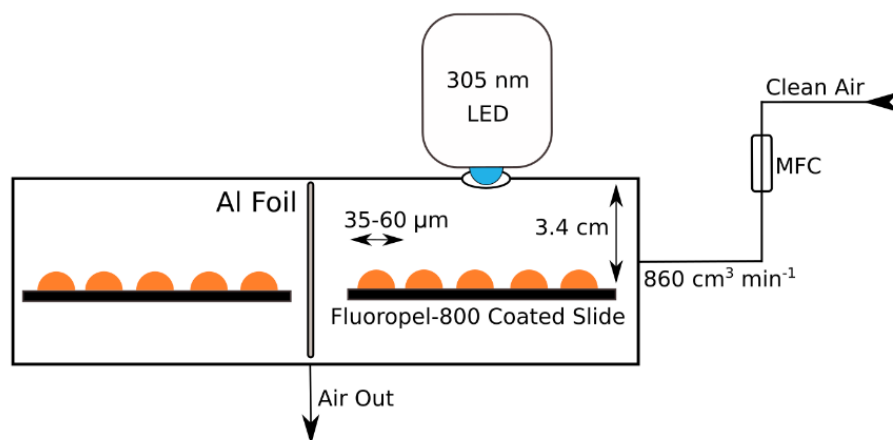


Figure 5. 1: The chamber used to irradiate SOA substrates. SOA substrates are placed in the chamber, 3.4 cm below a 305 nm LED. Control samples are shielded from the UV radiation using a sheet of high purity aluminum foil. Clean air flows into the chamber using a mass flow controller (MFC) at a flow rate of $860 \text{ cm}^3 \text{ min}^{-1}$. Both aged and control samples are exposed to the same amount of air flow during the aging experiment.

The incident power of the LED (Thorlabs Inc., model M300L4) was 2.4 mW, measured using a power meter (Coherent PS19Q) at the same distance between the LED and the SOA containing substrate (3.4 cm vertical distance between LED and substrate). With the 2.8 cm² area of the power meter, this corresponds to a peak spectral flux of 1.0×10^{15} photons cm⁻² s⁻¹. Previous experiments demonstrated that similar power meter measurements agree with actinometry experiments.^{74,80} This compares reasonably well to the flux of 4.1×10^{14} photons cm⁻² s⁻¹ additionally measured with a radiometer (StellarNet Inc., Black-Comet UV-VIS Spectrometer). To age an SOA sample, it was irradiated with the LED centered at $\lambda = 305$ nm for 12 days. This equals to an exposure of approximately 6–14 days in Los Angeles, CA, based on the overlap of the UV-LED spectral flux density with the 24 h average (including day and night) spectral flux density in Los Angeles from 290 to 330 nm (on June 20, 2017; see Fig. 5.2). An irradiation time of 12 days was chosen to ensure the formation of a non-degrading, photo-recalcitrant fraction, as determined by Baboomian et al (Chapter 4).⁷⁸ If integrated over the 290-330 nm range, where reasonable photochemical activity is expected, the flux from the UV-LED source is of the same order of magnitude as the solar flux. It should be pointed out that the UV-LED photons are, on average, more energetic than the solar photons, and the UV-LED has a very different spectrum, making the exact comparison difficult. Here, a single wavelength LED was used instead of a full solar spectrum, in order to target the $n \rightarrow \pi^*$ carbonyl transitions in photolabile compounds, which lead to Norrish type I and II reactions.^{80,135} In addition, using an LED instead of a solar simulator avoids heating of the sample with visible and near-infrared radiation.

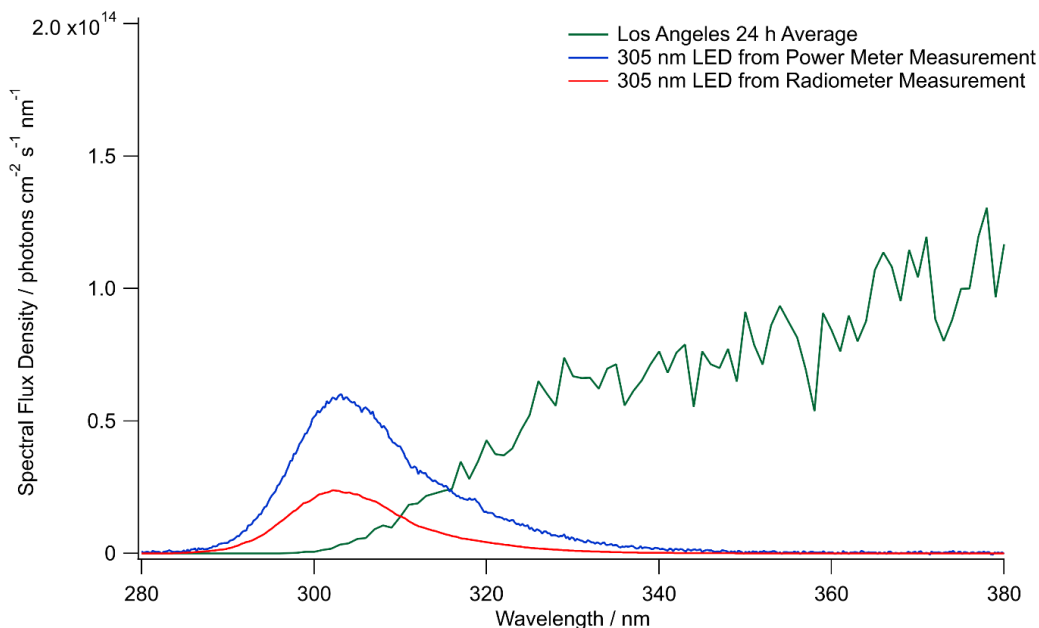


Figure 5. 2: Spectral flux density of the M300L4 305 nm LED and the 24-h averaged Los Angeles conditions (including day and night). Los Angeles spectral flux densities were obtained using the TUV model.²⁹⁹ The radiometer measurement in red is more accurate; the power meter measurement is less accurate but included because it was used in previous work⁷⁸ as a metric for the UV LED light intensity. The following parameters were input into the Quick TUV calculator: Latitude/Longitude: 34°/-118°; Date and Time: June 20, 2017 – data from each hour in the day were acquired and averaged to obtain a *24-hour average* spectral flux density or 19:00:00 GMT, representative of the summer solstice maximum; Overhead Ozone: 300 du; Surface Albedo: 0.1; Ground Altitude: 0 km; Measured Altitude: 0 km; Clouds Optical Depth/Base/Top: 0.00/4.00/5.00; Aerosols Optical Depth/S-S Albedo/Alpha: 0.235/0.990/1.000; Sunlight Direct Beam/Diffuse Down/Diffuse Up: 1.0/1.0/1.0; 4 streams transfer model

To estimate the UV-exposure time of SOA under atmospheric conditions, it was assumed that the photodegradation rate scales in proportion to the convolution of spectral flux $F(\lambda)$, quantum yield $\phi(\lambda)$, and absorption cross section $\sigma(\lambda)$

$$J = \int F(\lambda)\phi(\lambda)\sigma(\lambda)d\lambda. \quad (5.1)$$

The absorption cross section and quantum yield of many organic molecules found in SOA become small at longer wavelengths^{1,9,81}. Thus, it is reasonable to limit the integration to the narrow range of the LED emission assuming that not much photodegradation occurs at longer wavelengths. For a narrow integration range, the scaling of photodegradation rates for two different light sources can be approximated as the ratio of integrated spectral flux densities

$$\text{scaling factor} = \frac{\int F(\lambda)_{LED} d\lambda}{\int F(\lambda)_{atmosphere} d\lambda}. \quad (5.2)$$

Using these equations, the spectral flux densities of the 305 nm LED and the 24-h average Los Angeles spectrum (at sea level) were integrated from 290-330 nm. The 305 nm LED has a spectral flux of 1.0×10^{15} photons $\text{cm}^{-2} \text{s}^{-1}$ using the power meter flux measurement. The more accurate radiometer flux measurement was 4.1×10^{14} photons $\text{cm}^{-2} \text{s}^{-1}$. The 24-h Los Angeles average spectrum has an average J_{NO_2} value of $4.05 \times 10^{-3} \text{s}^{-1}$ and spectral flux of 8.7×10^{14} photons $\text{cm}^{-2} \text{s}^{-1}$. The calculated experimental scaling factor of 0.47 and 1.2 (for radiometer and power meter measurements, respectively) was used to convert experimental exposure times of 12 days into 6-14 days of time spent in the Los Angeles atmosphere.

5.3.3 Measurement of SOA Viscosity as a Function of Relative Humidity

The viscosity of the particles was measured at different RH values using the poke-flow technique.^{53,111,312,314} For the poke-flow experiments, a slide with SOA particles was placed into a RH-controlled flow cell coupled to an inverted optical microscope (AmScope, model ME1400TC-INF). The SOA particles were conditioned at the respective RH of the poke-flow experiment by continuously passing a flow ($\sim 0.5 \text{ L min}^{-1}$) of dry or humidified nitrogen (Praxair, 5.0 grade) over the particles. The dew point within the flow cell was continuously monitored using a hygrometer (Hygro M4/E4, General Eastern Instruments). Similarly, the temperature of the flow cell was continuously monitored using a thermocouple (Omega, model: FF-T-20-100) and maintained at $T = 292 \pm 0.3 \text{ K}$ for all experiments. The RH within the flow cell was calculated from the measured dewpoint and temperature. For most experiments, the SOA particles were conditioned at the respective RH for 2 h. In addition, for SOA generated by ozonolysis of d-limonene in an environmental chamber, conditioning times ranging from 1 to 24 h were used (Fig. 5.3). Viscosities were identical within the uncertainties after conditioning for 1 – 24 h, indicating that a conditioning time of 2 h is sufficient for near equilibrium conditions. Also, separate tests showed that evaporation of the SOA particles during the poke-flow experiments, even after 24 h, was less than could be detected with an optical microscope (Fig. 5.4).

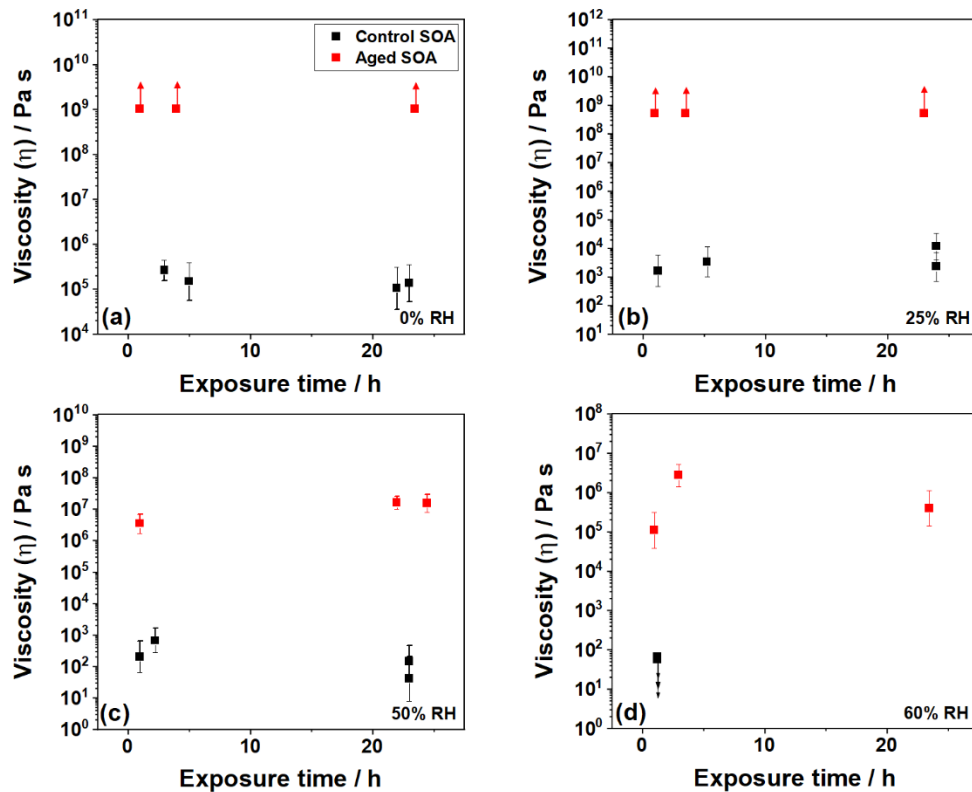


Figure 5. 3: Dependence of viscosity on the time particles spent in the poke-flow cell before the measurement. To ensure that particles were at equilibrium at a given RH, viscosities of d-limonene aged and control SOA were obtained as a function of exposure time at different RH levels. Panels correspond to (a) 0% RH, (b) 25% RH, (c) 50% RH, and (d) 60% RH in the poking chamber. Viscosities are identical within uncertainties after conditioning for 1 – 24 h. SOA was produced by ozonolysis in an environmental chamber.

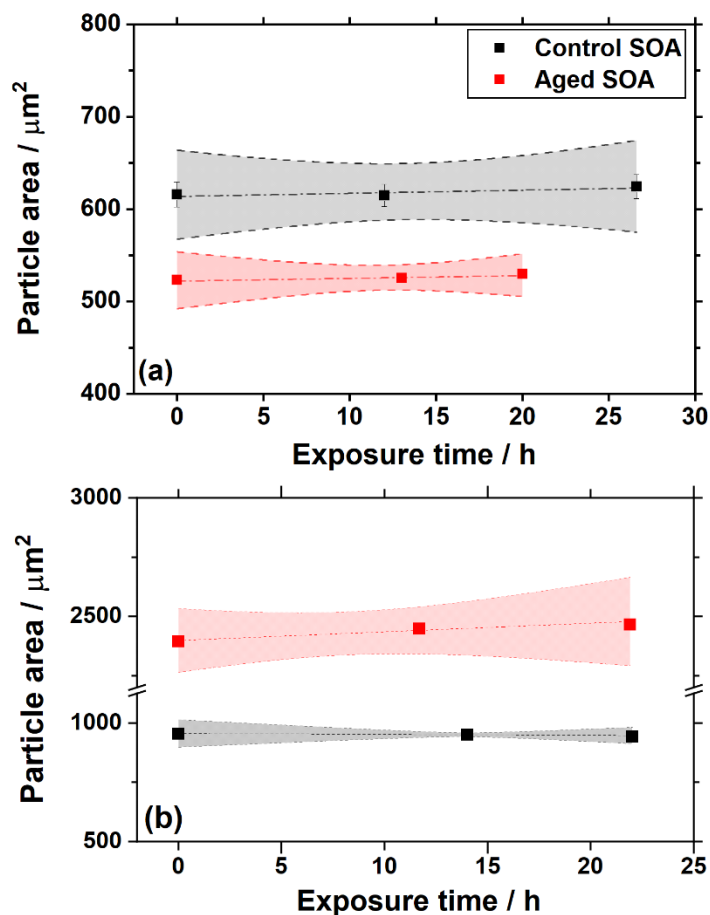


Figure 5. 4: Particle evaporation tests in the flow cell used for poke-flow experiments. To check for possible evaporation of the particles during poke-flow experiments, the particle area was monitored over the course of 24 h for d-limonene aged and control SOA. Panel (a) represents exposure times under dry conditions ($\approx 0\%$ RH) in the poking chamber, and panel (b) represents exposure times under 60% RH. The confidence bands represent the standard deviation of repeated particle area measurements of a single particle at a given time point. SOA was produced by ozonolysis in an environmental chamber.

During poke flow measurements, SOA particles with diameters of approximately $35\text{--}60\ \mu\text{m}$ were poked with a tungsten needle ($20\ \mu\text{m}$ diameter, Roboz Surgical Instruments Co.) coated to make it oleophobic (CYTONIX, OilSlip 110). The morphology of the poked particles was continuously monitored using a CCD camera, capturing images at a rate of three frames per second. Poking introduced a hole within the particles, usually leading to particles with a half-torus geometry. After poking, the particle material flowed and returned to its energetically preferred spherical cap geometry. The time required for the area of the hole (A) to decrease to one quarter of its initial size, referred to as the experimental flow time ($\tau_{\text{exp,flow}}$), was determined and used to extract the

particle viscosity.^{111,321} For highly viscous ($\eta \gtrsim 10^8$ Pa s) particles that do not flow, a lower limit of $\tau_{\text{exp,flow}}$ was obtained, by assuming the radius of the initial hole decreased by $0.5 \mu\text{m}$ during the observation time in the experiments. Lower limit experimental flow times are denoted by upward pointing arrows (e.g., Fig. 5.5). A decrease of $0.5 \mu\text{m}$ in radius defines the spatial resolution of the microscope and corresponds to a change in area of approximately 5–10%. For particles that cracked upon poking, a lower limit of $\tau_{\text{exp,flow}}$ was obtained by assuming one of the edges of the cracked particle moved by $0.5 \mu\text{m}$ during the observation time in the experiments. These cases also denote lower limits and are thus also denoted by upwards pointing arrows (e.g., Fig. 5.5). Conversely, for particles with very low viscosities ($\eta < 10^3$ Pa s), $\tau_{\text{exp,flow}}$ was shorter than the time between images captured with the CCD camera. In these cases, an upper limit of $\tau_{\text{exp,flow}}$ was obtained by setting $\tau_{\text{exp,flow}}$ as the time between images. Upper limit flow times are denoted by downward pointing arrows (e.g., Fig 5.5).

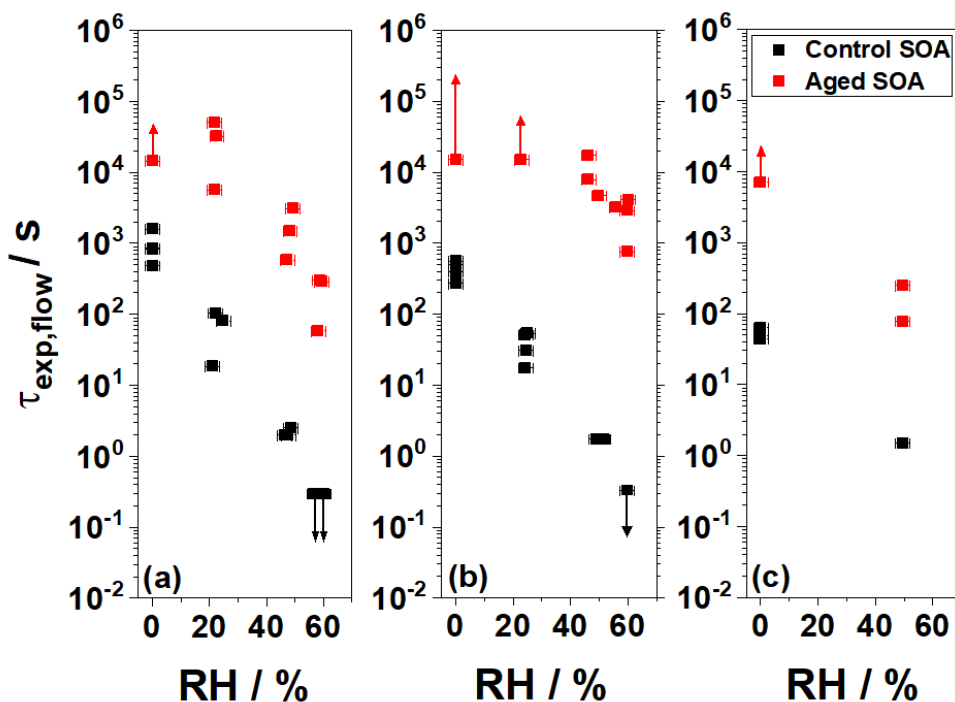


Figure 5. 5: Summary of the experimental flow times ($\tau_{\text{exp,flow}}$) as a function of relative humidity obtained from room temperature (292 K) poke-flow experiments. Black squares correspond to control SOA, red circles correspond to aged SOA. Panel (a) corresponds to d-limonene SOA produced in an environmental chamber, panel (b) corresponds to d-limonene SOA prepared in the flow tube and panel (c) represents α -pinene prepared in the flow tube.

To obtain viscosities from the experimental flow times, fluid dynamics modelling was performed to simulate the flow of the material in the poke flow experiments, using the COMSOL Multiphysics® software (COMSOL Inc., v5.4), as detailed previously.³²¹ Within the model, the flow of the SOA material was simulated using the observed $\tau_{\text{exp,flow}}$ as an input parameter, together with the following material properties: density, slip length, surface tension, and contact angle.³¹² The values of these material properties are summarized in Table 5.2. The particle viscosity in the COMSOL simulations were varied until the modelled flow time ($\tau_{\text{mod,flow}}$) agreed with the experimental flow time ($\tau_{\text{exp,flow}}$) to within 1%. Changes in the slip length has the largest effect on the derived viscosity, followed by surface tension, and lastly contact angle. In the COMSOL simulations the slip length, surface tension, and contact angle parameters were systematically varied in order to obtain upper and lower bounds for the SOA viscosity.

Table 5. 2: COMSOL parameters used to simulate the experimentally observed flow times and determine the upper and lower bounds of viscosities of the SOA particles.

SOA type	Surface tension / mN m^{-1}	Slip length / m	Contact angle / $^{\circ}$
d-limonene Control	25.9 ^a –45 ^b	5×10^{-9} – 1×10^{-6} ^c	50.4–83.7 ^d
d-limonene Aged	25.9 ^a –45 ^b	5×10^{-9} – 1×10^{-6} ^c	55.5–65.0 ^d
α -pinene Control and Aged	25.3 ^a –45 ^b	5×10^{-9} – 1×10^{-6} ^c	52.7–67.7 ^d

^a As a conservative lower limit to the surface tension of the d-limonene and α -pinene SOA, the surface tension of the pure liquids were used. Surface tensions were determined with the ACD/Labs Percepta Platform-PhysChem Module, retrieved from ChemSpider January 14, 2022. ^b This upper limit is consistent with surface tension measurements of SOA at $\text{RH} \lesssim 65\%$ RH and surface tensions reported for alcohols, organic acids, esters, and ketones, as well as surface tension measurements of water solutions containing SOA products.^{322–325} ^c Range based on measurements of the slip length of organic compounds and water on hydrophobic surfaces.^{326–338} ^d Contact angles determined by measuring the height and radii of individual droplets using a confocal microscope following the method of Chesna et al.³³⁹ Note: the simulated viscosities depend only weakly on the contact angle. Changing the contact angle by $\pm 10\%$ changes the simulated viscosity on average by $\pm 15\%$, which is small compared to the overall uncertainties associated with the simulated viscosities.

5.3.4 High-Resolution Mass Spectrometry (HRMS) Analysis

The HRMS data were obtained using Ultra Performance Liquid Chromatography (UPLC) coupled with a Thermo Q Exactive Plus orbitrap mass spectrometer equipped with an electrospray ionization (ESI) source. The instrument is further discussed in Chapter 1 Section 1.6.4. The UPLC-ESI-HRMS was operated in negative ion mode with a mass resolving power of $\sim 10^5$ at m/z 200, and a spray voltage of 2.5 kV. The solvent consisted of a 1:1 (v/v) mixture of acetonitrile (Sigma Aldrich, purity $\geq 99.9\%$) and water (Sigma-Aldrich, HPLC grade). SOA were extracted from the PTFE-filters, by submerging each filter in 15 mL of solvent within an orbital shaker (Thermolyne, 37600 Mixer) for 15 min, followed by dilution, achieving typical concentrations of around $400 \mu\text{g mL}^{-1}$. Sections of the ion chromatogram with strong analyte intensity (intensity greater than 1×10^7) were integrated (3–16 min). Each PTFE filter extraction was run in triplicate through the instrument and only HRMS-peaks that appeared in all three trials were used for molecular assignment. In addition to the samples, a solvent blank was prepared following the same procedure above, but using a control substrate without analyte.

The method applied here combining/coupling UPLC and HRMS is more accurate in measuring relative ion abundances due to the chromatographic separation, compared to the previous study (Chapter 4), where direct infusion of the analyte containing solvent into the MS-inlet was utilized, which is prone to matrix effects.⁷⁸ Matrix effects due to direct infusion have been shown to result in changes in the ionization efficiency of analytes, ion suppression through charge competition, or enhancement due to the presence of certain compounds, such as inorganic salts.^{340–342} Thus, separating compounds before the ionization source can be effective in reducing the artifacts of direct infusion.³⁴⁰

HRMS-peaks were assigned molecular formulas following previous work.^{73,78} HRMS-peak positions and relative abundances were extracted using the Decon2LS software package³⁴³ and peaks containing ^{13}C isotopes were removed. All HRMS-peaks were assigned to the formulas $\text{C}_x\text{H}_y\text{O}_z$ with an accuracy of $\pm 0.001 m/z$ units while constraining the assignments to H/C of 0.30–2.25 and O/C of 0.00–2.30. Assignments were also constrained to closed-shell ions with even nominal masses. The assigned ion formulas were corrected for the ionization mechanism. The assumed ionization mechanism was deprotonation of the molecular compounds resulting in $[\text{M}-\text{H}]^-$ for negative ions. All the HRMS results are reported as formulas of neutral SOA compounds.

5.4 Results

5.4.1 Viscosity of SOA with and without UV-aging

Figure 5.6 shows the measured viscosity of SOA generated by 1) ozonolysis of d-limonene in an environmental chamber, 2) ozonolysis of d-limonene in a flow tube, and 3) ozonolysis of a-pinene in a flow tube (see Chapter 1 Section 1.6). Aging by UV irradiation was achieved by placing a substrate with deposited SOA into a flow cell, where it was irradiated by a UV-light emitting diode (LED, centered at $\lambda = 305$ nm) while passing particle and VOC-free air continuously over it (see Section 5.3.2). A control sample was prepared by exposing SOA to the same amount of particle and VOC-free air but without exposure to the UV radiation. The viscosity of control and aged SOA particles was determined using the poke-flow technique (see Section 5.3.3).

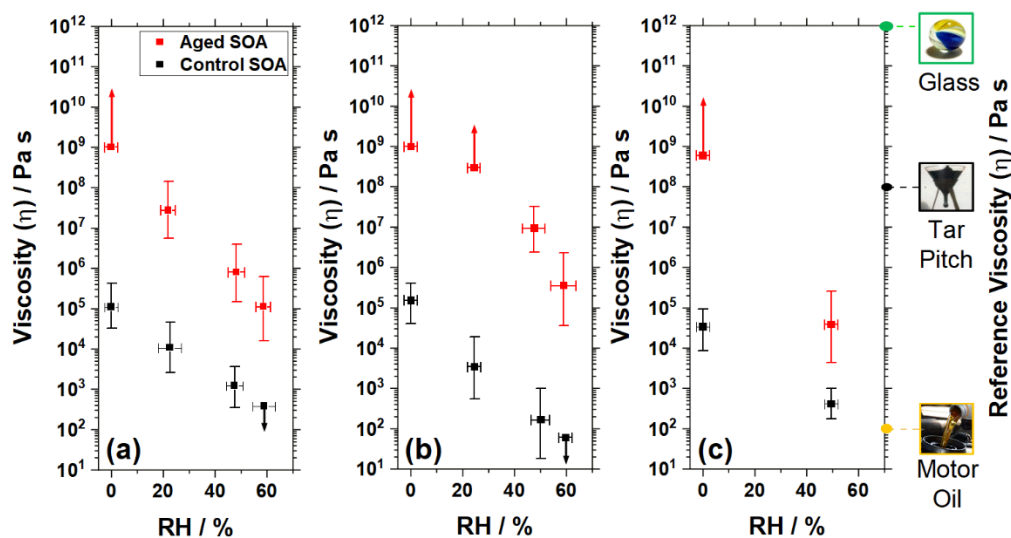


Figure 5. 6: Viscosity of SOA derived from ozonolysis of d-limonene and a-pinene measured at room temperature (292 K). Shown are viscosities of control (black squares) and aged by UV exposure (red squares) SOA particles. Panel (a) corresponds to d-limonene SOA produced in an environmental chamber, (b) corresponds to d-limonene SOA produced in a flow tube, and (c) corresponds to a-pinene SOA produced in a flow tube. Error bars in the y-direction correspond to the upper and lower limits of viscosities from the poke-flow experiments, error bars in the x-direction correspond to the uncertainty in the relative humidity through measurement of the dewpoint using a chilled mirror hygrometer. Upward arrows indicate lower viscosity limits, downward arrows indicate upper viscosity limits.

Figure 5.6 shows the viscosities for the control and aged SOA derived from d-limonene ozonolysis, produced in an environmental chamber. The viscosities were calculated from the flow times (Fig. 5.5) observed during the poke-flow measurements. The measured viscosities of control limonene

SOA are similar to previous measurements with similar mass concentrations (Fig. 5.7),^{297,344,345} which suggests that control samples are representative of fresh, unaged SOA.

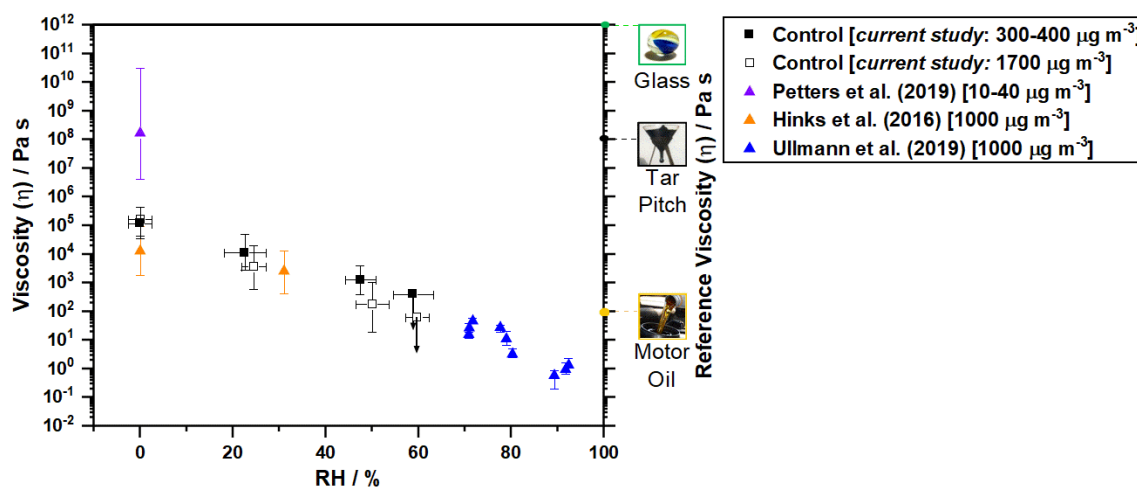


Figure 5. 7: Comparison of previously published viscosities of limonene SOA to the control d-limonene SOA produced in an environmental chamber and flow tube. Mass concentrations used in the production of SOA are listed for comparison.^{297,344,345} Error bars from Petters et al. correspond to the uncertainty in the temperature extrapolated glass transition temperature of ± 10 K.³⁴⁴

A striking result is the increase in SOA particle viscosity by several orders of magnitude after UV exposure, across all RH values investigated. For instance, under dry conditions, aging resulted in an increase in viscosity from 10^5 Pa s in the control d-limonene ozonolysis samples to at least 10^9 Pa s in the aged samples. A control experiment was conducted to ensure that 12 days of UV exposure (the same exposure used for the SOA samples) did not degrade the hydrophobic coating and inadvertently effect the viscosity measurements (Fig. 5.8).

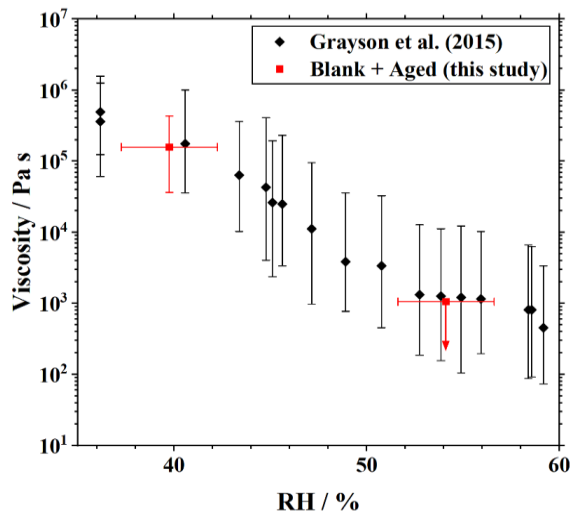


Figure 5. 8: Control Experiments show that aging of hydrophobic coatings on glass slides by UV exposure does not affect the viscosity measurements. This was done by nebulizing sucrose-water particles onto a hydrophobic glass slide coated with Fluoropel 800 (CYTONIX) after the glass slide had been aged by UV-radiation (for 12 days). After nebulization, the viscosity of sucrose-water particles were determined and compared to that reported in Grayson et al. (2015).³²¹ COMSOL simulation parameters used were those reported by Grayson et al. (2015).³²¹

The same trend of increasing viscosity after UV exposure is observed for SOA generated from ozonolysis of d-limonene in a flow tube (Fig. 5.6b). The similar results for d-limonene generated in an environmental chamber and flow tube with different ozone concentrations and SOA mass (Table 5.1), suggests relatively low sensitivity of the results to ozone exposure and SOA mass concentrations.

An increase in viscosity driven by UV-aging was also observed for the SOA generated from ozonolysis of α -pinene in a flow tube (Fig. 5.6c). This shows that the effect of aging on viscosity is not unique to SOA from ozonolysis of d-limonene. The measured viscosities of control α -pinene SOA are at the lower end of previous measurements for fresh SOA (Fig. 5.9),^{312,346} and similar to predictions based on explicit modelling of gas-phase oxidation of α -pinene.³⁴⁷ The relative increase in viscosity after UV-aging is apparent in all of the measurements and is expected to occur for monoterpene derived SOA irrespective of the initial SOA viscosity.

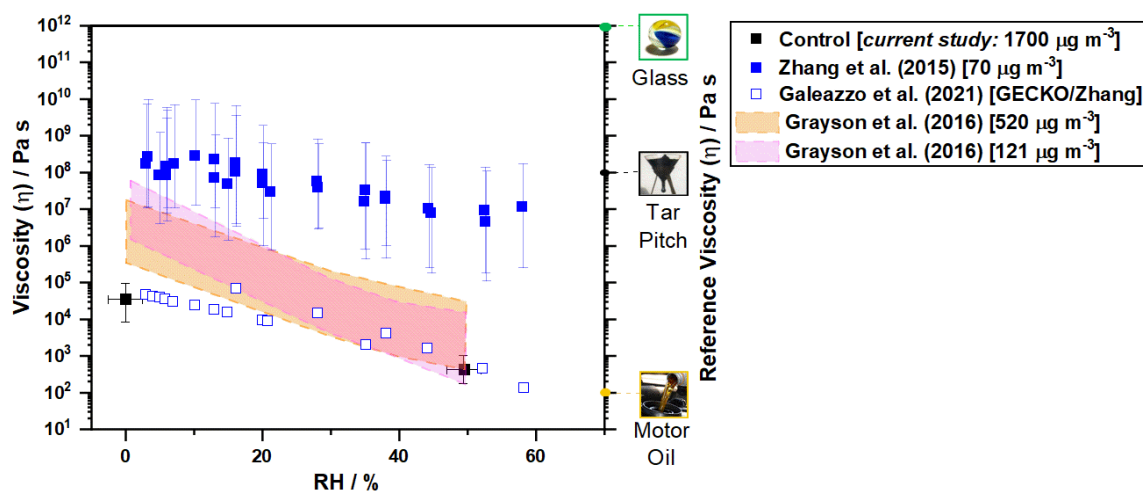


Figure 5. 9: Comparison of previously published viscosities of α -pinene SOA to the control α -pinene SOA. Mass concentrations used in the production of SOA are listed for comparison of viscosities.^{312,346,347} For Galeazzo et al. (2021),³⁴⁷ explicit modelling of gas-phase oxidation was performed using GECKO-A model.

The viscosity of all samples increased by 4 orders of magnitude after aging at 0% RH and upwards of 2 orders of magnitude at 50% RH (Fig. 5.6). Increasing the RH led to a decrease in the viscosity for both the control and aged SOA samples, due to water uptake into the particle phase (Fig. 5.6). This behavior is expected as water is known to act as a plasticizer that decreases the viscosity of the SOA material.^{78,82,138,314}

5.4.2 Chemical composition of SOA after UV-aging

Figure 5.10a shows the mass spectra of control and aged d-limonene SOA samples generated in an environmental chamber, as analyzed by liquid chromatography coupled to HRMS. All spectra were normalized to the sum of peak abundance in each sample. Spectra were collected in triplicates and only compounds present in all three independent runs were assigned to $C_xH_yO_z$ molecular formulas (see Section 5.3.4). In HRMS experiments, control samples had 1003 assignable formulas, and aged samples had 1428 assignable formulas including 673 assigned compounds that were unique to the aged SOA. Highlighted in Fig. 5.10a are the monomer, dimer, and trimer regions. Comparison of the mass spectra of control and aged SOA revealed that UV-aging led to a smoothing of the mass distribution of organic compounds. This is evident from the “filling-in” of the valleys between the monomer and the dimer, as well as between the dimer and trimer regions of the mass spectra shown in Fig. 5.10a.

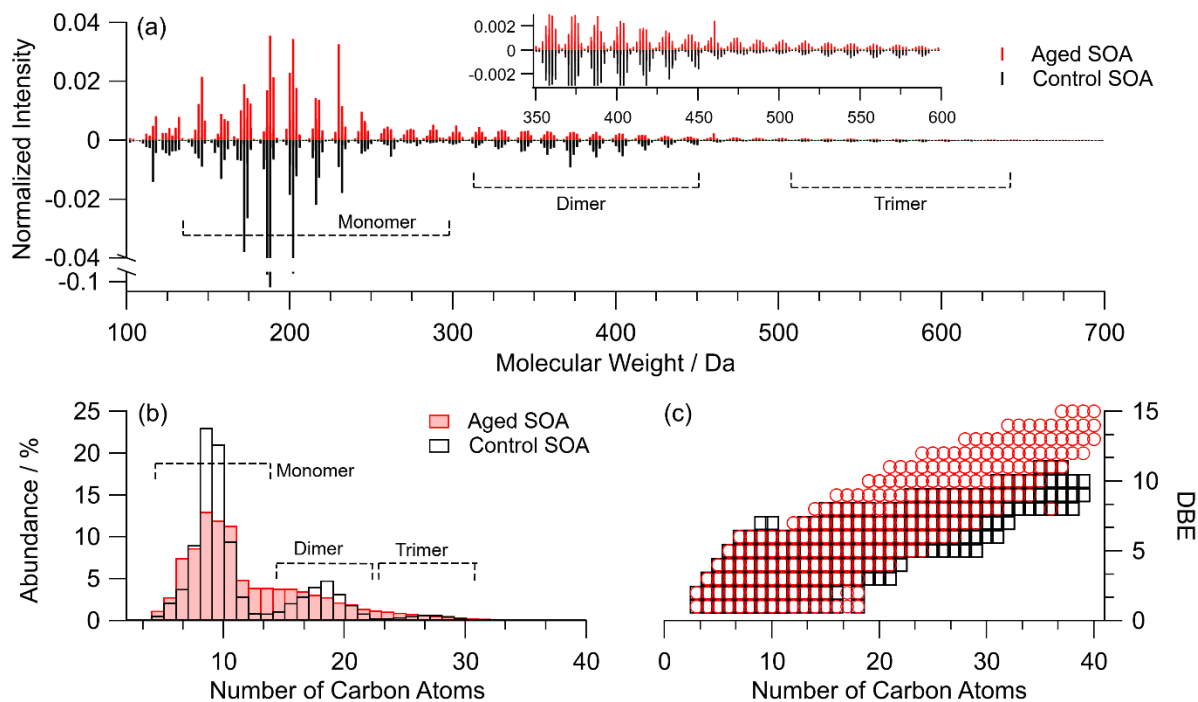


Figure 5.10: Chemical composition of control and aged d-limonene ozonolysis SOA. High resolution mass spectrometry results of SOA produced from d-limonene ozonolysis in an environmental chamber and changes in chemical composition due to UV-aging. Spectra were normalized to the sum of peak abundances per sample. Panel (a) shows mass spectra of the control and aged samples. The control sample has well-defined monomer, dimer, and trimer regions, indicated by the boxes, that are smoothed after UV-aging. A magnified view of the spectrum above 350 Da is also shown. Panel (b) shows the distribution of the number of carbon atoms per assigned compound that smooths in the aged samples. Panel (c) shows the double bond equivalent (DBE) as a function of the number of carbon atoms in assigned molecules. The aged SOA compounds tend to have a higher DBE compared to the control sample.

This smoothing of the mass distribution is even more apparent in Fig. 5.10b, where the distribution of the number of carbon atoms per assigned compound is shown. Unlike the control samples, where the regions for monomer, dimer, and trimer appear as distinctly different modes, the distribution of the aged samples appear considerably more continuous. This smoothing corresponds to an increase in the average molecular weight from 245.6 g mol^{-1} to 270.3 g mol^{-1} , an increase of $\sim 10\%$ (Table 5.3).

Figure 5.10c shows the double bond equivalent (DBE) as a function of the number of carbon atoms per assigned molecule.³⁴⁸ The aged SOA sample had compounds with increased DBE, particularly at higher molecular weights and carbon atom numbers, compared to compounds in the control

SOA sample. This is in contrast to known reduction in DBE in photodegraded dissolved organic matter samples.³⁴⁹

Table 5. 3: Summary of chemical composition characteristics of d-limonene ozonolysis SOA produced in an environmental chamber and a flow tube, and of flow tube produced α -pinene ozonolysis SOA. Dimer-to-monomer ratio is the ratio of combined peak abundances above 300 Da to that below 300 Da. This threshold was chosen as the center between the modes of the monomer (peaking around 200 Da) and dimer (peaking around 400 Da) compounds. All averages are weighted by the normalized peak abundance in the mass spectra. Both $T_{g,org}$ and $T_{g,org,uncorr}$ are included in the table to show the glass transition temperature with and without any corrections for the higher ionization efficiency of higher molecular weight compounds in the HRMS measurements.

	Dimer: Monomer Ratio	Avg. MW / g mol ⁻¹	Avg. O:C	Avg. H:C	Avg. DBE	Avg #C	$T_{g,org}$ / K	$T_{g,org,uncorr}$ / K
Control Chamber d-limonene SOA	0.332	245.6	0.54	1.52	4.14	11.24	273.1	287.1
Aged Chamber d-limonene SOA	0.463	270.3	0.61	1.44	4.92	11.89	283.3	297.6
Difference (aged – control)	↑ 0.130 (39.2%)	↑ 24.7 (10.0%)	↑ 0.07 (12.2%)	↓ 0.08 (5.4%)	↑ 0.77 (18.7%)	↑ 0.65 (5.8%)	↑ 10.2 (3.7%)	↑ 10.5 (3.7%)
Control Flow Tube d-limonene SOA	0.625	281.0	0.47	1.52	4.14	13.39	273.3	294.3
Aged Flow Tube d-limonene SOA	0.871	313.9	0.55	1.42	5.21	14.22	287.0	307.4
Difference (aged – control)	↑ 0.246 (39.4%)	↑ 32.9 (11.7%)	↑ 0.08 (17.0%)	↓ 0.10 (6.6%)	↑ 1.07 (25.8%)	↑ 0.83 (6.2%)	↑ 13.7 (5.0%)	↑ 13.1 (4.4%)
Control Flow Tube α-pinene SOA	0.600	265.0	0.46	1.45	3.91	12.94	273.3	290.6

Aged Flow Tube α-pinene SOA	0.765	290.1	0.51	1.39	4.63	13.56	283.1	300.5
Difference (aged – control)	↑ 0.165 (27.5%)	↑ 25.1 (9.5%)	↑ 0.05 (10.9%)	↓ 0.06 (4.1%)	↑ 0.72 (18.4%)	↑ 0.62 (4.8%)	↑ 9.8 (3.6%)	↑ 10 (3.4%)

Overall, UV-aging of environmental chamber d-limonene SOA resulted in an average increase in molecular weight, elemental oxygen-to-carbon ratio (O:C), number of carbon atoms per molecule, and DBE by 10%, 12%, 6%, and 19%, respectively; while the hydrogen-to-carbon ratio (H:C) decreased by 5% (Table 5.3). Similar changes in composition were also found in SOA particles generated by ozonolysis of d-limonene and α -pinene in a flow tube (see Table 5.3, Figs. 5.11 - 5.12). An increase in molecular weight, O:C ratio, and number of carbon atoms per molecule have all been correlated to an increase in particle viscosity.^{106,350,351} Hence, the increase in particle viscosity resulting from UV exposure observed here is most likely due to changes in these chemical properties.

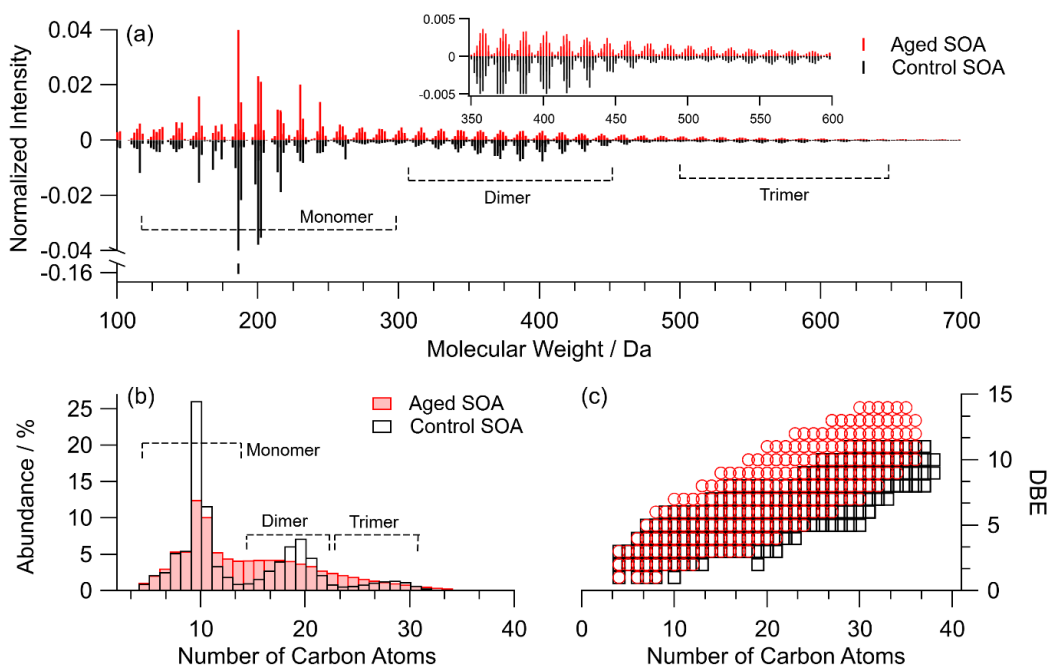


Figure 5. 11: HRMS analysis of d-limonene ozonolysis SOA produced in the flow tube and changes in chemical composition due to aging. Panel (a) shows mass spectra of the aged and control samples. Control sample has well-defined monomer, dimer, and trimer regions that are flattened after aging, as indicated by the boxes. Panel (b) shows

the distribution of the number of carbon atoms in assigned compounds that flattens in the aged sample. Panel (c) shows the double bond equivalent (DBE) as a function of the number of carbon atoms per assigned molecule for both aged and control samples. Aged sample compounds have a higher DBE compared to control samples.

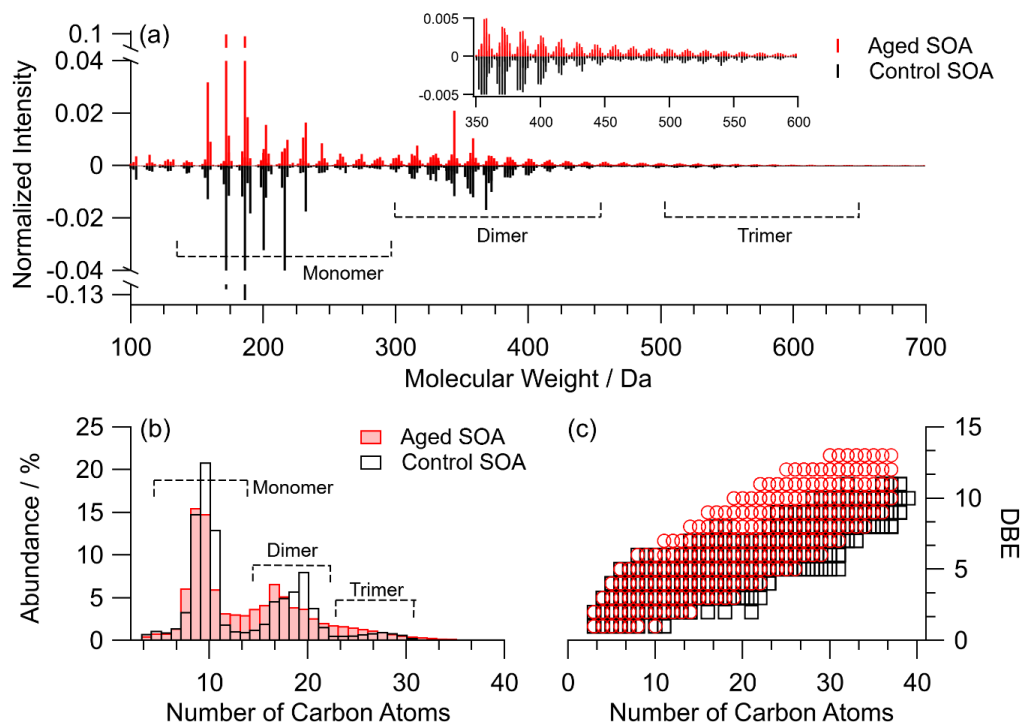


Figure 5. 12: HRMS analysis of α -pinene ozonolysis SOA produced in the flow tube and changes in chemical composition due to aging. Panel (a) shows mass spectra of the aged and control samples. Control sample has well-defined monomer, dimer, and trimer regions that are flattened after aging, as indicated by the boxes. Panel (b) shows the distribution of the number of carbon atoms in assigned compounds that flattened in the aged samples. Panel (c) shows the double bond equivalent (DBE) as a function of the number of carbon atoms per assigned molecule for both aged and control samples. Aged SOA compounds have a higher DBE compared to control samples.

The smoothing of the distribution (Figs. 5.10a,b – 5.12a,b) and the increase in the average molecular weight (Table 5.3) are caused by the condensed-phase photochemical reactions occurring during the aging process. Previous studies have also found a smoother molecular weight distribution after UV-aging of SOA.^{78,79} Tropospheric UV irradiation ($\lambda > 300$ nm) has been shown to efficiently break carbonyl compounds through Norrish type-I and type-II reactions resulting in free radicals.^{80,135,352} The size of the radicals depends on the placement of the carbonyl group within the molecular skeleton. Because of the wide distribution of radical sizes and their secondary reactions, such as radical-radical recombination, they can produce a wider distribution of organic compounds, thus smoothing the distinction between the monomer and dimer compounds that is

present in the control SOA material. The results in Figs. 5.10a,b - 5.12a,b are consistent with a radical-radical recombination mechanism, with compounds unique to aged SOA appearing at higher carbon numbers. The smoother distribution may also be attributed to a Norrish photochemical mechanism,^{78,79,97} followed by the possible formation of carboxylic acid functional groups and subsequent dehydration and esterification reactions.^{79,94,156,353}

The results shown in Figure 5.10 and Table 5.3 further highlight an interesting difference between photolytic studies of organic compounds in SOA samples at low relative humidities versus photolytic studies of SOA in dilute aqueous solutions, where the average molecular weight decreases and both dimers and trimers have been reported to become degraded.^{47,275} While the underlying reason for this is still unknown, the difference could be due to changes in diffusion times of radicals that are produced during the UV exposure. Another possibility is the larger oxygen depletion in studies using SOA particles, compared to photolysis in dilute aqueous solutions. Additional studies are needed to better understand the specifics of the photochemical processes in different phases.

In the previous work (Chapter 4), using similarly prepared SOA material, but using direct infusion instead of liquid chromatography HRMS, an increase in molecular weight after UV-aging was not observed.⁷⁸ The current study is more accurate in measuring relative ion abundances due to chromatographic separation reducing matrix effects that can occur with direct infusion.³⁴⁰⁻³⁴² The current results are consistent with a recent study that observed an increase in average number of carbon atoms, O:C ratio, and DBE after UV-aging of SOA.⁷⁹

5.4.3 Prediction of SOA Viscosity Based on HRMS Data

To link viscosity data (Fig. 5.6) to the molecular composition (Fig. 5.10) the HRMS data were used to predict viscosities, following the approach of DeRieux et al.³⁵⁰ Viscosity as a function of RH was predicted using the method described by DeRieux et al. (2018).³⁵⁰ This method involves predicting the glass transition temperature from molecular composition. Following this approach, the glass transition temperature $T_{g,i}$ for a single compound i is given by:

$$T_{g,i} = (n_C^0 + \ln(n_C))b_C + \ln(n_H)b_H + \ln(n_C) \ln(n_H) b_{CH} + \ln(n_O) b_O + \ln(n_C) \ln(n_O) b_{CO}, \quad (5.3)$$

where n_C , n_H , and n_O are the number of carbon, hydrogen, and oxygen atoms in compound i , respectively. Values of coefficients are 12.13, 10.95, -41.82, 21.61, 118.96, -24.38 for n_C^0 , b_C , b_H , b_{CH} , b_O , and b_{CO} , respectively.

The T_g of the SOA under dry conditions ($T_{g,org}$) was estimated using the Gordon-Taylor equation (eq. 5.4), and assuming a Gordon Taylor constant of 1 for each organic component within the SOA.³⁵⁴

$$T_{g,org} = \sum_i w_i T_{g,i} , \quad (5.4)$$

where w_i is the mass fraction of an organic compound i in the mixture.³⁵⁴ For all HRMS-based viscosity predictions, w_i was calculated using the peak abundances from the HRMS data (I_i) while correcting for the overionization of compounds with higher unsaturation (represented by the $(H:C)_i$ ratio) and molecular weight (M_i) using the method developed by Nguyen et al. (2013) (eq. 5.5).³⁵⁵ Note that assumed the effective limit of detection was assumed to be zero. This is a reasonable approximation, as previous work has demonstrated that limit of detection decreased quickly at higher adjusted mass.³⁵⁵ In these experiments, over 90% of detected compounds have an adjusted mass larger than 250 Da, resulting in a small LOD. For comparison, the T_g of the SOA under dry conditions, not correcting for overionization of compounds, ($T_{g,org,uncorr}$) was also calculated using eq. 5.4, but setting $w_i = I_i$, and is shown in Table 5.3.

$$w_i = \frac{I_i}{adjusted\ mass} = \frac{I_i}{(H:C)_i \times M_i} . \quad (5.5)$$

The $T_{g,org}$ was then used to calculate the corresponding viscosity using modified forms of the Vogel-Tammann-Fulcher (VTF) equation:³⁵⁰

$$\eta(RH, T) = \eta_{\infty} e^{\frac{T_0(RH)D_{frag}}{T-T_0(RH)}} , \quad (5.6)$$

where η_{∞} is the viscosity at infinite temperature (10^{-5} Pa s),^{356,357} D_{frag} is the fragility parameter, and $T_0(RH)$ is the RH-dependent Vogel temperature. Rearranging eq. 5.6 and solving for $T_0(RH)$ yields:

$$T_0(RH) = \frac{\ln\left(\frac{\eta(RH, 292 \text{ K})}{\eta_\infty}\right) * (292 \text{ K})}{D_{\text{frag}} + \ln\left(\frac{\eta(RH, 292 \text{ K})}{\eta_\infty}\right)}. \quad (5.7)$$

The fragility parameter describes the deviation from an ideal Arrhenius behavior of the temperature dependence of viscosity.³⁵⁰ Here, a value of $D_{\text{frag}} = 10$ was assumed based on DeRieux et al.³⁵⁰ and Shiraiwa et al.¹¹⁵ who showed a correlation between D_{frag} and molar mass, with the fragility reaching a lower limit of 10.3 at higher molar masses, starting at $\sim 200 \text{ g mol}^{-1}$ (overlapping with the average molar mass of SOA studied here). It is further assumed that the fragility parameter is independent of RH, as done previously.^{115,350,358,359}

Modifying the VTF equation (eq. 5.6 and 5.7) by assuming the viscosity at infinite temperature to be 10^{-5} Pa s , and the viscosity at the glass transition temperature to be 10^{12} Pa s ³⁵⁷ yields:

$$\log(\eta) = -5 + 0.434 \frac{T_0 D_{\text{frag}}}{T - T_0}, \quad (5.8)$$

$$T_0(RH) = \frac{39.17 T_{g,org}}{D_{\text{frag}} + 39.17}. \quad (5.9)$$

Here, η is the viscosity of the organic mixture, D_{frag} is the fragility constant (assumed to have a value of 10; see above), and T is the temperature that the viscosity measurements were performed (292 K).

Figure 5.13 shows a comparison of the experimentally measured viscosity values under dry conditions (filled circles) and those predicted by the parametrization (open squares). The predicted viscosities for the control SOA samples are 2–3 orders of magnitude higher than the measurements, depending on the SOA type. Nevertheless, a difference in predicted viscosities between control and aged samples is evident with a UV-induced increase in viscosity by 2–3 orders of magnitude. This further confirms that the experimentally observed increases in viscosity is driven by the changes in chemical composition.

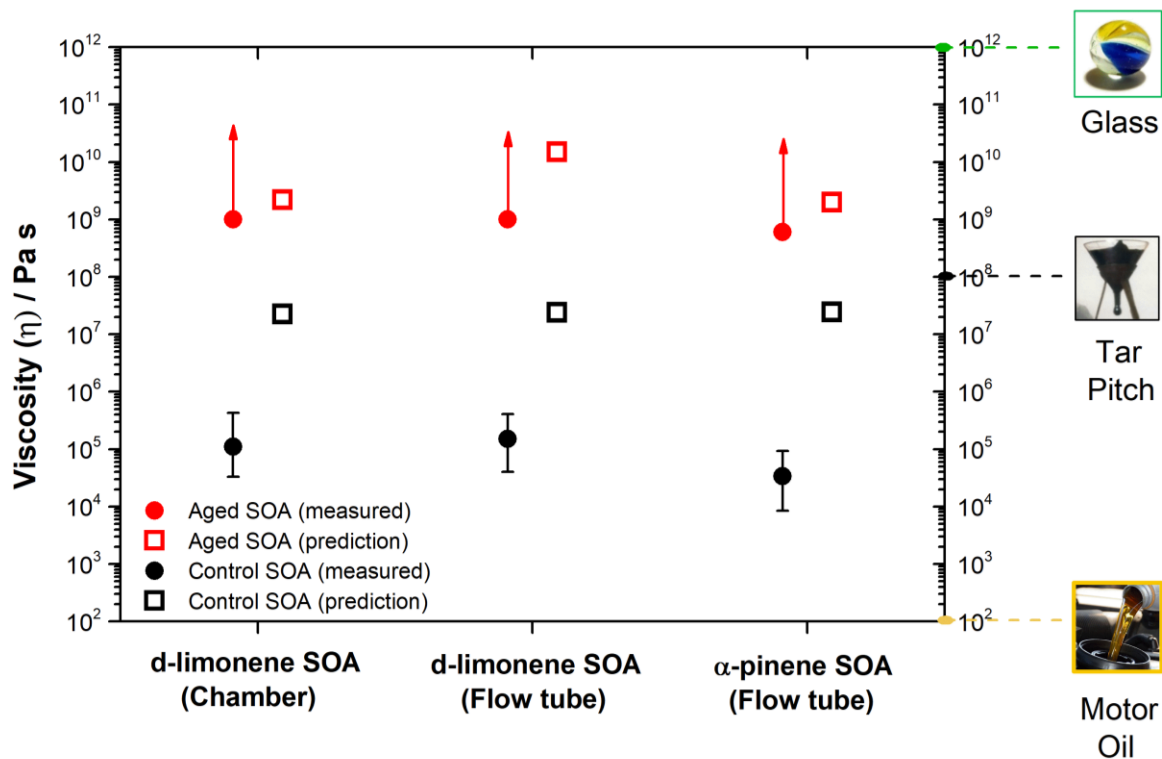


Figure 5. 13: Chemical composition-based viscosity predictions. Measured viscosities of ozonolysis derived control and aged SOA (red and black filled circles) along with predicted viscosities (red and black open squares) under dry conditions. Viscosities were predicted using the approach of DeRieux et al.³⁵⁰ with the high-resolution mass spectrometry composition (Figs. 5.10-5.12) as input. Error bars in the y-direction correspond to the upper and lower limits of viscosities from the poke-flow experiments. Upward arrows indicate lower limits.

The overestimated viscosity predicted by the approach of DeRieux et al.³⁵⁰ could be due to uncertainties in the parameters used within the parametrization. An important limitation that should be noted is that this parameterization does not consider molecular structure or functionality explicitly. The overestimated viscosities could also be due to uncertainties in the assumptions used to calculate relative abundance of each compound in the SOA mixture from the high-resolution mass spectrometry data.

A more definitive metric in comparing the effects of UV-aging on SOA viscosity is the value of T_g itself because its prediction depends on fewer parameters compared to the prediction of the sample viscosity. Predictions of T_g rely solely on the chemical formulas of the organics in the SOA samples. Comparing these values reveals an increase in T_g by 10.2 K, 13.7 K, and 9.8 K for environmental chamber produced d-limonene ozonolysis SOA, flow tube produced d-limonene ozonolysis SOA, and a-pinene ozonolysis SOA, respectively (Table 5.3). Overall, both prediction

metrics show that UV-aging of SOA results in a substantial increase in viscosity and indicate that the experimentally determined increases in viscosity can be attributed to the changes in chemical composition.

5.5 Atmospheric Implications

In the troposphere, the RH often varies from 10% to 100%, and the temperature often varies from approximately 205 K to 300 K.³⁶⁰ To extrapolate the results to other RH values and temperatures, a parameterization was developed to calculate the viscosity of control and aged SOA as a function of both RH and temperature based on the experimental room temperature data. The parameterization is discussed below.

5.5.1 Calculations and Parameterizations for Viscosity and Mixing Times of Organic Molecules within SOA

5.5.1.1 Diffusion Coefficients and Mixing Times of Organic Molecules

Viscosities (η) can be used to calculate diffusion coefficients of the organic molecules (D_{org}) within the SOA, using the (classical) Stokes-Einstein (SE) relation:³⁶¹

$$D_{\text{org}}(RH, T) = \frac{kT}{6\pi\eta(RH, T)R_{\text{diff}}}, \quad (5.10)$$

where k is the Boltzmann constant, T is the absolute temperature in units of Kelvin, and R_{diff} denotes the hydrodynamic radius of the diffusing organic molecule. Here, R_{diff} was estimated to be 0.44 nm and 0.42 nm for UV-aged and control SOA particles, respectively, for SOA derived from d-limonene ozonolysis.¹¹¹ These estimates are based on the average molecular weights of the SOA (270 g mol⁻¹ for aged SOA; 246 g mol⁻¹ for control SOA; see Table 5.3), an assumed material density of 1.3 g cm⁻³,³⁶²⁻³⁶⁴ and assuming spherical geometry for the diffusing organic molecules. Diffusion coefficients estimated using the SE equation have been found to be in reasonable agreement with measured diffusion coefficients of organic molecules, if the radius of the diffusing molecules is equal to or greater than the radius of the molecules making up the (organic) matrix, and if the SOA particle viscosities are between 10⁻³ to 10¹⁰ Pa s.³⁶⁵

The diffusion coefficients were converted to characteristic mixing times, $\tau_{\text{mix,dp,org}}$, using the following equation:³⁶⁶

$$\tau_{\text{mix,dp,org}}(RH, T) = \frac{d_p^2}{4\pi^2 D_{\text{org}}(RH, T)}, \quad (5.11)$$

where d_p is the diameter of the SOA particles. Mixing times denote the characteristic time required for the concentration of the diffusing organic molecules at the center of the aerosol particle to deviate from the thermodynamic equilibrium concentration by less than $1/e$, assuming nonreactive gas-particle partitioning.³⁶⁶ Mixing times for SOA particles having a diameter of 200 nm were calculated, typical for atmospheric SOA,^{28,367,368} and corresponding to accumulation mode particles.¹ The calculated mixing times are shown below.

5.5.1.2 Prediction of SOA Viscosity as a Function of Relative Humidity and Temperature

The particle viscosities as a function of RH can be predicted using a mole-fraction based Arrhenius mixing rule.^{359,369} This approach has previously been applied to experimentally determined viscosities for SOA derived from β -caryophyllene ozonolysis.³¹⁴ Following a similar approach, the mixing rule can be expressed as:³⁷⁰

$$\log(\eta_{\text{org,wet}}) = \chi_{\text{org}} \log(\eta_{\text{org,dry}}) + (1 - \chi_{\text{org}}) \log(\eta_o), \quad (5.12)$$

where $\eta_{\text{org,wet}}$ is the viscosity of the SOA-water mixture, $\eta_{\text{org,dry}}$ is the viscosity of the dry SOA material, free of water and corresponding to the experimental results at 0% RH, η_o is the viscosity of pure water (10^{-3} Pa s at $T = 293$ K),³⁷¹ and χ_{org} denotes the mole-fraction of organics in the SOA-water mixture. The mole-fraction of organics was calculated as:

$$\chi_{\text{org}} = \frac{\frac{w_{\text{org}}}{M_{\text{org}}}}{\frac{w_{\text{org}}}{M_{\text{org}}} + \frac{1 - w_{\text{org}}}{M_{\text{H}_2\text{O}}}}, \quad (5.13)$$

where w_{org} is the weight fraction of the SOA, M_{org} is the average molecular weight of the SOA determined by high resolution mass spectrometry (see Table 5.3).

Values of w_{org} were calculated as:³⁵⁹

$$w_{\text{org}} = \left(1 + \kappa \left(\frac{a_w}{1 - a_w} \right) \right)^{-1}, \quad (5.14)$$

where a_w is the activity of water, and κ is a mass-based hygroscopicity parameter of the SOA material³⁷². Upon fitting eq. 5.12 to the RH-dependent viscosity data, κ values were determined to be 0.025 for both aged and control d-limonene SOA (Fig. 5.14). These κ values are solely used for the parameterization of viscosity, and not to derive physical meaning from them. Parameterized viscosity as a function of RH for aged and control d-limonene SOA produced in an environmental chamber are shown in Fig. 5.14.

In order to extrapolate the RH-dependent, room-temperature viscosity values $\eta(RH, 292\text{ K})$ to other temperatures found in the troposphere $\eta(RH, T)$, the VTF equation was used (eq. 5.6).³⁵⁰

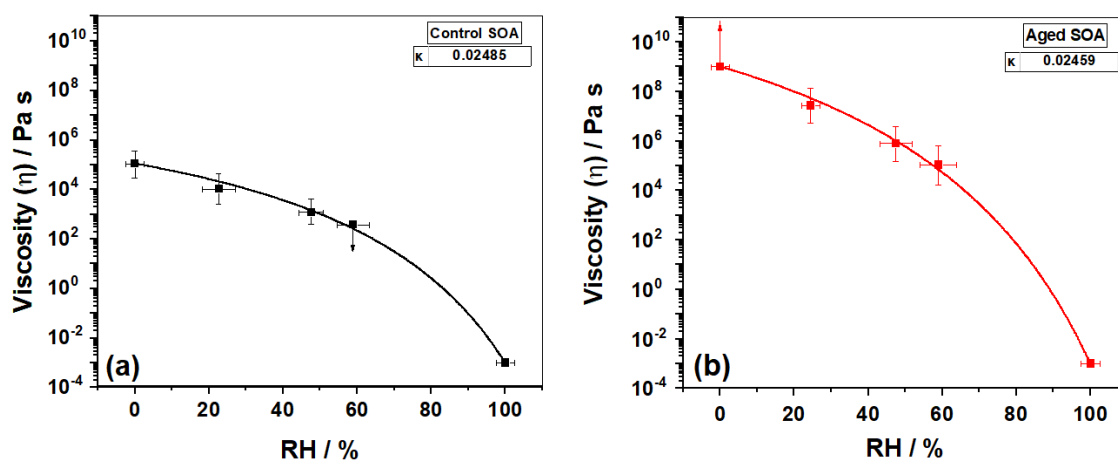


Figure 5. 14: Parametrization of the dependence of viscosity on water activity for (a) control, and (b) aged SOA derived from d-limonene ozonolysis.

5.5.2 Viscosity and Organic Mixing Time Profiles in the Atmosphere

The following data focuses on the results of d-limonene SOA generated in an environmental chamber (Fig. 5.15a,b), but similar results are expected for d-limonene SOA and α -pinene SOA generated in a flow tube. The parameterization (Section 5.5.1.2) as a function of both RH and temperature revealed that the viscosity of SOA particles, especially after UV-aging, can be very high when the temperature is below 285 K and the RH is below 80% (Fig. 5.15a,b). The parameterization also shows that UV-aging will increase viscosity by several orders of magnitude for a range of RH and temperature conditions (Fig. 5.15c).

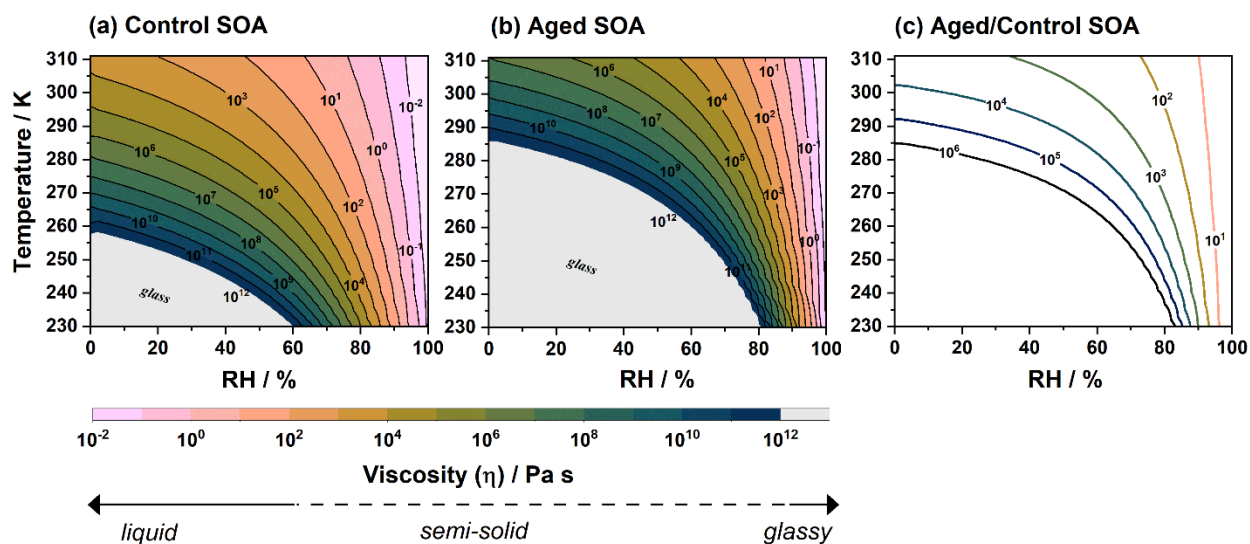


Figure 5. 15: Viscosity of control and aged d-limonene SOA as a function of RH and temperature. Panels (a) and (b) show the viscosity of control and aged d-limonene SOA, respectively. Panel (c) represents the ratio of the viscosity of aged to control d-limonene SOA, demonstrating the increase in viscosity from UV-aging. Grey shaded areas indicate when the viscosity is larger than 10^{12} Pa s, which corresponds to a glass state. Data shown corresponds to SOA produced in an environmental chamber by ozonolysis.

To estimate zonally-averaged SOA particle viscosities in the troposphere, the parameterization for the viscosity of control and aged SOA as a function of RH and temperature (Fig. 5.15a,b) was combined with annual averaged RH and temperatures profiles in the troposphere from a global climate chemistry model for the years 2005–2009.³¹⁹ The results are shown in Fig. 5.16. After UV-aging, viscosities are high ($\eta > 10^6$ Pa s) for most parts of the free troposphere (1–18 km) (Fig. 5.16b). In addition, viscosities are often several orders of magnitude larger for aged SOA compared to control SOA at the same altitude (Fig. 5.16c).

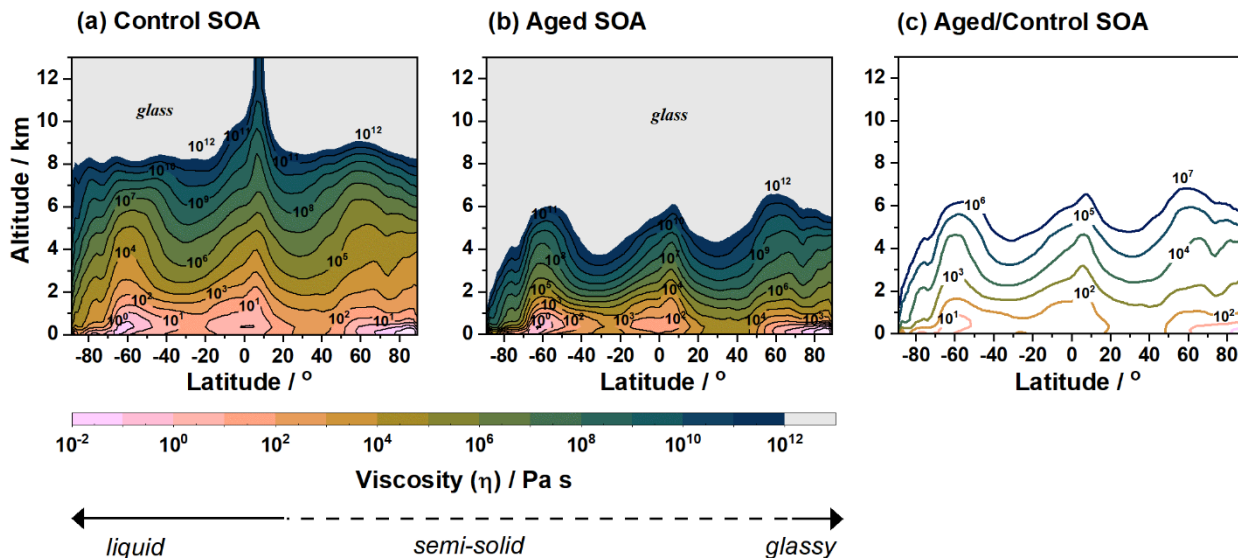


Figure 5. 16: Zonally-averaged SOA viscosity as a function of altitude and latitude in the troposphere. A comparison of the effect of aging by UV-radiation on the zonally-averaged SOA viscosity as a function of altitude and latitude in the troposphere. Panels (a) and (b) represent viscosity for control and aged d-limonene SOA respectively. Panel (c) represents the ratio of viscosity of aged and control d-limonene SOA. Grey shaded areas indicate viscosities were above 10^{12} Pa s, which corresponds to a glass state. Data shown correspond to SOA produced in an environmental chamber by ozonolysis.

The viscosities of SOA can be used to infer the phase state of the SOA particles (Fig. 5.16). SOA will be liquid when the viscosity is below 10^2 Pa s, semi-solid when the viscosity is between 10^2 to 10^{12} Pa s, and glassy when the viscosity is greater than 10^{12} Pa s.¹²⁹ On average, control SOA will mostly be in a liquid phase state below about 2 km, a semi-solid phase state between 2 to 8 km, and a glassy phase state at altitudes above 8 km (Fig. 5.16a). In contrast, after UV-aging, the SOA particles will most often have a liquid phase state at 1 km and below, a semi-solid phase state between 1 to 6 km, and a glassy phase state above 6 km (Fig. 5.16b).

While the role of organic aerosols for ice nucleation is still a matter of ongoing debate,³⁰³ one key conclusion emerging from previous studies^{373–381} is that the phase state of organic aerosol strongly affects their ice nucleation ability, with organic aerosol particles requiring highly viscous or glassy phase states to potentially act as heterogeneous nuclei for ice clouds.^{368,373,375,380} As discussed above, UV-aging leads to a glassy phase state at approximately 2 km lower altitudes in the troposphere (Fig. 5.16). Therefore, if the effects of UV-aging on SOA viscosity observed here

extend to atmospheric SOA, such aging processes could denote unrecognized sources of nuclei for ice clouds, with important implications for Earth's energy budget and climate.

Mixing times of organic molecules within SOA particles are important for predicting the growth, evaporation, and size distribution of SOA, and hence, air pollution and climate. It is often assumed in chemical transport models, which are used to assess air quality and aerosol-climate effects, that the mixing of organic molecules within SOA particles occurs faster than the time step used in the models, which is on the order of 0.5 to 1 h.^{114,368} To estimate mixing times of organic molecules within SOA particles from the viscosity data, the zonally-averaged viscosities shown in Fig. 5.16 were used to estimate mixing times of organic molecules within SOA particles with a diameter of 200 nm (Fig. 5.17). A particle diameter of 200 nm was used to represent typical atmospheric accumulation mode SOA particles.¹ The results, shown in Fig. 5.17, reveal that after UV-aging, mixing times within 200 nm SOA particles can often be larger than 0.5 h for most parts of the free troposphere contrary to the assumptions frequently used in chemical transport models. Furthermore, the mixing times after UV-aging is several orders of magnitude longer than for control SOA (Fig. 5.17c). Hence, UV-aging should be considered when estimating mixing times of organic molecules within SOA and when modelling the growth, evaporation, and size distributions of SOA.

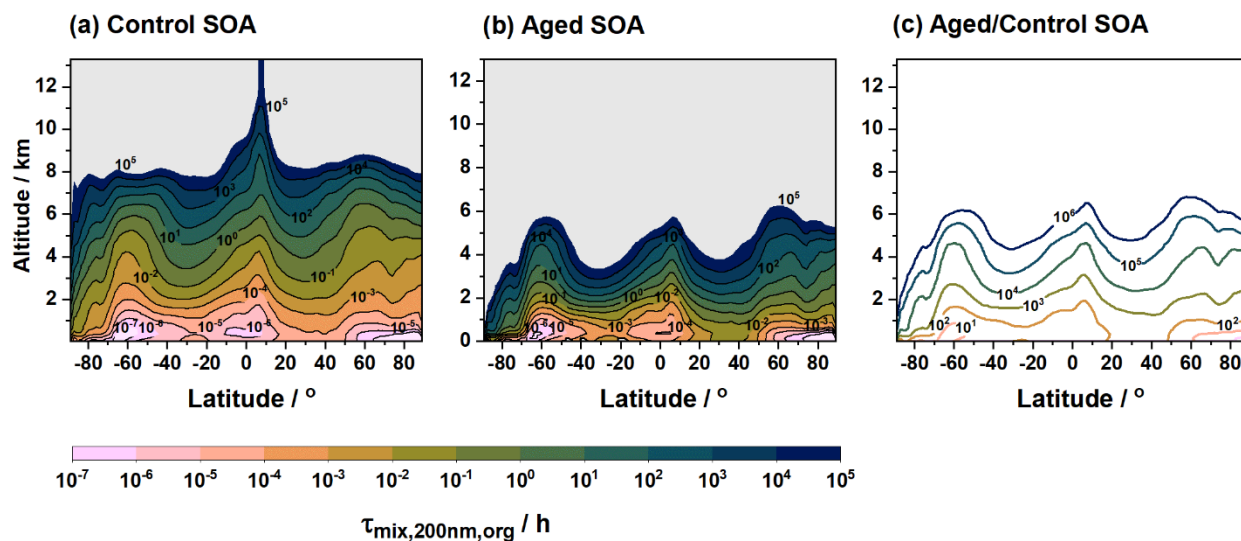


Figure 5. 17: Zonally-averaged mixing times of organic molecules within 200 nm SOA. A comparison of the effect of aging by UV-radiation on the zonally-averaged mixing times of organic molecules within 200 nm SOA. Panels (a) and (b) represent spatial distribution of mixing times of organic molecules for control and aged d-limonene SOA,

respectively. Panel (c) represents the ratio of mixing times of organic molecules of aged and control d-limonene SOA. Grey shaded areas indicate that mixing times of organic molecules were not-determined; since the viscosities used to calculate mixing times were above 10^{12} Pa s, and the Vogel-Tammann-Fulcher equation does not accurately predict viscosities above 10^{12} Pa s. Data shown correspond to SOA produced in an environmental chamber by ozonolysis.

While the findings indicate that UV-aging of d-limonene and α -pinene derived SOA leads to an increase in viscosity, the modelling studies did not account for the change in mass loading with altitude and other atmospheric aging processes.¹¹⁵ In tandem, these processes would lead to even lower viscosities than predicted with this parameterization. Further studies are necessary with SOA generated with lower mass loadings. Additional studies are also needed to determine if these findings apply to other aerosol types, such as SOA from isoprene and aromatic hydrocarbons and aerosols from biomass burning. Also, studies are necessary to determine the effect of UV aging on the ice nucleating ability of SOA.

In summary, this study makes the first attempt to quantify the effect and magnitude of UV-aging on the viscosity of SOA particles. Results show that aging of SOA by exposure to UV-radiation over multiple days can increase viscosity by several orders of magnitude or more. The increased viscosity likely leads to increased abundance of highly viscous, glassy SOA particles that can potentially act as ice nucleation particles and impact ice cloud formation and climate. In addition, these results show that the mixing times of organic molecules within a SOA particle increase significantly after UV-aging, with implications for predicting of growth, evaporation, and the size distribution of SOA. Overall, the results underscore the need to consider the effects of UV-aging when predicting the properties of SOA and their environmental impacts.

Chapter 6: Summary and Future Work

6.1 Research Goals

Secondary organic aerosols (SOA) constitute a significant fraction of particulate matter (PM) and since SOA is not well understood, it remains a large source of uncertainty in climate prediction models. SOA are formed in the atmosphere through the oxidation and subsequent particle phase partitioning of volatile organic compounds (VOCs). VOCs are emitted from various natural and anthropogenic sources. Biogenic terpenes (e.g., isoprene, α -pinene, d-limonene, β -caryophyllene) and anthropogenic compounds (e.g., toluene, naphthalene, diesel, p-xylene) are some of the most studied SOA precursors. SOA chemical composition is extremely complex, which heavily contributes to the uncertainty on the net effect of aerosols on Earth's climate. This uncertainty is enhanced by the fact that SOA can chemically and physically transform as it slowly disperses through the atmosphere, a process known as aging. There are multiple pathways through which aging can occur. An aging pathway of particular interest is condensed-phase photochemical aging driven by ultraviolet (UV) solar radiation. The goals of this research were to investigate the condensed-phase photochemical aging of SOA in order to better understand and predict the effects of SOA on air pollution and climate.

More specifically, the research questions of this dissertation were: 1) How can photosensitized reactions change the chemical composition of SOA? 2) What types of compounds can be oxidized into the particle phase through photosensitized reactions? 3) How fast do these photosensitized reactions occur? 4) What are the photolytic lifetimes of SOA from various precursors? 5) How does relative humidity affect the photodegradation rates of SOA? 6) What are the chemical composition changes due to long term photodegradation? 7) What effect does this composition change have on the physical and chemical properties of SOA?

6.2 Studying the Photosensitized Reactions Occurring in Anthropogenic SOA

Chapters 2 and 3 discussed the photosensitized reactivity occurring in naphthalene derived SOA. Chapter 2 examined the triplet reactivity of select carbonyl compounds that are known photosensitizers that can be found in SOA using nanosecond transient absorption spectroscopy. The SOA arising from the photooxidation of naphthalene was also investigated and was found to exhibit photosensitized chemistry. The lifetime of the transient states decreased with increasing halide concentration, indicating a reaction between the two with quenching rate constants ranging from $10^9 \text{ M}^{-1} \text{ s}^{-1}$ with iodide ions to less than $10^5 \text{ M}^{-1} \text{ s}^{-1}$ with chloride ions. The halide-triplet state

reactions produced the corresponding radical anion (e.g., $I_2^{\bullet-}$, $Cl_2^{\bullet-}$) along with halogenated and more oxidized organic compounds as identified using liquid chromatography and mass spectrometry. Combining the study of these individual and known photosensitizers with those formed in the atmosphere demonstrates that tropospheric photosensitization may involve a large variety of compounds and will introduce previously unconsidered chemical pathways that impact atmospheric multiphase chemistry.

Chapter 3 extended the discussion of photosensitized reactivity by studying the photosensitized uptake of SO_2 (a key pollutant) into naphthalene photooxidation SOA. SOA was produced in an oxidation flow reactor, size selected, and flown into a relative humidity (RH) controlled flow tube surrounded by UV lights. SO_2 was injected into the flow tube where the photosensitized particle growth occurred. The aerosol particles were observed to grow in size and sustain photosensitized processes resulting in the production of particle phase sulfate ($0.2 - 0.3 \mu\text{g m}^{-3} \text{h}^{-1}$). Sulfate was also formed in the dark, probably due to the presence of organic peroxides. The dark and photochemical pathways exhibited different trends with RH, which suggested different contributions from bulk and surface chemistry. Aerosol particles were also observed to grow in size by the photosensitized uptake of d-limonene and β -pinene. As naphthalene and other polycyclic aromatics are important SOA precursors in the urban and suburban areas, these photosensitized reactions are likely to play an important role in sulfate and SOA formation.

A logical next step in this study would be to investigate the photosensitized uptake of VOCs that could take place during biomass burning events. These events produce aerosol plumes that contain photosensitizing aromatic compounds such as nitrocatechol and nitrophenol.^{382,383} Experiments can be done where biomass burning organic aerosol (BBOA) is produced and collected onto a substrate, followed by exposing the BBOA to sunlight and a VOC flow. The VOC concentration could then be monitored during the photosensitizing process in order to calculate an effective uptake coefficient of the VOC to incorporate into models.

6.3 Studying the Photodegradation of SOA

Chapters 4 and 5 discussed the long term photodegradation of SOA and what effect it has on its physicochemical properties. Chapter 4 discussed the long term photodegradation of SOA derived from biogenic and anthropogenic sources. The SOA photodegradation rates were measured using

a quartz crystal microbalance (QCM). In all 305 nm irradiation experiments, the initial mass loss rate was high (corresponding to 1–5% fractional mass loss per hour), but it slowed down after 24 h of irradiation, with a photorecalcitrant fraction of SOA degrading much slower (<1% fractional mass loss per hour). The mass loss rates were observed to increase at a higher relative humidity because volatile photoproducts could diffuse out of SOA faster. Long-term changes in the chemical composition of d-limonene ozonolysis SOA were examined using high-resolution mass spectrometry (HRMS) and revealed a more complex mixture of species after photodegradation compared to the initial SOA. These experiments confirmed that condensed phase photodegradation is an important aging mechanism to consider during long range transport and the degradation profiles reported in this chapter should be used in aerosol mass prediction models.

Chapter 5 expanded on the results from Chapter 4 by attempting to answer the question: what is the viscosity of SOA that has undergone long term photochemical aging? These experiments involved UV aging biogenic derived SOA (i.e., d-limonene and α -pinene SOA) over the equivalent exposure of 6-14 days in the Los Angeles atmosphere followed by measuring the SOA viscosity. Results indicated that the viscosity and characteristic mixing times of organic molecules within a 200 nm diameter SOA particle can be as much as five orders of magnitudes larger for aged SOA compared to unaged SOA throughout most of the troposphere. This increase in viscosity and mixing times was consistent with an increase in average molecular mass and oxygen-to-carbon ratio of the organic molecules constituting the SOA material, as determined by HRMS. The increase in viscosity likely leads to an increased abundance of glassy SOA particles that can act as ice nuclei in the atmosphere. Furthermore, the increase in viscosity and mixing times can impede gas-particle partitioning and heterogeneous chemistry. Overall, results clearly demonstrate that UV-aging needs to be considered when predicting the environmental impacts of SOA. Future studies should be conducted investigating if this increase in viscosity and mixing times due to UV aging is also observed in SOA derived from anthropogenic precursors (e.g., naphthalene, toluene) and BBOA.

Furthermore, it will be important to quantify the mass loss rates of BBOA due to UV degradation. Smoke plumes from biomass burning events can loft aerosols high into the troposphere, where they can spend a long-time aging and can potentially have a significant on the Earth's climate. Some preliminary work has been done on this topic, and it is discussed below.

6.4 Preliminary Results on the UV degradation of Ambient BBOA

BBOA contributes to a substantial amount of PM in the atmosphere and heavily affects the Earth's climate and air pollution. As such, it is important to fully understand photochemical lifetimes of BBOA in the atmosphere as well as its effects on the global VOC budget. During biomass burning events, smoke plumes can loft aerosols high into the troposphere where they can spend a long time interacting with sunlight and undergo photochemical aging. In order to better understand the fates of these aerosols as well as compare results from laboratory generated aerosols to ambient aerosols, experiments were conducted investigating the photodegradation rates of ambient BBOA along with the VOC photoproducts produced during photodegradation.

Ambient BBOA was collected onto QCM crystals using a micro orifice uniform deposit impactor (MOUDI) during the Bond Fire biomass burning event taking place on December 3, 2020 in the Santiago Canyon, California ([33.777°N 117.638°W](#)). Sampling took place at Rowland Hall Irvine, CA (33.644683°N, 117.843770°W) over the course of 24 h with a 23 L min⁻¹ inlet flow. Three samples could be collected during this time (Figure 6.1). The collected material included not only BBOA but also background aerosol but the presence of biomass smoke in the air was obvious from its characteristic odor.



Figure 6. 1: Ambient BBOA sampling on December 3, 2020. Bond fire samples were collected onto three QCM crystals using a MOUDI over the course of 24 h at 23 L min⁻¹ inlet flow.

Photodegradation experiments were conducted using the setup shown in Figure 6.2, similar to the experimental setup in Chapter 4. Briefly, the setup features a proton transfer time of flight mass spectrometer (PTR-MS) and QCM to measure the photoproduct VOC concentrations and mass loss rates, respectively. A 305 nm LED was used as the irradiation source at the same power as previous experiments (Chapters 4 & 5). That is to say, the LED flux (4.1×10^{14} photons $\text{cm}^{-2} \text{s}^{-1}$) over the wavelength range of 290 – 330 nm is roughly equally to the 24 h average flux (8.7×10^{14} photons $\text{cm}^{-2} \text{s}^{-1}$) in the Los Angeles summer over the same wavelength range. The PTR-MS sampled the headspace of the QCM substrate at a flow rate of 80 $\text{cm}^3 \text{min}^{-1}$ (sccm) while a clean air generator supplied 70 sccm of air flow, and the remaining 10 sccm was supplied from the room air through a HEPA filter to remove any particles. This was done to ensure the QCM system was not being pressurized, as this would affect the QCM stability, and to provide a consistent total flow of 80 sccm over the BBOA substrate. Having the PTR-MS sample at 80 sccm with 80 sccm flow from the clean air generator (without the HEPA filter) resulted in pressure fluctuations (observed in QCM data), likely due to small fluctuations in the PTR-MS inlet flow.

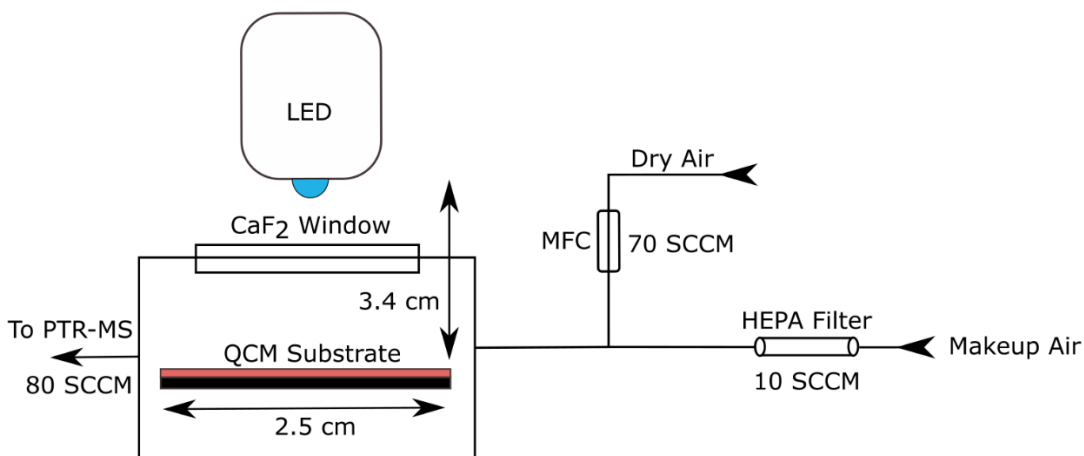


Figure 6. 2: Ambient BBOA photodegradation setup with a 305 nm LED as the irradiation source. The PTR-MS sampled the headspace of the QCM substrate to measure the photoproduct VOC concentrations while the QCM measured the mass change due to photodegradation.

6.4.1 Ambient BBOA Photodegradation Rates from QCM Analysis

Figure 6.3a shows the QCM data fractional mass loss rate (FMLR) of the Bond fire organic aerosol, where 0.05 h^{-1} represents 5% of the mass being lost after 1 h of photodegradation (as discussed in

Chapter 4). The FMLR profile of d-limonene ozonolysis SOA (data from Chapter 4 using the same 305 nm LED) is also plotted for comparison and shows similar degradation rates during the irradiation time period shaded in blue. After the LED was turned off, the Bond fire degradation decayed back to zero. Note that the d-limonene ozonolysis SOA photodegradation continues after the blue shaded region because the d-limonene SOA data are taken from the long-term photodegradation experiments (Chapter 4). Due to the low amount of ambient BBOA collected on each sample, and the fact that calculating FMLR requires normalizing to the collected aerosol mass, the noise in the data is amplified. This is visible when comparing BBOA data with $\sim 63 \mu\text{g}$ of aerosol mass collected with d-limonene ozonolysis data with $\sim 1 \text{ mg}$ of aerosol mass collected. Another experiment was conducted where the LED was turned on and off to ensure that the FMLR was greater than zero during photodegradation and returned back to zero in the absence of UV radiation (Fig. 6.4a). In both figures, the spikes in the data are due to the LED being switched on and off, which causes a sudden shift in the QCM crystal temperature, which subsequently affects the oscillation frequency and calculated FMLR.

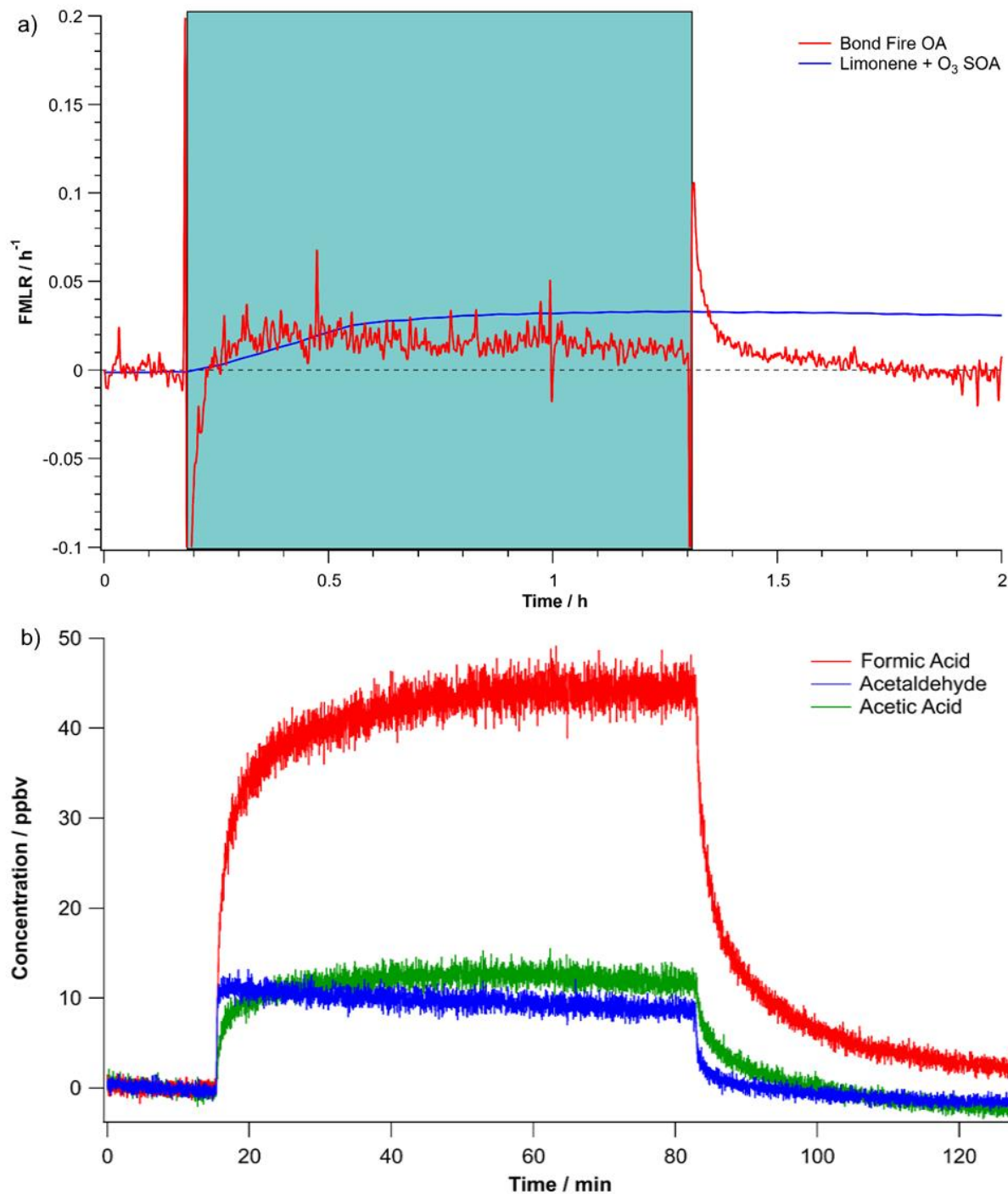


Figure 6. 3: a) QCM data showing the FMLR of Bond Fire Organic Aerosol compared to d-limonene ozonolysis SOA FMLR using the same 305 nm LED. The blue shaded region indicates when the LED was turned on for the Bond fire organic aerosol experiment. The d-limonene ozonolysis SOA photodegradation continues after the blue shaded region because it is data taken from the long-term photodegradation experiments (Chapter 4). b) PTR-MS data showing the

photoproduced VOC concentrations while photodegradation takes places. PTR-MS and QCM data were acquired at the same time.

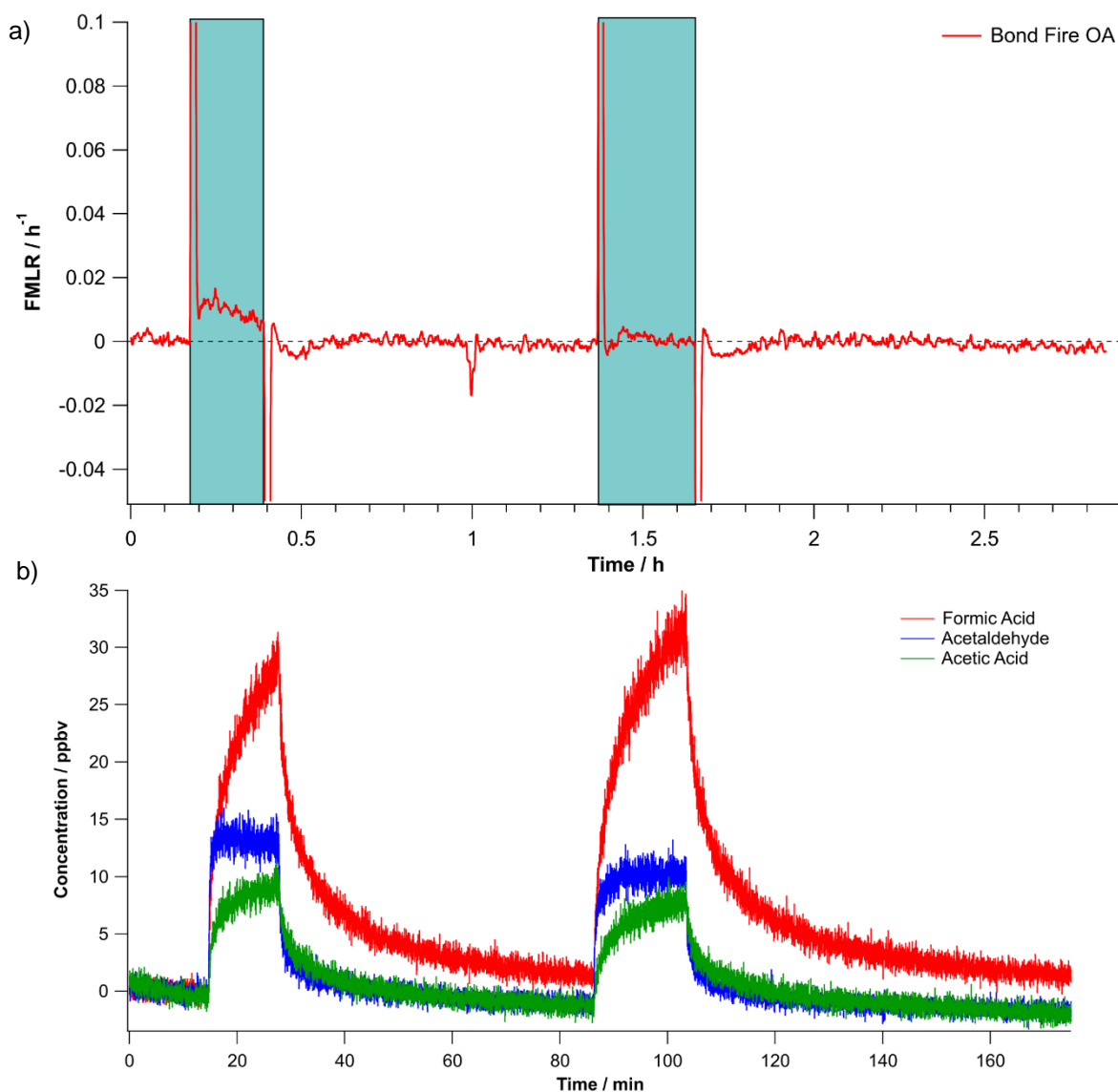


Figure 6. 4: a) Cyclical photodegradation of Bond Fire organic aerosol. FMLR decays back to zero after the irradiation (blue shaded region) ends. b) PTR-MS data showing the photoproduced VOC concentrations while photodegradation takes places. PTR-MS and QCM data were acquired at the same time.

Comparing the three photodegradation periods in Figures 6.3a and 6.4a shows that there is a large variation in the FMLR values from $1.1 \times 10^{-3} \text{ h}^{-1}$ to $2.1 \times 10^{-2} \text{ h}^{-1}$, thus an average value of $1.05 \times 10^{-2} \pm 8 \times 10^{-3} \text{ h}^{-1}$ is tentatively assumed based on the admittedly small sample size. One reason for the large variation in FMLR values is that the QCM samples used in each trial were from

different stages of the MOUDI, where each stage collects aerosols of a different size range. Thus, the particles collected and photodegraded on Stage 7 (Fig. 6.3a) may have a different chemical composition than the photodegraded particles on stage 8 (Fig. 6.4a).

As discussed in Chapter 4, the photodegradation FMLR values of aerosols are not constant and can decay substantially over longer irradiation periods. Thus, a more long-term investigation on the photodegradation rates of BBOA (with more aerosol mass deposited) is needed. This would also show if there is a photorecalictrant fraction present, which may have an increased viscosity with implications for cloud formation and toxic pollutant transport (Chapter 5).

6.4.2 Photoproduct VOC Concentrations from Ambient BBOA Photodegradation

As the QCM monitored change in mass during the photodegradation process, the PTR-MS was sampling the headspace of the QCM substrate to monitor the photoproduct VOC concentrations. This is shown in Figures 6.3b and 6.4b, with formic acid, acetic acid, and formaldehyde being released from the irradiated BBOA. These compounds are expected to be formed as a product of Norrish type photolysis, as discussed in previous studies^{80,81,135} and in Chapters 4 & 5. It is important to note that the VOC concentrations were corrected so that the concentration before the irradiation period was zero, but this correction was small (typically less than 2 ppbv). VOC concentrations increased exponentially after irradiation began until reaching a steady state concentration (Fig. 6.3b). VOC concentrations decayed back to zero after the LED was turned off, indicating that the VOC production is due to BBOA photodegradation. This is more evident in Figure 6.4b where the VOC concentrations follow the cyclical irradiation periods, with VOC production during irradiation, production returning to zero after the LED is turned off, and increasing again once the LED was turned back on. Formic acid concentrations seem to take longer to decay back to zero, likely due to formic acid adsorbing reversibly onto the PTR-MS inlet tubing.

These photoproduct VOC concentrations can be converted into the normalized rate of mass loss (i.e., FMLR) from BBOA material due to a given photoproduct using the equations below. Under the steady state conditions of the experiment, the rate of production of a given VOC, rate (molecules s⁻¹), can be related to the concentration (C) of the VOC in the flow and the flow rate (F) of clean air through the QCM system.

$$rate = F \times C \quad (6.1)$$

Normalizing this rate to the mass of BBOA collected on the substrate, m_{BBOA} (g), and converting from mixing ratio to number concentration, and from molecules to the mass of the photoproduct, $m_{product}$ (g), yields the following equation for the fraction of BBOA mass lost per unit time (FMLR) due to a given photoproduct.

$$FMLR = \frac{1}{m_{BBOA}} \frac{dm_{product}}{dt} = F \times 2.46 \cdot 10^{13} \times \frac{MW}{N_A} \times \frac{X}{m_{BBOA}} \quad (6.2)$$

Here, MW (g mol⁻¹) is the molecular mass of the photoproduct, N_A (molecules mol⁻¹) is Avogadro's number, F is the flow rate of clean air through the QCM system ($F = 1.33$ cm³ s⁻¹), and the numeric factor (2.46×10^{13}) accounts for the conversion from ppmv to molecules cm⁻³ at 1 atm and 25°C. The last term of the equation (X/m_{BBOA}) is the steady state concentration of the VOC, X (ppmv), normalized by the mass of BBOA collected.

Calibration experiments (Fig. 6.5) were done to ensure the PTR-MS VOC measurements were accurate. This was done by creating a standard solution with known VOC concentrations and using the PTR-MS to measure the concentration of the VOCs in the smog chamber after serial injections of the solution through a heated inlet (30°C) into the chamber. This calibration was done in triplicate using the same PTR-MS parameters used in the photodegradation experiments.

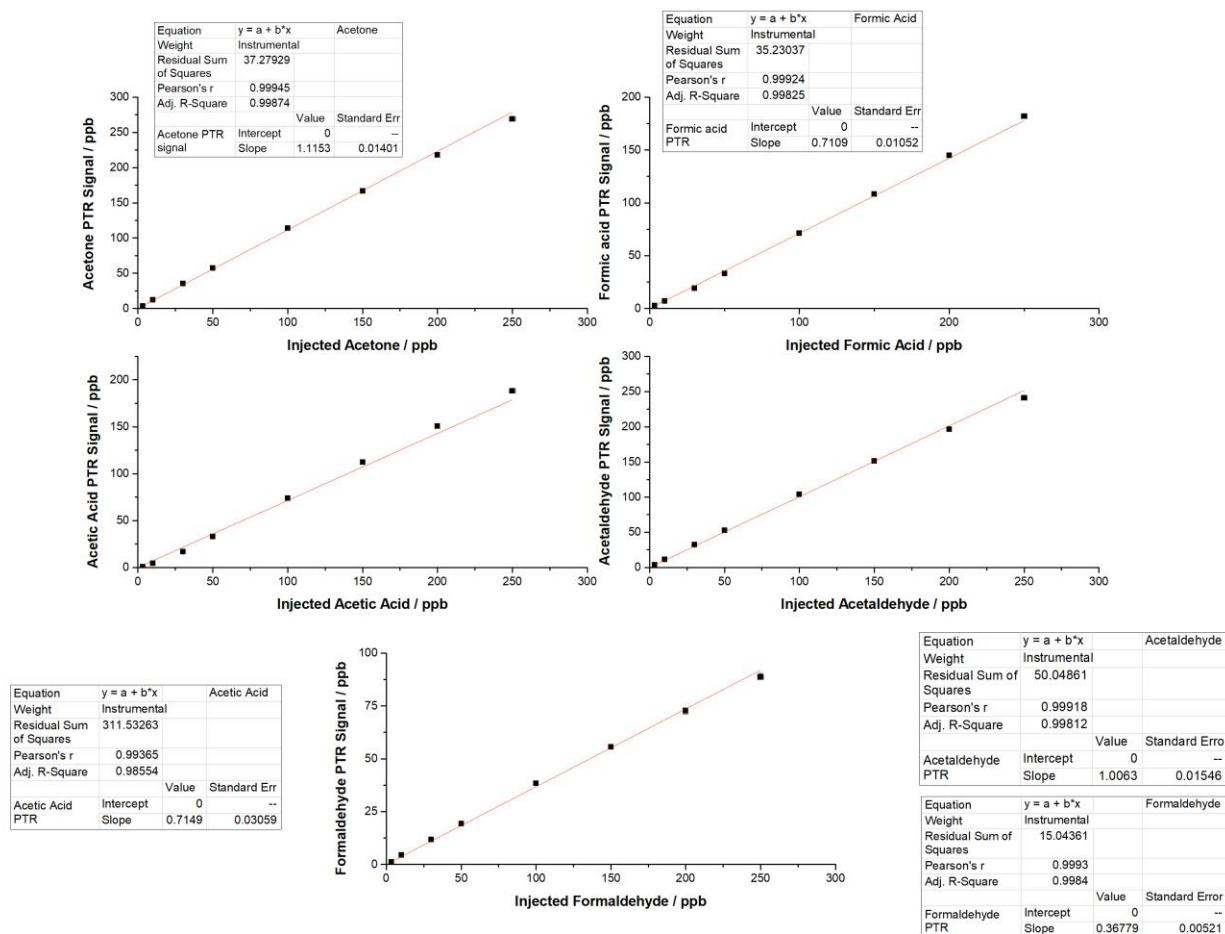


Figure 6. 5: Calibration experiments used to correct the VOC concentration measurements detected by the PTR-MS. Calibration experiments were conducted with serial injection of a prepared standard solution containing acetone, formic acid, acetic acid, acetaldehyde, and formaldehyde into the smog chamber through a heated inlet. Calibrations were done in triplicate with 1σ error bars plotted in both the x and y-axis.

The average FMLR from the combined production of formic acid, acetaldehyde, and acetic acid was calculated to be $9.0 (\pm 0.1) \times 10^{-3} \text{ h}^{-1}$. This is similar to the average FMLR calculated from QCM experiments ($1.05 (\pm 0.8) \times 10^{-2} \text{ h}^{-1}$), indicating that approximately 86% of the total mass loss detected by QCM experiments can be explained by the photoproduction of these three VOCs. These FMLR values correspond to approximately 1% of the BBOA mass being lost after 1 h of irradiation. After 24 h, approximately 20% of the mass is expected to be lost due to photodegradation if this rate is sustained.

Table 6. 1: Calculated FMLR values for specific photoproduct VOCs, a VOC with an average mass of 50 g mol⁻¹, and the summed FMLR from formic acid, acetic acid, and acetaldehyde being produced. Values were calculated based on corrected VOC concentrations and error is expressed as a 95% confidence interval.

Photoproduct	FMLR / h⁻¹ (Fig. 6.3)	FMLR / h⁻¹ (Fig. 6.4)	Average FM. FMLR / h⁻¹
Formic acid	4.18 x 10 ⁻³ ± 6.19 x 10 ⁻⁵	6.27 x 10 ⁻³ ± 9.27 x 10 ⁻⁵	5.23 x 10 ⁻³ ± 5.57 x 10 ⁻⁵
Acetic acid	2.56 x 10 ⁻³ ± 1.10 x 10 ⁻⁴	2.31 x 10 ⁻³ ± 9.88 x 10 ⁻⁵	2.44 x 10 ⁻³ ± 7.39 x 10 ⁻⁵
Acetaldehyde	8.80 x 10 ⁻⁴ ± 1.35 x 10 ⁻⁵	1.78 x 10 ⁻³ ± 2.74 x 10 ⁻⁵	1.33 x 10 ⁻³ ± 1.53 x 10 ⁻⁵
Average VOC (50 g mol⁻¹)	2.56 x 10 ⁻³ ± 3.82 x 10 ⁻⁵	3.59 x 10 ⁻³ ± 4.46 x 10 ⁻⁵	3.08 x 10 ⁻³ ± 2.94 x 10 ⁻⁵
Sum (Formic acid + acetic acid + acetaldehyde)	7.63 x 10 ⁻³ ± 1.27 x 10 ⁻⁴	1.04 x 10 ⁻² ± 1.38 x 10 ⁻⁴	9.02 x 10 ⁻³ ± 9.38 x 10 ⁻⁵

These FMLR values are high and warrant further investigation, as these results are based on an admittedly small number of samples. More experiments are necessary to make more conclusive remarks on the photodegradation rates and VOC concentrations. Nonetheless, these results indicate that ambient BBOA photodegrade quite readily and can be an important source of VOCs into the atmosphere.

6.4.3 Composition of Ambient BBOA

The chemical composition of the ambient BBOA was also examined using Ultra Performance Liquid Chromatography (UPLC) coupled with a Thermo Q Exactive Plus orbitrap mass spectrometer equipped with an electrospray ionization (ESI) source (UPLC-ESI-HRMS). The

UPLC-ESI-HRMS was operated in negative ion mode with a mass resolving power of $\sim 10^5$ at m/z 200, and a spray voltage of 2.5 kV. Details of this instrument are discussed in Chapter 1, Section 1.6.4. The HPLC-HRMS sample was prepared by extracting one of the collected samples into a 1:1 (v/v) mixture of acetonitrile (Sigma Aldrich, purity $\geq 99.9\%$) and water (Sigma-Aldrich, HPLC grade), evaporating the solvent using a rotary evaporator, and then redissolving the analyte into the same solvent achieving a final concentration of $200 \mu\text{g ml}^{-1}$. The sample was run in triplicate through the instrument and only HRMS peaks that appeared in all three trials were used for molecular assignment. Sections of the ion chromatogram with strong analyte intensity were integrated. In addition to the samples, a solvent blank was prepared following the same procedure above, but using a control substrate without analyte.

HRMS peaks were assigned molecular formulas following previous work.^{73,78} HRMS-peak positions and relative abundances were extracted using the Decon2LS software package³⁴³ and peaks containing ^{13}C isotopes were removed. All HRMS-peaks were assigned to the formulas $\text{C}_{1-40}\text{H}_{0-80}\text{O}_{0-35}\text{N}_{0-3}\text{S}_{0-1}$ with an accuracy of $\pm 0.001 m/z$ units while constraining the assignments to H/C of 0.30–2.25 and O/C of 0.00–2.30. The assigned ion formulas were corrected for the ionization mechanism. The assumed ionization mechanism was deprotonation of the molecular compounds resulting in $[\text{M}-\text{H}]^-$ for negative ions. All the HRMS results are reported as formulas of neutral SOA compounds (Fig. 6.6).

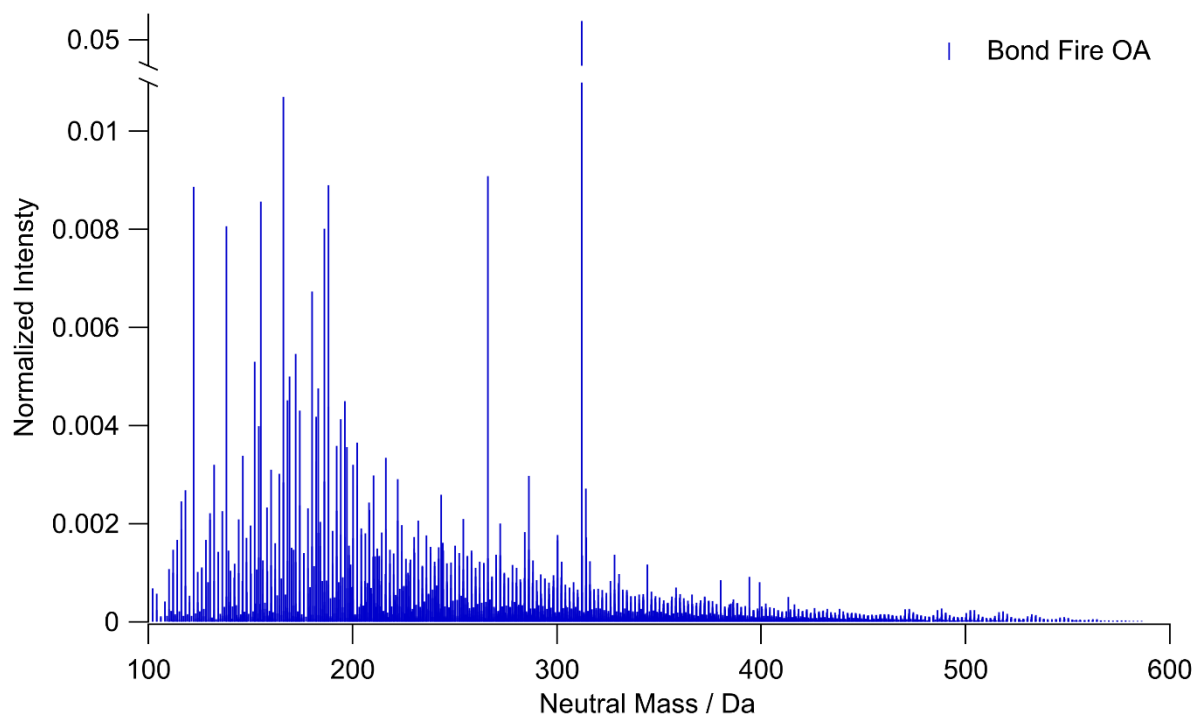


Figure 6. 6: Mass spectrum of ambient BBOA collected during the bond fire. The y-axis shows the intensity of the peaks normalized to the sum of all assigned peaks.

Formulas of the most abundant compounds in the ambient sample are listed in Table 6.2, and include known tracers of a biomass burning events such as nitro-catechol ($C_6H_5O_4N$) (0.86% of the total intensity). In fact, nitro-catechol was the sixth largest detected compound out of the 3316 total assigned compounds. Although lower intensity, an assigned peak corresponding the formula of the well-known tracer, levoglucosan, was also found in the sample (0.16% of the total intensity). The prominent abundance of these biomass burning tracers indicates that the ambient sampling conducted at least partially captured the biomass burning plume.

Table 6. 2: Top 20 most abundant compounds present in ambient BBOA collected during the Bond fire. Peak intensities are expressed a percentage of the total sample intensity (i.e., with the sum of all peak abundances set to 100%).

Neutral Formula	Neutral Mass / Da	Normalized Intensity / %
$C_{17}H_{28}O_3S_1$	311.167	5.4
$C_8H_6O_4$	165.019	1.1
$C_{12}H_{26}O_4S_1$	265.148	0.91
$C_9H_{16}O_4$	187.098	0.89

C ₇ H ₆ O ₂	121.030	0.89
C ₆ H ₅ O ₄ N	154.015	0.86
C ₇ H ₆ O ₃	137.024	0.81
C ₉ H ₁₄ O ₄	185.082	0.80
C ₉ H ₈ O ₄	179.035	0.67
C ₈ H ₁₂ O ₄	171.066	0.55
C ₈ H ₈ O ₃	151.040	0.53
C ₇ H ₇ O ₄ N	168.030	0.50
C ₇ H ₅ O ₅ N	182.010	0.48
C ₈ H ₈ O ₄	167.035	0.45
C ₉ H ₈ O ₅	195.030	0.45
C ₈ H ₁₂ O ₅	187.061	0.44
C ₈ H ₁₄ O ₄	173.082	0.43
C ₈ H ₆ O ₅	181.014	0.42
C ₁₀ H ₁₀ O ₄	193.051	0.41
C ₇ H ₆ O ₄	153.019	0.40

6.4.4 Conclusions

These preliminary experiments show that the photodegradation and subsequent VOC production rates of ambient BBOA particles are worth investigating. The photodegradation rates are quite high at 1% h⁻¹ with large amounts of VOCs being produced in the process. More studies are needed to investigate the long term photodegradation rates of ambient BBOA, as they can change quite substantially over longer irradiation periods (see Chapter 4). The VOC production rates here are also high, particularly for formic acid with a production rate constant of $5.23 \times 10^{-3} \pm 5.57 \times 10^{-5}$ h⁻¹. A back of the envelope calculation, assuming the BBOA concentration is equal to that assumed of SOA (0.95 Tg),³⁰ these preliminary results suggest that formic acid would be produced at a rate of 44 Tg yr⁻¹. This accounts for approximately half of the underpredicted formic acid emissions in the atmosphere, which are underpredicted by 90 Tg yr⁻¹ out of total yearly emissions of 120 Tg yr⁻¹.³⁸⁴ More experiments with a larger sample size with ambient BBOA samples from different regions in order to better constrain the photoproducted formic acid formation rate and confirm if it is indeed this high.

References

1. Finlayson-Pitts, B. J. & Pitts, J. N. *Chemistry of the Upper and Lower Atmosphere: Theory, Experiments, and Applications*. (Academic Press, 2000).
2. Peixoto, J. P. & Oort, A. H. Physics of climate. *Reviews of Modern Physics* **56**, 365–429 (1984).
3. Bates, D. R. & Nicolet, M. The photochemistry of atmospheric water vapor. *Journal of Geophysical Research* **55**, 301–327 (1950).
4. Haagen-Smit, A. J. Chemistry and Physiology of Los Angeles Smog. *Industrial & Engineering Chemistry* **44**, 1342–1346 (1952).
5. Stephens, E. R., Hanst, P. L., Doerr, R. C. & Scott, W. E. Reactions of Nitrogen Dioxide and Organic Compounds in Air. *Industrial and Engineering Chemistry* **48**, 1498–1504 (1956).
6. Montalti, M., Credi, A., Prodi, L. & Gandolfi, M. T. Handbook of Photochemistry. *Handbook of Photochemistry* (2006) doi:10.1201/9781420015195.
7. Okabe, H. *Photochemistry of small molecules*. vol. 431 (Wiley, 1978).
8. INN, E. C. Y. & TANAKA, Y. Ozone Absorption Coefficients in the Visible and Ultraviolet Regions. in *Ozone Chemistry and Technology* 263–268 (1959). doi:10.1021/ba-1959-0021.ch037.
9. Fagnoni, M. Modern Molecular Photochemistry of Organic Molecules. By Nicholas J. Turro, V. Ramamurthy and Juan C. Scaiano. *Angewandte Chemie International Edition* **49**, 6709–6710 (2010).
10. Philen, D. L., Watson, R. T. & Davis, D. D. A quantum yield determination of O(1D) production from ozone via laser flash photolysis. *The Journal of Chemical Physics* **67**, 3316 (2008).
11. Zafiriou, O. C. & Bonneau, R. Wavelength dependent quantum yield of OH radical formation from photolysis of nitrite ion in water. *Photochemistry and Photobiology* **45**, 723–727 (1987).
12. Abbatt, J. P. D. & Wang, C. The atmospheric chemistry of indoor environments. *Environmental Science: Processes and Impacts* **22**, 25–48 (2020).
13. Pöschl, U. & Shiraiwa, M. Multiphase Chemistry at the Atmosphere-Biosphere Interface Influencing Climate and Public Health in the Anthropocene. *Chemical Reviews* vol. 115 4440–4475 (2015).
14. Molina, M. J., Tso, T. L., Molina, L. T. & Wang, F. C. Y. Antarctic stratospheric chemistry of chlorine nitrate, hydrogen chloride, and ice: Release of active chlorine. *Science (1979)* **238**, 1253–1257 (1987).
15. Galloway, M. M. *et al.* Glyoxal uptake on ammonium sulphate seed aerosol: Reaction products and reversibility of uptake under dark and irradiated conditions. *Atmospheric Chemistry and Physics* **9**, 3331–3345 (2009).
16. Chang, W. L. *et al.* Heterogeneous atmospheric chemistry, ambient measurements, and model calculations of N₂O₅: A review. *Aerosol Science and Technology* **45**, 665–695 (2011).

17. Thornton, J. A., Braban, C. F. & Abbatt, J. P. D. N₂O₅ hydrolysis on sub-micron organic aerosols: the effect of relative humidity, particle phase, and particle size. *Physical Chemistry Chemical Physics* **5**, 4593 (2003).
18. Hallquist, M. *et al.* The formation, properties and impact of secondary organic aerosol: Current and emerging issues. *Atmospheric Chemistry and Physics* **9**, 5155–5236 (2009).
19. Pöschl, U. Atmospheric aerosols: Composition, transformation, climate and health effects. *Angewandte Chemie - International Edition* vol. 44 7520–7540 (2005).
20. George, C., Ammann, M., D’Anna, B., Donaldson, D. J. & Nizkorodov, S. A. Heterogeneous Photochemistry in the Atmosphere. *Chemical Reviews* **115**, 4218–4258 (2015).
21. Pye, H. O. T. *et al.* On the implications of aerosol liquid water and phase separation for organic aerosol mass. *Atmospheric Chemistry and Physics* **17**, 343–369 (2017).
22. Kanakidou, M. *et al.* Organic aerosol and global climate modelling: A review. *Atmospheric Chemistry and Physics* **5**, 1053–1123 (2005).
23. Lee Ng, N. *et al.* Nitrate radicals and biogenic volatile organic compounds: Oxidation, mechanisms, and organic aerosol. *Atmospheric Chemistry and Physics* **17**, 2103–2162 (2017).
24. Lenner, M. Nitrogen dioxide in exhaust emissions from motor vehicles. *Atmospheric Environment (1967)* **21**, 37–43 (1987).
25. Song, C., Na, K. & Cocker, D. R. Impact of the hydrocarbon to NO_x ratio on secondary organic aerosol formation. *Environmental Science and Technology* **39**, 3143–3149 (2005).
26. Zhang, J., Huff Hartz, K. E., Pandis, S. N. & Donahue, N. M. Secondary organic aerosol formation from limonene Ozonolysis: Homogeneous and heterogeneous influences as a function of NO_x. *Journal of Physical Chemistry A* **110**, 11053–11063 (2006).
27. Sato, K., Hatakeyama, S. & Imamura, T. Secondary organic aerosol formation during the photooxidation of toluene: NO_x dependence of chemical composition. *Journal of Physical Chemistry A* **111**, 9796–9808 (2007).
28. Riipinen, I. *et al.* Organic condensation: A vital link connecting aerosol formation to cloud condensation nuclei (CCN) concentrations. *Atmospheric Chemistry and Physics* **11**, 3865–3878 (2011).
29. Pankow, J. F. An absorption model of the gas/aerosol partitioning involved in the formation of secondary organic aerosol. *Atmospheric Environment* **28**, 189–193 (1994).
30. Hodzic, A. *et al.* Rethinking the global secondary organic aerosol (SOA) budget: Stronger production, faster removal, shorter lifetime. *Atmospheric Chemistry and Physics* **16**, 7917–7941 (2016).
31. Donahue, N. M., Robinson, A. L., Stanier, C. O. & Pandis, S. N. Coupled partitioning, dilution, and chemical aging of semivolatile organics. *Environmental Science and Technology* **40**, 2635–2643 (2006).
32. Robinson, A. L. *et al.* Rethinking organic aerosols: Semivolatile emissions and photochemical aging. *Science (1979)* **315**, 1259–1262 (2007).

33. Brook, R. D. *et al.* Particulate matter air pollution and cardiovascular disease: An update to the scientific statement from the American Heart Association. *Circulation* **121**, 2331–2378 (2010).
34. Pope, C. A. *et al.* Lung cancer, cardiopulmonary mortality, and long-term exposure to fine particulate air pollution. *J Am Med Assoc* **287**, 1132–1141 (2002).
35. Pope, C. A., Ezzati, M. & Dockery, D. W. Fine-particulate air pollution and life expectancy in the United States. *New England Journal of Medicine* **360**, 376–386 (2009).
36. Shiraiwa, M. *et al.* Aerosol Health Effects from Molecular to Global Scales. *Environmental Science and Technology* vol. 51 13545–13567 (2017).
37. Dockery, D. W. *et al.* An Association between Air Pollution and Mortality in Six U.S. Cities. *New England Journal of Medicine* **329**, 1753–1759 (1993).
38. Sisler, J. F. & Malm, W. C. The relative importance of soluble aerosols to spatial and seasonal trends of impaired visibility in the United States. *Atmospheric Environment* **28**, 851–862 (1994).
39. Charlson, R. J. *et al.* Climate forcing by anthropogenic aerosols. *Science (1979)* **255**, 423–430 (1992).
40. Kaufman, Y. J. & Fraser, R. S. The effect of smoke particles on clouds and climate forcing. *Science (1979)* **277**, 1636–1639 (1997).
41. Bond, T. C. & Sun, K. Can reducing black carbon emissions counteract global warming? *Environmental Science and Technology* **39**, 5921–5926 (2005).
42. Ramanathan, V. *et al.* Warming trends in Asia amplified by brown cloud solar absorption. *Nature* **448**, 575–578 (2007).
43. Haywood, J. & Boucher, O. Estimates of the direct and indirect radiative forcing due to tropospheric aerosols: A review. *Reviews of Geophysics* **38**, 513–543 (2000).
44. IPCC *et al.* *AR5 Climate Change 2013: The Physical Science Basis — IPCC*. (2013).
45. Pilinis, C., Pandis, S. N. & Seinfeld, J. H. Sensitivity of direct climate forcing by atmospheric aerosols to aerosol size and composition. *Journal of Geophysical Research* **100**, 18739–18754 (1995).
46. Walser, M. L., Desyaterik, Y., Laskin, J., Laskin, A. & Nizkorodov, S. A. High-resolution mass spectrometric analysis of secondary organic aerosol produced by ozonation of limonene. *Physical Chemistry Chemical Physics* **10**, 1009–1022 (2008).
47. Romonosky, D. E., Laskin, A., Laskin, J. & Nizkorodov, S. A. High-resolution mass spectrometry and molecular characterization of aqueous photochemistry products of common types of secondary organic aerosols. *Journal of Physical Chemistry A* **119**, 2594–2606 (2015).
48. Kourtchev, I. *et al.* Molecular composition of biogenic secondary organic aerosols using ultrahigh-resolution mass spectrometry: Comparing laboratory and field studies. *Atmospheric Chemistry and Physics* **14**, 2155–2167 (2014).
49. Nozière, B. *et al.* The Molecular Identification of Organic Compounds in the Atmosphere: State of the Art and Challenges. *Chemical Reviews* **115**, 3919–3983 (2015).

50. Forstner, H. J. L., Flagan, R. C. & Seinfeld, J. H. Secondary organic aerosol from the photooxidation of aromatic hydrocarbons: Molecular composition. *Environmental Science and Technology* **31**, 1345–1358 (1997).
51. Hatfield, M. L. & Huff Hartz, K. E. Secondary organic aerosol from biogenic volatile organic compound mixtures. *Atmospheric Environment* **45**, 2211–2219 (2011).
52. Ahlberg, E. *et al.* Secondary organic aerosol from VOC mixtures in an oxidation flow reactor. *Atmospheric Environment* **161**, 210–220 (2017).
53. Smith, N. R. *et al.* Viscosity and liquid–liquid phase separation in healthy and stressed plant SOA. *Environmental Science: Atmospheres* **1**, 140–153 (2021).
54. Henze, D. K. *et al.* Global modeling of secondary organic aerosol formation from aromatic hydrocarbons: high- vs. low-yield pathways. *Atmospheric Chemistry and Physics* **8**, 2405–2420 (2008).
55. Ervens, B. *et al.* Secondary organic aerosol yields from cloud-processing of isoprene oxidation products. *Geophysical Research Letters* **35**, 2816 (2008).
56. Zhang, Y. *et al.* Limited formation of isoprene epoxydiols-derived secondary organic aerosol under NO_x-rich environments in Eastern China. *Geophysical Research Letters* **44**, 2035–2043 (2017).
57. D'Ambro, E. L. *et al.* Molecular composition and volatility of isoprene photochemical oxidation secondary organic aerosol under low- and high-NO_x conditions. *Atmospheric Chemistry and Physics* **17**, 159–174 (2017).
58. Hoffmann, T. *et al.* Formation of organic aerosols from the oxidation of biogenic hydrocarbons. *Journal of Atmospheric Chemistry* **26**, 189–222 (1997).
59. Faust, J. A., Wong, J. P. S., Lee, A. K. Y. & Abbatt, J. P. D. Role of Aerosol Liquid Water in Secondary Organic Aerosol Formation from Volatile Organic Compounds. *Environmental Science & Technology* **51**, 1405–1413 (2017).
60. Lambe, A. T. *et al.* Effect of oxidant concentration, exposure time, and seed particles on secondary organic aerosol chemical composition and yield. *Atmospheric Chemistry and Physics* **15**, 3063–3075 (2015).
61. Gao, S. *et al.* Particle phase acidity and oligomer formation in secondary organic aerosol. *Environmental Science and Technology* **38**, 6582–6589 (2004).
62. Iinuma, Y., Böge, O., Gnauk, T. & Herrmann, H. Aerosol-chamber study of the α -pinene/O₃ reaction: Influence of particle acidity on aerosol yields and products. *Atmospheric Environment* **38**, 761–773 (2004).
63. Balkanski, Y. J., Jacob, D. J., Gardner, G. M., Graustein, W. C. & Turekian, K. K. Transport and residence times of tropospheric aerosols inferred from a global three-dimensional simulation of 210Pb. *Journal of Geophysical Research* **98**, (1993).
64. Jaenicke, R. Atmospheric aerosols and global climate. *Journal of Aerosol Science* vol. 11 577–588 (1980).

65. Brönnimann, S. *Climate of the Free Troposphere and Mountain Peaks. Oxford Research Encyclopedia of Climate Science* (Oxford University Press, 2020). doi:10.1093/acrefore/9780190228620.013.755.
66. Tsigaridis, K. & Kanakidou, M. Global modelling of secondary organic aerosol in the troposphere: A sensitivity analysis. *Atmospheric Chemistry and Physics* **3**, 1849–1869 (2003).
67. George, I. J. & Abbatt, J. P. D. Heterogeneous oxidation of atmospheric aerosol particles by gas-phase radicals. *Nature Chemistry* **2**, 713–722 (2010).
68. Kessler, S. H. *et al.* OH-initiated heterogeneous aging of highly oxidized organic aerosol. *Journal of Physical Chemistry A* **116**, 6358–6365 (2012).
69. George, I. J. & Abbatt, J. P. D. Chemical evolution of secondary organic aerosol from OH-initiated heterogeneous oxidation. *Atmospheric Chemistry and Physics* **10**, 5551–5563 (2010).
70. Aljawhary, D., Zhao, R., Lee, A. K. Y., Wang, C. & Abbatt, J. P. D. Kinetics, Mechanism, and Secondary Organic Aerosol Yield of Aqueous Phase Photo-oxidation of α -Pinene Oxidation Products. *Journal of Physical Chemistry A* **120**, 1395–1407 (2016).
71. Hems, R. F. & Abbatt, J. P. D. Aqueous Phase Photo-oxidation of Brown Carbon Nitrophenols: Reaction Kinetics, Mechanism, and Evolution of Light Absorption. *ACS Earth and Space Chemistry* **2**, 225–234 (2018).
72. Romonosky, D. E. *et al.* Aqueous Photochemistry of Secondary Organic Aerosol of α -Pinene and α -Humulene Oxidized with Ozone, Hydroxyl Radical, and Nitrate Radical. *Journal of Physical Chemistry A* **121**, 1298–1309 (2017).
73. Klodt, A. L. *et al.* Aqueous Photochemistry of Secondary Organic Aerosol of α -Pinene and α -Humulene in the Presence of Hydrogen Peroxide or Inorganic Salts. *ACS Earth and Space Chemistry* **3**, 2736–2746 (2019).
74. Malecha, K. T. & Nizkorodov, S. A. Feasibility of Photosensitized Reactions with Secondary Organic Aerosol Particles in the Presence of Volatile Organic Compounds. *Journal of Physical Chemistry A* **121**, 4961–4967 (2017).
75. Monge, M. E. *et al.* Alternative pathway for atmospheric particles growth. *Proc Natl Acad Sci U S A* **109**, 6840–6844 (2012).
76. Wang, X. *et al.* Atmospheric Photosensitization: A New Pathway for Sulfate Formation. *Environmental Science and Technology* **54**, 3114–3120 (2020).
77. Wang, X. *et al.* Naphthalene-derived secondary organic aerosols interfacial photosensitizing properties. *Geophysical Research Letters* e2021GL093465 (2021) doi:10.1029/2021gl093465.
78. Baboomian, V. J., Gu, Y. & Nizkorodov, S. A. Photodegradation of Secondary Organic Aerosols by Long-Term Exposure to Solar Actinic Radiation. *ACS Earth and Space Chemistry* **4**, 1078–1089 (2020).
79. Walhout, E. Q., Yu, H., Thrasher, C., Shusterman, J. M. & O'Brien, R. E. Effects of Photolysis on the Chemical and Optical Properties of Secondary Organic Material Over Extended Time Scales. *ACS Earth and Space Chemistry* **3**, 1226–1236 (2019).

80. Malecha, K. T. & Nizkorodov, S. A. Photodegradation of Secondary Organic Aerosol Particles as a Source of Small, Oxygenated Volatile Organic Compounds. *Environmental Science and Technology* **50**, 9990–9997 (2016).
81. Malecha, K. T., Cai, Z. & Nizkorodov, S. A. Photodegradation of Secondary Organic Aerosol Material Quantified with a Quartz Crystal Microbalance. *Environmental Science and Technology Letters* **5**, 366–371 (2018).
82. Arroyo, P. C., Malecha, K. T., Ammann, M. & Nizkorodov, S. A. Influence of humidity and iron(III) on photodegradation of atmospheric secondary organic aerosol particles. *Physical Chemistry Chemical Physics* **20**, 30021–30031 (2018).
83. Lignell, H. *et al.* Experimental and theoretical study of aqueous cis-pinonic acid photolysis. *Journal of Physical Chemistry A* **117**, 12930–12945 (2013).
84. Rudich, Y., Donahue, N. M. & Mentel, T. F. Aging of Organic Aerosol: Bridging the Gap Between Laboratory and Field Studies. *Annual Review of Physical Chemistry* **58**, 321–352 (2007).
85. Henry, K. M. & Donahue, N. M. Photochemical aging of α -pinene secondary organic aerosol: Effects of OH radical sources and photolysis. *Journal of Physical Chemistry A* **116**, 5932–5940 (2012).
86. Hildebrandt Ruiz, L. *et al.* Aging of secondary organic aerosol from small aromatic VOCs: changes in chemical composition, mass yield, volatility and hygroscopicity. *Atmospheric Chemistry and Physics Discussions* **14**, 31441–31481 (2014).
87. Riva, M., Robinson, E. S., Perraudin, E., Donahue, N. M. & Villenave, E. Photochemical aging of secondary organic aerosols generated from the photooxidation of polycyclic aromatic hydrocarbons in the gas-phase. *Environmental Science and Technology* **49**, 5407–5416 (2015).
88. Jang, M., Czoschke, N. M., Lee, S. & Kamens, R. M. Heterogeneous atmospheric aerosol production by acid-catalyzed particle-phase reactions. *Science (1979)* **298**, 814–817 (2002).
89. George, I. J., Slowik, J. & Abbatt, J. P. D. Chemical aging of ambient organic aerosol from heterogeneous reaction with hydroxyl radicals. *Geophysical Research Letters* **35**, L13811 (2008).
90. Beilke, S. & Gravenhorst, G. Heterogeneous SO₂-oxidation in the droplet phase. *Atmospheric Environment (1967)* **12**, 231–239 (1978).
91. Dentener, F. J. & Crutzen, P. J. Reaction of N₂O₅ on tropospheric aerosols: impact on the global distributions of NO_x, O₃, and OH. *Journal of Geophysical Research* **98**, 7149–7163 (1993).
92. Epstein, S. A., Blair, S. L. & Nizkorodov, S. A. Direct Photolysis of α -Pinene Ozonolysis Secondary Organic Aerosol: Effect on Particle Mass and Peroxide Content. *Environmental Science and Technology* **48**, 11251–11258 (2014).
93. Hems, R. F., Schnitzler, E. G., Liu-Kang, C., Cappa, C. D. & Abbatt, J. P. D. Aging of Atmospheric Brown Carbon Aerosol. *ACS Earth and Space Chemistry* **5**, 722–748 (2021).
94. Pospisilova, V. *et al.* Photodegradation of α -Pinene Secondary Organic Aerosol Dominated by Moderately Oxidized Molecules. *Environmental Science and Technology* **55**, 6936–6943 (2021).

95. Gomez, A. L., Park, J., Walser, M. L., Lin, A. & Nizkorodov, S. A. UV photodissociation spectroscopy of oxidized undecylenic acid films. *Journal of Physical Chemistry A* **110**, 3584–3592 (2006).
96. Dubowski, Y. *et al.* Interaction of gas-phase ozone at 296 K with unsaturated self-assembled monolayers: A new look at an old system. *Journal of Physical Chemistry A* **108**, 10473–10485 (2004).
97. O'Brien, R. E. & Kroll, J. H. Photolytic Aging of Secondary Organic Aerosol: Evidence for a Substantial Photo-Recalcitrant Fraction. *Journal of Physical Chemistry Letters* **10**, 4003–4009 (2019).
98. Sinclair, D. & La Mer, V. K. Light scattering as a measure of particle size in aerosols. The production of monodisperse aerosols. *Chemical Reviews* **44**, 245–267 (1949).
99. Zhang, X., Pandis, S. N. & Seinfeld, J. H. Diffusion-limited versus quasi-equilibrium aerosol growth. *Aerosol Science and Technology* **46**, 874–885 (2012).
100. Kolb, C. E. *et al.* An overview of current issues in the uptake of atmospheric trace gases by aerosols and clouds. *Atmospheric Chemistry and Physics* vol. 10 10561–10605 (2010).
101. Abbatt, J. P. D., Lee, A. K. Y. & Thornton, J. A. Quantifying trace gas uptake to tropospheric aerosol: Recent advances and remaining challenges. *Chemical Society Reviews* **41**, 6555–6581 (2012).
102. Pöschl, U., Rudich, Y. & Ammann, M. Kinetic model framework for aerosol and cloud surface chemistry and gas-particle interactions - Part 1: General equations, parameters, and terminology. *Atmospheric Chemistry and Physics* **7**, 5989–6023 (2007).
103. Pankow, J. F. An absorption model of gas/particle partitioning of organic compounds in the atmosphere. *Atmospheric Environment* **28**, 185–188 (1994).
104. Donahue, N. M., Epstein, S. A., Pandis, S. N. & Robinson, A. L. A two-dimensional volatility basis set: 1. organic-aerosol mixing thermodynamics. *Atmospheric Chemistry and Physics* **11**, 3303–3318 (2011).
105. Donahue, N. M. *et al.* How do organic vapors contribute to new-particle formation? *Faraday Discussions* **165**, 91–104 (2013).
106. Reid, J. P. *et al.* The viscosity of atmospherically relevant organic particles. *Nature Communications* vol. 9 1–14 (2018).
107. Virtanen, A. *et al.* An amorphous solid state of biogenic secondary organic aerosol particles. *Nature* **467**, 824–827 (2010).
108. Vaden, T. D., Imre, D., Beránek, J., Shrivastava, M. & Zelenyuk, A. Evaporation kinetics and phase of laboratory and ambient secondary organic aerosol. *Proc Natl Acad Sci U S A* **108**, 2190–2195 (2011).
109. Perraud, V. *et al.* Nonequilibrium atmospheric secondary organic aerosol formation and growth. *Proc Natl Acad Sci U S A* **109**, 2836–2841 (2012).

110. Pajunoja, A. *et al.* Estimating the viscosity range of SOA particles based on their coalescence time. *Aerosol Science and Technology* (2014) doi:10.1080/02786826.2013.870325.
111. Renbaum-Wolff, L. *et al.* Viscosity of α -pinene secondary organic material and implications for particle growth and reactivity. *Proc Natl Acad Sci U S A* **110**, 8014–8019 (2013).
112. Pfrang, C., Shiraiwa, M. & Pöschl, U. Chemical ageing and transformation of diffusivity in semi-solid multi-component organic aerosol particles. *Atmospheric Chemistry and Physics* (2011) doi:10.5194/acp-11-7343-2011.
113. Shiraiwa, M., Ammann, M., Koop, T. & Pöschl, U. Gas uptake and chemical aging of semisolid organic aerosol particles. *Proc Natl Acad Sci U S A* (2011) doi:10.1073/pnas.1103045108.
114. Shiraiwa, M. & Seinfeld, J. H. Equilibration timescale of atmospheric secondary organic aerosol partitioning. *Geophysical Research Letters* (2012) doi:10.1029/2012GL054008.
115. Shiraiwa, M. *et al.* Global distribution of particle phase state in atmospheric secondary organic aerosols. *Nature Communications* **8**, 1–7 (2017).
116. Boyd, C. M., Nah, T., Xu, L., Berkemeier, T. & Ng, N. L. Secondary Organic Aerosol (SOA) from Nitrate Radical Oxidation of Monoterpenes: Effects of Temperature, Dilution, and Humidity on Aerosol Formation, Mixing, and Evaporation. *Environmental Science and Technology* **51**, 7831–7841 (2017).
117. vander Wall, A. C., Perraud, V., Wingen, L. M. & Finlayson-Pitts, B. J. Evidence for a kinetically controlled burying mechanism for growth of high viscosity secondary organic aerosol. *Environmental Science: Processes & Impacts* **22**, 66–83 (2020).
118. Kidd, C., Perraud, V., Wingen, L. M. & Finlayson-Pitts, B. J. Integrating phase and composition of secondary organic aerosol from the ozonolysis of α -pinene. *Proc Natl Acad Sci U S A* **111**, 7552–7557 (2014).
119. Saukko, E. *et al.* Humidity-dependent phase state of SOA particles from biogenic and anthropogenic precursors. *Atmospheric Chemistry and Physics* **12**, 7517–7529 (2012).
120. Wilson, J., Imre, D., Beránek, J., Shrivastava, M. & Zelenyuk, A. Evaporation kinetics of laboratory-generated secondary organic aerosols at elevated relative humidity. *Environmental Science and Technology* **49**, 243–249 (2015).
121. Li, Y. & Shiraiwa, M. Timescales of secondary organic aerosols to reach equilibrium at various temperatures and relative humidities. *Atmospheric Chemistry and Physics* **19**, 5959–5971 (2019).
122. Liu, P. *et al.* Highly Viscous States Affect the Browning of Atmospheric Organic Particulate Matter. *ACS Central Science* (2018) doi:10.1021/acscentsci.7b00452.
123. Li, Y. J. *et al.* Chemical Reactivity and Liquid/Nonliquid States of Secondary Organic Material. *Environmental Science and Technology* **49**, 13264–13274 (2015).
124. Zelenyuk, A. *et al.* Synergy between secondary organic aerosols and long-range transport of polycyclic aromatic hydrocarbons. *Environmental Science and Technology* **46**, 12459–12466 (2012).

125. Mu, Q. *et al.* Temperature effect on phase state and reactivity controls atmospheric multiphase chemistry and transport of PAHs. *Science Advances* **4**, eaap7314 (2018).
126. Keyte, I. J., Harrison, R. M. & Lammel, G. Chemical reactivity and long-range transport potential of polycyclic aromatic hydrocarbons—a review. *Chemical Society Reviews* vol. 42 9333–9391 (2013).
127. Shrivastava, M. *et al.* Global long-range transport and lung cancer risk from polycyclic aromatic hydrocarbons shielded by coatings of organic aerosol. *Proc Natl Acad Sci U S A* **114**, 1246–1251 (2017).
128. Friedman, C. L., Pierce, J. R. & Selin, N. E. Assessing the influence of secondary organic versus primary carbonaceous aerosols on long-range atmospheric polycyclic aromatic hydrocarbon transport. *Environmental Science and Technology* **48**, 3293–3302 (2014).
129. Koop, T., Bookhold, J., Shiraiwa, M. & Pöschl, U. Glass transition and phase state of organic compounds: Dependency on molecular properties and implications for secondary organic aerosols in the atmosphere. *Physical Chemistry Chemical Physics* vol. 13 19238–19255 (2011).
130. Alpert, P. A. *et al.* Photolytic radical persistence due to anoxia in viscous aerosol particles. *Nature Communications* **12**, 1–8 (2021).
131. Lignell, H., Hinks, M. L. & Nizkorodov, S. A. Exploring matrix effects on photochemistry of organic aerosols. *Proc Natl Acad Sci U S A* **111**, 13780–13785 (2014).
132. Zaveri, R. A. *et al.* Rapid growth of anthropogenic organic nanoparticles greatly alters cloud life cycle in the Amazon rainforest. *Science Advances* **8**, 329 (2022).
133. Wolf, M. J. *et al.* A biogenic secondary organic aerosol source of cirrus ice nucleating particles. *Nature Communications* **11**, 1–9 (2020).
134. Walser, M. L., Park, J., Gomez, A. L., Russell, A. R. & Nizkorodov, S. A. Photochemical Aging of Secondary Organic Aerosol Particles Generated from the Oxidation of d-Limonene. *The Journal of Physical Chemistry A* **111**, 1907–1913 (2007).
135. Mang, S. A. *et al.* Contribution of Carbonyl Photochemistry to Aging of Atmospheric Secondary Organic Aerosol. *Journal of Physical Chemistry A* **112**, 8337–8344 (2008).
136. Park, J., Gomez, A. L., Walser, M. L., Lin, A. & Nizkorodov, S. A. Ozonolysis and photolysis of alkene-terminated self-assembled monolayers on quartz nanoparticles: Implications for photochemical aging of organic aerosol particles. *Physical Chemistry Chemical Physics* **8**, 2506–2512 (2006).
137. Hung, H. M., Chen, Y. Q. & Martin, S. T. Reactive aging of films of secondary organic material studied by infrared spectroscopy. *Journal of Physical Chemistry A* **117**, 108–116 (2013).
138. Wong, J. P. S., Zhou, S. & Abbatt, J. P. D. Changes in secondary organic aerosol composition and mass due to photolysis: Relative humidity dependence. *Journal of Physical Chemistry A* **119**, 4309–4316 (2015).
139. Pan, X., Underwood, J. S., Xing, J.-H., Mang, S. A. & Nizkorodov, S. A. Photodegradation of secondary organic aerosol generated from limonene oxidation by ozone studied with chemical ionization mass spectrometry. *Atmospheric Chemistry and Physics* **9**, 3851–3865 (2009).

140. Zawadowicz, M. A. *et al.* Photolysis Controls Atmospheric Budgets of Biogenic Secondary Organic Aerosol. **54**, 3861–3870 (2020).
141. Kamboures, M. A., Nizkorodov, S. A. & Gerber, R. B. Ultrafast photochemistry of methyl hydroperoxide on ice particles. *Proc Natl Acad Sci U S A* **107**, 6600–6604 (2010).
142. Liu, J. *et al.* Optical properties and aging of light-absorbing secondary organic aerosol. *Atmospheric Chemistry and Physics* **16**, 12815–12827 (2016).
143. Romonosky, D. E. *et al.* Effective absorption cross sections and photolysis rates of anthropogenic and biogenic secondary organic aerosols. *Atmospheric Environment* **130**, 172–179 (2016).
144. Tsui, W. G., Rao, Y., Dai, H. L. & McNeill, V. F. Modeling Photosensitized Secondary Organic Aerosol Formation in Laboratory and Ambient Aerosols. *Environmental Science and Technology* **51**, 7496–7501 (2017).
145. Aregahegn, K. Z., Nozière, B. & George, C. Organic aerosol formation photo-enhanced by the formation of secondary photosensitizers in aerosols. *Faraday Discussions* **165**, 123–134 (2013).
146. McNeill, K. & Canonica, S. Triplet state dissolved organic matter in aquatic photochemistry: Reaction mechanisms, substrate scope, and photophysical properties. *Environmental Science: Processes and Impacts* **18**, 1381–1399 (2016).
147. Choudhry, G. G., Roof, A. A. M. & Hutzinger, O. Mechanisms in sensitized photochemistry of environmental chemicals. *Toxicological and Environmental Chemistry Reviews* **2**, 259–302 (1979).
148. Canonica, S., Jans, U., Stemmler, K., Hoigné, J. & Organic, N. Transformation Kinetics of Phenols in Water: Photosensitization by Dissolved Natural Organic Material and Aromatic Ketones. *Environmental Science and Technology* **29**, 1822–1831 (1995).
149. Manfrin, A. *et al.* Reactive Oxygen Species Production from Secondary Organic Aerosols: The Importance of Singlet Oxygen. *Environmental Science and Technology* **53**, 8553–8562 (2019).
150. Teich, M., Van Pinxteren, D., Kecorius, S., Wang, Z. & Herrmann, H. First Quantification of Imidazoles in Ambient Aerosol Particles: Potential Photosensitizers, Brown Carbon Constituents, and Hazardous Components. *Environmental Science and Technology* **50**, 1166–1173 (2016).
151. Hamilton, J. F. *et al.* Partially oxidised organic components in urban aerosol using GCXGC-TOF/MS. *Atmospheric Chemistry and Physics* **4**, 1279–1290 (2004).
152. Fan, Z., Kamens, R. M., Jianxin, H. U., Zhang, J. & Mcdow, S. Photostability of nitro-polycyclic aromatic hydrocarbons on combustion soot particles in sunlight. *Environmental Science and Technology* **30**, 1358–1364 (1996).
153. Jang, M. & Mcdow, S. R. Benz[a]anthracene Photodegradation in the Presence of Known Organic Constituents of Atmospheric Aerosols. *Environmental Science and Technology* **29**, 2654–2660 (1995).
154. Rossignol, S. *et al.* Glyoxal induced atmospheric photosensitized chemistry leading to organic aerosol growth. *Environmental Science and Technology* **48**, 3218–3227 (2014).

155. Donaldson, D. J. & Vaida, V. The influence of organic films at the air-aqueous boundary on atmospheric processes. *Chemical Reviews* vol. 106 1445–1461 (2006).
156. Vlasenko, A., George, I. J. & Abbatt, J. P. D. Formation of Volatile Organic Compounds in the Heterogeneous Oxidation of Condensed-Phase Organic Films by Gas-Phase OH. *Journal of Physical Chemistry A* **112**, 1552–1560 (2008).
157. Gilman, J. B. & Vaida, V. Permeability of acetic acid through organic films at the air-aqueous interface. *Journal of Physical Chemistry A* **110**, 7581–7587 (2006).
158. Herrmann, H., Hoffmann, D., Schaefer, T., Brüner, P. & Tilgner, A. Tropospheric Aqueous-Phase Free-Radical Chemistry : Radical Sources , Spectra , Reaction Kinetics and Prediction Tools. 3796–3822 (2010) doi:10.1002/cphc.201000533.
159. Anastasio, C.; Faust, B. C.; Rao, C. J. Aromatic carbonyl compounds as aqueous-phase photochemical sources of hydrogen peroxide in acidic sulfate aerosols, fogs, and clouds 0.1. Non-phenolic methoxybenzaldehydes and methoxyacetophenones with reductants (phenols). *Environmental Science and Technology* **31**, 218–232. (1997).
160. Vione, D., Maurino, V., Minero, C., Pelizzetti, E. & Harrison, M. A. J. Photochemical reactions in the tropospheric aqueous phase and on particulate matter. 441–453 (2006) doi:10.1039/b510796m.
161. Chen, Y. *et al.* Secondary organic aerosol formation from 3C*-initiated oxidation of 4-ethylguaiaicol in atmospheric aqueous-phase. *Science of the Total Environment* **723**, 137953 (2020).
162. Jang, M. & Mcdow, S. R. Products of benz[a]anthracene photodegradation in the presence of known organic constituents of atmospheric aerosols. *Environmental Science and Technology* **31**, 1046–1053 (1997).
163. Kaur, R., Hudson, B. M., Draper, J., Tantillo, D. J. & Anastasio, C. Aqueous reactions of organic triplet excited states with atmospheric alkenes. *Atmospheric Chemistry and Physics* **19**, 5021–5032 (2019).
164. Richards-Henderson, N. K., Pham, A. T., Kirk, B. B. & Anastasio, C. Secondary organic aerosol from aqueous reactions of green leaf volatiles with organic triplet excited states and singlet molecular oxygen. *Environmental Science and Technology* **49**, 268–276 (2015).
165. Smith, J. D., Sio, V., Yu, L., Zhang, Q. & Anastasio, C. Secondary organic aerosol production from aqueous reactions of atmospheric phenols with an organic triplet excited state. *Environmental Science and Technology* **48**, 1049–1057 (2014).
166. Tinel, L., Dumas, S. & George, C. A time-resolved study of the multiphase chemistry of excited carbonyls: Imidazole-2-carboxaldehyde and halides. *Comptes Rendus Chimie* **17**, 801–807 (2014).
167. Yu, L. *et al.* Chemical characterization of SOA formed from aqueous-phase reactions of phenols with the triplet excited state of carbonyl and hydroxyl radical. *Atmospheric Chemistry and Physics* **14**, 13801–13816 (2014).
168. Canonica, S., Hellrung, B. & Wirz, J. Oxidation of phenols by triplet aromatic ketones in aqueous solution. *Journal of Physical Chemistry A* **104**, 1226–1232 (2000).

169. Canonica, S., Hellrung, B., Müller, P. & Wirz, J. Aqueous Oxidation of Phenylurea Herbicides by Triplet Aromatic Ketones. *Environmental Science and Technology* **40**, 6636–6641 (2006).
170. Jammoul, A., Dumas, S., D'Anna, B. & George, C. Photoinduced oxidation of sea salt halides by aromatic ketones: a source of halogenated radicals. *Atmospheric Chemistry and Physics Discussions* **9**, 7681–7706 (2009).
171. Hönninger, G., von Friedeburg, C. & Platt, U. Multi axis differential optical absorption spectroscopy (MAX-DOAS). *Atmospheric Chemistry and Physics* **4**, 231–254 (2004).
172. Sherwen, T. *et al.* Effects of halogens on European air-quality. *Faraday Discussions* **200**, 75–100 (2017).
173. Simpson, W. R., Brown, S. S., Saiz-Lopez, A., Thornton, J. A. & von Glasow, R. Tropospheric Halogen Chemistry: Sources, Cycling, and Impacts. *Chemical Reviews* **115**, 4035–4062 (2015).
174. Platt, U. & Moortgat, G. K. Heterogeneous and Homogeneous Chemistry of Reactive Halogen Compounds in the Lower Troposphere. *Journal of Atmospheric Chemistry* 1999 34:1 **34**, 1–8 (1999).
175. Tomaz, S. Study of polycyclic aromatic compounds in the atmosphere: molecular characterization and chemical processes related to organic aerosols. (2015).
176. Tomaz, S. *et al.* One-year study of polycyclic aromatic compounds at an urban site in Grenoble (France): Seasonal variations, gas/particle partitioning and cancer risk estimation. *Science of the Total Environment* **565**, 1071–1083 (2016).
177. Cautreels, W. & van Cauwenberghe, K. Experiments on the distribution of organic pollutants between airborne particulate matter and the corresponding gas phase. *Atmospheric Environment (1967)* **12**, 1133–1141 (1978).
178. Schauer, J. J., Kleeman, M. J., Cass, G. R. & Simoneit, B. R. T. Measurement of Emissions from Air Pollution Sources. 2. C1 through C30 Organic Compounds from Medium Duty Diesel Trucks. *Environmental Science and Technology* **33**, 1578–1587 (1999).
179. Schauer, J. J., Kleeman, M. J., Cass, G. R. & Simoneit, B. R. T. Measurement of Emissions from Air Pollution Sources. 3. C1–C29 Organic Compounds from Fireplace Combustion of Wood. *Environmental Science and Technology* **35**, 1716–1728 (2001).
180. Ketseridis, G., Hahn, J., Jaenicke, R. & Junge, C. The organic constituents of atmospheric particulate matter. *Atmospheric Environment (1967)* **10**, 603–610 (1976).
181. Lin, P. *et al.* Molecular Characterization of Brown Carbon in Biomass Burning Aerosol Particles. *Environmental Science and Technology* **50**, 11815–11824 (2016).
182. Aiona, P. K. *et al.* Effect of Photolysis on Absorption and Fluorescence Spectra of Light-Absorbing Secondary Organic Aerosols. *ACS Earth and Space Chemistry* **2**, 235–245 (2018).
183. Ciuraru, R. *et al.* Photosensitized production of functionalized and unsaturated organic compounds at the air-sea interface. *Scientific Reports* (2015) doi:10.1038/srep12741.

184. Mekić, M. *et al.* Formation of Toxic Unsaturated Multifunctional and Organosulfur Compounds From the Photosensitized Processing of Fluorene and DMSO at the Air-Water Interface. *Journal of Geophysical Research: Atmospheres* **125**, e2019JD031839 (2020).
185. Brigante, M., Charboullot, T., Vione, D. & Mailhot, G. Photochemistry of 1-nitronaphthalene: A potential source of singlet oxygen and radical species in atmospheric waters. *Journal of Physical Chemistry A* **114**, 2830–2836 (2010).
186. Reeser, D. I. *et al.* Photoenhanced reaction of ozone with chlorophyll at the seawater surface. *Journal of Physical Chemistry C* **113**, 2071–2077 (2009).
187. Goetz, M. & Hussein, B. H. M. Photoionization of xanthone via its triplet state or via its radical anion. *Physical Chemistry Chemical Physics* **6**, 5490–5497 (2004).
188. Lutz, H., Duval, M. C., Bréhéret, E. & Lindqvist, L. Solvent effects on acetophenone photoreduction studied by laser photolysis. *The Journal of Physical Chemistry* **76**, 821–822 (1972).
189. Lutz, H., Bréhéret, E. & Lindqvist, L. Effects of solvent and substituents on the absorption spectra of triplet acetophenone and the acetophenone ketyl radical studied by nanosecond laser photolysis. *Journal of Physical Chemistry* **77**, 1758–1762 (1973).
190. Tang, R., Zhang, P., Li, H., Liu, Y. & Wang, W. Photosensitized xanthone-based oxidation of guanine and its repair: A laser flash photolysis study. *Journal of Photochemistry and Photobiology B: Biology* **105**, 157–161 (2011).
191. Avila, V. & Previtali, C. M. Triplet state properties of flavone in homogeneous and micellar solutions. A laser flash photolysis study. (1995).
192. BRAUN, A., MAURETTE, M.-T. & OLIVEROS, E. *Technologie photochimique*. (Presses polytechniques romandes, 1986).
193. Wagner, P. J. & Spoerke, R. W. Triplet Lifetimes of Cyclic Ketones. *J Am Chem Soc* **91**, 4437–4440 (1969).
194. Grewer, C. & Brauer, H. D. Mechanism of the triplet-state quenching by molecular oxygen in solution. *Journal of Physical Chemistry* **98**, 4230–4235 (1994).
195. Wagner, P. J., Truman, R. J., Puchalski, A. E. & Wake, R. Extent of Charge Transfer in the Photoreduction of Phenyl Ketones by Alkylbenzenes. 7727–7738 (1986)
doi:10.1021/ja00284a041.
196. Merkel, P. B. & Dinnocenzo, J. P. Thermodynamic energies of donor and acceptor triplet states. **193**, 110–121 (2008).
197. Geissman, T. A. & Friess, S. L. Flavanones and Related Compounds. VI. The Polarographic Reduction of Some Substituted Chalcones, Flavones and Flavanones. *J Am Chem Soc* **71**, 3893–3902 (2002).
198. Day, R. A. & Biggers, R. E. Polarography of p-Chlorobenzophenone and Xanthone. *J Am Chem Soc* **75**, 738–739 (2002).

199. Hammond, G. S. *et al.* Mechanisms of Photochemical Reactions in Solution. XXII.1 Photochemical cis-trans Isomerization. *J Am Chem Soc* **86**, 3197–3217 (2002).
200. Lancelot, J. *et al.* A pulse radiolysis study of the quenching of aromatic carbonyl triplets by norbornadienes and quadricyclenes. The mechanism of interconversion. *J Am Chem Soc* **100**, 1814–1820 (2002).
201. Farid, S. *et al.* Reexamination of the rehm-weller data set reveals electron transfer quenching that follows a sandros-boltzmann dependence on free energy. *J Am Chem Soc* **133**, 11580–11587 (2011).
202. Ebersson, L. Electron Transfer in Chemistry. in *Advances in Physical Organic Chemistry* (eds. Gold, V. & Bethell, D.) vol. 18 79–185 (Academic Press, 1982).
203. Parker, K. M. & Mitch, W. A. Halogen radicals contribute to photooxidation in coastal and estuarine waters OH. **113**, 5868–5873 (2016).
204. Devonshire, R. & Weiss, J. J. Nature of the Transient Species in the Photochemistry of Negative Ions in Aqueous Solution. **7**, 7–12 (1968).
205. Lampre, I. *et al.* Oxidation of Bromide Ions by Hydroxyl Radicals : Spectral Characterization of the Intermediate BrOH • -. (2013) doi:10.1021/jp310759u.
206. Ershov, B. G. & Janata, E. The one electron reduction of Hg²⁺ by 1-hydroxyalkyl radicals in aqueous solution: A pulse radiolysis study. *Radiation Physics and Chemistry* **69**, 55–57 (2004).
207. Mártire, D. O. *et al.* Kinetic study of the reactions of chlorine atoms and Cl₂•- radical anions in aqueous solutions. II. Toluene, benzoic acid, and chlorobenzene. *Journal of Physical Chemistry A* **105**, 5385–5392 (2001).
208. Roveretto, M. *et al.* Real-Time Detection of Gas-Phase Organohalogenes from Aqueous Photochemistry Using Orbitrap Mass Spectrometry. *ACS Earth and Space Chemistry* **3**, 329–334 (2019).
209. Mehrdad, Z., Schweitzer, C. & Schmidt, R. Formation of O₂(1Σg⁺), O₂(1Δg), and O₂(3Σg⁻) during Oxygen quenching of nπ triplet phenyl ketones: The role of charge transfer and sensitizer-oxygen complex structure. *Journal of Physical Chemistry A* **106**, 228–235 (2002).
210. Mehrdad, Z., Noll, A., Grabner, E. W. & Schmidt, R. Sensitization of singlet oxygen via encounter complexes and via exciplexes of ππ* Triplet excited sensitizers and oxygen. *Photochemical and Photobiological Sciences* **1**, 263–269 (2002).
211. Xing, W. *et al.* *Oxygen Solubility, Diffusion Coefficient, and Solution Viscosity. Rotating Electrode Methods and Oxygen Reduction Electrocatalysts* (Elsevier B.V., 2014). doi:10.1016/B978-0-444-63278-4.00001-X.
212. Kautzman, K. E. *et al.* Chemical composition of gas- and aerosol-phase products from the photooxidation of naphthalene. *Journal of Physical Chemistry A* **114**, 913–934 (2010).
213. Lee, H. J., Aiona, P. K., Laskin, A., Laskin, J. & Nizkorodov, S. A. Effect of solar radiation on the optical properties and molecular composition of laboratory proxies of atmospheric brown carbon. *Environmental Science and Technology* **48**, 10217–10226 (2014).

214. Fischer, A., Kliger, D., Winterle, J. & Mill, T. PRIMARY PHOTOCHEMICAL PROCESSES IN PHOTOLYSIS MEDIATED BY HUMIC SUBSTANCES. *National Meeting - American Chemical Society, Division of Environmental Chemistry* **25**, 359–363 (1985).
215. Martin, M. v. *et al.* Transient spectroscopic characterization and theoretical modeling of fulvic acid radicals formed by UV-A radiation. *Journal of Photochemistry and Photobiology A: Chemistry* (2017) doi:10.1016/j.jphotochem.2016.10.007.
216. Power, J. F., Sharma, D. K., Langford, C. H., Bonneau, R. & Jousset-Dubien, J. Laser Flash Photolytic Studies of a Well-Characterized Soil Humic Substance. in (1987). doi:10.1021/bk-1987-0327.ch012.
217. Jimenez, J. L. *et al.* Evolution of organic aerosols in the atmosphere. *Science* (1979) **326**, 1525–1529 (2009).
218. Saxena, P. & Seigneur, C. On the oxidation of SO₂ to sulfate in atmospheric aerosols. *Atmospheric Environment* (1967) **21**, 807–812 (1987).
219. Eatough, D. J., Caka, F. M. & Farber, R. J. The Conversion of SO₂ to Sulfate in the Atmosphere. *Israel Journal of Chemistry* **34**, 301–314 (1994).
220. Nel, A. ATMOSPHERE: Enhanced: Air Pollution-Related Illness: Effects of Particles. *Science* (1979) **308**, 804–806 (2005).
221. Fuzzi, S. *et al.* Particulate matter, air quality and climate: Lessons learned and future needs. *Atmospheric Chemistry and Physics* **15**, 8217–8299 (2015).
222. Zhang, Q. *et al.* Ubiquity and dominance of oxygenated species in organic aerosols in anthropogenically-influenced Northern Hemisphere midlatitudes. *Geophysical Research Letters* **34**, 1–6 (2007).
223. Sun, J. *et al.* Key Role of Nitrate in Phase Transitions of Urban Particles: Implications of Important Reactive Surfaces for Secondary Aerosol Formation. *Journal of Geophysical Research: Atmospheres* **123**, 1234–1243 (2018).
224. Li, S. *et al.* Photochemical aging of atmospherically reactive organic compounds involving brown carbon at the air-aqueous interface. *Atmospheric Chemistry and Physics* **19**, 9887–9902 (2019).
225. González Palacios, L. *et al.* Heterogeneous photochemistry of imidazole-2-carboxaldehyde: HO₂ radical formation and aerosol growth. *Atmospheric Chemistry and Physics* **16**, 11823–11836 (2016).
226. Fankhauser, A. M. *et al.* Impact of Environmental Conditions on Secondary Organic Aerosol Production from Photosensitized Humic Acid. *Environ Sci Technol* **54**, 5385–5390 (2020).
227. Zhang, Z., Lin, L. & Wang, L. Atmospheric oxidation mechanism of naphthalene initiated by OH radical. A theoretical study. *Physical Chemistry Chemical Physics* **14**, 2645–2650 (2012).
228. Sudakin, D. L., Stone, D. L. & Power, L. Naphthalene mothballs: Emerging and recurring issues and their relevance to environmental health. *Current Topics in Toxicology* **7**, 13–19 (2011).

229. McWhinney, R. D., Zhou, S. & Abbatt, J. P. D. Naphthalene SOA: Redox activity and naphthoquinone gas-particle partitioning. *Atmospheric Chemistry and Physics* **13**, 9731–9744 (2013).
230. Wang, X. *et al.* Chemical Characteristics of Organic Aerosols in Shanghai: A Study by Ultra-High-Performance Liquid Chromatography Coupled with Orbitrap Mass Spectrometry. *Journal of Geophysical Research: Atmospheres* 1–20 (2017) doi:10.1002/2017JD026930.
231. Delhomme, O., Millet, M. & Herckes, P. Determination of oxygenated polycyclic aromatic hydrocarbons in atmospheric aerosol samples by liquid chromatography-tandem mass spectrometry. *Talanta* **74**, 703–710 (2008).
232. Oda, J., Nomura, S., Yasuhara, A. & Shibamoto, T. Mobile sources of atmospheric polycyclic aromatic hydrocarbons in a roadway tunnel. *Atmospheric Environment* **35**, 4819–4827 (2001).
233. Wang, X. *et al.* Chemical Characteristics and Brown Carbon Chromophores of Atmospheric Organic Aerosols Over the Yangtze River Channel: A Cruise Campaign. *Journal of Geophysical Research: Atmospheres* **125**, 1–13 (2020).
234. de Lucas, N. C. *et al.* Photosensitizing properties of triplet furano and pyrano-1,2-naphthoquinones. *Journal of Photochemistry and Photobiology A: Chemistry* **276**, 16–30 (2014).
235. Gemayel, R. *et al.* Quenching of ketone triplet excited states by atmospheric halides. *Environmental Science: Atmospheres* **1**, 31–44 (2021).
236. Watne, Å. K. *et al.* Fresh and Oxidized Emissions from In-Use Transit Buses Running on Diesel, Biodiesel, and CNG. *Environmental Science and Technology* **52**, 7720–7728 (2018).
237. Yli-Juuti, T. *et al.* Factors controlling the evaporation of secondary organic aerosol from α -pinene ozonolysis. *Geophysical Research Letters* **44**, 2562–2570 (2017).
238. Li, Z. *et al.* Effect of Decreased Temperature on the Evaporation of α -Pinene Secondary Organic Aerosol Particles. *ACS Earth and Space Chemistry* **3**, 2775–2785 (2019).
239. Dupart, Y. *et al.* Mineral dust photochemistry induces nucleation events in the presence of SO₂. *Proceedings of the National Academy of Sciences* **109**, 20842–20847 (2012).
240. Kalalian, C. *et al.* Influence of indoor chemistry on the emission of mVOCs from *Aspergillus niger* molds. *Science of the Total Environment* **741**, 140148 (2020).
241. Sarangi, B., Aggarwal, S. G., Sinha, D. & Gupta, P. K. Aerosol effective density measurement using scanning mobility particle sizer and quartz crystal microbalance with the estimation of involved uncertainty. *Atmospheric Measurement Techniques* **9**, 859–875 (2016).
242. Allan, J. D. *et al.* Submicron aerosol composition at Trinidad Head, California, during ITCT 2K2: Its relationship with gas phase volatile organic carbon and assessment of instrument performance. *Journal of Geophysical Research D: Atmospheres* **109**, 1–16 (2004).
243. Wang, X. K. *et al.* Molecular characterization of atmospheric particulate organosulfates in three megacities at the middle and lower reaches of the Yangtze River. *Atmospheric Chemistry and Physics* **16**, 2285–2298 (2016).

244. Lin, P., Rincon, A. G., Kalberer, M. & Yu, J. Z. Elemental composition of HULIS in the Pearl River Delta Region, China: Results inferred from positive and negative electrospray high resolution mass spectrometric data. *Environmental Science and Technology* **46**, 7454–7462 (2012).
245. Slade, J. H. *et al.* Cloud droplet activation through oxidation of organic aerosol influenced by temperature and particle phase state. *Geophysical Research Letters* **44**, 1583–1591 (2017).
246. Wang, S. *et al.* Organic Peroxides and Sulfur Dioxide in Aerosol: Source of Particulate Sulfate. *Environmental Science and Technology* **53**, 10695–10704 (2019).
247. Ye, J., Abbatt, J. P. D. & Chan, A. W. H. Novel pathway of SO₂ oxidation in the atmosphere: reactions with monoterpene ozonolysis intermediates and secondary organic aerosol. *Atmospheric Chemistry and Physics* **18**, 5549–5565 (2018).
248. Yao, M. *et al.* Multiphase Reactions between Secondary Organic Aerosol and Sulfur Dioxide: Kinetics and Contributions to Sulfate Formation and Aerosol Aging. *Environmental Science and Technology Letters* **6**, 768–774 (2019).
249. Olson, T. M. & Hoffmann, M. R. Hydroxyalkylsulfonate formation: Its role as a S(IV) reservoir in atmospheric water droplets. *Atmospheric Environment (1967)* **23**, 985–997 (1989).
250. LuValle, J. E. The Reaction of Quinone and Sulfite. I. Intermediates. *J Am Chem Soc* **74**, 2970–2977 (1952).
251. Hodas, N., Zuend, A., Mui, W., Flagan, R. C. & Seinfeld, J. H. Influence of particle-phase state on the hygroscopic behavior of mixed organic-inorganic aerosols. *Atmospheric Chemistry and Physics* **15**, 5027–5045 (2015).
252. Ye, Q. *et al.* Mixing of secondary organic aerosols versus relative humidity. *Proc Natl Acad Sci U S A* **113**, 12649–12654 (2016).
253. Ye, Q. *et al.* Following Particle-Particle Mixing in Atmospheric Secondary Organic Aerosols by Using Isotopically Labeled Terpenes. *Chem* **4**, 318–333 (2018).
254. Kroll, J. A., Frandsen, B. N., Kjaergaard, H. G. & Vaida, V. Atmospheric Hydroxyl Radical Source: Reaction of Triplet SO₂ and Water. *Journal of Physical Chemistry A* **122**, 4465–4469 (2018).
255. Martins-Costa, M. T. C., Anglada, J. M., Francisco, J. S. & Ruiz-López, M. F. Photochemistry of SO₂ at the Air-Water Interface: A Source of OH and HOSO Radicals. *J Am Chem Soc* **140**, 12341–12344 (2018).
256. Yli-Juuti, T. *et al.* Factors controlling the evaporation of secondary organic aerosol from α -pinene ozonolysis. *Geophysical Research Letters* **44**, 2562–2570 (2017).
257. Cheng, Y. *et al.* Reactive nitrogen chemistry in aerosol water as a source of sulfate during haze events in China. *Science Advances* **2**, e1601530 (2016).
258. Hung, H. M. & Hoffmann, M. R. Oxidation of Gas-Phase SO₂ on the Surfaces of Acidic Microdroplets: Implications for Sulfate and Sulfate Radical Anion Formation in the Atmospheric Liquid Phase. *Environmental Science and Technology* **49**, 13768–13776 (2015).

259. Kuang, B. Y., Yeung, H. S., Lee, C. C., Griffith, S. M. & Yu, J. Z. Aromatic formulas in ambient PM_{2.5} samples from Hong Kong determined using FT-ICR ultrahigh-resolution mass spectrometry. *Analytical and Bioanalytical Chemistry* **410**, 6289–6304 (2018).
260. Chan, A. W. H. *et al.* Secondary organic aerosol formation from photooxidation of naphthalene and alkylnaphthalenes: Implications for oxidation of intermediate volatility organic compounds (IVOCs). *Atmospheric Chemistry and Physics* **9**, 3049–3060 (2009).
261. Osburn, C. L. & Morris, D. P. Photochemistry of chromophoric dissolved organic matter in natural waters. in *UV effects in aquatic organisms and ecosystems* vol. 1 185–217 (The Royal Society of Chemistry Cambridge, 2003).
262. Huang, G. *et al.* Potentially Important Contribution of Gas-Phase Oxidation of Naphthalene and Methyl-naphthalene to Secondary Organic Aerosol during Haze Events in Beijing. *Environmental Science and Technology* **53**, 1235–1244 (2019).
263. Huang, Y. *et al.* Coexistence of three liquid phases in individual atmospheric aerosol particles. *Proceedings of the National Academy of Sciences* **118**, e2102512118 (2021).
264. Sindelarova, K. *et al.* Global data set of biogenic VOC emissions calculated by the MEGAN model over the last 30 years. *Atmospheric Chemistry and Physics* **14**, 9317–9341 (2014).
265. Kroll, J. H. & Seinfeld, J. H. Chemistry of secondary organic aerosol: Formation and evolution of low-volatility organics in the atmosphere. *Atmospheric Environment* **42**, 3593–3624 (2008).
266. Mellouki, A., Wallington, T. J. & Chen, J. Atmospheric Chemistry of Oxygenated Volatile Organic Compounds: Impacts on Air Quality and Climate. *Chemical Reviews* **115**, 3984–4014 (2015).
267. Shrivastava, M. *et al.* Recent advances in understanding secondary organic aerosol: Implications for global climate forcing. *Reviews of Geophysics* **55**, 509–559 (2017).
268. Moise, T., Flores, J. M. & Rudich, Y. Optical Properties of Secondary Organic Aerosols and Their Changes by Chemical Processes. *Chemical Reviews* **115**, 4400–4439 (2015).
269. Donahue, N. M., Robinson, A. L., Trump, E. R., Riipinen, I. & Kroll, J. H. Volatility and Aging of Atmospheric Organic Aerosol. in *Atmospheric and Aerosol Chemistry* vol. 339 97–143 (Springer, Berlin, Heidelberg, 2012).
270. Hodzic, A. *et al.* Organic photolysis reactions in tropospheric aerosols: effect on secondary organic aerosol formation and lifetime. *Atmospheric Chemistry and Physics* **15**, 9253–9269 (2015).
271. Heald, C. L. *et al.* Exploring the vertical profile of atmospheric organic aerosol: Comparing 17 aircraft field campaigns with a global model. *Atmospheric Chemistry and Physics* **11**, 12676–12696 (2011).
272. Heald, C. L. *et al.* A large organic aerosol source in the free troposphere missing from current models. *Geophysical Research Letters* **32**, 1–4 (2005).
273. Bianchi, F. *et al.* New particle formation in the free troposphere: A question of chemistry and timing. *Science (1979)* **352**, 1109–1112 (2016).

274. Bateman, A. P., Nizkorodov, S. A., Laskin, J. & Laskin, A. Photolytic processing of secondary organic aerosols dissolved in cloud droplets. *Physical Chemistry Chemical Physics* **13**, 12199 (2011).
275. Nguyen, T. B., Laskin, A., Laskin, J. & Nizkorodov, S. A. Direct aqueous photochemistry of isoprene high-NO_x secondary organic aerosol. *Physical Chemistry Chemical Physics* **14**, 9702–9714 (2012).
276. Wong, J. P. S. *et al.* Atmospheric evolution of molecular-weight-separated brown carbon from biomass burning. *Atmospheric Chemistry and Physics* **19**, 7319–7334 (2019).
277. Veghte, D. P. *et al.* Heating-Induced Transformations of Atmospheric Particles: Environmental Transmission Electron Microscopy Study. *Analytical Chemistry* **90**, 9761–9768 (2018).
278. Hinks, M. L. *et al.* Effect of relative humidity on the composition of secondary organic aerosol from the oxidation of toluene. *Atmospheric Chemistry and Physics* **18**, 1643–1652 (2018).
279. Chen, X., Hopke, P. K. & Carter, W. P. L. Secondary organic aerosol from ozonolysis of biogenic volatile organic compounds: Chamber studies of particle and reactive oxygen species formation. *Environmental Science and Technology* **45**, 276–282 (2011).
280. Krapf, M. *et al.* Labile Peroxides in Secondary Organic Aerosol. *Chem* **1**, 603–616 (2016).
281. Sauerbrey, G. Verwendung von Schwingquarzen zur Wägung dünner Schichten und zur Mikrowägung. *Zeitschrift für Physik* **155**, 206–222 (1959).
282. Wentworth, G. R. & Al-Abadleh, H. A. DRIFTS studies on the photosensitized transformation of gallic acid by iron(III) chloride as a model for HULIS in atmospheric aerosols. *Physical Chemistry Chemical Physics* **13**, 6507–6516 (2011).
283. Camredon, M. *et al.* Distribution of gaseous and particulate organic composition during dark & alpha-pinene ozonolysis. *Atmospheric Chemistry and Physics* **10**, 2893–2917 (2010).
284. Meusinger, C. *et al.* Chemical and isotopic composition of secondary organic aerosol generated by α -pinene ozonolysis. *Atmospheric Chemistry and Physics* **17**, 6373–6391 (2017).
285. Ji, Y. *et al.* Reassessing the atmospheric oxidation mechanism of toluene. *Proc Natl Acad Sci U S A* **114**, 8169–8174 (2017).
286. Shemesh, D., Blair, S. L., Nizkorodov, S. A. & Gerber, R. B. Photochemistry of aldehyde clusters: Cross-molecular versus unimolecular reaction dynamics. *Physical Chemistry Chemical Physics* **16**, 23861–23868 (2014).
287. Epstein, S. A., Shemesh, D., Tran, V. T., Nizkorodov, S. A. & Gerber, R. B. Absorption spectra and photolysis of methyl peroxide in liquid and frozen water. *Journal of Physical Chemistry A* **116**, 6068–6077 (2012).
288. Barsotti, F. *et al.* Photochemical Formation of Nitrite and Nitrous Acid (HONO) upon Irradiation of Nitrophenols in Aqueous Solution and in Viscous Secondary Organic Aerosol Proxy. *Environmental Science & Technology* **51**, 7486–7495 (2017).

289. Sangwan, M. & Zhu, L. Absorption Cross Sections of 2-Nitrophenol in the 295–400 nm Region and Photolysis of 2-Nitrophenol at 308 and 351 nm. *The Journal of Physical Chemistry A* **120**, 9958–9967 (2016).
290. Grygoryeva, K. *et al.* Photochemistry of Nitrophenol Molecules and Clusters: Intra- vs Intermolecular Hydrogen Bond Dynamics. *The Journal of Physical Chemistry A* **120**, 4139–4146 (2016).
291. Kundu, S., Fisseha, R., Putman, A. L., Rahn, T. A. & Mazzoleni, L. R. Atmospheric Chemistry and Physics High molecular weight SOA formation during limonene ozonolysis: insights from ultrahigh-resolution FT-ICR mass spectrometry characterization. *Atmos. Chem. Phys* **12**, 5523–5536 (2012).
292. Bateman, A. P., Nizkorodov, S. A., Laskin, J. & Laskin, A. Time-resolved molecular characterization of limonene/ozone aerosol using high-resolution electrospray ionization mass spectrometry. *Physical Chemistry Chemical Physics* **11**, 7931–7942 (2009).
293. Koch, B. P. & Dittmar, T. From mass to structure: an aromaticity index for high-resolution mass data of natural organic matter. *Rapid Communications in Mass Spectrometry* **30**, 250–250 (2016).
294. Koch, B. P. & Dittmar, T. From mass to structure: an aromaticity index for high-resolution mass data of natural organic matter. *Rapid Communications in Mass Spectrometry* **20**, 926–932 (2006).
295. Du, Y., Zhang, Y., Chen, F., Chang, Y. & Liu, Z. Photochemical reactivities of dissolved organic matter (DOM) in a sub-alpine lake revealed by EEM-PARAFAC: An insight into the fate of allochthonous DOM in alpine lakes affected by climate change. *Science of the Total Environment* **568**, 216–225 (2016).
296. Zhang, Y. *et al.* Photobleaching Response of Different Sources of Chromophoric Dissolved Organic Matter Exposed to Natural Solar Radiation Using Absorption and Excitation-Emission Matrix Spectra. *PLoS ONE* **8**, (2013).
297. Hinks, M. L. *et al.* Effect of viscosity on photodegradation rates in complex secondary organic aerosol materials. *Physical Chemistry Chemical Physics* **18**, 8785–8793 (2016).
298. Atmospheric Chemistry Observations & Modeling division / NCAR. Tropospheric Ultraviolet and Visible (TUV) Radiation Model. <https://www2.acom.ucar.edu/modeling/tropospheric-ultraviolet-and-visible-tuv-radiation-model> (2015).
299. Madronich, S. Tropospheric ultraviolet and visible (TUV) radiation model. <https://www2.acom.ucar.edu/modeling/tropospheric-ultraviolet-and-visible-tuv-radiation-model>.
300. Kroll, J. H., Lim, C. Y., Kessler, S. H. & Wilson, K. R. Heterogeneous Oxidation of Atmospheric Organic Aerosol: Kinetics of Changes to the Amount and Oxidation State of Particle-Phase Organic Carbon. *Journal of Physical Chemistry A* **119**, 10767–10783 (2015).
301. Smith, J. N. *et al.* Chemical composition of atmospheric nanoparticles formed from nucleation in Tecamac, Mexico: Evidence for an important role for organic species in nanoparticle growth. *Geophysical Research Letters* **35**, L04808 (2008).
302. Yu, P. *et al.* Efficient transport of tropospheric aerosol into the stratosphere via the Asian summer monsoon anticyclone. *Proc Natl Acad Sci U S A* **114**, 6972–6977 (2017).

303. Knopf, D. A., Alpert, P. A. & Wang, B. The Role of Organic Aerosol in Atmospheric Ice Nucleation: A Review. *ACS Earth and Space Chemistry* (2018) doi:10.1021/acsearthspacechem.7b00120.
304. Pope, C. A. & Dockery, D. W. Health effects of fine particulate air pollution: Lines that connect. *Journal of the Air and Waste Management Association* (2006) doi:10.1080/10473289.2006.10464485.
305. Lelieveld, J., Evans, J. S., Fnais, M., Giannadaki, D. & Pozzer, A. The contribution of outdoor air pollution sources to premature mortality on a global scale. *Nature* **525**, 367–371 (2015).
306. Lelieveld, J. *et al.* Loss of life expectancy from air pollution compared to other risk factors: A worldwide perspective. *Cardiovascular Research* **116**, 1910–1917 (2020).
307. Spracklen, D. v. *et al.* Aerosol mass spectrometer constraint on the global secondary organic aerosol budget. *Atmospheric Chemistry and Physics* **11**, 12109–12136 (2011).
308. Guenther, A. B. *et al.* The model of emissions of gases and aerosols from nature version 2.1 (MEGAN2.1): An extended and updated framework for modeling biogenic emissions. *Geoscientific Model Development* **5**, 1471–1492 (2012).
309. Maria Yanez-Serrano, A. *et al.* Monoterpene chemical speciation in a tropical rainforest: variation with season, height, and time of day at the Amazon Tall Tower Observatory (ATTO). *Atmospheric Chemistry and Physics* **18**, 3403–3418 (2018).
310. Guenther, A. A global model of natural volatile organic compound emissions. *Journal of Geophysical Research* **100**, 8873–8892 (1995).
311. Capouet, M. *et al.* Modeling aerosol formation in alpha-pinene photo-oxidation experiments. *Journal of Geophysical Research Atmospheres* **113**, (2008).
312. Grayson, J. W. *et al.* Effect of varying experimental conditions on the viscosity of α -pinene derived secondary organic material. *Atmospheric Chemistry and Physics* **16**, 6027–6040 (2016).
313. Champion, W. M., Rothfuss, N. E., Petters, M. D. & Grieshop, A. P. Volatility and Viscosity Are Correlated in Terpene Secondary Organic Aerosol Formed in a Flow Reactor. *Environmental Science and Technology Letters* (2019) doi:10.1021/acs.estlett.9b00412.
314. Maclean, A. M. *et al.* Humidity-Dependent Viscosity of Secondary Organic Aerosol from Ozonolysis of β -Caryophyllene: Measurements, Predictions, and Implications. *ACS Earth and Space Chemistry* **5**, 305–318 (2021).
315. Song, M. *et al.* Liquid-liquid phase separation and viscosity within secondary organic aerosol generated from diesel fuel vapors. *Atmospheric Chemistry and Physics* **19**, 12515–12529 (2019).
316. Li, Y., Carlton, A. G. & Shiraiwa, M. Diurnal and Seasonal Variations in the Phase State of Secondary Organic Aerosol Material over the Contiguous US Simulated in CMAQ. *ACS Earth and Space Chemistry* **5**, 1971–1982 (2021).
317. Maclean, A. M. *et al.* Mixing times of organic molecules within secondary organic aerosol particles: A global planetary boundary layer perspective. *Atmospheric Chemistry and Physics* **17**, 13037–13048 (2017).

318. Schmedding, R. *et al.* Predicting secondary organic aerosol phase state and viscosity and its effect on multiphase chemistry in a regional-scale air quality model. *Atmospheric Chemistry and Physics* **20**, 8201–8225 (2020).
319. Maclean, A. M. *et al.* Global Distribution of the Phase State and Mixing Times within Secondary Organic Aerosol Particles in the Troposphere Based on Room-Temperature Viscosity Measurements. *ACS Earth and Space Chemistry* **5**, 3458–3473 (2021).
320. Madronich, S. & Flocke, S. The role of solar radiation in atmospheric chemistry. *Handbook of Environmental Chemistry* (P. Boule, ed.) 1–26 (1998).
321. Grayson, J. W., Song, M., Sellier, M. & Bertram, A. K. Validation of the poke-flow technique combined with simulations of fluid flow for determining viscosities in samples with small volumes and high viscosities. *Atmospheric Measurement Techniques* **8**, 2463–2472 (2015).
322. Demond, A. H. & Lindner, A. S. Estimation of Interfacial Tension between Organic Liquids and Water. *Environmental Science and Technology* **27**, 2318–2331 (1993).
323. Gray Bé, A. *et al.* Cloud Activation Potentials for Atmospheric α -Pinene and β -Caryophyllene Ozonolysis Products. *ACS Central Science* **3**, 715–725 (2017).
324. Hritz, A. D., Raymond, T. M. & Dutcher, D. D. A method for the direct measurement of surface tension of collected atmospherically relevant aerosol particles using atomic force microscopy. *Atmospheric Chemistry and Physics* **16**, 9761–9769 (2016).
325. Gorkowski, K., Donahue, N. M. & Sullivan, R. C. Aerosol Optical Tweezers Constrain the Morphology Evolution of Liquid-Liquid Phase-Separated Atmospheric Particles. *Chem* **6**, 204–220 (2020).
326. Churaev, N. V, Sobolev, V. D. & Somov, A. N. Slippage of liquids over lyophobic solid surfaces. *Journal of Colloid And Interface Science* **97**, 574–581 (1984).
327. Zhu, L., Attard, P. & Neto, C. Reconciling slip measurements in symmetric and asymmetric systems. *Langmuir* **28**, 7768–7774 (2012).
328. Baudry, J., Charlaix, E., Tonck, A. & Mazuyer, D. Experimental evidence for a large slip effect at a nonwetting fluid-solid interface. *Langmuir* **17**, 5232–5236 (2001).
329. Joseph, P. & Tabeling, P. Direct measurement of the apparent slip length. *Physical Review E - Statistical, Nonlinear, and Soft Matter Physics* **71**, 1–4 (2005).
330. Vinogradova, O. I., Koynov, K., Best, A. & Feuillebois, F. Direct measurements of hydrophobic slippage using double-focus fluorescence cross-correlation. *Physical Review Letters* **102**, 1–4 (2009).
331. Tretheway, D. C. & Meinhart, C. D. Apparent fluid slip at hydrophobic microchannel walls. *Physics of Fluids* **14**, (2002).
332. McBride, S. P. & Law, B. M. Viscosity-dependent liquid slip at molecularly smooth hydrophobic surfaces. *Physical Review E - Statistical, Nonlinear, and Soft Matter Physics* **80**, 2–5 (2009).

333. Jing, D. & Bhushan, B. Boundary slip of superoleophilic, oleophobic, and superoleophobic surfaces immersed in deionized water, hexadecane, and ethylene glycol. *Langmuir* **29**, 14691–14700 (2013).
334. Craig, V. S. J., Neto, C. & Williams, D. R. M. Shear-Dependent boundary slip in an aqueous newtonian liquid. *Physical Review Letters* **87**, 54504-1-54504-4 (2001).
335. Cottin-Bizonne, C. *et al.* Nanorheology: An investigation of the boundary condition at hydrophobic and hydrophilic interfaces. *European Physical Journal E* **9**, 47–53 (2002).
336. Cottin-Bizonne, C., Cross, B., Steinberger, A. & Charlaix, E. Boundary slip on smooth hydrophobic surfaces: Intrinsic effects and possible artifacts. *Physical Review Letters* **94**, 1–4 (2005).
337. Cho, J. H. J., Law, B. M. & Rieutord, F. Dipole-dependent slip of Newtonian liquids at smooth solid hydrophobic surfaces. *Physical Review Letters* **92**, 1–4 (2004).
338. Bhushan, B., Wang, Y. & Maali, A. Boundary slip study on hydrophilic, hydrophobic, and superhydrophobic surfaces with dynamic atomic force microscopy. *Langmuir* **25**, 8117–8121 (2009).
339. Chesna, J. W. *et al.* Aerial wetting contact angle measurement using confocal microscopy. *Measurement Science and Technology* **27**, (2016).
340. Kourtchev, I. *et al.* Comparison of Heated Electrospray Ionization and Nanoelectrospray Ionization Sources Coupled to Ultra-High-Resolution Mass Spectrometry for Analysis of Highly Complex Atmospheric Aerosol Samples. *Analytical Chemistry* **92**, 8396–8403 (2020).
341. Silva, F. M. A. *et al.* Chemotaxonomy of the Amazonian Unonopsis Species Based on Leaf Alkaloid Fingerprint Direct Infusion ESI-MS and Chemometric Analysis. *Article J. Braz. Chem. Soc* **27**, 599–604 (2016).
342. Chekmeneva, E. *et al.* Optimization and Application of Direct Infusion Nanoelectrospray HRMS Method for Large-Scale Urinary Metabolic Phenotyping in Molecular Epidemiology. *Journal of Proteome Research* **16**, 1646–1658 (2017).
343. Jaitly, N. *et al.* Decon2LS: An open-source software package for automated processing and visualization of high resolution mass spectrometry data. *BMC Bioinformatics* **10**, 1–15 (2009).
344. Petters, S. S., Kreidenweis, S. M., Grieshop, A. P., Ziemann, P. J. & Petters, M. D. Temperature- and Humidity-Dependent Phase States of Secondary Organic Aerosols. *Geophysical Research Letters* **46**, 1005–1013 (2019).
345. Ullmann, D. A. *et al.* Viscosities, diffusion coefficients, and mixing times of intrinsic fluorescent organic molecules in brown limonene secondary organic aerosol and tests of the Stokes-Einstein equation. *Atmospheric Chemistry and Physics* **19**, 1491–1503 (2019).
346. Zhang, Y. *et al.* Changing shapes and implied viscosities of suspended submicron particles. *Atmospheric Chemistry and Physics* **15**, 7819–7829 (2015).
347. Galeazzo, T. *et al.* Estimation of secondary organic aerosol viscosity from explicit modeling of gas-phase oxidation of isoprene and α -pinene. *Atmospheric Chemistry and Physics* **21**, 10199–10213 (2021).

348. Bae, E. *et al.* Study of double bond equivalents and the numbers of carbon and oxygen atom distribution of dissolved organic matter with negative-mode FT-ICR MS. *Analytical Chemistry* **83**, 4193–4199 (2011).
349. Gonsior, M. *et al.* Photochemically induced changes in dissolved organic matter identified by ultrahigh resolution fourier transform ion cyclotron resonance mass spectrometry. *Environmental Science and Technology* **43**, 698–703 (2009).
350. DeRieux, W. S. W. *et al.* Predicting the glass transition temperature and viscosity of secondary organic material using molecular composition. *Atmospheric Chemistry and Physics* **18**, 6331–6351 (2018).
351. Li, Y., Day, D. A., Stark, H., Jimenez, J. L. & Shiraiwa, M. Predictions of the glass transition temperature and viscosity of organic aerosols from volatility distributions. *Atmos. Chem. Phys* **20**, 8103–8122 (2020).
352. Quinkert, G. Photochemistry. Von J. G. Calvert und J. N. Pitts, jr. John Wiley & Sons, Inc., New York-London-Sydney 1966. 1. Aufl., XVII, 899 S., zahlr. Abb., geb. DM 84.–. *Angewandte Chemie* **79**, 730–730 (1967).
353. Cope, J. D., Abellar, K. A., Bates, K. H., Fu, X. & Nguyen, T. B. Aqueous Photochemistry of 2-Methyltetrol and Erythritol as Sources of Formic Acid and Acetic Acid in the Atmosphere. *ACS Earth and Space Chemistry* **5**, 1265–1277 (2021).
354. Dette, H. P., Qi, M., Schröder, D. C., Godt, A. & Koop, T. Glass-forming properties of 3-methylbutane-1,2,3-tricarboxylic acid and its mixtures with water and pinonic acid. *Journal of Physical Chemistry A* **118**, 7024–7033 (2014).
355. Nguyen, T. B., Nizkorodov, S. A., Laskin, A. & Laskin, J. An approach toward quantification of organic compounds in complex environmental samples using high-resolution electrospray ionization mass spectrometry. *Analytical Methods* **5**, 72–80 (2013).
356. Angell, C. A. Relaxation in liquids, polymers and plastic crystals - strong/fragile patterns and problems. *Journal of Non-Crystalline Solids* **131–133**, 13–31 (1991).
357. Angell, C. A. Liquid fragility and the glass transition in water and aqueous solutions. *Chemical Reviews* **102**, 2627–2650 (2002).
358. Marsh, A. *et al.* Amorphous phase state diagrams and viscosity of ternary aqueous organic/organic and inorganic/organic mixtures. *Physical Chemistry Chemical Physics* **20**, 15086–15097 (2018).
359. Rothfuss, N. E. & Petters, M. D. Characterization of the temperature and humidity-dependent phase diagram of amorphous nanoscale organic aerosols. *Physical Chemistry Chemical Physics* **19**, 6532–6545 (2017).
360. Ruzmaikin, A., Aumann, H. H. & Manning, E. M. Relative humidity in the troposphere with AIRS. *Journal of the Atmospheric Sciences* **71**, 2516–2533 (2014).
361. Einstein, A. On the motion of small particles suspended in liquids at rest required by the molecular-kinetic theory of heat. *Annalen der Physik* **17**, 549–560 (1905).
362. Chen, X. & Hopke, P. K. Secondary organic aerosol from α -pinene ozonolysis in dynamic chamber system. *Indoor Air* **19**, 335–345 (2009).

363. Ng, N. L., Keywood, M. D., Bahreini, R., Lee, A. & Goldstein, A. H. Contribution of First- versus Secondary Organic Aerosols Formed Hydrocarbons. *Environmental Science & Technology* **40**, 2283–2297 (2006).
364. Saathoff, H. *et al.* Temperature dependence of yields of secondary organic aerosols from the ozonolysis of α -pinene and limonene. *Atmospheric Chemistry and Physics* **9**, 1551–1577 (2009).
365. Evoy, E. *et al.* Predictions of diffusion rates of large organic molecules in secondary organic aerosols using the Stokes-Einstein and fractional Stokes-Einstein relations. *Atmospheric Chemistry and Physics* **19**, 10073–10085 (2019).
366. Seinfeld, J. H. & Pandis, S. N. *Atmospheric Chemistry and Physics*. (Wiley, 2006).
367. Pöschl, U. *et al.* Rainforest aerosols as biogenic nuclei of clouds and precipitation in the Amazon. *Science (1979)* **329**, 1513–1516 (2010).
368. Murray, B. J. *et al.* Heterogeneous nucleation of ice particles on glassy aerosols under cirrus conditions. *Nature Geoscience* **3**, 233–237 (2010).
369. Centeno, G., Sánchez-Reyna, G., Ancheyta, J., Muñoz, J. A. D. & Cardona, N. Testing various mixing rules for calculation of viscosity of petroleum blends. *Fuel* **90**, 3561–3570 (2011).
370. Zhmud, B. Viscosity Blending Equations. *Lube Magazine* 2–5 (2014).
371. Crittenden, J. C., Trussell, R. R., Hand, D. W., Howe, K. J. & Tchobanoglous, G. *MWH 's Water Treatment - Principles and Design*. (John Wiley & Sons, Inc., Hoboken, New Jersey, 2012).
372. Petters, M. D. & Kreidenweis, S. M. A single parameter representation of hygroscopic growth and cloud condensation nucleus activity. *Atmospheric Chemistry and Physics* 1961–1971 (2007) doi:10.5194/acp-13-1081-2013.
373. Ignatius, K. *et al.* Heterogeneous ice nucleation of viscous secondary organic aerosol produced from ozonolysis of α -pinene. *Atmospheric Chemistry and Physics* **16**, 6495–6509 (2016).
374. Wagner, R. *et al.* Ice cloud processing of ultra-viscous/glassy aerosol particles leads to enhanced ice nucleation ability. *Atmospheric Chemistry and Physics* **12**, 8589–8610 (2012).
375. Wilson, T. W. *et al.* Glassy aerosols with a range of compositions nucleate ice heterogeneously at cirrus temperatures. *Atmospheric Chemistry and Physics* **12**, 8611–8632 (2012).
376. Zobrist, B. *et al.* Oxalic acid as a heterogeneous ice nucleus in the upper troposphere and its indirect aerosol effect. *Atmospheric Chemistry and Physics* **6**, 3115–3129 (2006).
377. Baustian, K. J. *et al.* State transformations and ice nucleation in amorphous (semi-)solid organic aerosol. *Atmospheric Chemistry and Physics* **13**, 5615–5628 (2013).
378. Charnawskas, J. C. *et al.* Condensed-phase biogenic–anthropogenic interactions with implications for cold cloud formation. *Faraday Discussions* **200**, 165–194 (2017).
379. Ladino, L. A., Zhou, S., Yakobi-Hancock, J. D., Aljawhary, D. & Abbatt, J. P. D. Factors controlling the ice nucleating abilities of α -pinene SOA particles. *Journal of Geophysical Research: Atmospheres* **119**, 9041–9051 (2014).

380. Wang, B. *et al.* The deposition ice nucleation and immersion freezing potential of amorphous secondary organic aerosol: Pathways for ice and mixed-phase cloud formation. *Journal of Geophysical Research: Atmospheres* **117**, 16209 (2012).
381. Schill, G. P., de Haan, D. O. & Tolbert, M. A. Heterogeneous ice nucleation on simulated secondary organic aerosol. *Environmental Science and Technology* **48**, 1675–1682 (2014).
382. Dalton, A. B. & Nizkorodov, S. A. Photochemical Degradation of 4-Nitrocatechol and 2,4-Dinitrophenol in a Sugar-Glass Secondary Organic Aerosol Surrogate. *Environ. Sci. Technol* **55**, 14586–14594 (1458).
383. Fleming, L. T. *et al.* Molecular composition and photochemical lifetimes of brown carbon chromophores in biomass burning organic aerosol. *Atmospheric Chemistry and Physics* **20**, 1105–1129 (2020).
384. Stavrakou, T. *et al.* Satellite evidence for a large source of formic acid from boreal and tropical forests. *Nature Geoscience* *2012 5:1* **5**, 26–30 (2011).